https://journals.vsu.ru/kcmf/about

ISSN 1606-867X
eISSN 2687-0711

КОНДЕНСИРОВАННЫЕ СРЕДЫ И МЕЖФАЗНЫЕ ГРАНИЦЫ

CONDENSED MATTER AND INTERPHASES

Том/Vol. 22, №/No. 1
2020

Condensed Matter and Interphases
(Kondensirovannye sredy i mezhfaznye granitsy)

Peer-reviewed scientific journal
Since January 1999
4 times a year

Volume 22, No. 1, 2020

eISSN 2687-0711

FOUNDER AND PUBLISHER
Voronezh State University

Condensed Matter and Interphases was founded by Dr. Sci. (Phys.-Math.), Dr. Sci. (Chem.), Prof. A. M. Khoviv (Voronezh) under the support of the Kurnakov Institute of General and Inorganic Chemistry RAS (Moscow) in January 1999

Registered by the Federal Service for Supervision of Communications, Information Technology and Mass Media (Roskomnadzor).
Certificate of registration
ПИ No ФС 77-28318 from 15.06.2007

The journal is included in the List of Russian Peer-Reviewed Scientific Journals recommended by the Higher Attestation Commission of the Russian Ministry of Education and Science that publishes dissertation abstracts submitted as partial fulfillment of the requirements for the degrees of Candidate and Doctor of Chemical Sciences, Physics Sciences (as per Russian classification of graduate degrees)

Condensed Matter and Interphases is indexed and archived in:
Russian Index of Scientific Citations, Scopus, RSCI,
Chemical Abstract, EBSCO,
DOAJ, CrossRef

Publisher and Editorial Office:
1, Universittetskaya pl., 394018
Voronezh,
Russian Federation
Telephone: +7 (473) 2208445
https://journals.vsu.ru/kcmf/about
E-mail: kcmf@main.vsu.ru

Date of publication 30 March 2020

All the materials of Condensed Matter and Interphases are available under Creative Commons "Attribution" 4.0 Global License

© Voronezh State University, 2020

EDITOR-IN-CHIEF
V. N. Semenov, DSc (Chem.), Prof. (Voronezh)

DEPUTY-EDITORS-IN-CHIEF:
V. A. Ketsko, DSc (Chem.) (Moscow)
E. P. Domashevskaya, DSc (Phys.-Math.), Prof. (Voronezh)

EDITORIAL BOARD:
N. N. Afonin, DSc (Chem.) (Voronezh)
A. V. Vvedenskii, DSc (Chem.), Prof. (Voronezh)
V. V. Gusarov, DSc (Chem.), Associate Member of the RAS (St. Petersburg)
V. E. Guterman, DSc (Chem.), Prof. (Rostov-on-Don)
B. M. Darinskii, DSc (Phys.-Math.), Prof. (Voronezh)
I. D. Zartsyn, DSc (Chem.), Prof. (Voronezh)
V. P. Zlomanov, DSc (Chem.), Prof. (Moscow)
V. M. Ievlev, DSc (Phys.-Math.), Full Academician of RAS (Moscow)
A. D. Izotov, DSc (Chem.), Associate Member of the RAS (Moscow)
A. N. Latyshev, DSc (Phys.-Math.), Prof. (Voronezh)
A. I. Marshakov, DSc (Chem.), Prof. (Moscow)
I. Ya. Mittova, DSc (Chem.), Prof. (Voronezh)
G. F. Novikov, DSc (Phys.-Math.), Prof. (Chernogolovka)
S. N. Saltykov, DSc (Chem.), Associate Prof. (Lipetsk)
V. F. Selemenev, DSc (Chem.), Prof. (Voronezh)
V. A. Terekhov, DSc (Phys.-Math.), Prof. (Voronezh)
E. A. Tutov, DSc (Phys.-Math.), Associate Prof., (Voronezh)
P. P. Fedorov, DSc (Chem.), Prof. (Moscow)
V. A. Khonik, DSc (Phys.-Math.), Prof. (Voronezh)
V. A. Shaposhnik, DSc (Chem.), Prof. (Voronezh)
A. B. Yaroslavtsev, DSc (Chem.), Associate Member of the RAS, (Moscow)

International members of editorial board:
M. B. Babanly, DSc(Chem.), Associate Member of the NASA (Baku, Azerbaijan)
T. Bellezze, DSc (Ancona, Italy)
P. M. Volovitch, PhD (Chem.), Habilitation (Paris, France)
V. B. Gorfinkel, DSc, Associate Prof., (Stony Brook, USA)
R. M. Mane, DSc (Kolhapur, India)
Nguyen Anh Tien, PhD (Chem.), Associate Prof. (Ho Chi Minh City, Vietnam)
V. V. Pan'kov, DSc, Prof. (Minsk, Belarus)
F. Scholz, DSc, Prof. (Greifswald, Germany)
M. S. Wickleder, DSc, Prof. (Köln, Germany)
V. Sivakov, DSc (Jena, Germany)

Responsible secretary
V. A. Logacheva, PhD (Chem.) (Voronezh)

CONTENTS

ORIGINAL ARTICLES

SHORT COMMUNICATIONS

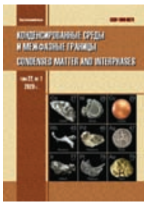

Condensed Matter and Interphases
(Kondensirovannye sredy i mezhfaznye granitsy)

Original articles

DOI: https://doi.org/10.17308/kcmf.2020.22/2524 eISSN 2687-0711
Received 26 January 2020
Accepted: 15 March 2020

Synthesis of Upconversion Luminophores Based on Calcium Fluoride

©2020 A. A. Alexandrov✉,[a,b], M. N. Mayakova[b], V. V. Voronov[b], D. V. Pominova[b], S. V. Kuznetsov[b], A. E. Baranchikov[c], V. K. Ivanov[c], E. I. Lysakova[a], P. P. Fedorov[b]

[a]*MIREA - Russian Technological University,*
86 Prospekt Vernadskogo, Moscow 119571, Russian Federation
[b]*Prokhorov General Physics Institute of the Russian Academy of Sciences, 38 Vavilov str., Moscow 119991, Russian Federation*
[c]*Kurnakov Institute of General and Inorganic Chemistry of the Russian Academy of Sciences,*
31 Leninsky prospekt, Moscow 119991, Russian Federation

Abstract
The aim of our study was to synthesize a luminophore based on calcium fluoride doped with rare-earth elements: 5 % Yb and 1 % Er, using the molten salt synthesis method.
$NaNO_3$ was used as a solvent and sodium fluoride NaF served as the fluorinating agent. The obtained samples were analysed and described using X-ray powder diffraction analysis, energy dispersive X-ray spectroscopy, scanning electron microscopy, and luminescence spectroscopy.
During the study we also investigated the effect of the synthesis conditions on the phase composition and the particles morphology. It was determined that single-phase samples (solid solutions based on calcium fluoride) can only be obtained at a temperature of at least 400 °C, with the optimal exposure time being 3 hours. The composition of the obtained samples was determined. It differs from the nominal composition and can be described as $Ca_{0.88}(Yb, Er)_{0.06}Na_{0.06}F_2$. It was demonstrated that the parallel insertion of sodium and rare-earth element ions increases the solubility limit of sodium fluoride in calcium fluoride. The luminescence efficiency was 1.21 %.
As a result of this study we obtained a new material with upconversion properties.

Keywords: luminophores, molten salt synthesis, inorganic fluorides, upconversion, nanopowders, rare-earth elements.

For citation: Alexandrov A. A., Mayakova M. N., Voronov V. V., Pominova D. V., Kuznetsov S. V., Baranchikov A. E., Ivanov V. K., Lysakova E. I., Fedorov P. P. Synthesis of upconversion luminophores based on calcium fluoride. *Kondensirovannye sredy i mezhfaznye granitsy = Condensed Matter and Interphases*. 2020; 22(1): 3–10. DOI: https://doi.org/10.17308/kcmf.2020.22/2524

1. Introduction

Anti-Stokes luminescence, or upconversion, occurs when a luminophore, excited by electromagnetic radiation at a certain wavelength, emits radiation with a shorter wavelength and thus with more energy. This phenomenon was independently discovered by V. Ovsyankin and P. Feofilov [1] and F. Auzel [2] in the mid-1960s. Since then, quite a number of upconversion luminophores have been synthesized. Fluorides are among the most promising classes of compounds used for synthesizing upconversion luminophores. Due to low-energy phonons, their mechanical and optical properties, as well as high isomorphic capacity, fluorides are good host matrices for doping with rare-earth ions. Due to the high upconversion efficiency of luminescence the most commonly used fluoride matrices include hexagonal modifications $NaYF_4$ [3] and

---

✉ Alexander A. Alexandrov,
e-mail: alexandrov1996@yandex.ru

$NaGdF_4$ [4], as well as fluorides of alkaline earth techniques, doped with Yb^{3+}, Er^{3+} [3,5–6].

At the moment, there are several common methods for the synthesis of fluorides, including coprecipitation from aqueous solutions [7–8], hydrothermal synthesis [9–10], solvothermal synthesis [5], the sol-gel method [11], mechanochemical synthesis [12], molten salt synthesis [13], combustion synthesis (CS) [6], and thermal decomposition of the precursors [14]. There are also methods which use ionic liquids as fluorinating agents, templates, and reaction media [15–16].

It is still important to search for new upconversion luminophores and develop new synthesis methods. Upconversion luminophores are applied in various areas of science and technology, including biomedicine [17], solar cells production [18], and thermometry [19]. Other applications of upconversion materials include the visualisation of infrared radiation [20] and synthesis of white light luminophores [21].

The aim of this study was to synthesise an upconversion luminophore based on a calcium fluoride matrix with a fluorite structure, doped with rare-earth elements (REE). Since the method of coprecipitation from aqueous solutions has certain drawbacks [6], our aim was also to determine the optimal conditions for the molten salt synthesis of single-phase calcium fluoride powders, doped with ytterbium and erbium. The choice of the concentrations of the doping rare-earth additives (5 mol% of Yb^{3+} and 1 mol% of Er^{3+}) was based on the fact that the highest upconversion efficiency of a similar fluorite matrix of SrF_2 was observed, when the concentration range of Yb^{3+} was between 2 mol% and 12 mol%, and of Er^{3+} between 0.25 mol% and 2.25 mol% [3,22].

2. Experimental

The starting materials were: calcium nitrate tetrahydrate $Ca(NO_3)_2 \cdot 4H_2O$ (Lanhit®, 99.99 %), yttrium(III) nitrate hexahydrate $Yb(NO_3)_3 \cdot 6H_2O$ (Lanhit®, 99.9%), erbium nitrate pentahydrate $Er(NO_3)_3 \cdot 5H_2O$ (Lanhit®, 99.99 %), sodium nitrate $NaNO_3$ (Chimmed Group, CP), and sodium fluoride NaF (Lanhit®, P.A.). All the substances were used without additional purification.

The samples were obtained by molten salt synthesis [13]. First, the weighed quantities of hydrates of calcium nitrate and REEs were homogenized in an agate mortar. Then, sodium nitrate was added to the mixture. It acted both as a solvent and the medium for the chemical reaction. Next, sodium fluoride was added, which acted as a fluorinating agent. The mixture was homogenized, put into a glazed porcelain crucible, covered, and annealed at a temperature of 300 or 400 °C for 1 or 3 hours. After the crucible cooled down, the reaction mass was taken out and put in a polypropylene reactor, where the nitrates were washed off the samples. The reactor is filled with 900 ml of double distilled water. Next, the anchor of the magnetic stirrer was put inside the reactor, and the mixture was stirred for 30 minutes. The presence of nitrate-ions was determined by the qualitative reaction with diphenylamine. It was usually enough to wash the samples three times to remove the nitrates. After the last washing the samples were dried in air at the temperature of 60 °C for 4 hours.

The characterisation of the obtained samples was performed using the X-ray powder diffraction analysis (XRD), scanning electron microscopy (SEM), energy dispersive X-ray spectroscopy (EDX), and luminescence spectroscopy. The XRD analysis was performed using a Bruker D8 Advanced diffractometer (Germany) with Cu$K\alpha$ radiation. The obtained diffraction pattern were analysed using DifWin and Powder2.0 software packages ($\Delta Q < 10$). The size of the particles and the morphology of the samples were studied by means of SEM using a Carl Zeiss NVision 40 scanning electron microscope (Germany) with an Oxford Instruments XMAX microprobe analyser (UK) (80 mm^2) for energy dispersive X-ray spectroscopy. The spectroscopic analysis included registering the spectra of upconversion luminescence and diffusely scattered laser radiation within the range of 300–1000 nm, and calculating the upconversion efficiency of upconversion luminescence. In order to conduct the measurements we used a combination of the fibre optic spectrometer LESA-01-BIOSPEC (BIOSPEC, Russia) with the UnoMomento software package, and a modified integrating sphere (Avantes, the Netherlands) connected by fibre-optic light carriers [23].

To carry out the measurements, the powder sample placed between two cover slips was put inside the integrating sphere. The radiation of the diode laser (974 nm wavelength) was focused on the sample so that the power density on the surface of the sample was 1 W/cm². The integrating sphere had been preliminary calibrated with LEDs of various wavelengths and known power, measured with a LabMax®-TO (Coherent, USA) [24]. The scattered laser radiation and upconversion luminescence were captured by optic fiber and transmitted to the spectrometer. The upconversion luminescence efficiency was calculated using the formula

$$EQ = \frac{P_e^S}{P_{974\_ab}^S} = \frac{P_e^S}{P_{974\_sc}^R - P_{974\_sc}^S}, \quad (1)$$

where P_e^S is the radiation power of the sample in the visible range, $P_{974\_ab}^S$ is the laser power absorbed by the sample.

The latter is calculated as the difference between $P_{974\_sc}^R$ – the power of the scattered radiation of the non-absorbing reference sample and $P_{974\_sc}^S$ – the power of the scattered radiation of the studied sample.

3. Results and discussion

In our study the synthesis was performed several times. The nominal composition of sample No. 1 was pure calcium fluoride. The other experiments were conducted in order to synthesise samples with the nominal composition $Ca_{0.94}Yb_{0.05}Er_{0.01}F_{2.06}$, using the equation:

$$\begin{aligned} &0.94\,Ca(NO_3)_2 \cdot 4\,H_2O + 0.05\,Yb(NO_3)_3 \cdot 6\,H_2O + \\ &+ 0.01\,Er(NO_3)_3 \cdot 5\,H_2O + 2.06\,NaF = \\ &= Ca_{0.94}Yb_{0.05}Er_{0.01}F_{2.06} + 4.11\,H_2O + 2.06\,NaNO_3\,. \end{aligned} \quad [2]$$

The conditions of the synthesis process and the actual yield are given in Table 1.

The X-ray diffraction patterns of the synthesised samples are shown in Fig.1. The calculated lattice parameters and the size of coherent scattering regions (CSR) are given in Table 2.

The peaks of the cubic phase were indexed on all the XRD patterns. They correspond to the cubic fluorite phase of calcium fluoride (JCPDS card No. 35-0816). Samples No. 2 and 3, in addition to the cubic phase, demonstrated the peaks of the hexagonal phase. The XRD patterns of samples No. 4 and 5 demonstrated five peaks. A (200) peak appeared, which was suppressed in case of pure calcium fluoride. A broadening of the cubic phase peaks was observed. The size of the CSRs was calculated according to the Scherrer equation.

The lattice parameters of the cubic phase of samples No. 2 and 3 coincide with the parameters of pure calcium fluoride a = 5.463 Å. Samples No. 4 and 5 are single-phase. The lattice parameters of their cubic phases should increase, since their unit cells contained ions of rare-earth elements [25]. However, the lattice parameters of samples No. 4 and 5 are lower than the lattice parameters of pure CaF_2. This means that the crystal lattice was intercalated with ions with smaller ionic radii, which is quite possible, since there was a lot of sodium in the system. According to the EDX results presented in Table 3, there actually was sodium in the samples, and its amount is comparable to the number of rare-earth ions. The concentration of erbium is within the margin of error for the EDX method.

Table 1. Synthesis conditions and actual yield

Sample No.	Sample code	Annealing temperature, °C	Annealing time, hours	Concentrations of the starting materials, mol. (M, Ln)$(NO_3)_x$: NaF:$NaNO_3$	Actual yield, %
1	F1804	300	1	1:3:2	87.0
2	F1814	300	1	1:3:2	86.2
3	F1826	300	3	1:3:2	91.2
4	F1699	400	1	1:3:10	77.2
5	F1836	400	3	1:3:2	76.0

Table 2. The results of the XRD analysis

Sample No.	Lattice parameter a (cubic phase), Å	CSR size, nm
1	5.460(1)	32
2	5.463(2)	24
3	5.464(1)	24
4	5.452(1)	23
5	5.455(1)	41

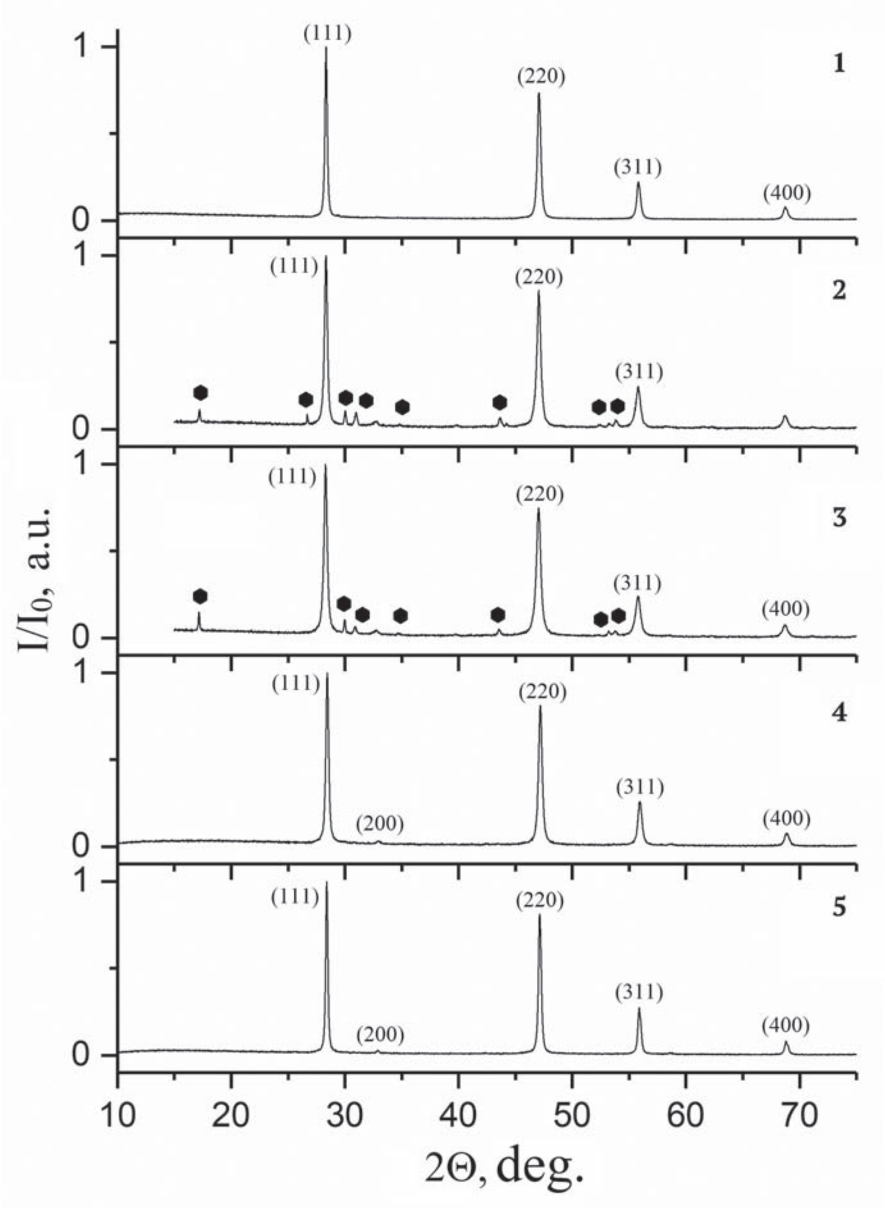

Fig. 1. Results of the XRD analysis. Dots denote the peaks of the hexagonal $NaYF_4$ phase. Sample numbers are the same as in Table 1

Table 3. The EDX results, in atomic percent

Sample No.	Na, at.%	Ca, at.%	Yb, at.%
4	6	88	6
5	6	88	6

Thus, the composition of the single-phase samples is different from the nominal composition. Certain lattices contained sodium, which was inserted together with REEs. Isomorphic substitutions can be represented as

$$2Ca^{2+} \rightarrow Na^{+} + Ln^{3+}, \quad (3),$$

where Ln = Yb, Er. This kind of joint intercalation means that the sodium ions had an increased solubility limit. The maximal solubility in the system NaF – CaF_2 is 2.2 mol.% [26]. Heterovalent isomorphism of this type is common for NaF – CaF_2 – LnF_3 systems [27-28].

SEM photographs of samples No. 3, 4, and 5 and their resolutions are given in Figures 2–4.

Fig. 2 shows a rod-like particle, several microns in size, with a hexagonal cross-section surrounded by an agglomeration of particles (a few dozen nanometres) with no definite faceting, which implicitly confirms that sample No. 3 is two-phase. Microphotogaphs in Fig. 3 and 4 demonstrate the morphological homogeneity

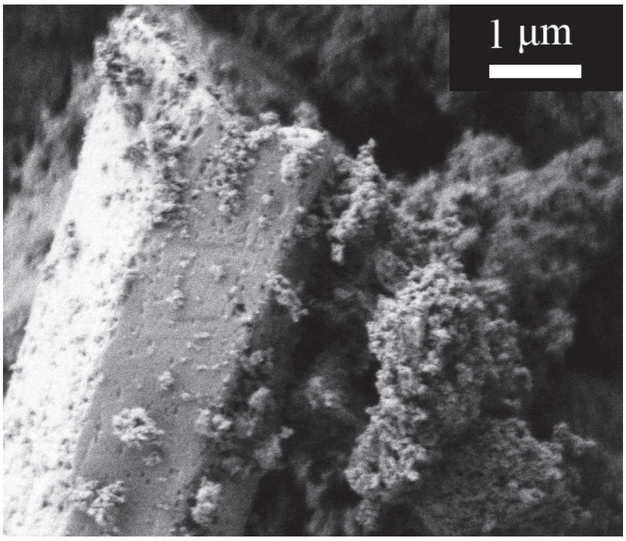

Fig. 2. SEM photograph of sample No. 3

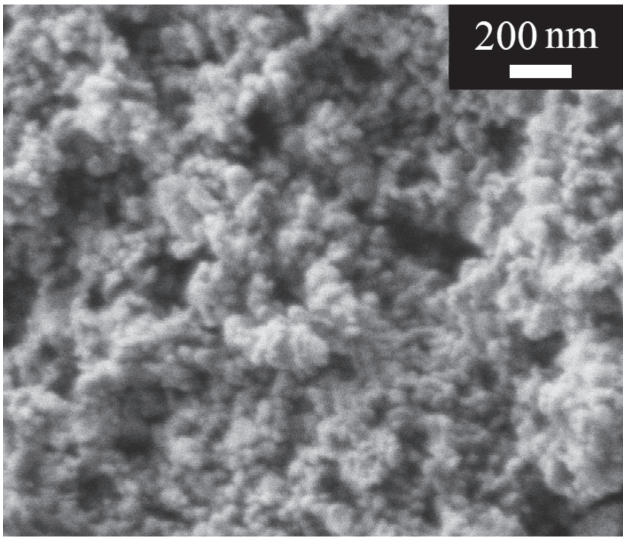

Fig. 3. SEM photograph of sample No. 4

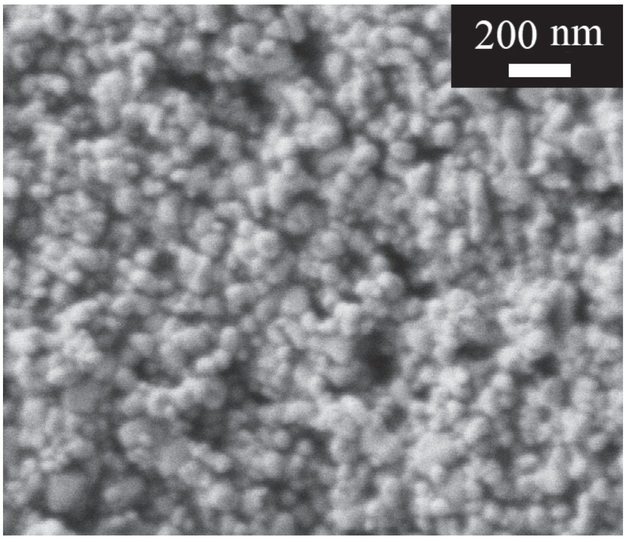

Fig. 4. SEM photograph of sample No. 5

and high dispersion of particles in samples No. 4 and 5. The particles in sample No. 5 are larger than those in sample No. 4, which complies with the calculations of CSR size. The average size of the particles in both samples is below 120 nm.

The luminescence spectra of samples No. 4 and 5 are given in Fig. 5.

The luminescence spectra of the samples show green (510–575 nm) and red (625–670 nm) bands, corresponding to the radiative transitions of the erbium ions $^2H_{11/2}, ^4S_{3/2} \rightarrow {}^4I_{15/2}$ and $^4F_{9/2} \rightarrow {}^4I_{15/2}$. The upconversion efficiency was 0.02 % for sample No. 4, and 1.21 % for sample No. 5. The difference in the values of upconversion efficiency may be accounted for by the larger size of the particles in sample No. 5 (resulting from the longer synthesis), which leads to the decrease in the surface area to volume ratio.

The obtained results lead to several conclusions. First, when the temperature is 300 °C, two-phase samples are formed. At higher temperatures the hexagonal phase $NaLnF_4$ disappears from the reaction system. According to the XRD results, the samples obtained at 400 °C are single-phase. Also, the calculated lattice parameters are lower than those of calcium fluoride, even though their crystal lattices were intercalated with REE ions. Our assumption that the lattice contained sodium ions was confirmed by the EDX results. The concentration of sodium is comparable to the concentration of Yb^{3+} and Er^{3+}. Thus, while developing the technology, we obtained a new material CaF_2:Na^+, Yb^{3+}, Er^{3+} with upconversion properties.

Second, the SEM analysis allowed us to describe the morphology of the particles of single-phase powders. The particles are spherical, highly homogeneous, and have particle size distribution within a narrow range. When the samples are annealed for a longer time, the particles continue growing, and their size reaches 60–120 nm. This results in a higher volume to surface area ratio, and hence increased luminescence.

The luminescence spectra confirm the upconversion properties of the material. When excited with IR laser at a wavelength of 974 nm, the material demonstrates two luminescence bands in the visible range: in the green and

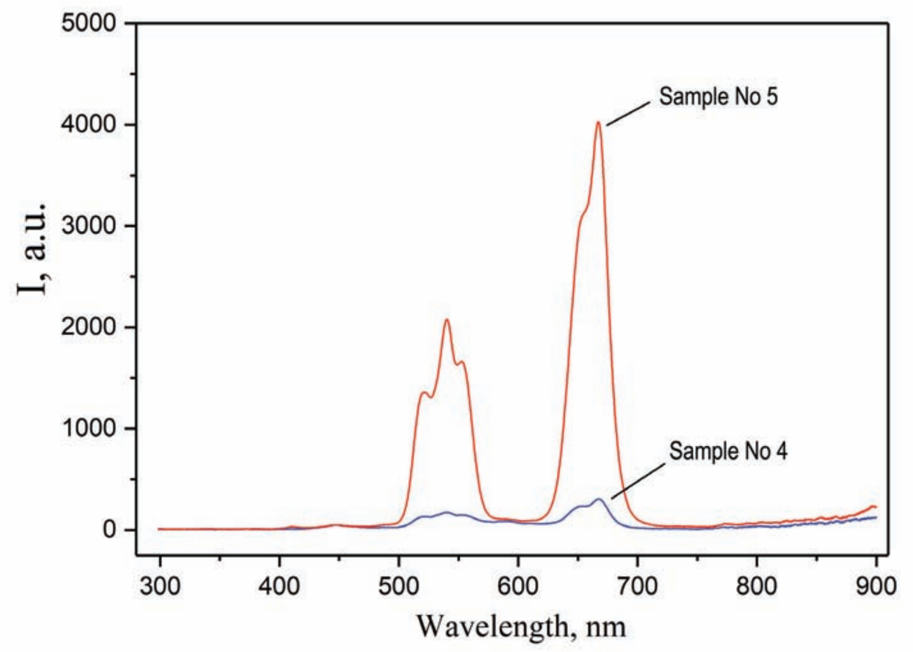

Fig. 5. Luminescence spectra of samples No. 4 and 5. The wavelength of the pumping laser is 974 nm

red spectra. The upconversion luminescence efficiency of the samples is lower than that of a similar material obtained by coprecipitation from aqueous solutions: 1.21 % as compared to 3.11 % [8]. This is partly accounted for by the insertion of sodium in the crystal lattice. Nevertheless, the molten salt synthesis method has a number of advantages. For instance, the pyrohydrolysis process is slower, and the EDX results confirm that the samples do not contain oxygen. The molten salt synthesis is also easy to perform, does not involve dangerous reagents, such as hydrofluoric acid, and there is no need to reconstruct the precise synthesis conditions to reproduce the results. Also, the adsorbed water can be removed without further thermal treatment.

4. Conclusions

During our study, we determined the conditions for the synthesis of calcium fluoride powder doped with ytterbium and erbium ions with upconversion properties. We obtained a single-phase sample with the composition $Ca_{0.88}(Yb, Er)_{0.06}Na_{0.06}F_2$, which differs from the nominal. It was determined, that the crystal lattice of the obtained solid solution included sodium ions. The joint intercalation of sodium and REE ions increases the solubility limit of sodium fluoride in calcium fluoride up to 6 mol. % against 2.2 mol. %, as determined by previous studies. The study demonstrated that the synthesis conditions influence the morphology and phase composition of the particles. Two-phase samples are obtained at 300 °C (CaF_2 + $NaLnF_4$), and single-phase samples at 400 °C. The size of the particles increases with longer annealing time. The obtained sample demonstrates upconversion properties. When pumped with 974 nm wavelength laser, green and red luminescence bands are detected. Due to its upconversion luminescence properties, the obtained material can find various applications in biomedicine.

Acknowledgements

All the experiments were performed on the equipment kindly provided by the Joint Research Centre for the Physical Methods of Research of Prokhorov General Physics Institute of the Russian Academy of Sciences and the Joint Research Centre for the Physical Methods of Research of Kurnakov Institute of General and Inorganic Chemistry of the Russian Academy of Sciences

Conflict of interests

The authors declare that they have no known competing financial interests or personal relationships that could have influenced the work reported in this paper.

References

1. Ovsjankin V. V., Feofilov P. P. O mehanizme summirovanija jelektronnyh vozbuzhdenij v aktivirovannyh kristallah [On the mechanism of combination of electron excitations in activated crystals]. *JETP Letters*. 1966;3(12): 494–497.

2. Auzel F. Compteur quantique par transfert d'energie entre deux ions de terres rares dans un tungstate mixte et dans un verre. *C. R. Acad. Sci. B*. 1966;262: 1016–1019.

3. Fedorov P. P., Kuznetsov S. V., Osiko V. V. Elaboration of nanofluorides and ceramics for optical and laser applications. In: Tressaud A., Poeppelmeier K. (eds.) *Photonic and electronic properties of fluoride materials: Progress in fluorine science series*. Amsterdam: Elsevier; 2016. p. 7–31. DOI: http://doi.org/10.1016/B978-0-12-801639-8.00002-7

4. Kostiv U., Rajsiglova L., Luptakova D., Pluhacek T., Vannucci L., Havlicek V., Engstova H., Jirak D., Slouf M., Makovicky P., Sedlacek R., Horak D. Biodistribution of upconversion/magnetic silica-coated $NaGdF_4$:Yb^{3+}/Er^{3+} nanoparticles in mouse models. *RSC Adv*. 2017;7: 45997–46006. DOI: https://doi.org/10.1039/c7ra08712h

5. Zhao J., Zhu Y.-J., Chen F. Microwave-assisted solvothermal synthesis and upconversion luminescence of CaF_2:Yb^{3+}/Er^{3+} nanocrystals. *J. Colloid Interface Sci.* 2015;440: 39–45. DOI: http://doi.org/10.1016/j.jcis.2014.10.031

6. Rakov N., Maciel G.S., Xiao M. Upconversion fluorescence and its thermometric sensitivity of Er^{3+}: Yb^{3+} co-doped SrF_2 powders prepared by combustion synthesis. *Electron. Mater. Lett.* 2014;10(5): 985–989. DOI: https://doi.org/10.1007/s13391-014-4030-9

7. Zhiping Z., Yingsen Y., Quamin S., Xiaotang L., Bingfu L., Yun Y. Preparation and characterization of CaF_2:Yb^{3+}, Er^{3+} up-conversion phosphor. *Sci. Adv. Mater*. 2017;9(3–4): 523–527. DOI: https://doi.org/10.1166/sam.2017.2334

8. Vakhrenev R. G., Mayakova M. N., Kuznetsov S. V., Ryabova A. V., Pominova D. V., Voronov V. V., Fedorov P. P. The research of synthesis and luminescent characteristics of calcium fluoride doped with ytterbium and erbium for biomedical application. *Kondensirovannye sredy i mezhfaznye granicy = Condensed Matter and Interphases*. 2016;18(4): 487–493. Available at: https://journals.vsu.ru/kcmf/article/view/157 (In Russ., abstract in Eng.)

9. Yu. S., Zhi Y., Su H. Hydrothermal synthesis and upconversion properties of CaF_2:Er^{3+}/Yb^{3+} nanocrystals. *J. Nanosci. Nanotechnol*. 2014;14: 3380–3386. DOI: https://doi.org/10.1166/jnn.2014.7991

10. Ansaru A. A., Yadav R., Rai S. B. Physiochemical properties of greatly enhanced photoluminescence of aqueous dispersible upconversion CaF_2:Yb/Er nanoparticles. *Photochem. Photobiol. Sci*. 2017;16: 890–896. DOI: https://doi.org/10.1039/c6pp00448b

11. Rehmer A., Scheurell K., Kemnitz E., Formation of nanoscopic CaF_2 via a fluorolytic sol–gel process for antireflective coatings. *J. Mater. Chem. C*. 2015;3: 1716–1723. DOI: http://doi.org/10.1039/c4tc02510e

12. Ritter B., Krahl T., Scholz G., Kemnitz E. Local Structures of Solid Solutions $Sr_{1-x}Y_xF_{2+x}$ (x = 0...0.5) with fluorite structure prepared by sol–gel and mechanochemical syntheses. *J. Phys. Chem. C*. 2016;120(16): 8992–8999. DOI: http://doi.org/10.1021/acs.jpcc.6b01834

13. Fedorov P. P., Mayakova M. N., Alexandrov A. A., Voronov V. V., Kuznetsov S. V., Baranchikov A. E., Ivanov V. K. The melt of sodium nitrate as a new medium for synthesis of fluorides. *Inorganics*. 2018;6: 1–17. DOI: https://doi.org/10.3390/inorganics6020038

14. Ha J.-W., Sohn E.-H., Park I. J., Lee S.-B. Preparation of CaF_2 microspheres by thermal decomposition of trifluoroacetate precursor in molten salt medium. *Mater. Lett.* 2017;209: 357–359. DOI: http://doi.org/10.1016/j.matlet.2017.08.029

15. Chen C., Sun L.-D., Li Z.-X., Li L.-L., Zhung J., Zhang Y.-W., Yan C.-H. Ionic liquid-based route to spherical $NaYF_4$ nanoclusters with the assistance of microwave radiation and their multicolor upconversion luminescence. *Langmuir*. 2010;26(11): 8797–8803. DOI: http://doi.org/10.1021/la904545a

16. Guo H., Guo Y., Noh H. M., Moon B. K., Park S. H., Jeong J. H., Kim K. H. Elaboration, structure and luminescence of sphere-like CaF_2:RE submicroparticles by ionic liquids based hydrothermal process. *J. Nanosci. Nanotechnol*. 2016;16: 1146–1150. DOI: https://doi.org/10.1166/jnn.2016.10800

17. Deng X., Dai Y., Liu J., Zhou Y., Ma P., Cheng Z., Chen Y., Deng K., Li X., Hou Z., Li C., Lin J. Multifunctional hollow CaF_2:Yb^{3+}/Er^{3+}/Mn^{2+}-poly(2-Aminoethyl methacrylate) microspheres for Pt(IV) pro-drug delivery and tri-modal imaging. *Biomaterials*. 2015;50: 154–163. DOI: https://doi.org/10.1016/j.biomaterials.2015.01.040

18. Liang L., Liu Y., Bu C., Guo L., Sun W., Nuang N., Peng T., Sebo B., Pan M., Liu W., Guo S., Zhao X.-Z. Highly uniform, bifunctional core/double shell structured β-$NaYF_4$:Er^{3+}, Yb^{3+} @ SiO_2@TiO_2 hexagonal sub microprisms for high performance dye sensitized solar cells. *Adv. Mater*. 2013;25: 2174–2180. DOI: https://doi.org/10.1002/adma.201204847

19. Balabhadra S., Debasu M. L., Brites C. D. S., Ferreira R. A. S. Upconverting nanoparticles working as primary thermometers in different media. *J. Phys. Chem. C.* 2017;121: 13962–13968. DOI: https://doi.org/10.1021/acs.jpcc.7b04827

20. Rozhnova Yu. A., Kuznetsov S. V., Voronov V. V., Fedorov P. P. Synthesis of up-conversion Ho^{3+} and Er^{3+} doped strontium fluoride luminophores for visualiser of two-micron radiation. *Kondensirovannye sredy i mezhfaznye granicy = Condensed Matter and Interphases.*

2016;18(3): 408–413. Available at: https://journals.vsu.ru/kcmf/article/view/150 (In Russ., abstract in Eng.)

21. Rozhnova Yu. A., Luginina A. A., Voronov V. V., Ermakov R. P., Kuznetsov S. V., Ryabova A. V., Pominova D. V., Arbenina V. V., Osiko V. V., Fedorov P. P. White light luminophores based on $Yb^{3+}/Er^{3+}/Tm^{3+}$-coactivated strontium fluoride powders. *Mater. Chem. Phys.* 2014; 148: 201–207. DOI: https://doi.org/10.1016/j.matchemphys.2014.07.032

22. Kuznetsov S., Ermakova Yu., Voronov V., Fedorov P., Busko D., Howard I. A., Richards B. S., Turshatov A. Up-conversion quantum yields of SrF_2: Yb^{3+}, Er^{3+} sub-micron particles prepared by precipitation from aqueous solution. *J. Mater. Chem. C*. 2018;6: 598–604. DOI: https://doi.org/10.1039/c7tc04913g

23. Yasyrkina D. S., Kuznetsov S. V., Ryabova A. V., Pominova D. V., Voronov V. V., Ermakov R.P., Fedorov P. P. Dependence of quantum yield of upconversion luminescence on the composition of fluorite-type solid solution $NaY_{1-x-y}Yb_xEr_yF_4$. *Nanosystems: physics, chemistry, mathematics*. 2013;4(5): 648–656. Available at: https://cyberleninka.ru/article/n/dependence-of-quantum-yield-of-up-conversion-luminescence-on-the-composition-of-fluorite-type-solid-solution-nay-1-x-yyb-xer-yf-4

24. Ryabova A. V., Pominova D. V., Krut'ko V. A., Komova M. G., Loschenov V. B. Spectroscopic research of upconversion nanomaterials based on complex oxide compounds doped with rare-earth ion pairs: Benefit for cancer diagnostics by upconversion fluorescence and radio sensitive methods. *Photon Lasers Med*. 2013;2: 117–128. DOI: https://doi.org/10.1515/plm-2013-0013

25. Fedorov P. P., Sobolev B. P. Concentration dependence of unit-cell parameters of phases $M_{1-x}R_xF_{2+x}$ with the fluorite structure. *Sov. Phys. Crystallogr*. 1992;37(5): 1210–1219.

26. Fedorov P. P., Mayakova M. N., Kuznetsov S. V., Maslov V. A., Pynenkov A. A., Uslamina M. A., Nishchev K. N., Sorokin N. I., Baranchikov A. E., Ivanov V. K. Phase diagram of the NaF–CaF_2 system and the electrical conductivity of a CaF_2-*based solid solution. Rus. J. Inorg. Chem*. 2016;61(11): 1529–1536. DOI: https://doi.org/10.1134/S003602361611005X

27. Sobolev B. P. *The rare earth trifluorides. P. 1. The high-temperature chemistry of the rare earth trifluorides*. Barcelona: Institut d'Estudis Catalans; 2000. 521 p.

28. Fedorov P. P., Rappo A. V. NaF-CaF_2-YbF_3 phase diagram. *Rus. J. Inorg. Chem*. 2008;53(7): 1210–1213. DOI: https://doi.org/10.1134/S0036023608070231

Information about the authors

Alexander A. Alexandrov, MSc student, MIREA – Russian Technological University, Institute of Fine Chemical Technologies named after Lomonosov, Moscow, Russian Federation; research technician, Prokhorov General Physics Institute of the Russian Academy of Sciences, Moscow, Russian Federation; e-mail: alexandrov1996@yandex.ru. ORCID iD: https://orcid.org/0000-0001-7874-7284.

Mariya N. Mayakova, PhD in Chemistry, Researcher, Prokhorov General Physics Institute of the Russian Academy of Science, Moscow, Russian Federation; e-mail: mn.mayakova@gmail.com. ORCID iD: https://orcid.org/0000-0003-0713-5357.

Valery V. Voronov, PhD in Physics and Mathematics, Head of the Laboratory, Prokhorov General Physics Institute of the Russian Academy of Science, Moscow, Russian Federation; e-mail: voronov@lst.gpi.ru. ORCID iD: https://orcid.org/0000-0001-5029-8560.

Daria V. Pominova, PhD in Physics and Mathematics, Researcher, Prokhorov General Physics Institute of the Russian Academy of Science, Moscow, Russian Federation; e-mail: pominovadv@gmail.com. ORCID iD: https://orcid.org/0000-0003-0713-5357.

Sergey V. Kuznetsov, PhD in Chemistry, Leading Researcher, Prokhorov General Physics Institute of the Russian Academy of Science, Moscow, Russian Federation; e-mail: kouznetzovsv@gmail.com. ORCID iD: https://orcid.org/0000-0002-7669-1106.

Alexander E. Baranchikov, PhD in Chemistry, Head of the Laboratory, Kurnakov Institute of General and Inorganic Chemistry of the Russian Academy of Sciences, Moscow, Russian Federation; e-mail: a.baranchikov@yandex.ru. ORCID iD: https://orcid.org/0000-0002-2378-7446.

Vladimir K. Ivanov, DSc in Chemistry, Associate Member of the Russian Academy of Sciences, Director of the Kurnakov Institute of General and Inorganic Chemistry of the Russian Academy of Sciences, Moscow, Russian Federation; e-mail: van@igic.ras.ru. ORCID iD: https://orcid.org/0000-0003-2343-2140.

Elena I. Lysakova, PhD in Chemistry, Associate Professor, MIREA - Russian Technological University, Institute of Fine Chemical Technologies named after Lomonosov, Moscow, Russian Federation; e-mail: elenalysakova@mail.ru. ORCID iD: https://orcid.org/0000-0001-6298-5712.

Pavel P. Fedorov, DSc in Chemistry, Head of the Department, Prokhorov General Physics Institute of the Russian Academy of Science, Moscow, Russian Federation; e-mail: ppfedorov@yandex.ru. ORCID iD: https://orcid.org/0000-0003-0713-5357.

All authors have read and approved the final manuscript.

Translated by Yulia Dymant.
Edited and proofread by Simon Cox.

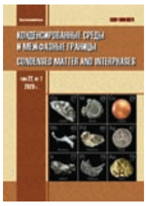
Condensed Matter and Interphases
(Kondensirovannye sredy i mezhfaznye granitsy)

Original articles

DOI: https://doi.org/10.17308/kcmf.2020.22/2471 eISSN 2687-0711
Received 22 January 2020
Accepted 15 March 2020

Studying of Viscoelastic Properties of Secondary Polymeric Materials in the Presence of Natural Plant Based Fillers

© 2020 R. M. Akhmetkhanov, A. R. Sadritdinov, V. P. Zakharov, A. S. Shurshina, E. I. Kulish✉

Bashkir State University, 32 Zaki Validi str., Ufa 450076 Russian Federation

Abstract

The purpose of this study was to investigate the rheological characteristics of a polymer composition based on secondary polypropylene and natural plant based fillers.

A sample of secondary polypropylene corresponding to the primary polypropylene of brand FF/3350 was used in this study. It is a crushed material from non-standard products produced by injection moulding in the technological production LLC “ZPI Alternative” (Russia, the Republic of Bashkortostan, Oktyabrsky). Industrial waste products, buckwheat husk, wheat chaff, rice husk and wood flour, were considered as fillers. The modelling of the processing of polymer materials was carried out in melt at the laboratory station (plastograph) “PlastographEC” (Brabender, Germany). The physical-mechanical properties of the polymer composites at break were determined by the tensile testing machine “ShimadzuAGS-X” (Shimadzu, Japan). Rheological measurements of the polymer composition melts was performed using a Haake Mars III rheometer.

The increase in the viscosity of the polypropylene melt occurring upon addition of fillers to the composition was revealed. The increase in filler content in the system increased not only the viscous properties, but also the elastic characteristics. It was established that as the polymer was filled with natural excipients, an increase in the storage modulus occurred, typical for systems showing elastic properties. Composites, characterized by high values of the storage modulus and correspondingly increased the values of Young’s modulus were formed, when rice husk and wood flour were used as fillers. It has been proven that the optimum filler content was a value corresponding to 10 mass.h.

Keywords: polymeric composition, rheology, secondary polypropylene, natural plant based fillers, viscoelastic properties.

Funding: The reported study was funded by RFBR, project number 19-33-90087.

For citation: Akhmetkhanov R. M., Sadritdinov A. R., Zakharov V. P., Shurshina A. S., Kulish E. I. Studying of viscoelastic properties of secondary polymeric materials in the presence of natural plant based fillers. *Kondensirovannye sredyimezhfaznyegranitsy = Condensed Matter and Interphases*. 2020;22(1): 11–17. DOI: https://doi.org/10.17308/kcmf.2020.22/2471

1. Introduction

The development and creation of polymer composite materials based on secondary polymer raw materials is a serious scientific task, especially important when it comes to the use of large-capacity polymers such as polyethylene or polypropylene [1–6]. Among the widest range of fillers used for creating composites, natural fillers, obtained on the basis of plant materials are of particular interest [7–13]. The introduction of natural fillers into the polymer matrix allows not only to reduce the cost of production by replacing part of the polymer with cheap raw materials, but also partially solve the biodegradability issue of the material, as well as to create a material with new properties [14–23].

Taking into consideration that the shear rate values realized in the processes of polymer processing by extrusion and injection moulding reach 1000 s^{-1}, the probability of occurrence of normal stresses caused by the manifestation of

---

✉ Elena I. Kulish, e-mail: onlyalena@mail.ru

elastic properties by the polymer melt is very high. The introduction of a filler to an even higher degree can complicate processing, due to an increase in the viscosity of the polymer melt [24]. Moreover, not only an increase in the viscosity, but also the elastic component of the viscous flow can take place. The fundamental importance of determining the elastic component is due to the fact that the elasticity that can become a factor determining flow anomalies, such as jet separation, the Weissenberg effect, etc., which limit productivity and can lead to spoilage [25–27].

The aim of this work was a comprehensive study of the rheological characteristics of the polymer composition based on secondary polypropylene (SPP) and plant based fillers. When choosing a filler, the following requirements were taken into account:

– low cost and availability;

– environmental safety of biodegradable products;

– the possibility of grinding with standard grinding equipment;

– high temperature of thermal decomposition;

– rapid biodegradation under environmental conditions.

2. Experimental

In the study, we used a SPP sample corresponding to the primary polypropylene (PP) of brand FF/3350, which is crushed material from non-standard products produced by injection moulding in the technological production LLC “ZPI Alternative” (Russia, the Republic of Bashkortostan, Oktyabrsky).

We considered industrial wastes: buckwheat husk, wheat chaff, rice husk, and wood flour as a filler. The characteristics of the used fillers are presented in Table 1. Before mixing, the filler was dried in an oven at 100 °C for 5 h.

The modelling of the processing of polymer materials was carried out in the melt at the laboratory station (plastograph) “PlastographEC” (Brabender, Germany) for 15 min at a load of 200 N at a temperature of 180 °C. The amount of loaded polymer composite was 25 g. The deformation-strength properties of the material were determined on pressed material samples with a thickness of 1 mm. The pressing was carried out on an automatic hydraulic press “AutoMH-NE” (Carver, USA) at 210 °C and pressure was held at 7000 kgf for 3 min. The physical-mechanical properties of polymer composites at break were determined according to GOST 11262-2017 using a “ShimadzuAGS-X” (Shimadzu, Japan) tensile testing machine at a temperature of 20 °C and a motion speed of the movable grip of the tensile testing machine of 1 mm/min. The melt flow rate (MFR) was determined at 190 °C with a load weight of 2.16 kg using a melt flow indexer. The composition was divided into segments every 30 s, the obtained samples were weighed and the average weight was calculated. Rheological measurements were carried out using a Haake Mars III modular dynamic rheometer at 220 °C in the oscillation mode in the oscillation frequency range from 0.01 to 100 Hz.

In oscillation mode, an alternating shear stress with a small amplitude was applied to the sample $\tau(t) = \tau_0 e^{iwt}$ and its deformation $\gamma(t) = \gamma_0 e^{(iwt+\delta)}$ with a phase shift δ relatively to the voltage was registered. Angular velocity ω related to the oscillation frequency was as follows:

$$\omega = 2\pi f,$$

where the frequency f in Hz (1 Hz = cycle/s); ω – 1/s or rad/s.

The total resistance of the sample to the applied deformation, called the complex modulus G^* was defined as:

$$G^* = G' + iG'' = \frac{\tau_0(t)}{Y_E(t)}.$$

In this equation, the quantities G' and G'':

$$G' = G^* \cos\delta = \frac{\tau_0}{\gamma_0}\cos\delta \text{ – storage modulus;}$$

Table 1. Characteristics of the used fillers

Filler	Chemical composition, % [28–31]		Average diameter, mm
	cellulose	lignin	
wood flour	42.0	31.0	0.17
rice husk	48.9	19.1	0.20
buckwheat husk	29.4	34.7	0.24
wheat chaff	51.0	19.5	0.19

$G'' = G^{*}\sin\delta = \dfrac{\tau_0}{\gamma_0}\sin\delta$ – loss modulus.

The term "storage modulus" indicates that the voltage energy was temporarily stored during the test, but can be returned later. The term "loss modulus" indicates that the energy used to initiate the flow is irreversibly converted into heat ("lost").

3. Results and discussion

It is well known that according to Newton's law, viscosity is a constant that should not depend on the shear rate $\dot{\gamma}$ nor on the frequency of exposure f (during test in the oscillation mode), i.e. $\eta \sim f^{n}$, where $n = 0$. Index n is easily defined as the slope of the logarithmic dependence of viscosity on the oscillation frequency. However, often the fluid flow disobeys Newton's law. For example, during the flow of pseudoplastic liquids, which include both solutions and polymer melts, a decrease in viscosity with an increase in shear rate (oscillation frequency) is characteristic, and the n value in the power dependence of viscosity on shear rate or oscillation frequency is $n < 1$.

The complex viscosity frequency of the oscillatory action curves in direct and logarithmic coordinates for a SPP white masterbatch melt filled with 2 and 10 % mass. wood flour are shown in Fig. 1. For the rest of the fillers, the curves were similar.

The analysis of the obtained data suggests that SPP melts, both in the absence of filler and in their presence, behave like typical pseudoplastic fluids, the viscosity of which decreases with increasing oscillation frequency. For all studied fillers, their addition to the composition leads to a clear increase in viscosity. Moreover, the more filler the composition contains, the more significant is the viscosity anomaly. This is evidenced by deviations of the slope depending on the complex viscosity on the frequency determined in the logarithmic coordinates (Table 2). For all the studied systems, the slope is non-zero, and the more filler that was in the composition, the higher was the value of the slope (in absolute value). The slope characterizes the degree of manifestation of the viscosity anomaly. It can be seen that for all four studied fillers, wood flour, rice husk, wheat chaff and buckwheat husk, the values of the slope deviate from the zero value characterizing a Newtonian fluid.

The accumulated data are presented in Table 2.

Also, as the filler content in the system increased, not only the viscous properties of the system increased, as evidenced by the complex viscosity values (Fig. 2) and MFR (Fig. 3), but also the elastic characteristics. This conclusion can be made based on an analysis of the dependences of the storage and loss modules on the oscillation frequency.

It was established that as the polymer is filled with plant components, a natural increase in the storage modulus occurs (Fig. 4). This behaviour of the system is characteristic of systems

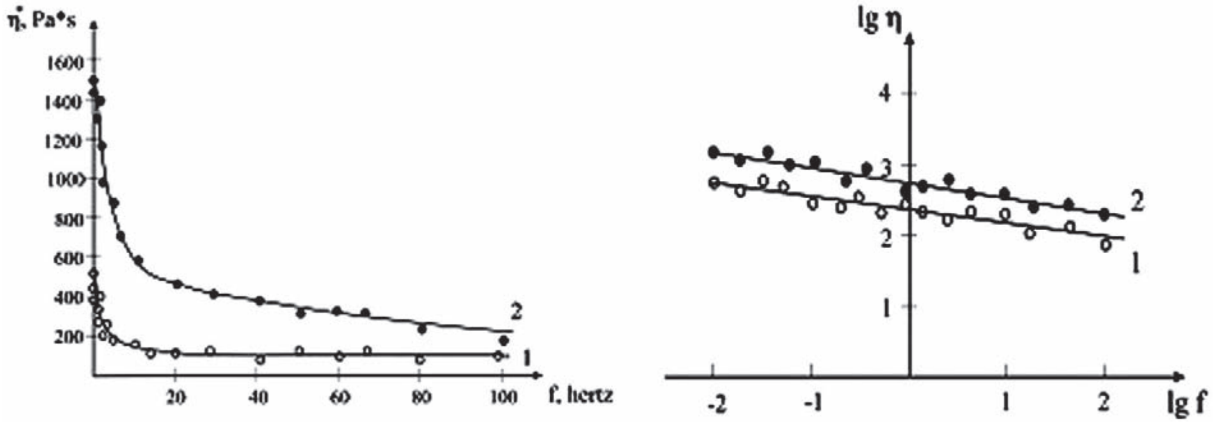

a b

Fig. 1. Dependence of complex viscosity of SPP determined in oscillatory mode in direct (a) and logarithmic (b) coordinates containing 2 (*1*) and 10 (*2*) mass.h. of wood flour

Table 2. Results of investigation of viscosity anomaly of secondary polymers filled with natural fillers

Polymer	Filler	Filler content, % mass.	Slope as a function of viscosity versus oscillation frequency
white master-batch	chaff	2	−0.15
		5	−0.16
		10	−0.18
		15	−0.21
		30	−0.26
	buckwheat husk	2	−0.15
		5	−0.16
		10	−0.17
		15	−0.18
		30	−0.19
	wood flour	2	−0.15
		5	−0.16
		10	−0.18
		15	−0.21
		30	−0.27
	rice husk	2	−0.12
		5	−0.15
		10	−0.16
		15	−0.18
		30	−0.24

exhibiting elastic properties. The highest values of the storage modulus were characteristic for composites filled with rice husk and wood flour. Buckwheat husk and chaff fillers increased the elastic properties of SPP melt to a lesser extent.

The value of the loss modulus from the filler content in the composite passes through a maximum (Fig. 5).

Moreover, it can be noted that when the filler content in the composition was higher than 10 mass.h. the general increase in the resistance of the system to the flow process was due to an increase in the elastic component of the viscous flow.

The study of the viscoelastic characteristics of secondary polymer raw materials in the presence of natural plant based fillers allowing to analyse the influence of the nature of the filler on the resistance of composites to mechanical stress.

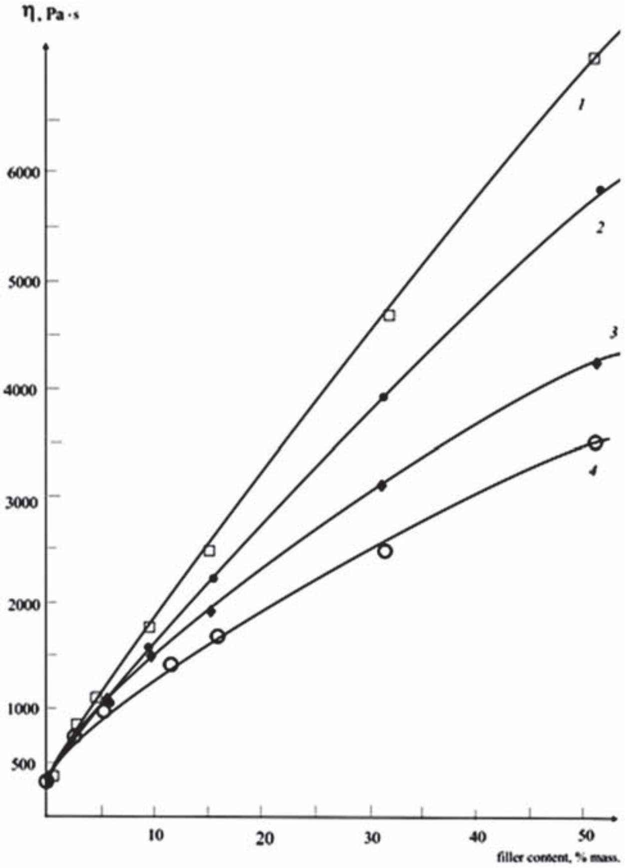

Fig. 2. Dependence of complex viscosity determined at oscillation frequency 0.01 Hz on content of rice husk (*1*), wood flour (*2*), buckwheat (*3*) and chaff (*4*) in the system

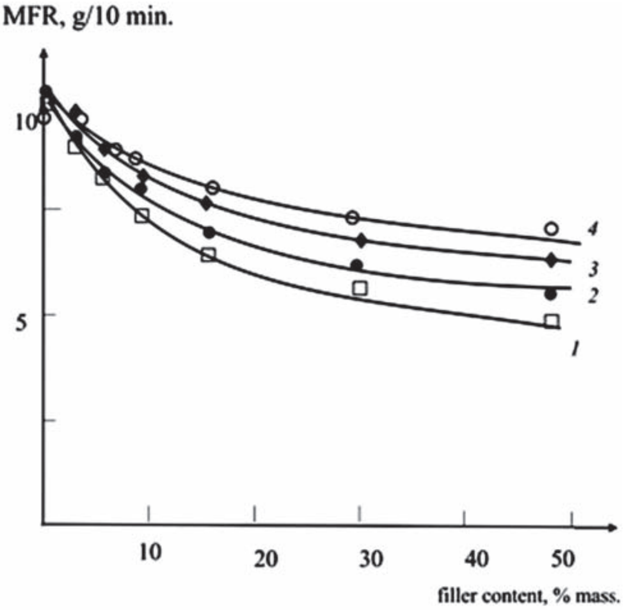

Fig. 3. Dependence of MFR of composition based on SPP at the content of rice husks (*1*), wood flour (*2*), buckwheat (*3*) and chaff (*4*) in the system

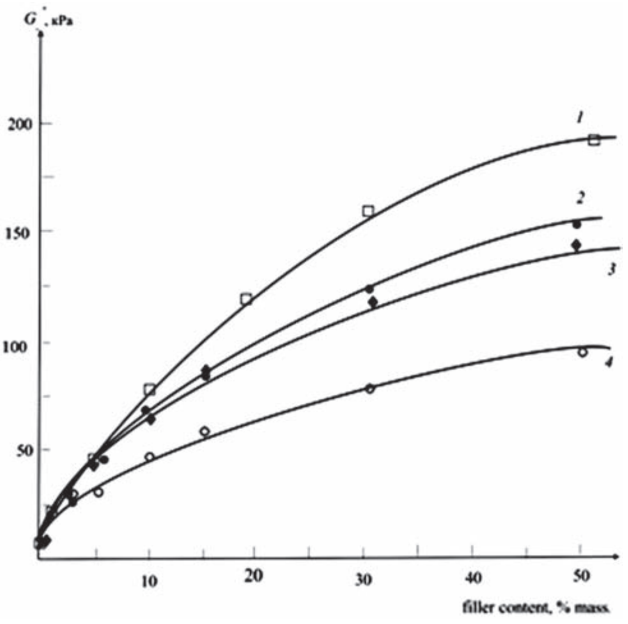

Fig. 4. Dependence of the storage modulus determined at an oscillation frequency of 100 Hz on the content of rice husks (*1*), wood flour (*2*), buckwheat (*3*) and chaff (*4*) in the system

For example, at a qualitative level there is a correlation of the rheological data determined in the oscillation mode and the elastic modulus values from the data of deformation-strength measurements. It can be noted that by the nature of the changes in Young's modulus *E* that all the analysed fillers unequivocally affected the polymer, they undergo an extreme change in the composition corresponding to 10% mass.h. of the filler (Fig. 6). The maximum values of Young's modulus were revealed for composites filled with rice husk and wood flour, e.g. for composites with maximum storage moduli.

Thus, based on an experiment conducted in the range of oscillation frequencies from 0.01 to 100 Hz, for the analysed SPP sample, the maximum viscosity values were realized when rice husk and wood flour were used as filler, and the minimum values were detected for chaff and buckwheat husks. Composites, characterized by high values of the storage modulus and correspondingly higher values of Young's modulus were formed when rice husks and wood flour were used as fillers. The optimal filler content had a value corresponding to 10 mass.h., which when exceeded, an increase in the elastic properties of the polymer melt was accompanied by a deterioration of the processing properties of the composites and their deformation-strength properties.

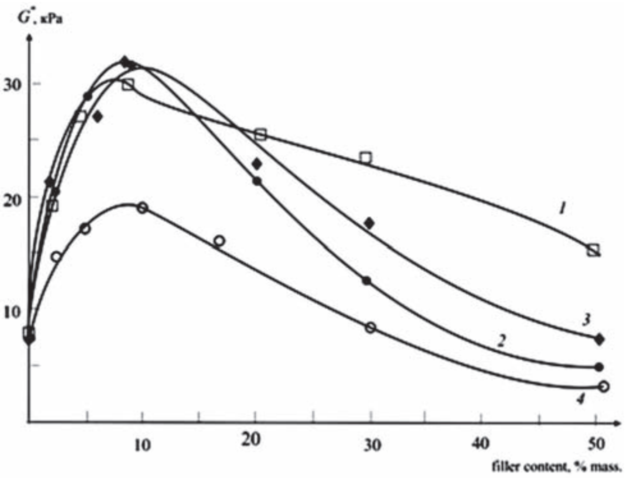

Fig. 5. Dependence of the loss modulus determined at an oscillation frequency of 100 Hz on the content of rice husks (*1*), wood flour (*2*), buckwheat (*3*) and chaff (*4*) in the system

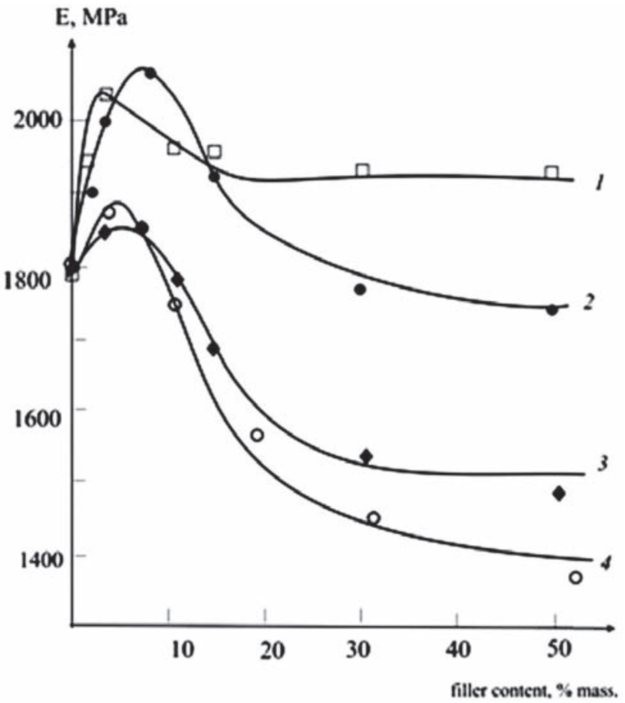

Fig. 6. Dependence of Young ‘s modulus of the composition based on SPP on the content of rice husks (*1*), wood flour (*2*), buckwheat (*3*) and chaff (*4*) in the system

4. Conclusions

1. The introduction of filler in all studied cases led to an increase in complex viscosity and a decrease in MFR. The more filler the composition

contained, the more significant was the viscosity anomaly, i.e., the dependence of viscosity on the oscillation frequency was stronger.

2. The increase in filler content in the system increased not only the viscous properties, but also the elastic characteristics. When the filler content in the composition was higher than 10 mass.h. the overall increase in the resistance of the system to the flow process was due to the increase in the elastic component of the viscous flow, since the storage modulus continued to increase, and the loss modulus started to decrease.

3. Based on the nature of the changes in Young's modulus, all analysed fillers possessed the same action on the polymer. They had maximum values in the composition region corresponding to a 10 mass.h. filler. Thus, the composition of a 10 mass.h. filler should be considered to be optimal.

Conflict of interests

The authors declare that they have no known competing financial interests or personal relationships that could have influenced the work reported in this paper.

References

1. Aizinson I. L. *Osnovnyye napravleniya razvitiya kompozitsionnykh termoplastichnykh materialov* [The main directions of development of composite thermoplastic materials]. Moscow: Khimiya Publ.; 1988. 48 p. (In Russ.)

2. Richardson M. *Promyshlennyye polimernyye kompozitsionnyye materialy* [Industrial Polymer Composite Materials]. Moscow: Khimiya Publ.; 1980. 472 p. (In Russ.)

3. Berlin Al. Al., Wolfson S. A., Oshmyan V. G., Enikolopyan N. S. *Printsipy sozdaniya kompozitsionnykh materialov* [The principles of creating composite materials]. Moscow: Khimiya Publ.; 1990. 238 p. (In Russ.)

4. Cherkashin A. N., Rassokha A. N. Polymeric compositions based on secondary polypropylene. *Actual scientific research in the modern world*. 2018;33(1–8): 125–131. Available at: https://elibrary.ru/item.asp?id=32366668 (In Russ.)

5. Tveritnikova I. S., Kirsh I. A., Pomogova D. A., Bannikova O. A., Beznaeva O. V., Romanova V. A. Development of multilayer packaging material based on polyolefin mixtures modified with a copolymer of ethylene with propylene for food storage. *Technique and technology of food production*. 2019;49(1): 135–143. Available at: https://elibrary.ru/item.asp?id=39276460 (In Russ.)

6. Kakhramanov N. T., Mustafayeva F. A., Allakhverdiyeva Kh. V. Technological features of extrusion of composite materials based on mixtures of high and low density polyethylene and mineral fillers. *Azerbaijan Chemical Journal*. 2019;4: 11–16. DOI: DOI: https://doi.org/10.32737/0005-2531-2019-4-11-16

7. Shkuro A. E., Glukhikh V. V., Krivonogov P. S., Stoyanov O. V. Fillers of agricultural origin for wood-polymer composites (review). *Bulletin of Kazan Technological University*. 2014;17(21): 160–163. Available at: https://www.kstu.ru/article.jsp?id_e=23840&id=1910 (In Russ.)

8. Katz G. S., Milevsky D. V. (eds.) *Napolniteli dlya polimernykh kompozitsionnykh materialov* [Fillers for polymer composite materials]. Moscow: Khimiya Publ.; 1981. 736 p. (In Russ.)

9. Alimov I. M., Magrupov F. A., Ilhamov G. U. The effect of the fractional composition of wood particles on the physicomechanical properties of wood-polymer materials based on secondary polyolefins. *Woodworking industry*. 2019;1: 18–25. Available at: http://dop1952.ru/catalogue-statue_id-298.html (In Russ.)

10. Dobah Y., Zampetakis I., Ward C., Scarpa F. Thermoformability characterization of flax reinforced polypropylene composite materials. *Composites Part B: Engineering*. 2020;184(1): 107727. DOI: https://doi.org/10.1016 / j.compositesb.2019.107727

11. Prachayawarakorn J., Pomdage W. Effect of carrageenan on properties of biodegradable thermoplastic cassava starch/low density polyethylene composites reinforced by cotton fibers. *Materials and Design*. 2014;61: 264–269. DOI: https://doi.org/10.1016/j.matdes.2014.04.051

12. Ibrahim H., Farag M., Megahed H., Mehanny S. Characteristics of starch-based biodegradable composites reinforced with date palm and flax fibers. *Carbohyd polym*. 2014; 101(1): 11–19. DOI: https://doi.org/10.1016 / j.carbpol.2013.08.08.051

13. Cavdar A. D., Mengeloplu F., Karakus K. Effect of boric acid and borax on mechanical, fire and thermal properties of wood flour filled high density polyethylene composites. *Measurement: Journal of the International Measurement Confederation*. 2015; 60: 6–12. DOI: https://doi.org/10.1016 /j.measurement.2014.09.0.078

14. Faruk O., Bledzki AK, Fink H. Biocomposites reinforced with natural fibers: 2000-2010. *Prog. Polym. Sci*. 2012;37(11): 1552–1596. DOI: https://doi.org/10.1016/j.progpolymsci.2012.04.003

15. Boudenne A., Ibos L., Candau Y., Thomas S. *Handbook of multiphase polymer systems*. Chichester: John Wiley and Sons Ltd.; 2011. 1034 p. DOI: https://doi.org/10.1002/9781119972020

16. Mohanty A. K., Misra M., Drzal L. T. *Natural fibers, biopolymers, and biocomposites*. USA: Taylor & Francis Group; 2005. 896 p. DOI: https://doi.org/10.1201/9780203508206

17. Faruk O., Sain M. *Biofiber reinforcements in composite materials*. Cambridge: Woodhead Publishing Ltd.; 2015. 772 p. DOI: https://doi.org/10.1016/b978-1-78242-122-1.50028-9

18. Jose J., Nag A., Nando G. B. Environmental aging studies of impact modified waste polypropylene. *Iran Polym. J.* 2014;23(8): 619–636. DOI: https://doi.org/10.1007 / s13726-014-0256-5

19. Utracki L. A. *Polymer blends handbook*. Dordrecht: Kluwer Academic Publishers; 2002. DOI: https://doi.org/10.1021/ja0335465

20. Wang Y.-Z., Yang K.-K., Wang X.-L., Zhou Q., Zheng C.-Y., Chen Z.-F. Agricultural application and environmental degradation of photo-biodegradable polyethylene mulching films. *J. Polym. Environ*. 2004;12: 7–10. DOI: https://doi.org/10.1023 / B: JOOE.0000003122.71316.8e

21. Koutny M., Sancelme M., Dabin C., Pichon N., Delort A.-M., Lemaire J. Acquired biodegradability of polyethylenes containing pro-oxidant additives. *Polym. Degrad. Stab.* 2006;91 (7): 1495–1503. DOI: https://doi.org/10.1016/j.polymdegradstab.2005.10.007

22. De La Orden M. U., Montes J. M., Martínez Urreaga J., Bento A., Ribeiro M. R., Pérez E., Cerrada M. L. Thermo and photo-oxidation of functionalized metallocene high density polyethylene: Effect of hydrophilic groups. *Polym. Degrad. Stabil.* 2015;11(10): 78–88. DOI: https://doi.org/10.1016/j.polymdegrad stab.2014.10.10.023

23. Yusak N. A. M., Mohamed R., Ramli M. A. Mechanical analyses of polyethylene/polypropylene blend with photodegradant. *J. Appl. Sci. Agric.* 2014;9(11): 300-305.

24. Lipatov Yu. S. *Fizicheskaya khimiya napolnennykh polimerov* [Physical chemistry of filled polymers]. Moscow: Khimiya Publ.; 1977. 304 p. (In Russ.)

25. Schramm G. *A practical approach to rheology and rheometry*. 2nd edition. Federal Republic of Germany, Karlsruhe: Gebrueder HAAKE GmbH; 2000. 291 p.

26. Sokolov A. V., Roedolf D. Introduction to the practical rheology of polymers. *Plastics.* 2018;(5–6): 31–34. Available at: https://elibrary.ru/item.asp?id=35193338 (In Russ.)

27. Lazdin R. Y., Zakharov V. P., Shurshina A. S., Kulish E. I. Assessment of rheological behavior of secondary polymeric raw materials in the conditions corresponding to processing of polymers by method of extrusion and injection molding. *Letters on Materials*. 2019;9(1): 70–74. DOI: https://doi.org/10.22226/2410-3535-2019-1-70-74

28. Bledzki A. K., Mamuna A. A., Volk J. Barley husk and coconut shell reinforced polypropylene composites: The effect of fiber physical, chemical and surface properties. *Composites Science and Technology*. 2010;70(5): 840–846. DOI: https://doi.org/10.1016/j.compscitech.2010.01.022

29. Nourbakhsh A., Ashori A., Tabrizi A. K. Characterization and biodegradability of polypropylene composites using agricultural residues and waste fish. *Composites Part B: Engineering*. 2014;56: 279–283. DOI: https://doi.org/10.1016/j.compositesb.2013.08.0.028

30. Ashori A., Nourbakhsh A. Mechanical behavior of agro-residue-reinforced polypropylene composites. *Journal of Applied Polymer Science*. 2008;111(5): 2616–2620. DOI: https://doi.org/10.1002/app.29345

31. Vurasko A. V., Minakova A. R., Gulemina N. N., Driker B. M. Physico-chemical properties of cellulose obtained by the oxidative-organosolvent method from plant materials. In: *Forests of Russia in the XXI century: Materials of the first international scientific and practical Internet conference, 30 June 2009.* St. Petersburg: St. Petersburg State Forestry University Publ.; 2009. p. 126–130. (In Russ.)

Information about the authors

Rinat M. Akhmetkhanov, DSc in Chemistry, Associate Professor, Dean, Bashkir State University, Ufa, Russian Federation; e-mail: rimasufa@rambler.ru. ORCID iD: https://orcid.org/0000-0003-0016-0218.

Ainur R. Sadritdinov, PhD student, Bashkir State University, Ufa, Russian Federation; e-mail: aynur.sadritdinov@mail.ru. ORCID iD: https://orcid.org/0000-0002-0517-9834

Vadim P. Zakharov, DSc in Chemistry, Professor, Vice-Rector for Research and Innovation, Bashkir State University, Ufa, Russian Federation; e-mail: zaharovvp@mail.ru. ORCID iD: https://orcid.org/0000-0002-5997-1886.

Angela S. Shurshina, PhD in Chemistry, Associate Professor, Bashkir State University, Ufa, Russian Federation; e-mail: anzhela_murzagil@mail.ru. ORCID iD: https://orcid.org/0000-0001-6737-7265.

Elena I. Kulish, DSc in Chemistry, Professor, Head of Department, Bashkir State University, Ufa, Russian Federation; e-mail: onlyalena@mail.ru. ORCID iD: https://orcid.org/0000-0002-6240-0718.

All authors have read and approved the final manuscript.

Translated by Valentina Mittova.
Edited and proofread by Simon Cox.

Condensed Matter and Interphases
(Kondensirovannye sredy i mezhfaznye granitsy)

Original articles

DOI: https://doi.org/10.17308/kcmf.2020.22/2525 eISSN 2687-0711
Received 04 February 2020
Accepted 15 March 2020

Influence of a Weak Pulsed Electromagnetic Field on the Atomic Structure of Natural Aluminosilicates Clinoptilolite, Montmorillonite and Palygorskit

based on the materials of the XXIII All-Russian Conference with International Participation «X-ray and electron spectra and chemical bonds» (Voronezh, October 1–4, 2019)

©2020 L. I. Belchinskaya[a], K. V. Zhuzhukin[b], K. A. Barkov[b], S. A. Ivkov[b], V. A. Terekhov[b], E. P. Domashevskaya*[b]

[a]*Voronezh State Forestry University named G. F. Morozov, 8 Timiryazev str., Voronezh, Russian Federation*

[b]*Voronezh State University, 1 Universitetskaya pl., Voronezh 394018, Russian Federation*

Abstract

Natural and artificial aluminosilicates are relevant research objects due to their wide using in medicine, food and chemical industries, and in agriculture. The aim of the work is to study the possible changes under the influence of a weak pulsed electromagnetic field of the atomic structure of powdery samples of three minerals clinoptilolite $KNa_2Ca_2(Si_{29}Al_7)O_{72}\cdot 24H_2O$, montmorillonite $Ca_{0.2}(AlMg)_2Si_4O_{10}(OH)_2\cdot 4H_2O$ and palygorskite $MgAlSi_4O_{10}(OH)\cdot 4H_2O$, belonging to the group of natural aluminosilicates, in which silicon-oxygen and aluminum-oxygen tetrahedra are linked by a common oxygen atom. The results of studies by X-ray diffraction and ultra-soft X-ray emission spectroscopy showed that 48 hours after exposure of a weak pulsed electromagnetic field to 71 mT for 30 seconds, the atomic and electronic subsystems of mineral samples still kept changes.

The influence of a weak pulsed electromagnetic field on the atomic structure of minerals manifested itself differently in three samples in the form of one or two additional weak superstructural lines in diffractograms. The influence of a weak pulsed electromagnetic field on the local environment of silicon by oxygen atoms in silicon-oxygen tetrahedra was manifested in the form of changes in the fine structure of the ultra-soft X-ray emission spectroscopy silicon Si $L_{2,3}$ spectra, indicating the restoration of stoichiometry of silicon suboxides $SiO_{1.8}$ in the composition of aluminosilicates of the initial powders into stoichiometry equal to or close to silicon dioxide SiO_2, in all three minerals.

Keywords: aluminosilicates, clinoptilolite, montmorillonite, palygorskite, weak pulsed electromagnetic field, crystal structure, X-ray diffraction, ultra-soft X-ray emission spectra.

Funding: This work was partially supported by the Ministry of Science and Education of the Russian Federation as part of the state assignment to universities in the field of scientific activity.

For citation: Belchinskaya L. I., Zhuzhukin K. V., Barkov K. A., Ivkov S. A., Terekhov V. A., Domashevskaya E. P. Influence of a weak pulsed electromagnetic field on the atomic structure of natural aluminosilicates clinoptilolite, montmorillonite and palygorskit. *Kondensirovannye sredy i mezhfaznye granitsy = Condensed Matter and Interphases*. 2020;22(1): 18–27. DOI: https://doi.org/10.17308/kcmf.2020.22/2525

1. Introduction

In the 70s of the last century it was established experimentally that electromagnetic treatment quite strongly affects the hydration of ions. Significant changes in ion hydration are observed in dilute solutions in which structural stabilizer ions are present: ions capable of forming complexes with water (Ni^{2+}, Cu^{2+}, Fe^{3+}) and the most hydrophilic ions (Ca^{2+}, Mg^{2+}, Li^{+}) [1–4]. A different change in the hydration of para- and diamagnetic ions can be tried to be associated with a change in the structure of

---

✉ Domashevskaya Evelina Pavlovna, e-mail: ftt@phys.vsu.ru

water. There are many facts confirming the weak changes that occur in water systems after exposure to weak electromagnetic pulses [3, 4]. First of all, water molecules are affected by weak magnetic fields, the connection of which with other molecules is somehow weakened. Molecules that retain strong hydrogen bonds are most easily exposed.

When an external magnetic field is applied to diamagnetic materials, one should first of all expect orientational effects of extended supramolecular structures and macromolecules due to the large anisotropy of the diamagnetic susceptibility of these formations in accordance with the prevailing ideas about the primary mechanisms of the magnetic field action on matter. When an external magnetic field is applied to diamagnetic materials, one should first of all expect orientational effects of extended polymer supramolecular structures and macromolecules due to the large anisotropy of the diamagnetic susceptibility of these formations in accordance with prevailing ideas about the primary mechanisms of the magnetic field on a substance.

The influence of weak electromagnetic pulses can be traced in aqueous systems by some changes in their physicochemical and physical properties. The change in the properties of a homogeneous liquid phase is insignificant. To a greater extent, magnetic treatment affects processes associated with phase transformations or heterogeneous water systems [3, 4]. The resulting effects are already more noticeable (in contrast to changes in the homogeneous liquid phase) and will remain for a long time. The results of studies of the hydration properties of clinoptilolite and glaukeonite from the group of aluminosilicates showed [5] that at relatively low electromagnetic field intensities, i.e. Under the influence of the so-called weak magnetic fields, the sorption capacity and specific surface area of the samples significantly increase, which is more noticeable for dilute solutions. At high electromagnetic fields, the effect decreases and becomes the opposite.

Aluminosilicates are one of the large groups of minerals, which, in turn, is included in the class of silicates. Simply put, silicates contain silicon and aluminum oxides. Natural species of this group are minerals located in the earth's crust. However, there is the possibility of obtaining them chemically using hydrothermal synthesis, simulating the natural geochemical processes that occur in an environment of superheated aqueous solutions under pressure.

The structural features of zeolites make it possible to modify their aluminosilicate properties by various methods without destroying their crystalline structure, while the modified structures expand the range of potential applications.

The difference between aluminosilicates and silicates is that silicon and aluminum have tetrahedral coordination in them, and part of the silicon in the aluminosilicate is replaced by aluminum and/or Na, K, Ca impurity atoms (Fig. 1). Silicon-oxygen and aluminum-oxygen tetrahedra, in turn, are interconnected by a common oxygen atom (oxygen Si-O-Si (Al) bridge bonds), and this bond is formed by flat grids, chains, ribbons, rings, three-dimensional frameworks [6].

These features of the atomic structure of natural and artificial aluminosilicates allow their use in medicine, food and chemical industries, in agriculture, as molecular sieves, catalysts, in water purification, fine purification and separation of gases, in the chromatographic analysis of gases and liquids, etc.

The aim of this work is to study possible changes in the atomic and electronic structure after exposure to a weak pulsed electromagnetic field on the atomic structure of natural aluminosilicates in the form of clinoptilolite, montmorillonite and palygorskite minerals by X-ray diffraction and ultra-soft X-ray spectroscopy methods.

2. Objects and methods of research

The objects of study of the weak pulsed electromagnetic field (WPEMF) influence were powdered samples of three aluminosilicate minerals. One of them, clinoptilolite has a rigid skeleton structure, its chemical formula is $KNa_2Ca_2(Si_{29}Al_7)O_{72}\cdot24H_2O$. It is an aluminosilicate of monoclinic syngony with a C2/m space group and unit cell parameters: $a = 17.671$ Å, $b = 17.912$ Å, $c = 7.410$ Å, $\alpha = 90°$, $\beta = 91.59°$, $\gamma = 90°$ [7].

The next montmorillonite sample has a layered expanding structure and no less

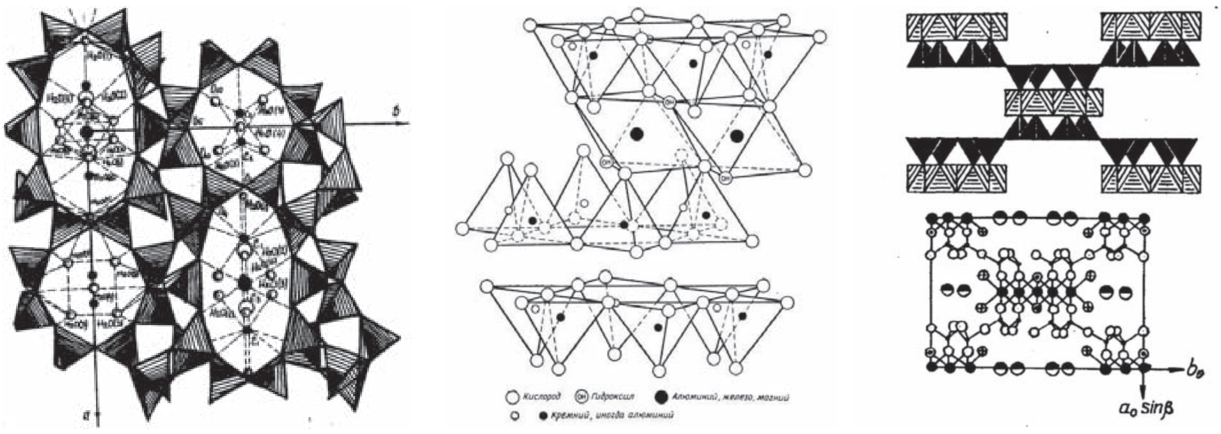

a *b* *c*

Fig. 1. Schematic representation of structures: a) clinoptilolite; b) montmorillonite; c) palygorskite

complex chemical formula $Ca_{0.2}\,(AlMg)_2Si_4O_{10}(OH)_2{\cdot}4H_2O$, the components of which form a hexagonal crystal lattice with parameters $a = 5.169$ Å, $b = 5.169$ Å, $c = 15.02$ Å, $\alpha = 90°$, $\beta = 90°$, $\gamma = 120°$ [8].

The third palygorskite sample has the chemical formula $MgAlSi_4O_{10}(OH){\cdot}4H_2O$ [9], different from the two aluminosilicates above, and the layered ribbon structure of the monoclinic syngony with the Pn space group and unit cell parameters $a = 17.864$ Å, $b = 12.681$ Å, $c = 5.127$ Å, $\alpha = 90°$, $\beta = 92.23°$, $\gamma = 90°$ [9].

The setting for creating weak pulsed electromagnetic fields (WPEMF) consists of four main parts: an energy source, energy storage, key and solenoid. The pulse generator provides the amplitude of the magnetic field from 0.5 to 120 mT. The pulse shape is half-sinusoidal. The exposure parameters are as follows: magnetic induction – 71 mT, pulse repetition period T – 10 ms; pulse supply frequency f – 100 Hz, pulse exposure time – 30 sec. For electromagnetic impulse treatment, a bucks with a powder of aluminosilicate of a certain mass were placed inside a solenoid, to which a current was applied to create an electromagnetic field.

Samples of the three listed powdered minerals both in the initial state and 48 hours after WPEMF exposure were studied by X-ray diffraction (XRD) and ultra-soft X-ray spectroscopy (USXES) methods.

X-ray phase analysis of the samples before and after irradiation was carried out on a diffractometer DRON-4-07 with X-ray radiation Co$K\alpha$, $\lambda = 1.69$ Å.

The distribution of the state of the valence electrons of silicon and aluminum in the valence band of the studied minerals before and after irradiation was analyzed by the energy distribution of the local partial density of the Si and Al valence states by ultra-soft X-ray emission spectroscopy (USXES) method on a RSM-500 laboratory X-ray spectrometer-monochromator [10–12]. X-ray emission Si and Al $L_{2,3}$-spectra were obtained upon excitation by electrons with an energy of 3 keV, corresponding to a sample analysis depth of 60 nm [11–13].

3. Results and discussion

3.1. X-ray diffraction

X-ray diffraction data show on Figures 2–4 the diffraction patterns from powder samples of three minerals obtained before (upper gray curves) and 48 hours after WPEMF irradiation (lower black curves).

Tables 1–3 show the values of interplanar distances d (Å) and intensities I (%) of Bragg reflections from the studied samples in comparison with the corresponding values for minerals from the International Center for Diffraction Data (ICDD) PDF Card 2012 (last columns). Of the numerous PDF ICDD maps of various modifications of each of the minerals, maps with d (Å) and I (%) values that were closest to our data were selected for comparison. Some differences even of these closest data from ours can be explained by the presence in the minerals of impurities characteristic of this deposit.

Comparison of d (Å) and I (%) obtained before and after WPEMF irradiation presented in

Figures 2–4 and Tables 1–3 shows that the vast majority of Bragg reflections characterizing one or another phase of aluminosilicates of each mineral retain position on the 2θ° scale and relative intensities. However, some weak reflections were better manifested or even appeared after WPEMF irradiation.

So, in the diffractogram of clinoptilolite (Fig. 2 and Table 1) after irradiation, two reflections appeared, corresponding to d = 4.261 Å and d = 4.040 Å, which are absent not only in the initial sample, but also in the sample from the ICDD database [7].

After irradiation of the sample, two reflections also appeared on the diffractogram of montmorillonite (Fig. 3 and Table 1), corresponding to d = 3.408 Å and d = 3.240 Å, one of which is missing in the comparison sample from the ICDD database [8].

And only on the diffraction pattern of palygorskite (Fig. 4) after irradiation did one weak reflection appear, corresponding to d = 1.973 Å (I = 10 %), which is present in the comparison sample with a barely noticeable intensity d = 1.964 Å (I = 1%) [8].

All these data indicate that a weak pulsed electromagnetic field affects the atomic structure of the crystal lattices of powdered natural minerals, clinoptilolite, montmorillonite and palygorskite, a slight deformation of which leads to the appearance of one or two additional superstructural diffraction lines.

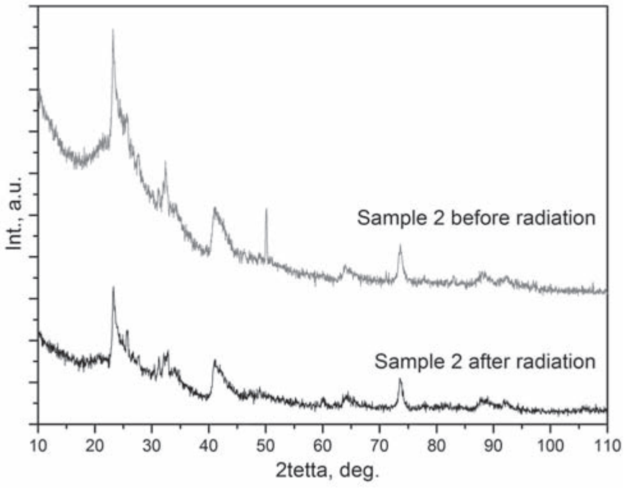

Fig. 3. Diffraction patterns of montmorillonite (Sample 2) before (upper gray curve) and after WPEMF irradiation (lower black curve)

3.2. *Ultra-soft X-ray emission Si $L_{2,3}$ spectra of silicon*

In solids of any composition under the influence of electronic or quantum excitation, electronic transitions arise from the valence band to vacancies in the core shells of all atoms of studied material with the formation of the characteristic X-ray emission valence bands (XEVB). The XEVB for elements of the third period, which include silicon and aluminum of minerals from the class of aluminosilicates, refers to the region of the ultra-soft X-ray spectrum (USXES) with nanometer wavelengths

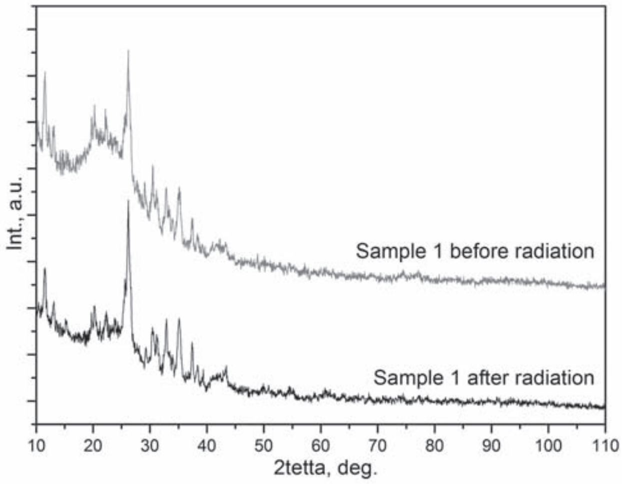

Fig. 2. Diffraction patterns of clinoptilolite (Sample 1) before (upper gray curve) and after WPEMF irradiation (lower black curve)

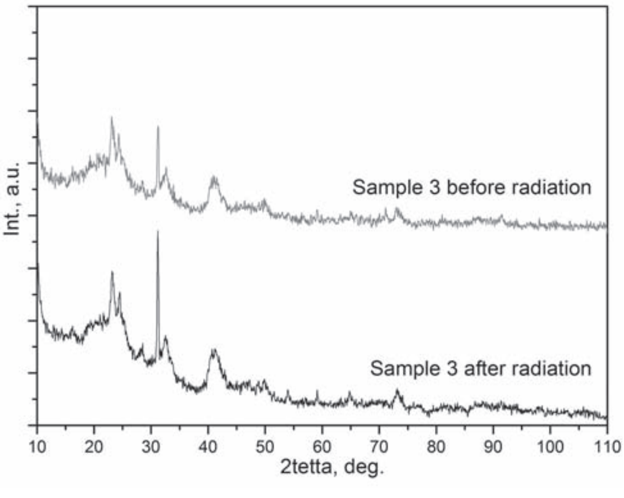

Fig. 4. Diffractograms of palygorskite (Sample 3) before (upper gray curve) and after WPEMF irradiation (lower black curve)

Table 1. The values of interplanar distances *d* (Å) and intensities *I* (%) for clinoptillolite samples before and after WPEMF irradiation in comparison with PDF Card 00-039-1383 [8] for monoclinic clinoptilolite Clinoptillolite-Ca C2/m, *a* = 15.838 Å, *b* = 17.912 Å, *c* = 7.410 Å, α = 90°, β = 91.59°, γ = 90° [7]

No.	Before irradiation		After irradiation		PDF 2012 00-039-1383 Clinoptillolite-Ca [7]	
	d, Å	Int. *I* (%)	*d*, Å	Int. *I* (%)	*d*, Å	Int. *I* (%)
1	9.972	22	9.829	7		
2	**8.896**	**63**	**8.896**	**33**	**8.950 (020)**	**100**
3	8.423	23				
4	7.817	25	7.847	15	7.930 (200)	13
5	6.746	12	6.790	11	6.780 (20-1)	9
6					5.940 (220)	3
7					5.590 (130)	5
8	5.219	43	5.232	20	5.240 (31-1)	10
9	5.092	53	5.117	22	5.120 (111)	12
10			4.866	14		
11	4.659	51	4.628	21	4.650 (13-1)	19
12	4.314	31	4.350	17	4.350 (40-1)	5
13			4.261	15		
14			4.040	45		
15					3.976 (131)	61
16	**3.949**	**100**	**3.949**	**100**	**3.955 (330)**	**63**
17					3.905 (240)	48
18					3.835 (221)	7
19					3.738 (24-1)	6
20					3.707 (041)	5
21	3.569	20	3.545	12	3.554 (31-2)	9
22	3.408	41	3.408	27	3.424 (22-2)	18
23	3.398	40			3.392 (40-2)	12
24	3.333	22	3.333	23	3.316 (002)	6
25	3.170	32	3.161	36	3.170 (42-2)	16
26			3.066	13	3.074 (13-2)	9
27					2.998 (35-1)	18
28	**2.968**	**41**	**2.964**	**40**	**2.971 (151)**	**47**
29	2.785	23	2.792	26	2.795 (62-1)	16
30	2.725	12	2.725	13	2.730 (26-1)	16
31			2.659	12	2.667 (202)	4

Table 2. The values of interplanar distances *d* (Å) and intensities *I* (%) for montmorillonite samples before and after irradiation in comparison with PDF Card 00-013-0135 [8], for hexagonal montmorillonite-15A: *a* = 5.169 Å, *b* = 5.169 Å, *c* = 15.02 Å, α = 90°, β = 90°, γ = 120° [8]

No.	Before irradiation		After irradiation		PDF 2012 00-013-0135 Montmorillonite-15A [8]	
	d, Å	Int. *I*, %	*d*, Å	Int. *I*, %	*d*, Å	Int. *I*, %
1					15.00 (001)	100
2					5.01 (003)	60
3	**4.451**	**100**	**4.442**	**100**	**4.50 (100)**	**80**
4	4.043	30	4.025	50		
5					3.77 (004)	20
6			3.408	14	3.50	10
7	3.337	10	3.323	26	3.30 (103)	10
8			3.240	*38*		
9	3.208	36	3.166	50	3.02 (005)	60
10	2.550	34	2.547	16	2.58 (110)	40
11					2.50 (006)	40
12	2.112	40	2.161	19	2.26 (200)	10
13					1.88 (008)	10
14	1.689	15	1.679	39	1.70 (210)	30
15					1.50 (00 10)	50
16	1.494	29	1.495	15	1.493 (300)	50
17	1.289	10	1.277	10	1.285 (221)	20
18	1.240	5			1.243 (310)	20

Table 3. The values of interplanar distances *d* (Å) and intensities *I* (%) for palygorskite samples before and after irradiation in comparison with PDF Card 2012 00-029-0855 [9] for monoclinic palygorskite Pn: *a* = 17. 864 Å, *b* = 12.681 Å, *c* = 5.127 Å, α = 90°, β = 92.23°, γ = 90° [9]

No.	Before irradiation		After irradiation		PDF 2012 00-029-0855 Palygorskite [9]	
	d, Å	Int. *I*, %	*d*, Å	Int., *I* %	*d*, Å	Int. *I*, %
1	**10.010**	**100**	**10.000**	**100**	**10.34 (110)**	**100**
2					**6.34 (020)**	**15**
3					5.38 (310)	7
4	**4.440**	**100**	**4.461**	**52**	4.47 (400)	8
5	4.237	40	4.219	37	4.27 (-211)	3
6					4.11 (130)	3
7					3.95 (-301)	1
8					3.65 (420)	4
9					3.45 (330)	1
10	**3.323**	**82**	**3.328**	**100**	3.35 (-321)	2
11					3.230 (-131)	3
12	3.228	32	3.199	25	**3.170 (040)**	**10**
13	2.535	51	2.547	30	2.536 (050)	6
14	2.122	17	2.121	10	2.113 (060)	1
15			*1.973*	*10*	1.964 (910)	1
16	1.814	22	1.815	10	1.814 (070)	1
17	1.662	10	1.672	10	1.672 (271)	1
18	1.501	26	1.502	14	1.507 (181)	2
19					1.488 (12 00)	2

and energies of up to several hundred electron volts, measured from the zero Fermi level. In this case, the distribution of the spectrum intensity of each element carries information on the local density of valence states near atoms of a given sort [10–13]. Sensitivity to changes in the chemical environment of the radiating atom is an advantage of X-ray emission spectroscopy. By changes of the XEVB fine structure, one can judge the change in the nearest environment, which allows not only elemental, but even phase analysis of the samples [14, 15]. And since in the study of REP the transition is used the valence bande-core level transitions, the advantage of the UMRES method is the relative simplicity of interpreting the compared to optical band-band spectra [10–13].

As for the basic elements of the three minerals of the group of aluminosilicates, silicon and aluminum, first in Fig. 5 we presented the Al L2,3 aluminum spectra and Si Si L2,3 spectra of all three clinoptilolite samples recorded in a single energy scale successively (Sample 1), montmorillonite (Sample 2) and palygorskite (Sample 3) before and after exposure to a weak pulsed electromagnetic field (71 mTl). The upper spectra in this figure belong to the reference SiO_2 and Al_2O_3 samples.

In the dipole approximation of the selection rules for X-ray transitions, the Si $L_{2,3}$- and Al $L_{2,3}$-spectra reflect the density distribution of the 3s, p (d) states of these elements in the valence band of the corresponding minerals. In this case, the second high-energy main maximum of these spectra corresponds to the hybridization of valence 3s, p-states with O 2p-states of oxygen, i.e. reflects ion-covalent bonds of silicon-oxygen and aluminum-oxygen tetrahedral bonds.

When analyzing the spectra in Fig. 5, we immediately note only a slight increase in intensity in the range 60–72 eV compared to the background at the site of the aluminum Al $L_{2.3}$ spectra compared to the intense silicon Si $L_{2.3}$ band. This circumstance is associated primarily with a significantly lower aluminum content compared to silicon in the chemical formulas of all the studied minerals. The next noticeable increase in intensity with a maximum at 76 eV corresponds to the so-called long-wave / low-energy satellite Si $L_{2,3}$ spectrum, which reflects the interaction of Si 3s, p + O 2s in the O 2s oxygen subband, i.e. due to the amount of oxygen bound to silicon. An increase in the intensity in this region of the weak palygarskite spectrum is due to the superposition of the Cu M2.3 spectrum of copper, from which the sample holder is made.

In the following Figures 6–8, we present separately for each mineral the results of modeling

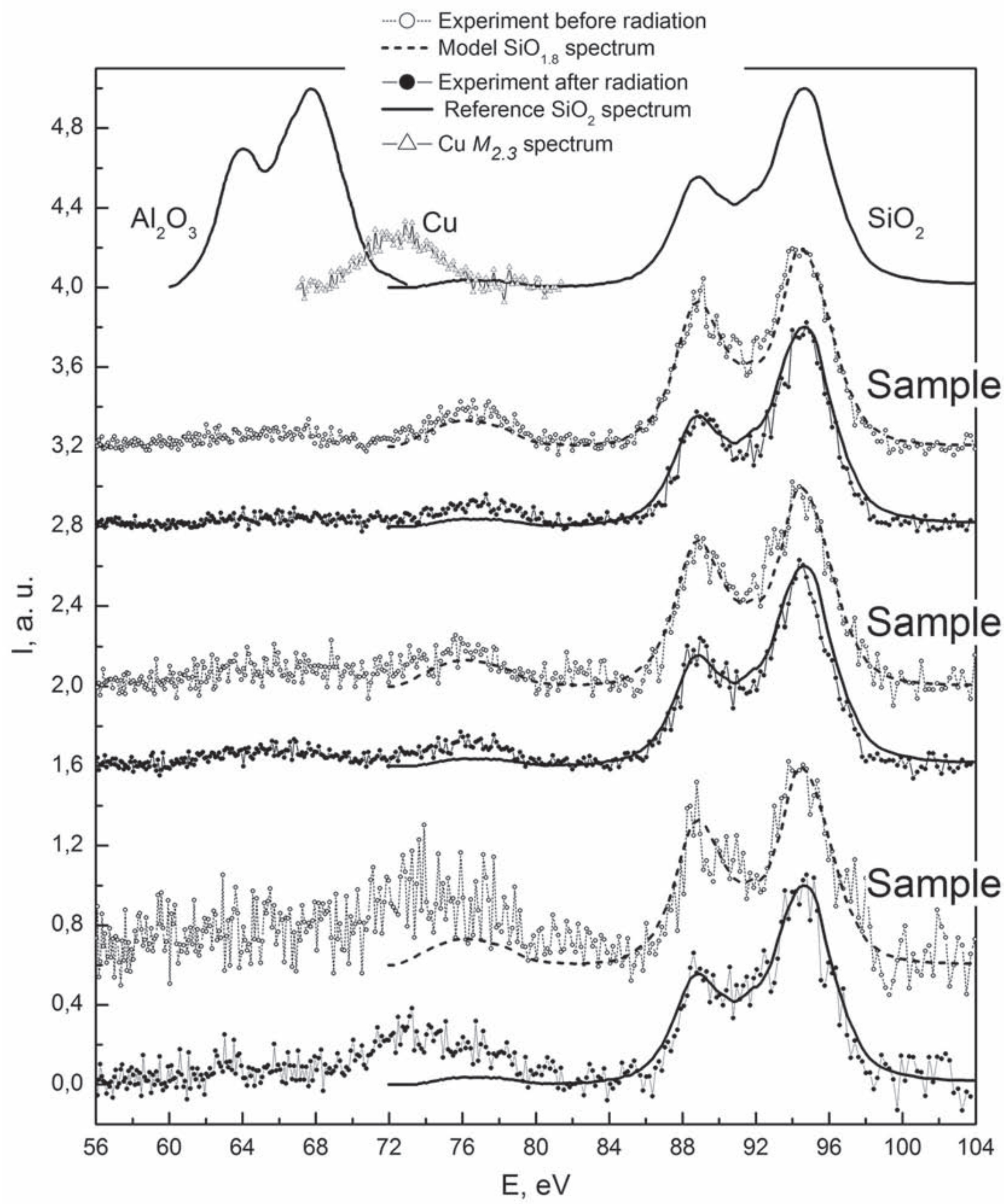

Fig. 5. USXES Al $L_{2,3}$ and Si $L_{2,3}$ spectra of clinoptilolite (Sample 1), montmorillonite (Sample 2) and palygorskite (Sample 3) before (thin lines with circles) and after WPEMF irradiation (lines with black dots). The uppermost spectra belong to the reference samples of SiO_2 and Al_2O_3

Si $L_{2,3}$-silicon spectra using reference spectra of silicon suboxides of different compositions and silicon dioxide and subsequent fitting to experimental spectra [14, 15], which was carried out to determine the phase composition silicon oxides in samples before and after exposure toWPEMF.

The simulation results of Si $L_{2,3}$ spectra showed that all initial samples contain only 40 % of the stoichiometric SiO_2 phase, and the remaining 60 % is silicon suboxide $SiO_{1,7}$, which is, in fact, non-stoichiometric dioxide with numerous oxygen vacancies. Thus, the average weighted statistically distributed composition of oxidized silicon in the starting aluminosilicates is $SiO_{1.8}$ = 40 % SiO_2 + 60 % $SiO_{1.7}$.

After WPEMF irradiation (solid lines with black dots in Figs. 6–8), silicon dioxide SiO2 becomes the predominant phase in all samples. Moreover, in the irradiated clinoptilolite (Fig. 6)

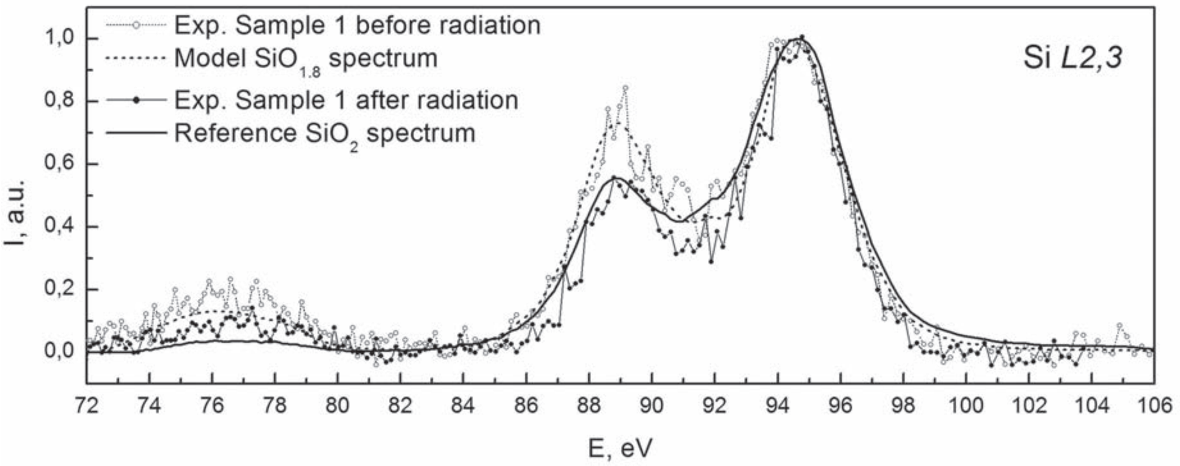

Fig. 6. USXES Si $L_{2,3}$-spectra of clinoptilolite (Sample 1) before (thin line with circles) and after WPEMF irradiation (line with black dots)

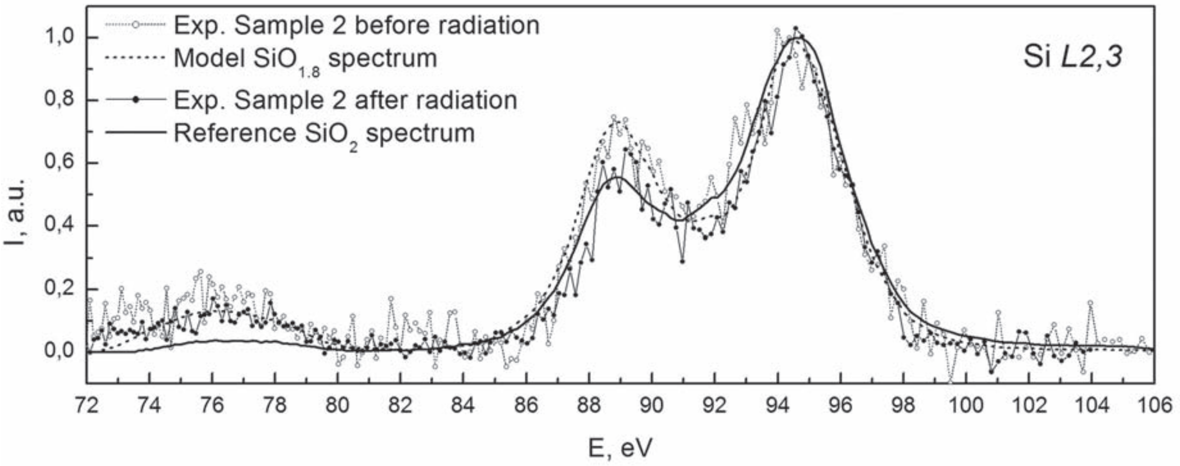

Fig. 7. USXES Si $L_{2,3}$-spectra of montmorillonite (Sample 2) before (thin line with circles) and after WPEMF irradiation (line with black dots)

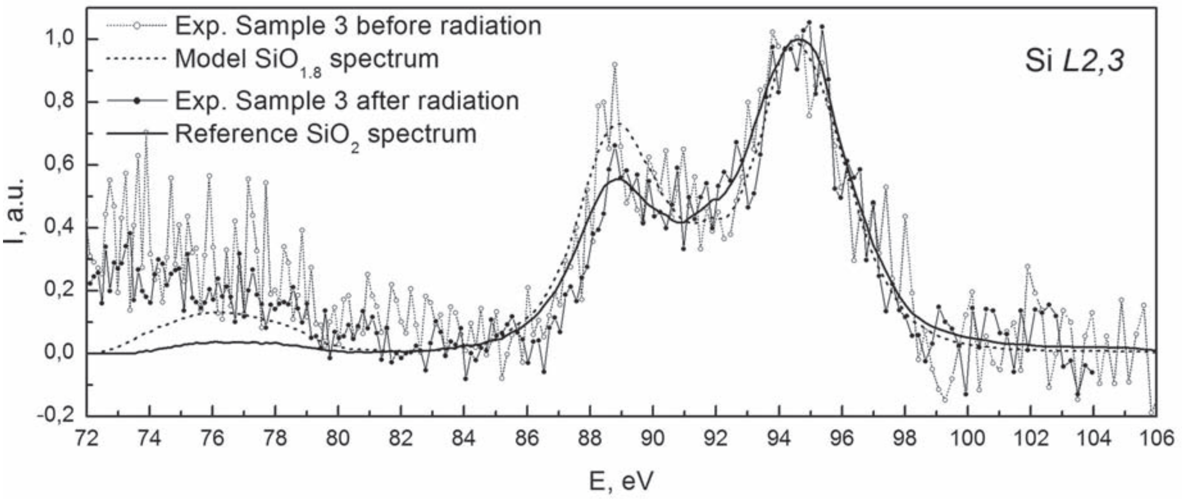

Fig. 8. USXES Si $L_{2,3}$- palygorskite spectra (Sample 3) before (thin line with circles) and after WPEMF irradiation (line with black dots)

and palygorskite (Fig. 8), the stoichiometric SiO_2 phase is unique, and in the irradiated montmorillonite (Fig. 7) its predominance after irradiation rose to 80 %, but did not reach 100 %, as in two other samples.

Nevertheless, a significant healing of defects in the form of numerous oxygen vacancies in the silicon-oxygen tetrahedra of the initial minerals under the influence of WIEMF can occur as a result of the transition of oxygen ions from air adsorbed by the samples, or from superstoichiometric oxygen, from structured water molecules of H_2O or OH groups to vacancy sites.

4. Conclusion

Comparing the experimental results on the effect of a weak pulsed electromagnetic field on the powders of three minerals from the group of natural aluminosilicates that we identified as clinoptilolite [7] $KNa_2Ca_2(Si_{29}Al_7)O_{72}\cdot 24H_2O$, montmorillonite [8] $Ca_{0.2}(AlMg)_2Si_4O_{10}(OH)_2\cdot 4H_2O$, and palygorskite $MgAlSi_4O_{10}(OH)\cdot 4H_2O$ [9], using two different methods of XRD and USXES, we can conclude that both methods, each in its own way, detected noticeable changes in the samples, which persist at least 48 hours after WPEMF irradiation.

The USXES method recorded changes in the local environment of silicon by oxygen atoms with a change in the average stoichiometry from $SiO_{1.8}$ in the initial samples to a near or equal SiO_2. in irradiated samples that occur as a result of filling vacancies in silicon-oxygen tetrahedra with oxygen, most likely from adsorbed air.

Unfortunately, it was not possible to register such changes in aluminum-oxygen tetrahedra due to the low aluminum content in the samples.

Nevertheless, the local short-range order changes observed by the USXES method in the silicon-oxygen tetrahedra affect the atomic structure of entire crystal lattice of all three aluminosilicates, and appear as one or two superstructural lines on the diffractograms of the samples after WPEMF irradiation.

Conflict of interests

The authors declare that they have no known competing financial interests or personal relationships that could have influenced the work reported in this paper.

References

1. Hack E. Z., Rick T. R. O vliyanii postoyannogo magnitnogo polya na kinetiku dvizheniya ionov v vodnykh rastvorakh sil'nykh elektrolitov [On the effect of a constant magnetic field on the kinetics of ion motion in aqueous solutions of strong electrolytes]. *Reports of the Academy of Sciences of the USSR*. 1967;175(4): 856–858. (In Russ.)

2. Martynova O. I., Gusev B. T., Leontiev E. A. K voprosu o mekhanizme vliyaniya magnitnogo polya na vodnye rastvory solei [To the question of the mechanism of the influence of the magnetic field on aqueous solutions of salts]. *Uspekhi Fizicheskikh Nauk*. Успехи физических наук. 1969;98: 25–31. (In Russ.)

3. Chesnokova L. N. *Voprosy teorii i praktiki magnitnoi obrabotki vody i vodnykh sistem* [Questions of the theory and practice of magnetic treatment of water and watersystems]. Moscow: Tsvetmetinformatsiya Publ.; 1971. 75 c.

4. Kronenberg K. Experimental evidence for the effects of magnetic fields on moving water. *IEEE Transactions on Magnetics*. 1985;21(5); 2059–2061. DOI: https://doi.org/10.1109/tmag.1985.1064019

5. Kotova D. L., Artamonova M. I., Krysanova T. A., Vasilenko M. S., Novikova L. A., Belchinskaya L. I., Petukhova G. A. The effect of a pulsed magnetic field on the hydration properties of clinoptilolite and glauconite. *Protection of Metals and Physical Chemistry of Surfaces*. 2018;54(4): 598–602. DOI: https://doi.org/10.1134/S2070205118030073

6. Vernadsky V. I., Kurbatov S. M. *Zemnye silikaty, alyumosilikaty i ikh analogi* [Earth silicates, aluminosilicates and their analogues. 4th ed.]. Moscow – Leningrad Publ.; 1937. 378 p.

7. CPDS – International Center for Diffraction Data. PDF Card 2012 00-039-1383

8. CPDS – International Center for Diffraction Data. PDF Card 2012 00-013-0135

9. CPDS – International Center for Diffraction Data. PDF Card 2012 00-029-0855

10. Zimkina T. M., Fomichev V. A. *Ul'tramyagkaya rentgenovskaya spektroskopiya* [Ultra-soft x-ray spectroscopy]. Leningrad: Leningrad State University Publ.; 1971. 132 p.

11. Shulakov A. S., Stepanov A. P. *Glubina generatsii ul'tramyagkogo rentgenovskogo izlucheniya v* SiO_2 [Ultrasoft X-ray Generation Depth in SiO_2]. *Physics, Chemistry and Mechanics of Surfaces*. 1988;10: 146–150. (in Russ.)

12. Terekhov V. A., Trostyansky S. N., Seleznev A. E., Domashevskaya E. P. Izmenenie plotnosti lokalizovannykh sostoyanii v poverkhnostnykh sloyakh amorfnogo gidrogenezirovannogo kremniya pri vakuumtermicheskikh otzhigakh [The change in the density of localized states in the surface layers of

amorphous hydrogenated silicon during vacuum thermal annealing] *Physics, Chemistry and Mechanics of Surfaces*. 1988;5: 74-80.

13. Domashevskaya E. P., Peshkov Y. A , Terekhov V. A., Yurakov Y. A., Barkov K. A. Phase composition of the buried silicon interlayers in the amorphous multilayer nanostructures $[(Co_{45}Fe_{45}Zr_{10})/a\text{-}Si{:}H]_{41}$ and $[(Co_{45}Fe_{45}Zr_{10})_{35}(Al_2O_3)_{65}/a\text{-}Si{:}H]_{41}$. *Surf. Interface Anal.* 2018;50(12–13): 1265–1270. DOI: https://doi.org/10.1002/sia.6515

14. Manukovsky E. Yu. Elektronnaya struktura, sostav i fotolyuminestsentsiya poristogo kremniya [Electronic structure, composition and photoluminescence of porous]. *Abstract of the candidate's thesis.* Voronezh: Voronezh State University; 2000. 16 p.

15. Domashevskaya E. P., Terekhov V. A., Turishchev S. Yu., Przhimov A. S., Kharin A. N., Parinova E. V, Rumyantseva N. A., Usoltseva D. S., Fomenko Yu. L., Belenko S. V. Atomic and electronic structure of amorphous and nanocrystalline layers of semi-insulating silicon obtained by chemical deposition at low pressure. *Journal of Surface Investigation: X-Ray, Synchrotron and Neutron Techniques*. 2015;6(6): 1228–1236. DOI: https://doi.org/10.1134/S1027451015060257

Information about the authors

Larisa I. Belchinskaya, DSc in Technical Sciences, Professor, Voronezh State Forestry University named after G. F. Morozov, Voronezh, Russian Federation; e-mail: chem@vglta.vrn.ru. ORCID iD: http://orcid.org/0000-0003-3921-8018.

Konstantin V. Zhuzhukin, postgraduate student, Voronezh State Forestry University named after G. F. Morozov, Voronezh, Russian Federation; e-mail: chem@vglta.vrn.ru. ORCID iD https://orcid.org/0000-0002-7093-3274.

Konstantin A. Barkov, postgraduate student, Head of the Laboratory, Department of Solid State Physics and Nanostructures, Voronezh State University, Voronezh, Russian Federation; e-mail: barkov@phys.vsu.ru. ORCID iD: https://orcid.org/0000-0001-8290-1088.

Sergey A. Ivkov, postgraduate, Leading Electronics, Voronezh State University, Voronezh, Russian Federation; e-mail: ivkov@phys.vsu.ru. ORCID iD: https://orcid.org/0000-0003-1658-5579.

Vladimir A. Terekhov, DSc in Physics and Mathematics, Full Professor, Department of Solid State Physics and Nanostructures, Voronezh State University, Voronezh, Russian Federation; e-mail: ftt@phys.vsu.ru. ORCID iD: https://orcid.org/0000-0002-0668-4138.

Evelina P. Domashevskaya, DSc in Physics and Mathematics, Full Professor, Head of the Department of Solid State Physics and Nanostructures, Voronezh State University, Voronezh, Russian Federation; e-mail: ftt@phys.vsu.ru. ORCID iD: https://orcid.org/0000-0002-6354-4799.

All authors have read and approved the final manuscript.

Translated by Valentina Mittova.
Edited and proofread by Simon Cox.

Condensed Matter and Interphases
(Kondensirovannye sredy i mezhfaznye granitsy)

Original articles

DOI: https://doi.org/10.17308/kcmf.2020.22/2526 eISSN 2687-0711
Received 11 January 2020
Accepted 15 February 2020

Synthesis, Structure and Magnetic Properties of Cobalt-Zinc Nanoferrite for Magnetorheological Liquids

© 2020 Yu. S. Haiduk✉,[a], E. V. Korobko[b], K. A. Shevtsova[b], D. A. Kotsikau[a], I. A. Svito[a], A. E. Usenka[a], D. V. Ivashenko[a], A. Fakhmi[c], V. V. Pankov[a]

[a]*Belarusian State University, 4 Nezalezhnastsi av., Minsk 220030, Republic of Belarus*

[b]*A. V. Luikov Heat and Mass Transfer Institute of the National Academy of Science,*
15 P. Brovki str., Minsk 220072, Republic of Belarus

[c]*University of Applied Sciences Marie Curie-Strasse 1D-47533 Kleve, Federal Republic of Germany*

Abstract

An upcoming trend in the application of micro- and nanosized magnetic particles is the development of magnetorheological fluids for the automatic systems of damping devices in which the particles play the role of a component in the complex dispersed phase. In the search for magnetic materials for magnetorheological fluids, the most important criteria in choosing are high shear stress of the suspension based on the particles vs. applied magnetic field and a low value of coercive force. The aim of the work was to investigate the structure, morphology, and magnetic properties of the nanoscaled powders of Co, Zn-ferrites and the evaluation of their effectiveness upon the rheological properties of the developed magnetorheological fluids.

The Co, Zn-ferrite nanopowderwas synthesized by spray-drying technique followed by heat treatment in the presence of the inert matrix. The features of its morphology were investigated by x-ray diffraction analysis, transmission electron microscopy, and IR-spectroscopy.

The powdered nanoferrite $Co_{0.65}Zn_{0.35}Fe_2O_4$, used as a filler of magnetic fluids, demonstrated values of coercive force H_c (10 K) = 10.8 kOe, H_c (300 K) = 0.4 kOe as well as relative residual magnetization M_r/M_s(10 K) = 0.75, M_r/M_s(300 K) = 0.24. The proposed synthesis technique allows obtaining crystallized particles of the ferrite with sizes not larger than 50 nm, which possess high shear stress in magnetorheological suspensions.

The synthesis technique allows controlling the magnetic properties of Co,Zn-ferrite (as a component of magnetorheological suspensions) by non-magnetic double-charged ion substitution of Co^{2+}, i.e. ions Zn^{2+}, in Co,Zn-spinel has been developed. The possibility has been established to decrease the coercive force and increase the magnetization up to the maximum cobalt content, corresponding to the composition formulae $Co_{0.65}Zn_{0.35}Fe_2O_4$. The high value of shear stress (10^3 Pa) at a relatively low value of magnetic induction (600 mT and higher) makes the material applicable as a filler for the magnetorheological suspensions of damping devices.

Keywords: cobalt zinc ferrite, magnetorheological liquids, magnetic nanoparticles.

For citation: Haiduk Yu. S., Korobko E. V., Shevtsova K. A., Kotikov D. A., Svito I. A., Usenka A. E., Ivashenko D. V., Fakhmi A., Pankov V. V.Synthesis, structure, and magnetic properties of cobalt-zinc nanoferrite for magnetorheological liquids. *Kondensirovannye sredy i mezhfaznye granitsy = Condensed Matter and Interphases*. 2020; 22(1):28–38. DOI: https://doi.org/10.17308/kcmf.2020.22/2526

1. Introduction

A promising area for the application of micro- and nanosized magnetic particles is the creation of magnetorheological fluids (MRF) for controlled hydraulic automation devices in which such particles are a component of the complex dispersed phase [1, 2]. Such liquids are used as an active medium for damping devices designed for the protection of vehicles, industrial equipment, buildings, and structures from vibrations and other mechanical influences, as well as for the

✉ Yulyan S. Haiduk, e-mail: j_hajduk@bk.ru

manufacture of various sensors, measuring elements, electromechanical converters, targeted drug delivery, and the diagnosis of diseases in biology and medicine [3–5].

Objects sensitive to the magnetic field can be obtained based on fluid compositions with dispersed solid-phase fillers possessing magnetic properties. In the presence of an external magnetic field, strong particle structural bonds are formed along the magnetic field vector in such compositions, leading to an increase in the viscosity of the compositions and is a necessary condition for creating controlled damping devices.

The magnetic properties of nanopowders, which can be components of these fluid compositions, are determined by the chemical composition, type of crystal lattice, degree of its defectiveness, particle size and shape, morphology (for structurally inhomogeneous particles), and the degree of interaction of the particles with the surrounding liquid and other particles. However, it is not always possible to control all these factors during the synthesis of nanoparticles of approximately the same size and chemical composition, therefore, the properties of nanomaterials of the same type can vary significantly.

For the use of nanoparticles in damping devices and biomedicine, their supermagnetic state with no coercivity, i.e. zero remanent magnetization, is desirable. In this case, in their normal state, without exposure to a magnetic field, they will not form agglomerates due to attractive interaction.

It is known that the dependence of the coercive force on the particle size is complex (Fig. 1) [6]. With a decrease in the size of the bulk sample, the fraction of the surface energy of its domain borders increases, and it becomes comparable with the total volume energy. In this case, the single-domain state of a sample or particle is considered energetically more efficient. Such a state will lead to an increase in the threshold field of the remagnetization of the particle and, consequently, to an increase in the coercive force. This increase is due to a change in the remagnetization – instead of the mechanism associated with the displacement of the domain borders, the rotation of the magnetic moment vector mechanism appears. With a decrease in the size of single-domain particles, their coercive force decreases, and at a certain size its value is equal to zero. This phenomenon is explained by the influence of thermal fluctuations on the magnetic anisotropy value and, consequently, on the coercive force, since the particle anisotropy energy depends on the angle between the directions of magnetization and the easy axis of magnetization. In the superparamagnetic state, the direction of the magnetic moment vector will spontaneously change.

It is known that for isolated nanoparticles with sizes of 1–30 nm, in addition to the Curie and Neel temperatures, there is also a blocking temperature on the temperature scale: $T_B < T_C(T_N)$, where T_C – Curie temperature, T_N – Neel temperature T_B – blocking temperature. Below the blocking temperature, the magnetic moment of the particle retains its spatial orientation, and the ensemble of particles exhibits magnetic hysteresis. At temperatures above T_B the particle changes to a superparamagnetic state. In the region of $T_B < T < T_C$ the particle has spontaneous magnetization and a non-zero total magnetic moment, easily changing the orientation in an external field [7].

A characteristic problem with the production of effective nanoscale magnetic particles for MRF is their significantly lower specific magnetization compared to micron particles. This is due to a violation of the magnetic order in the subsurface layer of ~ 1 nm. In such a layer, the magnetic moments of atoms usually behave the same as

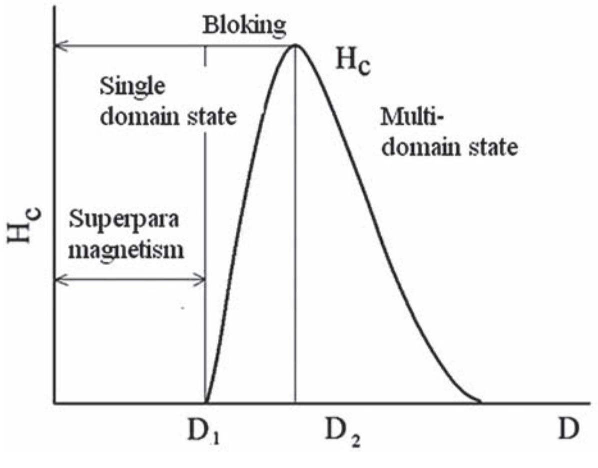

Fig. 1. The dependence of the coercive force on particle size

in spin glasses [8]. Therefore, there is a need to reduce the contribution of the surface layer into the specific magnetization of the material by increasing the fraction of the crystallized core of the nanoparticle. For this purpose, heat treatment is usually used, which, in turn, leads to an aggregation of particles and significant increase in their size, as well as to the appearance of residual magnetization and an increase in coercive force. Therefore, the search for new methods of influencing the microstructure of nanoobjects is relevant, for example, the use of pulsed photon processing was considered in the study [9].

The hysteretic behaviour of materials with a high coercive force in an alternating magnetic field or under dynamic shear loads leads to a decrease in their effectiveness for use in damping devices and for biomedical applications. The influence of the coercive force is particularly critical when using high-frequency fields or variable mechanical loads, when the remagnetization of particles does not have time to take effect due to the long relaxation time of magnetic properties.

Cobalt-zinc ferrites are being actively studied as promising ferrimagnetic materials with high magnetic characteristics. These materials are usually obtained by coprecipitation [10–12] or by the sol-gel method [13], electrostatic spraying [14] and other methods. The purposeful synthesis of ferrites for various applications requires information about the distribution of metal cations in the crystal lattice, since the magnetic characteristics of the samples directly depend on this distribution. Zinc ferrite has a normal crystallographic structure in accordance with the distribution of cations in the spinel sublattices, while cobalt ferrite has a reversible structure. It is known that structural deviations lead to a nonequilibrium distribution of cations in ferrites and cause a change in their magnetic properties [15, 16]. Thus, the ability to influence the cation distribution becomes a tool for tuning magnetic properties [17]. For cobalt-zinc ferrites, for example, the presence of a non-magnetic Zn^{2+} ion with a strong preference for tetrahedral positions will cause the migration of Fe^{3+} ions into the region of octahedral positions, leading to an increase in the magnetic moment.

We are developing dispersed ferrimagnetic nanosized particles for MRF, which, in addition to ferromagnetic particles of carbonyl iron, contains nanosized ferrimagnetic particles, allowing the enhancement of the magneto-control of damping liquids [1, 2]. Cobalt-zinc ferrite nanopowders were chosen as such particles and the analysis of their characteristics was carried out in this work. The aim of the work was the investigation of the structure, morphology, and magnetic properties of Co,Zn ferrite nanopowders and the evaluation of their effectiveness in magnetic fields upon the rheological properties of the developed MRF.

2. Experimental

Based on the highest specific magnetization the optimal composition of Co,Zn ferrite with a molar ratio (cobalt and zinc) of 0.65:0.35 was established [18].

Samples of $CoSO_4{\cdot}7H_2O$ weighing 16.25 g, $ZnCl_2$ weighing 4.26 g, and $Fe\ (NO_3)_3$ weighing 49.81 g were dissolved in 1.5 l of distilled water. The solution was stirred with magnetic stirrer for 5 min to obtain complete homogenization. An ammonia solution was poured into the resulting salt solution with vigorous stirring and the pH level was monitored to ensure it remained at 11 using indicator paper. The suspension was heated to 90 °C. The precipitate was washed by magnetic decantation, after which the aqueous suspension consisting of the precipitate of the previous stage and a NaCl solution in a mass ratio (precipitate - salt) 1: 5 was prepared.

The cobalt-zinc ferrite nanopowder was obtained by spray-drying technique. The suspension was sprayed at a temperature of 220 °C with a feed rate of 2.5 ml/min with subsequent high-temperature heat treatment in the presence of an unreacted inert matrix (NaCl), preventing the intensive growth of crystallites during heat treatment. Heat treatment was carried out in air at 740 °C for 8 h. The spray-drying method allowed obtaining micro-fine particles of salts and the products of their decomposition (100–300 °C). Subsequent annealing of such a product together with NaCl leads to the formation of the Co,Zn ferrite phase. Non-agglomerated micro-fine magnetic cobalt zinc ferrite particles are formed subsequently after the removal of the matrix (NaCl) by dissolution.

X-ray studies were performed using a DRON-3 diffractometer (Co-$K_{\alpha 1}$-radiation, $\lambda = 0.179026$ nm). Scanning was carried out in the range of angles $2\theta = 6–90°$. The sizes of coherent scattering regions (CSR) corresponding to the physical sizes of crystallites in polycrystalline samples were determined by the broadening of diffraction reflections (Scherrer method).

Crystal density was calculated using the formula:

$$d_x = \frac{8M}{a^3 N_\text{A}}, \tag{1}$$

where M – formal molecular weight; a – the lattice parameter, Å; N_A – Avogadro number.

The degree of crystallinity of the samples was determined using the ratio:

$$\left(1 - \frac{I_\text{b}}{I_{311}}\right) \times 100\,\%, \tag{2}$$

where I_{311} – the reflex intensity for the spinel, corresponding to the crystallographic direction 311; I_b - the intensity of the spectrum background line of the x-ray diffraction pattern.

Dislocation density δ (number of lines per 1 m^2) was calculating using the formula:

$$\delta = \frac{1}{D^2}. \tag{3}$$

Scanning electron microscopy was used to study the surface structure of polycrystalline and film samples by use of a LEO 1420. Simultaneously the ratio of the concentration of metal atoms in ferrite powders and the features of their distribution on the surface of the particles were determined by energy dispersive x-ray spectroscopy (EDX-analysis).

IR-spectra were recorded using an AVATAR 330 spectrometer (Thermo Nicolet) in the wavenumber region (ν) 400–700 cm^{-1} with an accuracy of ± 1 cm^{-1}. Recording was performed by diffusion reflection using the Smart Diffuse Reflectance accessory.

The magnetic characteristics were studied using a Cryogen Free Measurement System from Cryogenic Ltd, where hysteresis loops were recorded at temperatures of 2 and 300 K and magnetic field induction B_max = 8 T. The weight of the sample, not including the capsule, was 0.09 g.

The dependence of the shear stress (τ) of the suspensions on the magnetic induction of the applied magnetic field was measured using a Physica MCR 301 Anton Paar rotational viscometer in constant shear rate mode (Mobil 22 binder, shear rate $\gamma = 200$ s^{-1}, $T = 20$ °C). Powder suspensions in a binder were prepared using a UZDM–2 ultrasonic dispersant with a frequency of 44 kHz.

3. Results and discussion

The choice of heat treatment conditions was determined by the search for the optimal combination of the solid-phase reaction time and relative heat treatment temperature for the prevention of excessive crystallite growth.

Fig. 2 represents TEM-images of the heat treatment product of the dried precursor suspensionin NaCl solution after heat treatment at 740 °C (8 h), before (Fig. 2a) and after (Fig. 2b) washing away the NaCl. Before washing, the product was represented by spheres, sometimes of irregular shape, hollow inside and consisting of agglomerated particles of the precursor solid phase and NaCl. The sizes of these particles were in the range of 0.5–0.9 μm. The size of the spheres was 1.5–3.5 μm. The spheres were a product obtained by drying the drops formed by spraying a precursor suspension. The water, as a result of evaporation, shifted the solid phase of the precursor to the surface of the drops, where a solid shell formed with the release of volume inside the spheres. Holes caused by the release of water vapour appeared in some places on the spheres.

After dissolving sodium chloride in water, the dried $Co_{0.65}Zn_{0.35}Fe_2O_4$ powder consisted of non-agglomerated particles with sizes up to 50 nm. TEM-images of $Co_{0.65}Zn_{0.35}Fe_2O_4$ showed that the particles were well separated from each other and not agglomerated. The average particle sizes were 25–30 nm and they were comparable with the CSR size, calculated according to x-ray phase analysis (Table 1). The shape of the particles was faceted in contrast to particles obtained using other production methods for Co, Zn-ferrite nanopowders under similar temperature conditions. The result was due to the use of the synthesis of individual particles in an inert NaCl matrix, provided by the proposed method.

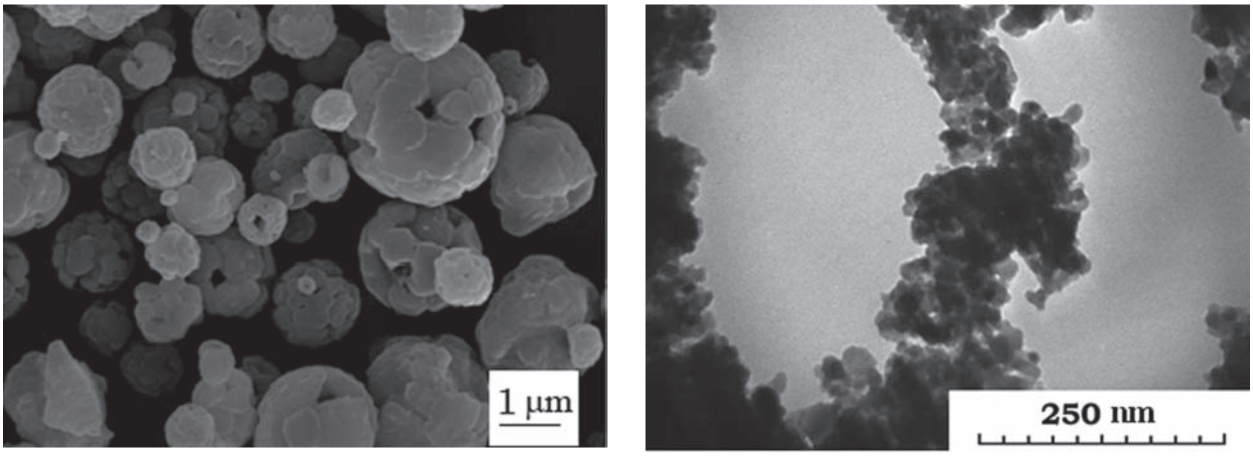

a *b*

Fig. 2. a) SEM images of $Co_{0.65}Zn_{0.35}Fe_2O_4$ particles in the NaCl matrix after heat treatment at 740 °C (8 h); b) TEM images of $Co_{0.65}Zn_{0.35}Fe_2O_4$ particles after washing away the NaCl)

Fig. 3 demonstrates typical x-ray diffraction patterns of the material obtained after heat treatment. It can be seen that after 8 h of heat treatment at a temperature of 740 °C, the solid-phase reaction with the formation of the spinel ferrite structure (space group Fd3m) was completed. Reflex positions and their relative intensities confirm that the powders represent only one phase with a spinel structure. The structural parameters of the crystal lattice of $Co_{0.65}Zn_{0.35}Fe_2O_4$ solid solution heat treated at 740 °C (8 h) are shown in Table 1. The composition of the nanoparticles was determined by energy dispersive x-ray

Table 1. The structural parameters of the crystal lattice of $Co_{0.65}Zn_{0.35}Fe_2O_4$ solid solution: (lattice constant *a*, size of the coherent scattering region *D*, dislocation density δ, crystal density $d_{x,}$ crystallinity)

Lattice constant *a*, Å	Size of coherent scattering region *D*, nm	Dislocation density $\delta \times 10^2$ nm^{-2}	x-ray density d_x, g/cm^3	The degree of crystallinity, %
8.3998	20	0.26	5.31	84.5

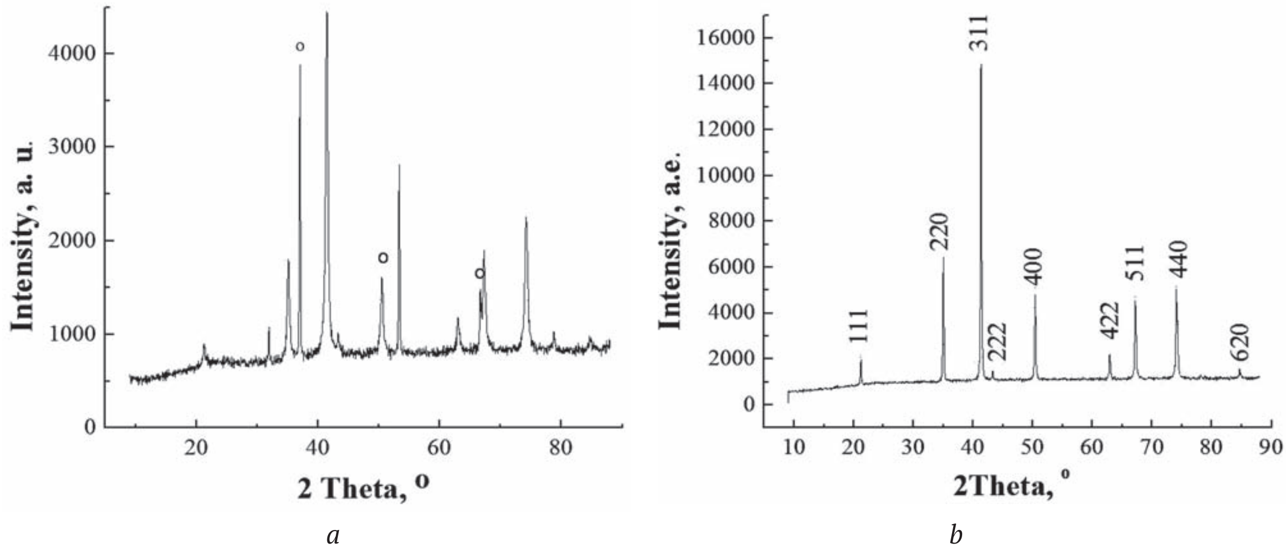

a *b*

Fig. 3. X-ray powder diffraction spectra of powders of $Co_{0.65}Zn_{0.35}Fe_2O_4$ solid solution, after heat treatment at 740 °C: a) for 2 hours; b) for 8 hours (reflexes related to Fe_2O_3 are marked with •)

spectroscopy. Intensive reflections related to the α-Fe_2O_3 phase (haematite) were still detected after 2 h of heat treatment.

Fig. 4 represents a typical IR -absorption spectrum for $Co_{0.65}Zn_{0.35}Fe_2O_4$ nanopowders after heat treatment.

The formation of the spinel structure of ferrites was evidenced by two main absorption bands, which were combined vibrational bands of Me–O bonds in the region of characteristic frequencies with extrema at 414 and 567 cm^{-1}. First ν_1 usually refers to the octahedral vibrations of the metal $Me_{octa}\leftrightarrow O$, and the ν_2 band at 567 cm^{-1} corresponds to the internal stretching vibrations of the metal in the tetrahedral site $Me_{tetra}\leftrightarrow O$ [12]. A high degree of resolution of the absorption bands may reflect a high ordering of the crystalline structure of the solid solution.

It is known that the absorption bands at ν_4 = 1600 cm^{-1} correspond to vibrations of adsorbed water [17]. The absorption near 2100–2300 cm^{-1} may be associated with CO_2 adsorbed from air, absorption bands in the range of 1500–1600 cm^{-1} may be associated with the vibrational oscillations of the N=O bond. Weak absorption bands near 1000 cm^{-1} were due to the presence of traces of nitrate-ions [11]. Absorption bands near wave numbers 1640 and 3400 cm^{-1} are associated with vibrations of O–H bonds [12]. Thus, the IR-spectrum of the sample confirms the formation of the cobalt-zinc ferrite phase and the presence of water in the material structure.

Fig. 5 shows the change in magnetization for $Co_{0.65}Zn_{0.35}Fe_2O_4$ nanopowders depending on the applied field. All prepared samples exhibited ferrimagnetic behaviour at room temperature. The obtained values of specific magnetization powder for $Co_{0.65}Zn_{0.35}Fe_2O_4$ coincided with the specific magnetization of cobalt-zinc ferrites of the same composition obtained by other methods, for example, by coprecipitation of inorganic salts from aqueous solutions (40–70 A·m^2·kg^{-1}, [19]), sol-gel method (60–80 A·m^2·kg^{-1} [20], 60–90 A·m^2·kg^{-1}, [21]).

We demonstrated that with an increase in the zinc content in the cobalt-zinc ferrite, an increase in the saturation magnetization was noted. Thus, for $Co_{0.65}Zn_{0.35}Fe_2O_4$ *M*s = 42.6 A·m^2·kg^{-1}, but for $CoFe_2O_4$ *M*s = 25.0–26.0 A·m^2·kg^{-1}.

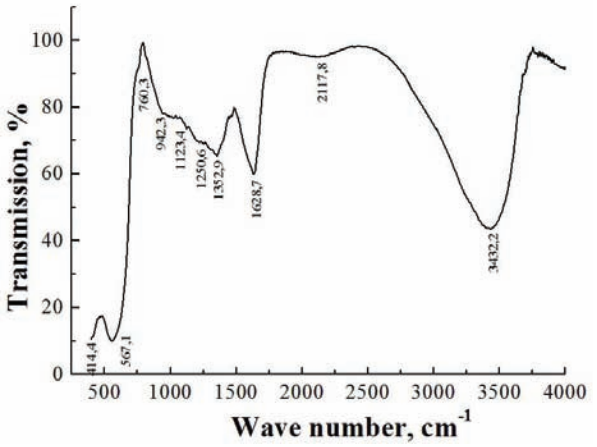

Fig. 4. IR absorption spectrum of $Co_{0.65}Zn_{0.35}Fe_2O_4$ after heat treatment at 740 °C for 8 h

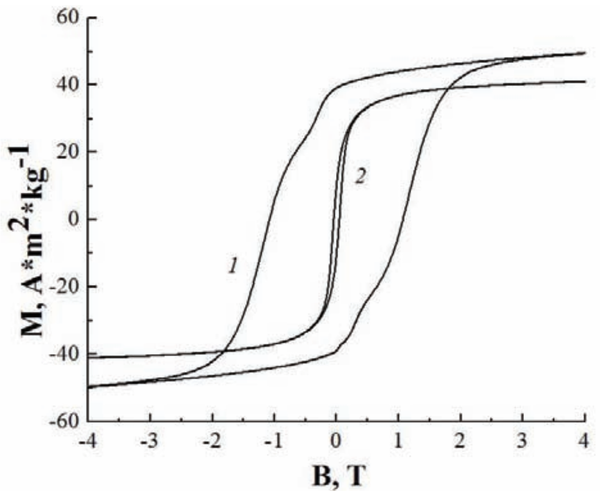

Fig. 5. Curves of the dependence of magnetization on magnetic field strength for $Co_{0.65}Zn_{0.35}Fe_2O_4$ powder at various temperatures of *1* - 10 K, *2* - 300 K

The magnetic ordering is associated with superexchange interaction between the ions of the octahedral (B) and tetrahedral (A) sublattices of the crystal structure for ferrimagnetic spinel ferrites.

JAB, JBB and *JAA* exchange integrals are usually negative and the antiferromagnetic A–B interaction is stronger than B–B and A–A interactions. This leads to ferrimagnetism of the compound, while B–B and A–A interactions are suppressed. The spins of magnetic ions will be parallel in each of the individual B–B and A–A sublattices, but in two different sublattices they are antiparallel.

As Zn^{2+} ion substitutes Co^{2+} ion, it pushes out Fe^{3+} ions from tetrahedral A-positions into octahedral B-positions. While the magnetic moment of A sublattice decreases due to an increased number of nonmagnetic Zn^{2+} ions in it, the magnetic moment of B sublattice increases due to an increased number of Fe $ions^{3+}$ in the B sublattice. Therefore, when in the present work the concentration of Zn^{2+} ions increased from 0 to 0.35, the total magnetization (M_{oct}–M_{tet}) for $Co_{1-x}Zn_xFe_2O_4$ also increased due to an increase in interlattice A–B superexchange interactions between the magnetic ions of A and B sublattices. Magnetic moments of Fe^{3+} ions in different sublattices of the crystal spinel structure (octahedral and tetrahedral) will not be mutually compensated as before.

However, at high levels of doping with Zn^{2+} ions ($x > 0.35$) the antiferromagnetic interaction of Fe^{3+} ions located in neighbouring positions in the octahedral sublattice begins. It turned out that the B–B interaction leads to a decrease in the total magnetic moment.

The explanation for this phenomenon is provided by the three-sublattice Yafet–Kittel model [22], demonstrating that with an increase in the B–B interaction, the A–B interaction decreases. When exchange interactions appear in a ferrimagnet inside B–B or A–A sublattices, they already start "competing" with the interlattice A–B interaction. Most likely, the reason for such an increase in the interaction in the B or A sublattices is the appearance of noncollinearity of spins in the sublattice, leading to a decrease in the values of the experimental magnetic moment.

According to the two-sublattice Neel model of ferromagnetism, the theoretical magnetic moment μ_B per formula unit in n_B^t is described as

$$n_B^m(x) = M_B(x) - M_A(x), \qquad (4)$$

Where $M_B(x)$ and $M_A(x)$ are the magnetic moments of the B and A sublattice in $\mu_B$respectively. The distribution of cations in $Co_{1-x}Zn_xFe_2O_4$ can be written as

$$(Zn_x^{2+}\,Fe_{1-x}^{3+})_A[Co_{1-x}^{2+}\,Fe_{1+x}^{3+}]_B\,O_4^{2-}. \qquad (5)$$

Depending on the concentration of Zn, the theoretical values of the magnetic moment, n_B^T in $Co_{1-x}Zn_xFe_2O_4$ are calculated using the distribution of cations and magnetic moments of Fe^{3+}, Co^{2+} and Zn^{2+} ions, equal to 4.85 μ_B, 2.78 μ_B and 0 μ_B, respectively. Experimental values of magnetic moments (n_B^e), per unit of the formula in Bohr magnetrons (μ_B), were calculated according to the ratio:

$$n_B^e = \frac{M_w M_s}{5585}, \qquad (6)$$

where M_w – molecular weight, M_s – saturation magnetization, and 5585 – magnetic factor [22].

It turned out that the theoretical magnetic moment increases linearly as a function of Zn^{2+} concentration, and the experimental magnetic moment increases with the concentration of Zn^{2+} in $Co_{0.65}Zn_{0.35}Fe_2O_4$ before $x = 0.35$, and then gradually decreases. For $Co_{0.65}Zn_{0\ .35}Fe_2O_4$composition $n_B^T = 4.95$ μ_B, and $n_B^E = 3.01$ μ_B.

The values of the magnetic parameters obtained for the hysteresis loops are summarized in Table 2.

Table 2. The parameters of the magnetization curves of $Co_{0.65}Zn_{0.35}Fe_2O_4$ particles (saturation magnetization M_s, adjusted remanent magnetization M_r/M_s, coercive force H_c)

T, K	M_s, $Am^2 \cdot kg^{-1}$	M_r/M_s	H_c, kOe
10	52.47	0.75	10.9
50	52.42	0.72	9.0
100	51.67	0.67	5.9
200	48.09	0.47	1.7
300	42.57	0.24	0.46

It was established that in terms of shape they are close to the known literature data for cobalt ferrite and are characterized by their significant rectangularity, which is reflected in the values of the adjusted remanent magnetization [23]. Saturation magnetization values M_s in the range of 5–300 K were slightly reduced. High values ofadjusted remanent magnetization can be associated with monodispersity of particles. Magnetization M_s values slightly decreased with a temperature increase in the range of 10–300 K, while the adjusted remanent magnetization M_r/M_s (M_r – residual induction M_s – saturation induction) and coercive force H_c values decreased significantly with the temperature increase, due to the influence of thermal fluctuations of the magnetization of individual particles [24].

It is known, that coercivity is associated with the characteristic constant of the material anisotropy. At the nanoscale, anisotropy depends on various factors, such as particle size, exchange biases, dipole interactions, particle shape, and crystalline nature. The comparison of H_c for the obtained Co,Zn-nanoferrite, with the magnetic properties of cobalt nanoferrite demonstrated a significant decrease of H_c upon the doping of Co,Zn-ferrite with zinc. For example, at 300 K, the coercive force for our $Co_{0.65}Zn_{0.35}Fe_2O_4$ sample was 2.5 times lower than for $CoFe_2O_4$ at the same particle sizes [13]. We obtained the same results for nanopowders synthesized by aerosol pyrolysis with the same heat treatment as for spray-drying technique. For $Co_{0.65}Zn_{0.35}Fe_2O_4$ H_c = 0.13 kOe, and $CoFe_2O_4H_c$ = 0.37 kOe [25]. Thus, for the synthesized Co,Zn ferrite nanoparticles, the substitution of cobalt atoms by zinc led to a decrease in anisotropy and, consequently, a decrease in the coercive force.

The adjusted residual magnetization (M_r/M_s) values of $Co_{0.65}Zn_{0.35}Fe_2O_4$ at different temperatures are presented in Table 2. It was found that they gradually decrease for higher temperatures. The Stoner-Wohlfarth model determines that for low temperatures M_r/M_S = 0.5 for randomly oriented uniaxial noninteracting particles ensembles and when the anisotropy of disordered and noninteracting nanoparticles is cubic, then M_r/M_s= 0.83. In our case, for $Co_{0.65}Zn_{0.35}Fe_2O_4$ samples at temperatures below 200 K, M_r/M_s is definitely higher than 0.5 and cubic anisotropy is more pronounced here. These results show that coercivity can be regulated and changed in the structure of Co, Zn-spinels by replacing cobalt ions with zinc ions.

On the hysteresis loop at low temperatures (Fig. 5) we also observed a distortion in the curve of the dependence of the magnetization on the field strength next to the residual magnetization in the form of unusual bends. The existence of such bends is associated with the two-phase behaviour of the hysteresis loop, interparticle interactions, etc. [26, 27]. It also seems that there is an interaction between the hard and soft anisotropy regimes. In addition, this phenomenon may depend on the polydispersity of the sizes, as well as on the shape of the particles.

The dependences of the shear stress of an MRF containing 20 wt.% $Co_{0.65}Zn_{0.35}Fe_2O_4$ powder, on shear rate in the absence of a magnetic field and on magnetic field induction at a shear rate of 200 s^{-1}, T = 20 °C were measured for the assessment of the effectiveness of the synthesized particles (Fig. 6). A high value of shear stress (1000 Pa) at relatively low values of the magnetic field induction (from 600 mT and above) allowed considering the obtained material to be suitable for practical use as a component of MRF filler. It is known that ferrimagnetic powders with a large value of the residual magnetization can exhibit a significantly lower increase in viscosity in a magnetic field. Thus, for example, zinc-containing an iron oxide powder at M_s (300 K) = 95 $A \cdot m^2 \cdot kg^{-1}$ exhibits insignificant viscosity change in a magnetic field (about 15 %) [1].

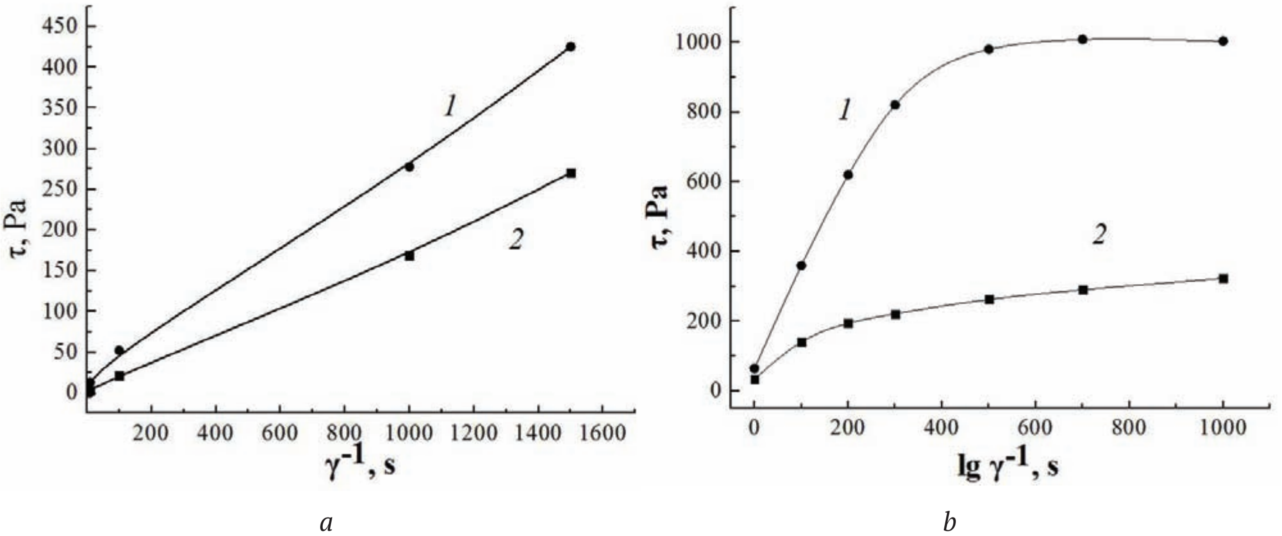

a *b*

Fig. 6. The dependence of the shear stress of an MRF containing 20 wt.% magnetic nanoparticles *1* – $Co_{0.65}Zn_{0.35}Fe_2O_4$; *2* – $Mn_{0.3}Fe_{2.7}O_4$ in Mobil 22 oil: a) on shear rate in the absence of a magnetic field; b) in a magnetic field at shear rate γ = 200 s^{-1}, T = 20 °C

From the dependence of the shear stress of a suspension prepared based on $Co_{0.65}Zn_{0.35}Fe_2O_4$ powder, it is also seen that the shear stress of the suspension increased with increased magnetic field induction and reached a maximum value of 1 kPa at 550 mT, which is significantly lower than for most other known materials based on doped magnetites and ferrites. In addition, $Co_{0.65}Zn_{0.35}Fe_2O_4$ powders have high oil absorption and form stable suspensions. This allows using them as a stabilizing and modifying filler in magnetorheological suspensions based on carbonyl iron in synthetic oil.

4. Conclusions

A technique has been developed that allows controlling the magnetic properties of cobalt-zinc ferrite as a component of magnetorheological suspensions by non-magnetic double charge ion substitution of cobalt ions, i. e. zinc ionsin the structure of Co,Zn spinel. The possibility to decrease the coercive force and increase magnetization up to maximum cobalt content corresponding to the composition formulae $Co_{0.65}Zn_{0.35}Fe_2O_4$ has been established. For the synthesis of cobalt-zinc ferrite, a spray-drying technique followed by heat treatment in the inert component NaCl matrix has been proposed. The proposed technique allows obtaining uniform crystallized cobalt-zinc ferrite nanoparticles with a diameter less than 50 nm, with a specific magnetization of about ~ 40 $A\cdot m^2\cdot kg^{-1}$, some of which were in a superparamagnetic state. The efficiency of $Co_{0.65}Zn_{0.35}Fe_2O_4$ in MRF composition with the industrial Mobil 22 oil (20% wt.) has been assessed, the dependence of the shear stress on the induction of the magnetic field was investigated. The high shear stress (1 kPa) with a relatively low magnetic field induction (from 600 mT and above) allowed us to consider the obtained material as being promising for use as an additional functional filler for the magnetorheological suspensions of damping devices.

Conflict of interests

The authors declare that they have no known competing financial interests or personal relationships that could have influenced the work reported in this paper.

References

1. Korobko E. V., Pankov V. V., Kotikov D. A., Novikova Z. A., Novik E. S. Nanodispersed fillers based on iron oxide for the complex dispersed phase of magnetically correctable hydraulic fluids. In: *Nanostructures in condensed matter: Collection of scientific articles, 20–23 August* 2018. Minsk: A. V. Lykov Heat and Mass Transfer Institute National Academy of Sciences of Belarus Publ.; 2018. p. 156–161. (In Russ.)

2. Dragašius E., Korobko E., Novikava Z., Sermyazhko E. Magnetosensitive Polymer composites and effect of magnetic field directivity on their properties. *Solid State Phenomena*. 2016;251: 3–7. DOI: https://doi.org/10.4028/www.scientific.net/SSP.251.3

3. Joseph A., Mathew S. Ferrofluids: synthetic strategies, stabilization, physicochemical features, characterization, and applications. *ChemPlusChem*. 2014;79(10):1382–1420. DOI: https://doi.org/10.1002/cplu.201402202

4. Genc S., Derin B. Synthesis and rheology of ferrofluids: a review. *Current Opinion in Chemical Engeeniring*. 2014;3(2): 118–124. DOI: https://doi.org/10.1016/j.coche.2013.12.006

5. Vekas L., Avdeev M. V., Bica D. Magnetic nanofluids: synthesis and structure. In: Donglu Shi (ed.) *Nanoscience in biomedicine*. Springer Berlin Heidelberg; 2009. 729 p. DOI: https://doi.org/10.1007/978-3-540-49661-8

6. Frolov G. I., Bachina O. I., Zav'yalova M. M., Ravochkin S. I. Magnetic properties of nanoparticles of 3D metals. *Technical physics*. 2008;53(8):1059–1064. DOI: https://doi.org/10.1134/S1063784208080136

7. Baraton M. I. Synthesis, functionalization, and surface treatment of nanoparticles, LA: Am. Sci. Publ.; 2002. 236 p.

8. Martínez B., Obradors X., Balcells L., Rouanet A., Monty C. Effect of aluminum doping on structural and magnetic properties of Ni Zn ferrite nanoparticles. *Physical Review Letters*. 1998;80(1): 181–184. DOI: https://doi.org/10.4236/wjnse.2015.53009

9. Mittova I. Ya., Sladkopevtsev B. V., Mittova V. O., Nguyen Anh Tien, Kopeichenko E. I., Khoroshikh N. V., Varnachkina I. A. Formation of nanoscale films of the (Y_2O_3–Fe_2O_3) on the monocrystal InP. *Kondensirovannye sredy i mezhfaznye granitsy = Condensed Matter and Interphases.* 2019;21 (3): 406–418. DOI: 10.17308/kcmf.2019.21/1156 (In Russ., Abstract in Eng.)

10. Mayekar J., Dhar V., Radha S. Synthesis, characterization and magnetic study of zinc ferrite nanoparticles. *International Journal of Innovative Research in Science, Engineering and Technology*. 2016;5(5): 8367–8371. DOI: https://doi.org/10.15680/IJIRSET.2016.0505268

11. Jansi Rani B., Ravina M., Saravanakumar B., Ravi G., Ganesh V., Ravichandran S., Yuvakkumar R. Ferrimagnetism in cobalt ferrite ($CoFe_2O_4$) nanoparticles. *Nano-Structures & Nano-Objects*. 2018;14: 84–91. DOI: https://doi.org/10.1016/j.nanoso.2018.01.012

12. Manouchehri S., Ghasemian Z., Shahbazi-Gahrouei D., Abdolah M. Synthesis and characterization of cobalt-zinc ferrite nanoparticles coated with DMSA. *Chem Xpress*. 2013;2(3): 147–152.

13. Singhal S., Namgyal T., Bansal S., Chandra K. Effect of Zn Substitution on the magnetic properties of cobalt ferrite nanoparticles prepared via sol-gel route. *Journal of Electromagnetic Analysis and Applications*. 2010;2(6): 376–381. DOI: https://doi.org/10.4236/jemaa.2010.26049

14. Rajendra S. G., Sang-Youn Ch., Rajaram S. M., Sung-Hwan H., Oh-Shim J. Cobalt ferrite nanocrystallites for sustainable hydrogen production application. *International Journal of Electrochemistry*. 2011;2011: 1–6. DOI: https://doi.org/10.4061/2011/729141

15. Ladole C. A.Preparation and characterization of spinel zinc ferrite $ZnFe_2O_4$. *International Journal of Chemical Science*. 2012;10(3): 1230–1234. Available at: https://www.tsijournals.com/articles/preparation-and-characterization-of-spinel-zinc-ferrite-znfe2o4.pdf

16. Raghuvanshi S., Kane S. N., Tatarchuk T. R., Mazaleyrat F. Effect of Zn addition on structural, magnetic properties, antistructuralmodeling of $Co_{1-x}Zn_xFe_2O_4$nanoferrite. *AIP Conference Proceedings*. 2018;1953(1): 030055. DOI: https://doi.org/10.1063/1.5032390

17. Sawadzky G. A., Van der Woude F., Morrish A. H. Cation distributions in octahedral and tetrahedral sites of the ferrimagnetic spinel $CoFe_2O_4$. *Journal of Applied Physics*. 1968;39(2): 1204–1206. DOI: https://doi.org/10.1063/1.1656224

18. Petrova E. G., Shavshukova Ya. A., Kotikov D. A., Yanushkevich K. I., Laznev K. V., Pan'kov V. V. Thermolysis of sprayed suspensions for obtaining highly spinel ferrite nanoparticles. *Journal of the Belarusian State University. Chemistry*. 2019;1: 14–21. Available at: https://journals.bsu.by/index.php/chemistry/article/view/1258 (In Russ., abstract in Eng.)

19. Ranjani M., Jesurani S., Priyadharshini M., Vennila S. Sol-gel synthesis and characterization of zinc substituted cobalt ferrite magnetic nanoparticles. *International Journal of Advanced Research*. 2016;4(7): 53–58. DOI: https://doi.org/10.21474/ijar01/1148

20. Lin Q., Xu J., Yang F., Lin J., Yang H., He Y. Magnetic and mцssbauer spectroscopy studies of zinc-substituted cobalt ferrites prepared by the sol-gel method. *Materials*. 2018;11(10): 1799. DOI: https://doi.org/10.3390/ma11101799

21. Copolla P., da Silva F. G., Gomide G., Paula F. L. O, Campos A. F. C., Perzynski R., Kern C., Depeyrot G., Aquino R. Hydrothermal synthesis of mixed zinc–cobalt ferrite nanoparticles: structural and magnetic properties. *Journal of Nanoparticle Research*. 2016;18(138): 1–15. DOI: https://doi.org/10.1007/s11051-016-3430-1

22. Yafet Y., Kittel C. Antiferromagnetic arrangements in ferrites. *Physical Review Journal*. 1952;87(2): 290–294. DOI: https://doi.org/10.1103/PhysRev.87.290

23. Praveena K., Sadhana K. Ferromagnetic properties of Zn substituted spinel ferrites for high frequency applications. *International Journal of Scientific and Research Publications*. 2015;5(4): 1–21. Available at: http://www.ijsrp.org/research-paper-0415.php?rp=P403877

24. Komogortsev S. V., Patrusheva T. N., Balaev D. A., Denisova E. A., Ponomarenko I. V. Cobalt ferrite nanoparticles in a mesoporous silicon dioxide matrix. *Technical Physics Letters*. 2009;35(19): 882–884. DOI: https://doi.org/10.1134/S1063785009100022

25. Komogortsev S. V., Iskhakov R. S., Balaev A. D., Kudashov A. G., Okotrub A. V., Smirnov S. I. Magnetic properties of Fe3C ferromagnetic nanoparticles encapsulated in carbon nanotubes. *Physics of the Solid State*. 2007;49(4): 734–738. DOI: https://doi.org/10.1134/S1063783407040233

26. Ivashenko D. V., Petrova E. G., Mittova I. Ya., Ivanets A. I., Pankov V. V. Synthesis of cobalt-zinc ferrite nanoparticles by modified aerosol pyrolysis. In: *Alternative Sources of Raw Materials and Fuels: Materials of the VII International Scientific and Technical Conference, 28–30 May 2019*. Minsk: 2019. p. 120. Available at: http://aist.ichnm.by/doc/Abstract_AICT_2019.pdf (In Russ.)

27. Gözüak, F., Koseoglu, Y., Baykal, A., Kavas H. Synthesis and characterization of $Co_xZn_{1-x}Fe_2O_4$ magnetic nanoparticles via a PEG-assisted route. *Journal of Magnetism and Magnetic Materials*. 2009;321(14): 2170–2177. DOI: https://doi.org/10.1016/j.jmmm.2009.01.008

28. Abdallah H. M. I., Moyo T., Ezekiel I. P., Osman N. S. E. Structural and magnetic properties of $Sr_{0.5}Co_{0.5}Fe_2O_4$ nanoferrite. *Journal of Magnetism and Magnetic Materials*. 2014;365(9): 83–87. DOI: https://doi.org/10.1016/j.jmmm.2014.04.041

Information about the authors

Yulyan S. Haiduk, Researcher, Belarusian State University, Minsk, Republic of Belarus; e-mail: j_hajduk@bk.ru. ORCID iD: https://orcid.org/0000-0003-2737-0434.

Evguenia V. Korobko, DSc in Engineering, Professor, Head of Laboratory, A. V. Luikov Heat and Mass Transfer Institute of the National Academy of Sciences of Belarus, Minsk, Belarus; e-mail: evkorobko@gmail.com. ORCID iD: https://orcid.org/0000-0002-2870-9658.

Kristsina A. Sheutsova, Engineer, A. V. Luikov Heat and Mass Transfer Institute of the National Academy of Sciences of Belarus, Minsk, Belarus; e-mail: kristina-shevcova@lenta.ru. ORCID iD: https://orcid.org/0000-0001-7360-5965.

Dzmitry A. Kotsikau, PhD in Chemistry,Associate Professor, Belarusian State University, Minsk, Belarus; e-mail: kotsikau@bsu.by. ORCID iD: https://orcid.org/0000-0002-3318-7620.

Ivan A. Svito, PhD in Physics and Mathematics, Senior researcher of Energy Physics Department, Belarusian State University, Minsk, Belarus; Email: ivansvito184@gmail.com. ORCID iDhttps://orcid.org/0000-0002-4510-0190.

Alexandra E. Usenka, PhD in Chemistry, Associate Professor, Belarusian State University, Minsk, Republic of Belarus; e-mail: usenka@bsu.by. ORCID iD: https://orcid.org/0000-0002-2251-619.

Dzimitry U. Ivashenka, Master of Chemistry Researcher, Belarusian State University, Minsk, Belarus; e-mail: ivashenkodm@gmail.com. ORCID ID: https://orcid.org/0000-0002-9149-7213.

Amir Fahmi, Doctor, Professor, University of Applied Sciences, Kleve, Germany; e-mail: Amir.Fahmi@hochschule-rhein-waal.de. ORCID iD: https://orcid.org/0000-0001-5283-4646.

Vladimir V. Pankov, DSc in Chemistry, Professor, Head of the Department of Physical Chemistry, Belarusian State University, Minsk, Belarus; e-mail: pankov@bsu.by. ORCID iD: https://orcid.org/0000-0001-5478-0194.

All authors have read and approved the final manuscript.

Translated by Valentina Mittova.
Edited and proofread by Simon Cox.

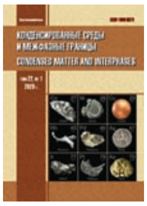

Condensed Matter and Interphases
(Kondensirovannye sredy i mezhfaznye granitsy)

Original articles

DOI: https://doi.org/10.17308/kcmf.2020.22/2527 eISSN 2687-0711
Received 31 January 2020
Accepted 15 March 2020

Characterization of the Properties of Thin Al_2O_3 Films Formed on Structural Steel by the Sol-Gel Method

© 2020 E. P. Grishina✉[a,b], N. O. Kudryakova[a], L. M. Ramenskaya[a]

[a]*G. A. Krestov Institute of Solution Chemistry of the Russian Academy of Sciences,*
1 ul. Akademicheskaya, Ivanovo 153045, Russian Federation

[b]*Ivanovo Fire and Rescue Academy of the State Fire Service of the Ministry of the Russian Federation for Civil Defence,*
Emergencies and Elimination of Consequences of Natural Disasters,
33 Stroiteley ave., Ivanovo153040, Russian Federation

Abstract

The sol-gel method was used to obtain single and double layer oxide-aluminium films on the surface of 08kp structural steel for protection against corrosion. The sol-gel system was prepared according to the Yoldas method by hydrolytic polycondensation of aluminium isopropoxide in the presence of acetic acid at a temperature of 85-90 °C. The pH, size, and zeta potential of boehmite particles were measured, and the corrosion behaviour of steel in the resulting colloids was studied. At room temperature, a boehmite hydrogel layer was applied by immersing the steel samples in a gel, incubating them in the gel, and drying them in the presence of ammonia vapour for the suppression of corrosion. Heat treatment at 500 °C in an air atmosphere was used for the decomposition of boehmite with the formation of alumina and for the fixation of the film on the surface of the substrate. A second film layer was applied in a similar manner on top of a fully formed first layer.

The surface morphology of the obtained films was studied by scanning electron and atomic force microscopy. Electrochemical research methods - potentiometry, voltammetry, and electrochemical impedance spectroscopy were used for a comparative study of the anticorrosion properties of single and double layer aluminium oxide coatings on steel in a 3.5% sodium chloride solution. It was shown that the coatings obtained according to the described scheme have good adhesion to the steel surface. Compared with the control sample, coated steel electrodes were characterized by a shift in the stationary potential by more than 0.6 V, and the onset of active electrochemical oxidation by more than 1 V in the positive direction. The kinetics of the anode and cathode processes changed, leading to a decrease in the corrosion current by more than two orders of magnitude.

The application of the method of electrochemical impedance spectroscopy allowed establishing a 2.5-hour high anticorrosive efficiency of a double layer oxide-aluminium coating on steel in a solution of sodium chloride.

Keywords: sol-gel method, alumina, films, deposition, structural steel, corrosion.

Funding: The research was funded by the Russian Foundation for Basic Research and the government of the Ivanovo region of the Russian Federation, grant No. 18-43-370030.

For citation: Grishina E. P., Kudryakova N. O., Ramenskaya L. M. Characterization of the properties of thin Al_2O_3 films formed on a structural steel by the sol-gel method. *Kondensirovannye sredy i mezhfaznye granitsy = Condensed Matter and Interphases*. 2020;22 (1): 39–47. DOI: https://doi.org/10.17308/kcmf.2020.22/2527

✉ Elena P. Grishina, e-mail: epg@isc-ras.ru

1. Introduction

Structural steels, including low-carbon ones, are known to be one of the most popular structural metals. At the same time, they are characterized by low corrosion resistance, therefore products require effective corrosion protection, which can be provided, in particular, by oxide (ceramic) coatings. Ceramic coatings (SiO_2, TiO_2, ZrO_2, Al_2O_3 and others) are of great practical interest, since they possess high chemical-thermal stability and therefore are usually deposited on metals for the improvement of their characteristics in high-temperature aggressive environments [1-5]. In aqueous solutions, these coatings usually have high electrochemical potentials and are cathode coatings; therefore, they can only perform their functions if they do not have pores, cracks, and form a physical barrier for the penetration of the solution to the steel substrate [6].

Various methods can be used for the deposition of oxide coatings on a metal base – chemical or physical vapour deposition, plasma deposition, electrophoresis, sol-gel deposition [7–12]. The sol-gel method of producing oxide films on metals, based on controlled hydrolytic polycondensation of organic or inorganic compounds of metals and/or silicon is of great interest [2, 13–15]. Moreover, the properties of the deposited layers are determined by both the size and shape of the synthesized particles, and their chemical nature. Thin films of aluminium oxide Al_2O_3 are characterized by their excellent dielectric properties and high thermal and chemical stability, and therefore are promising materials for study [16]. However, with the deposition of coating, for example, on low alloy steel, problems associated with the corrosive action of the sol-gel system on the substrate during film formation occur (the stage of immersion in a colloidal solution and drying of the layer), shrinkage of the film during drying, and heat fixing [17]. This leads to a deterioration in the adhesion of the coating to the substrate, the penetration of solutions through the through pores of the coating to the metal/film interface. Multilayer Al_2O_3 films are characterized by more reliable protective properties [6]. The methods of deposition the layers and, accordingly, the protective effects can vary significantly. This work presents the results of comparative studies of the properties of protective single layer and double layer Al_2O_3 coatings obtained on 08kp low alloy steel by the sol-gel method using the Yoldas process.

2. Experimental

2.1. Production of the sol-gel system

The boehmite dispersion was prepared from aluminium isopropoxide (AIPO), Acros organics, 98 %, in accordance with the Yoldas process [18]. AIPO was dissolved in hot (85–90 °C) distilled water with continuous stirring. During dissolution, the AIPO hydrolysis reaction proceeded with the formation of boehmite sol AlO(OH):

$$C_9H_{21}AlO_3 + 2\ H_2O \rightarrow AlO(OH) + 3\ C_3H_7OH.$$

Peptization of the obtained particles was carried out for about 24 h at a temperature of 85–90 °C using acetic acid (chemically pure). The molar ratio of the components of the reaction mixture AIPO/N_2O/acid was 1/100/0.15. A sol-gel transition with the formation of a translucent gel was observed after ~12 h of the incubation of the solution at the indicated temperature. Physicochemical characteristics of colloidal systems were determined using a Kellymeter pH-009 (I) (Kelly Union Electronics, Hong Kong) pH meter and a Zetasizer Nano particle size and zeta potential analyser (Malvern Instruments Ltd., the UK).

2.2. Preparation of 08kp steel samples

The coating was applied to 08kp carbon structural steel (composition, %: Fe ~98 %, C 0.05–0.11; Si up to 0.03; P up to 0.035; As up to 0.08; S up to 0.04; Mn 0.25–0.5; Ni up to 0.25; Cr up to 0.1; up to 0.25 [19]). Samples were degreased in acetone, then in an alkaline solution at a temperature of 70–75 °C for 30 min, washed with hot water and dried.

2.3. Deposition of coating

Samples were immersed in boehmite gel, incubated in it for 3 min, and then removed. The boehmite hydrogel layer was dried in an air-ammonia medium at room temperature [17]. Afterwards, the sample with a dried film was heat treated in an air atmosphere at a temperature of 500 °C for 1 h. In order to obtain a double layer coating, a second layer was applied over the thermofixed first layer, dried and heat treated, in the same manner as the first layer. According to the literature data [7, 13, 20, 21], as a result of heat treatments at a specified temperature, boehmite decomposes with the formation γ-Al_2O_3. The introduced organic anions also decompose into CO_2 and H_2O.

2.4. Investigation of properties of Al_2O_3 coatings

The morphology of the Al_2O_3 coatings was studied by electron scanning microscopy, SEM (scanning electron microscope Vega 3 SBH, Tescan, Czech Republic) and atomic force microscopy, AFM (scanning atomic force microscope SOLVER 47 PRO, "NT-MDT ", Russian Federation)

The corrosion properties of the metal/oxide system (Al_2O_3) were studied in a 3.5% aqueous NaCl solution at a temperature of 25±1 °C. Potentiometric and voltammetric studies were carried out in a three-electrode electrochemical cell using a PI 50-Pro-3 pulse potentiostat with automatic data recording and PS Pack2 software (OOO "Elins", Russian Federation). The reference electrode was a saturated silver chloride electrode, the loop electrode was Pt. The method of electrochemical impedance spectroscopy was used for the evaluation of the protective properties of the coating at an open circuit potential, the cell voltage was 10 mV, the frequency range of the alternating current was 10^{-2}–10^{6} Hz, the counter electrode was Pt/Pt-black. The studies were carried out using a Solartron SI 1260A impedance and amplitude-phase characteristics analyser (Solartron Analytical, the UK), and ZPlot and ZView2 software packages.

3. Results and discussion

3.1. Corrosion behaviour of steel in boehmite hydrogel

As a result of the hydrolysis of aluminium isopropoxide, the boehmite dispersion had the following characteristics: pH = 8, average particle size of 1234 nm, zeta potential of 0.4-0.6 mV. For the peptization of boehmite particles and sol-gel transition according to the Yoldas process, acetic acid was introduced. As a result, the obtained colloidal solution had a pH of 5, an average particle size of 300 nm, and a zeta potential of 32–35 mV. At pH = 8, alloys with a high iron content were sufficiently corrosion-resistant, however with increasing acidity, the risk of developing a corrosion process increased. The change in the potential of steel samples in the initial dispersion and AlO(OH) hydrogel is shown in Fig. 1. A multidirectional change of the stationary potential E_{st} was observed due to the difference in the hydrogen ion exponent of colloidal systems. In a slightly alkaline solution, a gradual refinement of the potential occurs, while in a slightly acidic solution, a gradual decrease in the value of E_{st} during the first 10 min and an abrupt decrease after 11–12 min of immersion were revealed. Probably, such changes in the steel potential also occur in a thin wet boehmite layer even after its extraction from the colloid, as a result of which signs of the development of a corrosion process appeared, specifically a staining of the layer, which is characteristic of Fe (III) compounds. It was found that this process negatively affects the adhesion of the coating to the substrate, and it can be eliminated by drying the hydrogel layer in an air-ammonia medium [17].

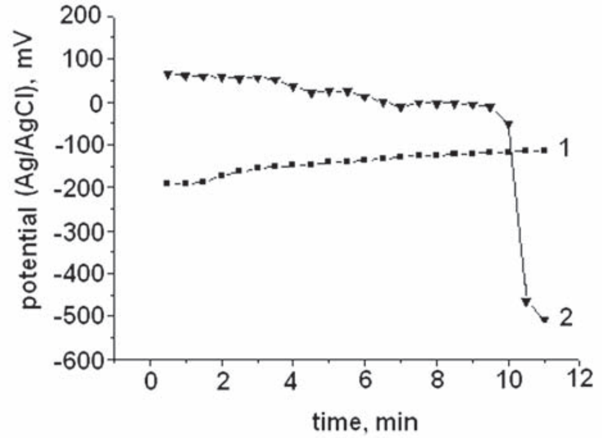

Fig. 1. Change in the potential of 08kp steel samples in colloidal systems without a peptizer (*1*) and with CH_3COOH (*2*) Temperature 23 °C

3.2. Morphology of Al_2O_3-coatings

The morphology of the initial and heat-treated steel surface, as well as a single layer Al_2O_3 coating deposited on steel is shown in Fig. 2. On SEM images, it is seen that the coating is thin and the initial structure of the substrate is visible. The film is impermeable to atmospheric oxygen, and iron oxidation products were not formed. The AFM image of the coating (Fig. 2d) showed that the aluminium oxide particles were uniform in size and shape, and their size did not exceed 200 nm.

The differences between single and double layer coatings, both in appearance and in relation to scratching, are shown in Fig. 3. As can be seen, the second coating layer was unevenly deposited on the previous layer. However, higher adhesion to the substrate and ductility of the coating were obvious.

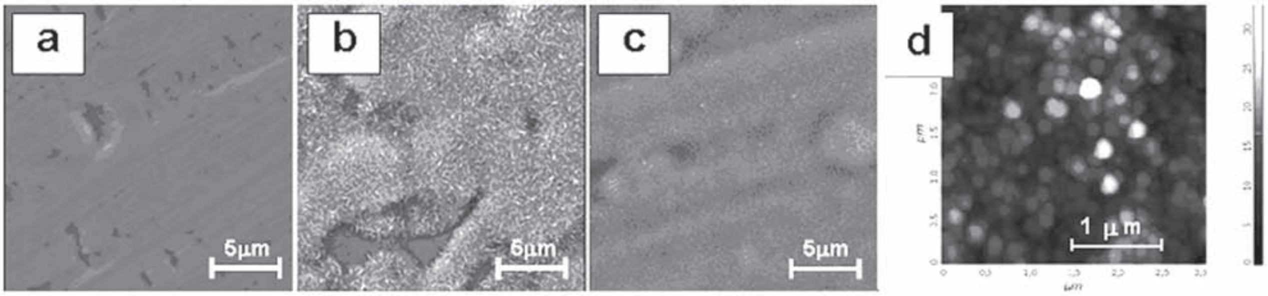

Fig. 2. SEM-images of the initial (a) and thermally oxidized (b) surface of the steel, steel with an aluminium oxide coating (c); AFM image of the coating (d)

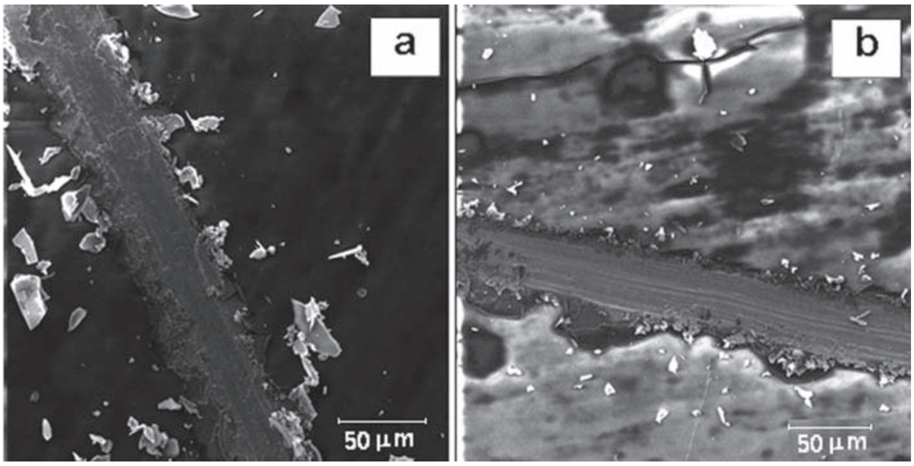

Fig. 3. SEM image of a scratch applied to a single layer (a) and double layer (b) aluminium oxide coating on steel

3.3. Corrosion behaviour of steel in a sodium chloride solution

The voltammetry and electrochemical impedance spectroscopy are highly informative electrochemical methods for studying the corrosion behaviour of metals in electrically conductive media [22, 23]. The corrosion diagrams (Evans diagrams) of the initial 08kp steel sample and samples with a single and double layer coating are shown in Fig. 4. The aluminium oxide films formed on the steel surface altered the corrosion-electrochemical behaviour of the metal, studied in a 3.5 % NaCl solution. As can be seen, the coating contributed to the shift of the stationary potential of the electrode in the positive direction by more than 600 mV, it changed the nature of the anodic and cathodic processes that occurred at the electrode|electrolyte interface. An analysis of the Evans diagram for an uncoated steel electrode showed that the corrosion process proceeds with a cathodic velocity control (due to the occurrence of the oxygen diffusion-limited current, the restoration of which provides the cathodic depolarization of the electrode).

Aluminium oxide has dielectric properties, and the film can isolate the surface of the metal from the electrolyte. Due to this, the active electrochemical oxidation of the film-coated steel was shifted by more than 1 V in the positive direction in comparison with the control sample. The change in the kinetics of the anodic and cathodic processes together led to a decrease in the corrosion current by more than two orders of magnitude. The electrode with a double layer coating has a slightly more positive stationary potential, but the nature of the polarization curves of electrodes with single and double layer coatings was similar.

The state of the electrode/electrolyte interface and the changes occurring when the electrolyte penetrated through the pores of the film to the metal surface were studied by the method of electrochemical impedance spectroscopy. The frequency dependences of the impedance module |Z| and the phase angle (Bode diagram) of 08kp steel samples after 0.5 h incubation in a 3.5 % NaCl solution are shown in Fig. 5. As can be seen, the

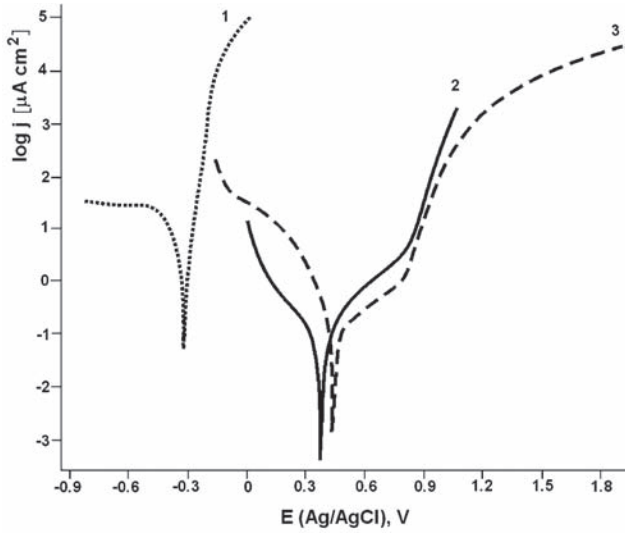

Fig. 4. Corrosion diagrams of a steel electrode without a protective coating (*1*) and with aluminium oxide single layer (*2*) and double layer (*3*) coatings

coated electrodes were characterized by higher impedance values and phase angle in comparison with the control sample. An analysis of the low-frequency part of the impedance spectrum showed a much more effective protection of the steel surface with a double layer coating: $f = 0.01$ Hz $|Z| > 10^6$ Ohm cm^2, while for electrodes with a single layer coating and without coating $|Z| < 10^4$ Ohm cm^2. In addition, the electrode with a double layer coating showed alternating current behaviour close to being purely capacitive (in a wide frequency range, the phase angle value approached −90°, and the $\log|Z| - \log f$ dependence was linear).

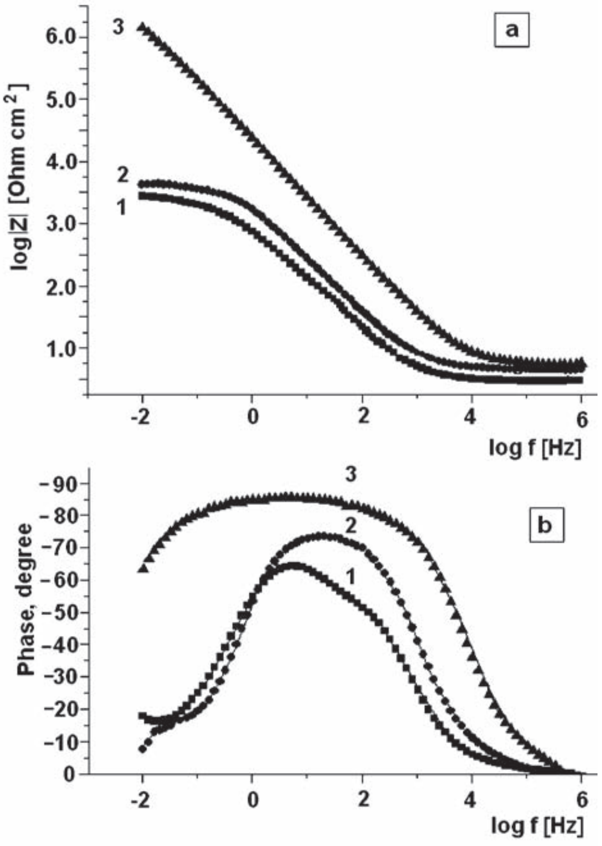

Fig. 5. Frequency dependences of the impedance module |Z| (a) and phase angle (b) of 08kp steel samples after 0.5 h exposure in a 3.5 % NaCl solution: without a coating (*1*), with an Al_2O_3 coating – single layer (*2*) and double layer (*3*)

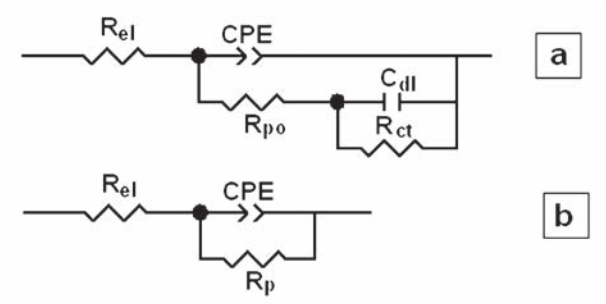

Fig. 6. Models of equivalent electrical circuits of corroding metal with a non-conductive coating (a) and metal with an insulating coating (b). Designations of EEC elements are given in the text

Probably, the single layer coating has a certain number of transverse pores. Therefore, according to the nature of the change, the frequency dependences of the impedance and phase angle of such an electrode and the initial sample were similar. The obtained dependences (Fig. 5a, b, curves *1* and *2*) were modelled by a standard equivalent electric circuit (EEC) for a corroding metal with a defective (porous) passive coating [7], shown in Fig. 6a. At the same time, for steel with a double layer coating (Fig. 5a, b, curves *3*), EEC for metal with a non-porous coating [24] was applicable, Fig. 6b. In these equivalent electrical circuits: R_{el} – electrolyte resistance, CPE – constant phase element, reflecting non-ideal coating capacitance, R_{po} – resistance of the coating/ layer of corrosion products, C_{dl} – the double layer capacitance at the metal|electrolyte interface, R_{ct} – charge transfer resistance, R_p – resistive component of the Al_2O_3-coating. Impedance Z_{CPE} is represented by the expression [25, 26]:

$$Z_{CPE} = \frac{1}{Q(j\omega)^n},$$

where Q – constant CPE element (F cm^{-2} s$^{-(1-n)}$); ω – circular frequency, $\omega = 2\pi f$ (rad s^{-1}); $j^2 = -1$ and

n – exponent of the CPE element (shows the depression angle, which characterizes the deformation of the capacitive loop in the Nyquist plot). In the case when $n = 1$, the CPE element is converted into capacitance.

The calculated EEC parameters for a corroding uncoated steel electrode and for coated electrodes are presented in the Table. From these data, it follows that a thin aluminium oxide film prevented the active development of the corrosion process and the formation of a loose layer of corrosion products. However, probably, due to the presence of transverse pores, within 0.5 h after the start of corrosion tests, the solution had already penetrated to the metal|electrolyte interface. By the end of the test the C_{dl} and R_{ct} of the control sample and the sample with a single layer coating had similar values.

The double layer coating was characterized by capacitance values lower by more than an order of magnitude when compared to a single layer coating and a very high value of the resistive component of the coating, which was associated with a higher thickness of the oxide layer. The value of the exponent $n > 0.9$. The study [27] demonstrated that for $1 > n > 0.9$, the value of Q (F cm^{-2} s$^{(1-n)}$) can be equated to the film (coating) capacitance C_f (F cm^{-2}) As can be seen from the Table and Fig. 7, after 2.5 h of contact with a corrosive medium, the sample with a double layer coating increased the capacitance by more than an order of magnitude. This finding indicated the filling of the pore space of the film with electrolyte and the actual termination of the protective effect of the coating. In this case, the alternating current behaviour of such an electrode resembles the behaviour of a single layer electrode.

4. Conclusions

Studies have shown the possibility of obtaining aluminium oxide films with satisfactory adhesion to the substrate using the sol-gel method on

Table. Parameters of the equivalent electrical circuit of the studied electrodesin 3.5 % sodium chloride solution depending on immersion time

Time, h	R_{el}, Ohm cm^2	Q, μF cm^{-2} s$^{-(1-n)}$	n	R_{po}, kOhm cm^2	$C_{dl,}$ mF cm^{-2}	R_{ct}, kOhm cm^2	R_p, kOhm cm^2
Uncoated steel							
0.5	7,2	311,7	0.75	2,80	21.9	3.7	–
1.0	7,3	353,7	0.76	2,52	16.6	1.9	–
1.5	7,2	387,4	0.76	2,28	13.2	1.5	–
2.0	7,2	418,2	0.76	2,14	12.9	1.6	–
2.5	7,2	457,6	0.76	2,06	13.2	1.7	–
3.0	7,2	492,1	0.76	2,06	13.7	1.7	–
Steel with a single layer Al_2O_3 coating							
0.5	4.5	105.9	0.86	3.96	8.1	1.1	–
1.0	4.5	125.7	0.85	2.86	8.5	1.5	–
1.5	4.4	143.6	0.85	2.42	9.4	1.6	–
2.0	4.4	162.4	0.86	2.18	10.3	1.5	–
2.5	4.5	173.6	0.86	1.86	12.2	1.3	–
3.0	4.6	197.0	0.85	1.87	14.0	1.5	–
Steel with a double layer Al_2O_3 coating							
0.08	8.5	6.10	0.92				7333
0.5	5.8	7.87	0.93	–	–	–	3994
1.0	5.7	9.29	0.92	–	–	–	3291
1.5	5.7	10.16	0.91	–	–	–	2829
2.0	5.7	11.12	0.90	–	–	–	2514
2.5*	5.6	12.33	0.89	–	–	–	2083
3.0	5.5	146.6	0.78	10.8	2.3	3.5	-

* this time limits the resistance of the coating to the penetrating effect of the electrolyte

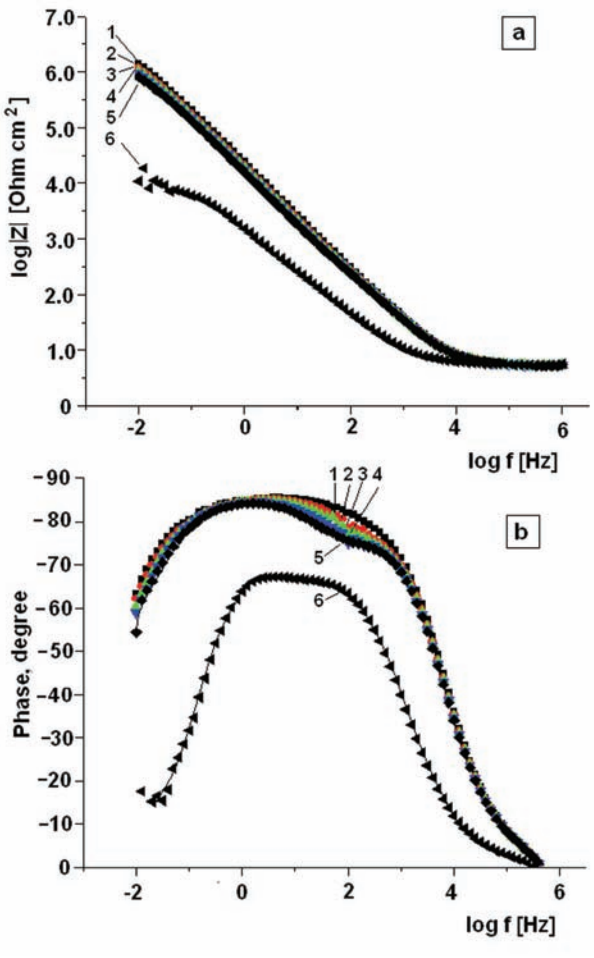

Fig. 7. Frequency dependences of the impedance module |Z| (a) and phase angle (b) of 08kp steel samples with a double layer coating after incubation in 3.5 % NaCl solution for 0.5 h (*1*); 1.0 h (*2*); 1.5 h (*3*); 2.0 h (*4*); 2.5 h (*5*) and 3.0 h (*6*)

low-alloy structural steel. The double layer film creates a physical barrier for the penetration of a corrosive solution to the surface of the metal, the effectiveness of which exceeds 2.5 h. However, the resulting coatings have a higher or lower permeability towards the components of the solution. This was due to the thermal decomposition and removal of the decomposition products of organic anions introduced into the film during the stage of preparation of boehmite hydrogels. Since the critical diameter of the acetic acid molecule is 5.1 Å (the radius is 2.55 Å, respectively) [28], the pore size formed during heat treatment of a hydrogel layer exceeds that of water molecules (1.9 Å [29]) and hydrated Cl$^-$ ions (2.28 Å [30]). Partial overlapping of the pores of the first aluminium oxide layer by the deposition of a second layer resulted in the formation of an effective protective film.

Acknowledgements

Electrochemical impedance spectroscopy and determination of particle size and zeta potential were carried out using the equipment of the Centre for the Collective Use "Upper Volga Regional Centre for Physical and Chemical Research".

Conflict of interests

The authors declare that they have no known competing financial interests or personal relationships that could have influenced the work reported in this paper.

References

1. Vert R., Carles P., Laborde E., Mariaux G., Meillo E., Vardelle A. Adhesion of ceramic coating on thin and smooth metal substrate: A novel approach with a nanostructured ceramic interlayer. *Journal of Thermal Spray Technology*. 2012; 21(6): 1128–1134. DOI: http://doi.org/10.1007 / s11666-012-9798-2

2. Guglielmi M. Sol-gel coatings on metals. *Journal of Sol-Gel Science and Technology*. 1997;8(1–3): 443–449. DOI: https://doi.org/10.1007/BF02436880

3. Bahuguna G., Mishra N. K., Chaudhary P., Kumar A., Singh R. Thin film coating through sol-gel technique. *Research Journal of Chemical Sciences*. 2016;6(7): 65–72. E-ISSN 2231-606X

4. Kobayashi Y., Ishizaka T., Kurokawa Y. Preparation of alumina films by the sol-gel method. *Journal of Materials Science*. 2005;40: 263–283. DOI: https://doi.org/10.1007/s10853-005-6080-8

5. Singh I. B., Modi O. P., Ruhi G. Development of sol-gel alumina coating on 9 Cr-1 Mo ferritic steel and their oxidation behavior at high temperature. *Journal of Sol-Gel Science and Technology*. 2015;74: 685–691. DOI: https: //DOI 10.1007 / s10971-015-3649-9

6. Masalski J., Gluszek J., Zabrzeski J., Nitsch K., Gluszek P. Improvement in corrosion resistance of the 316l stainless steel by means of Al_2O_3 coatings deposited by the sol-gel method. *Thin solid films*. 1999;349: 186–190. DOI: https://doi.org/10.1016/S0040-6090(99)00230-8

7. Tiwari S. K., Sahu R. K., Pramanick A. K., Singh R. Development of conversion coating on mild steel prior to sol gel nanostructured Al_2O_3 coating for enhancement in corrosion resistance. *Surface and Coatings Technology*. 2011;205: 4960–49677. DOI: https://doi.org/10.1016/j.surfcoat.2011.04.087

8. Oks M. E., Tyunkov A. V., Yushkov Yu. G., Zolotukhin D. B. Ceramic coating deposition by electron beam evaporation. *Surface and Coatings*

Technology. 2017;325: 1–6. DOI: https://doi.org/10.1016/j.surfcoat.2017.06.0.042

9. Xu P., Coyle T. W., Pershin L., Mostaghimi J. Superhydrophobic ceramic coating: Fabrication by solution precursor plasma spray and investigation of wetting behavior. *Journal Colloid Interface Science*. 2018; 1(523): 35–44. DOI: https://doi.org/10.1016/j.jcis.2018.03.018

10. Shu-Wei Y., Guan-Jun Y., Cheng-Xin L., Chang-Jiu L. Improving erosion resistance of plasma-sprayed ceramic coatings by elevating the deposition temperature based on the critical bonding temperature. *Journal of Thermal Spray Technology*. 2018; 27 1–2): 25–34. DOI: https://doi.org/10.1007/s11666-017-0633-7

11. Katagiri K., Tanaka Y., Uemura K., Inumaru K., Seki T., Takeoka Y. Structural color coating filters composed of an amorphous array of colloidal particles via electrophoretic deposition. *NPG Asia Materials*. 2017;9(e355): 1–7. DOI: https://doi.org/10.1038/am.2017.13

12. Alan G., Sajin G., Tinu T., Vibhath K., Sreejith M. Corrosion behavior of sol-gel derived nano-alumina film. *International Journal. Scientific & Engineering Research*. 2016;7(3): 130–139. ISSN 2229-5518

13. Wang D., Bierwagen G. P. Sol – gel coatings on metals for corrosion protection. *Progress in Organic Coatings*. 2009;64(4): 327–338. DOI: https://doi.org/10.1016/j.porgcoat.2008.08.01.01

14. Stambolova I., Yordanov S., Lakov L., Blaskov V., Vassilev S., Alexandrova M., Jivov B., Kostova Y., Simeonova S., Balashev K. Development of new nanosized sol gel coatings on steel with enhanced corrosion resistance. *Materials Science. Non-Equilibrium Phase Transformations*. 2018;4(1): 18–20. Available at: https://stumejournals.com/journals/ms/2018/1/18.full.pdf

15. Kiele E., Senvaitiene J., Grigucevičiené A., Ramanauskas R., Raudonis R., Kareiva A. Sol-gel derived coatings for the conservation of steel. *Processing and Application of Ceramics*. 2015;9(2): 81–89. DOI: https://doi.org/10.2298/PAC1502081K

16. Nofz M. Alumina Thin Films. In: Klein L., Aparicio M., Jitianu A. (eds.) *Handbook of Sol-Gel Science and Technology*. Switzerland: Springer International Publishing, Inc.; 2016. 765–808 pp DOI: https://doi.org/10.1007/978-3-319-32101-1_133

17. Grishina E. P., Kudryakova N. O., Ramenskaya L. M. *Primenenie zol'-gel 'metoda dlya naneseniya oksidno-alyuminievogo pokrytiya na nizkolegirovannuyu stal'* [Application of sol-gel method for the formation of alumina coating on low-alloyed steel]. *Gal'vanotekhnika i obrabotka vertkhnosti*. 2019;27(2): 59–68. Available at: http://www.galvanotehnika.info/articles.php?y=2019&n=2&a=6 (In Russ., abstract in Eng.)

18. Yoldas B. E., Transparent activated non-particulate alumna and method of preparing same *Patent United States, No. 3,944,658*. 1976.

19. GOST 1050-88. *Prokat sortovoj, kalibrovanyj, so special'noj otdelkoj revhnosti iz uglerodistoj kachestvennoj konstrukcionnoj stali. Obshhie tehnicheskie uslovija*. [High-quality rolled products, calibrated, with a special surface finish made of high-quality carbon structural steel. General specifications] Moscow: Standartinform Publ. (In Russ.)

20. Yang Q. I. Synthesis of γ-Al_2O_3 nanowires through a boehmite precursor route. *Bulletin of Materials Science*. 2011;34(2): 239–244. DOI: https://doi.org/10.1007/s12034-011-0062-z

21. Boumaza A., Favaro L., Ledion J., Sattonnay G., Brubach J. B., Berthet P., Huntz A. M., Roy P., Tetot R. Transition alumina phases induced by heat treatment of boehmite: An X-ray diffraction and infrared spectroscopy study. *Journal of Solid State Chemistry*. 2009; 182: 1171–1176. DOI: https://DOI: 10.1016 / j.jssc.2009.02.006.

22. Aparicio M., Mosa J. Electrochemical characterization of sol-gel coatings for corrosion protection of metal substrates. *Journal of Sol-Gel Science and Technology*. 2018; 88: 77–89. **DOI:** https://doi.org/10.1007/s10971-018-4785-9

23. Lazar A.-M., Wolfgang W. P., Marcelin S., Рйвиге N., Samйlor D., Tendero C., Vahlas C. Corrosion protection of 304L stainless steel by chemical vapor deposited alumina coatings. *Corrosion science*. 2014;81: 125–131. DOI: https://doi.org/10.1016/j.corsci.2013.12.01.01

24. Gaberšček M., Pejovnik S. Impedance spectroscopy as a technique for studying the spontaneous passivation of metals in electrolytes. *Electrochimica Acta*. 1996;41(7/8): 1137–l142. DOI: https://doi.org/10.1016/0013-4686(95)00464-5

25. Yuan X.-Z. R., Song C., Wang H., Zhang J. Electrochemical impedance spectroscopy in PEM fuel cells: fundamentals and applications. London: Springer, Inc.; 2010. 420 p.

26. Pyun S.-I., Shin H.-C., Lee J.-W., Go J.-Y. Electrochemistry of insertion materials for hydrogen and lithium. Berlin: Springer, Inc.; 2012. 250 p.

27. Orazem M. E., Frateur I., Tribollet B., Vivier V., Marcelin S., Рйвиге N., Bunge A. L., White E. A., Riemer D. P., Musiani M.. Dielectric properties of materials showing constant-phase-element (CPE) impedance response. *Journal of the Electrochemical Society*. 2013;160(6): C215–C225. DOI: https://doi.org/10.1149/2.033306jes

28. KNT group. *Production of sorbents and catalysts*. Available at: https://www.kntgroup.ru/en/information/adsorptive

29. Fok M. V. *Geometricheskaya forma molekul vody*. [The geometrical shape of a water molecule]. *Kratkie soobshchenia po fizike fian*. 2002;3: 28–32. Available at: https://cyberleninka.ru/article/n/geometricheskaya-forma-molekul-vody/viewer (In Russ.)

30. Tanganov B. B. *O razmerah gidratirovannyh ionov (k probleme opresnenija morskoj vody)* [On the size of hydrated ions (on the problem of desalination of sea water)]. *Uspehi sovremennogo estestvoznanija*. 2009;12: 25–26. Available at: http://www.natural-sciences.ru/en/article/view?id=14059 (In Russ.)

Information about the authors

Elena P. Grishina, DSc in Engineering, Chief Researcher of the Laboratory Structure and Dynamics of Molecular and Ion-Molecular Solutions, G. A. Krestov Institute of Solution Chemistry of the Russian Academy of Sciences, Ivanovo; Professor of Department of Natural Sciences, Ivanovo Fire and Rescue Academy of the State Fire Service of the Ministry of the Russian Federation for Civil Defence, Emergencies and Elimination of Consequences of Natural Disasters, Ivanovo, Russian Federation; e-mail: epg@isc-ras.ru. ORCID iD: https://orcid.org/0000-0001-8693-2930

Nadezhda O. Kudryakova, PhD in Engineering, Researcher of the Laboratory Structure and Dynamics of Molecular and Ion-Molecular Solutions, G. A. Krestov Institute of Solution Chemistry of the Russian Academy of Sciences, Ivanovo, Russian Federation; e-mail: kno@isc-ras.ru. . ORCID iD: https://orcid.org/0000-0002-1721-4422.

Lyudmila M. Ramenskaya, PhD in Chemistry, Research Fellow of the Laboratory Structure and Dynamics of Molecular and Ion-Molecular Solutions, G. A. Krestov Institute of Solution Chemistry of the Russian Academy of Sciences, Ivanovo, Russian Federation; e-mail: lmr@ isc-ras.ru. ORCID iD: https://orcid.org/0000-0003-1492-8195.

All authors have read and approved the final manuscript.

Translated by Valentina Mittova.
Edited and proofread by Simon Cox.

Condensed Matter and Interphases
(Kondensirovannye sredy i mezhfaznye granitsy)

Original articles

DOI: https://doi.org/10.17308/kcmf.2020.22/2528 eISSN 2687-0711
Received 29 November 2019
Accepted 15 December 2019

Parameters of Oxide Films Anodically Formed on Ag-Zn Alloys with Different Concentrations of Vacancy Defects in the Surface Layer

© 2020 S. N. Grushevskaya✉, A. V. Vvedenskii, V. O. Zaitseva

Voronezh State University, 1 Universitetskaya pl., Voronezh 394018, Russian Federation

Abstract

The nature and the properties of oxide films anodically formed on metals and alloys depend on the chemical composition and energetic state of the electrode surface.
This study was aimed at revealing the composition and the parameters of oxide films formed in 0.1 M KOH on silver-zinc alloys (up to 30 at.% of Zn) with different concentrations of vacancy defects in the surface layer.
The enhanced concentration of vacancy defects in the alloys surface layer was created by preliminary selective dissolution of zinc at different potentials in 0.01 M HNO_3 + 0.09 M KNO_3. These alloys were moved into 0.1 M KOH for the formation of oxide films. The composition of films was monitored by cathodic voltammetry. The film thickness was calculated from the anodic coulometry taking into account the current efficiency. The latter was determined by cathodic coulometry. The morphology of the electrode surface was monitored by scanning electron microscopy (SEM).
It was revealed that the concentration of superequilibrium vacancies formed in the surface layer depended on the potential of the selective dissolution of zinc from the alloy. The peak of Ag(I) oxide reduction was registered on the cathodic voltammograms of the alloys after their anodic oxidation. The current efficiency of oxide formation on Ag-Zn alloys was less than 100%. It decreased with zinc concentration in the alloys. The thickness of Ag(I) oxide on alloys did not exceed 25 nm. SEM images showed the uniform distribution of oxide particles along the electrode surface. The shape of the particles was close to spherical.
The Ag(I) oxide was the main product of oxidation of silver-zinc alloys (up to 30 at% of Zn) with different vacancy defects of the surface layer. The current efficiency and the thickness of Ag(I) oxide films formed on alloys with an increased concentration of vacancy defects were less as compared with the current efficiency and the thickness of Ag(I) oxide films formed on pure silver. However, these parameters were higher as compared with the parameters of Ag(I) oxide films formed on alloys with an equilibrium concentration of vacancy defects. It was found that the diameter of the Ag(I) oxide particles decreased, and their quantity on the unit of the electrode surface increased with an increase of the concentration of vacancy defects in the alloys surface layer.

Keywords: silver-zinc alloys, Ag(I) oxide, selective dissolution, anodic oxide formation.

For citation: Grushevskaya S. N., Vvedenskii A. V., Zaitseva V. O. Parameters of oxide films anodically formed on Ag-Zn alloys with different concentrations of vacancy defects in the surface layer. *Kondensirovannye sredy i mezhfaznye granitsy = Condensed Matter and Interphases*. 20120;22(1): 48–57. DOI: https://doi.org/10.17308/kcmf.2020.22/2528

1. Introduction

Silver and zinc oxides, in particular nanosized ones, are considered to be functional materials with the desired properties [1–4]. Structures of the oxide/oxide [5, 6] or oxide/metal type [7–10] play a decisive role in anode and corrosion processes. They are also used in modern semiconductor technologies and in the manufacture of sensors. The scope of application for oxide structures is determined by a set of their main parameters, depending on the method and conditions of their preparation.

One of the possible ways to obtain the oxide phase and control its parameters is the

---

✉ Svetlana N. Grushevskaya, e-mail: sg@chem.vsu.ru

anodic oxidation of homogeneous alloys with different contents of their components. During the transition from individual metals to alloys, the composition of oxidation products and the structure of the oxide film become more complicated [11–13]. In addition, a number of side electrochemical reactions can occur at the potentials of oxide growth; therefore, data on the current efficiency of the anodic oxide formation process are required for the correct evaluation of its thickness. Finally, during the anodic oxidation of alloys, the possibility of their selective dissolution (SD) should be taken into account, as a result of which the electronegative component predominantly passes into the solution, and the surface zone of the alloy is enriched with the electropositive component and superequilibrium vacancies [14–17]. Due to a significant increase in the concentration of vacancies in comparison with the equilibrium concentration, the energy saturation of the system as a whole also increases, which can be reflected both in the kinetics of further oxide formation and in the properties of anodically formed oxides. The concentration of vacancy defects in the surface layer of the alloy can be controlled by changing the conditions of the SD.

The goal of this study was the calculation of the current efficiency of the anodic oxide formation and determination of the composition and thickness of oxide films anodically formed in 0.1 M KOH on silver-zinc alloys with different concentrations of vacancy defects in the surface layer.

2. Experimental

Homogeneous polycrystalline alloys were made of silver and zinc (metal purity of 99.99 at%) in vacuum quartz ampoules with exposure at a temperature of 1273 K for at least two hours and their subsequent slow cooling. Predicted zinc concentration N_{Zn} was from 5 to 30 at% (Table 1). The phase (a-phase) and chemical compositions of the alloys were confirmed by X-ray diffractometry and energy-dispersive microanalysis [18]. Samples were mounted in epoxy resin in such a way that the working surface with the geometric area S_g from 0.4 to 0.5 cm^2 remained open (Table 1). The preparation of the surface of the electrodes for the experiment included mechanical processing on abrasive paper, polishing on suede and degreasing with isopropyl alcohol.

Electrochemical studies were carried out using an IPC-Compact potentiostat (Institute of Physical chemistry and Electrochemistry, RAS, Moscow). Anodic oxide formation and determination of current efficiency were performed in 0.1 M KOH (pH 12.89), prepared on double distilled water from a chemically pure reagent and deaerated by sparging with chemically pure argon. The sequence of stages was as follows:

1. Cathodic polarization in an alkaline solution for 300 s at a potential E_c = –1.1 V for reduction of oxide traces and standardization of the surface.

2. Potential-controlled and charge-controlled anodic synthesis of Ag(I) oxide of a specified thickness (34 nm under the assumption of 100% current efficiency of the anodic formation of Ag_2O) at potential E_a = 0.56 V. This value was chosen based on the results of anodic voltammetry and corresponds to the maximum growth rate of Ag(I) oxide on silver in 0.1 M KOH [18].

3. Change of alkaline solution in a cell in a sealed argon atmosphere for the removal of soluble oxidation products of silver or zinc.

4. Potentiodynamic cathodic polarization at a scan rate of 1 mV s^{-1} from open-circuit potential E_0 to E_c.

In a separate series of experiments, after the completion of stage 2, the dependence of the open-circuit potential E_0 from time was recorded for 20 min, after the solution was changed (stage 3) and the cathodic potentiodynamic reduction of the oxidation products remaining on the electrode surface was performed (stage 4).

For the determination of the role of super-equilibrium vacancies before anodic oxide

Table 1. Symbols and the geometric surface of Ag-Zn alloys (α-phase) with different concentration of zinc N_{Zn}

N_{Zn}, at%	5	10	15	20	30
Symbol	Ag5Zn	Ag10Zn	Ag15Zn	Ag20Zn	Ag30Zn
Surface, cm^2	0.40	0.44	0.43	0.42	0.48

formation, the potential-controlled and charge-controlled SD of Ag15Zn and Ag30Zn alloys in 0.01 M HNO_3 + 0.09 M KNO_3 (pH 2.16) solution, prepared on double distilled water from chemically pure reagents and deaerated by sparging with chemically pure argon was performed. The sequence of stages was as follows:

1′. Immersion of the working electrode for 240 s in acid solution under protection potential $E_c = -1.1$ V, eliminating the ionization of both components for the reduction of traces of oxides and standardization of the surface.

2′. Anodic selective dissolution for 60 s at potentials $E_1^{SD} = 0.4$ V, $E_2^{SD} = 0.5$ V or $E_3^{SD} = 0.6$ V. Potential values were selected based on the results of anodic voltammetry (Fig. 1) and correspond to the thermodynamic stability region of the electropositive component of the alloy.

On the alloys obtained as a result of stages 1′ and 2′, the oxide was formed with the subsequent determination of the current efficiency (stages 1–4).

The current efficiency Ψ of the anodic oxidation process in all experiments was calculated as the ratio of the cathodic charge of film reduction Q_c to the anodic charge of its formation Q_a:

$$\Psi = Q_c/Q_a. \tag{1}$$

The determined current efficiency was used for the calculation of the thickness of the formed oxide layer:

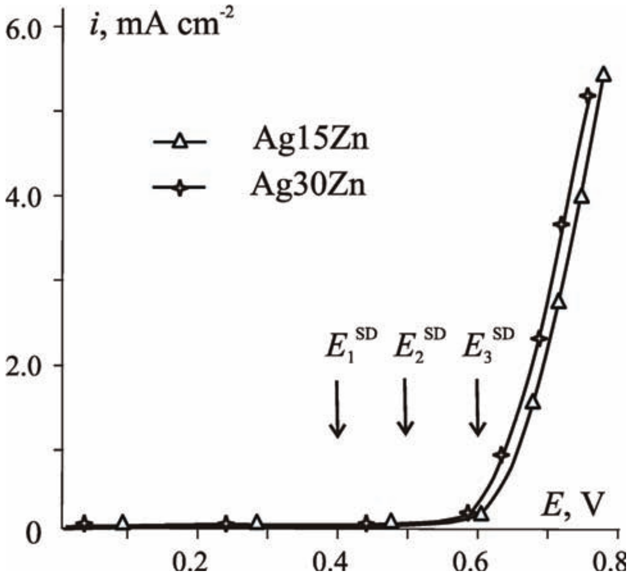

Fig. 1. Anodic voltammograms of Ag-Zn alloys in 0.01 M HNO_3 + 0.09 M KNO_3

$$L = \Psi M q_a/(zF\rho), \tag{2}$$

where M and ρ are the molar mass and density of the oxide; q_a is the density of the anodic charge; z is the number of electrons involved in oxide formation; $F = 96485$ C mol^{-1} is Faraday constant.

The control of surface morphology and composition was carried out using scanning electron microscope JSM 6380LV with microanalysis system INCAx-sight 250 (JEOL, Japan)[*]. Images were obtained using the secondary electron mode with an accelerating voltage of 20 kV.

3. Results and Discussion

3.1. Anodic oxidation of Ag–Zn *alloys without preliminary selective dissolution*

On chronoamperograms obtained in deaerated 0.1 M KOH on silver and Ag–Zn alloys at a potential $E = 0.56$ V, a sharp and then smoother decrease of current was observed (Fig. 2a). At times greater than 10–20 s, the current density reached an almost constant value.

According to (2), for the formation of an Ag_2O film with an estimated thickness of 34 nm, assuming 100% current efficiency, it is necessary to accumulate a charge density of 20 mC cm^{-2}. Fig. 2a shows that with an increase in the initial concentration of zinc in the alloy, the polarization time required for the accumulation of a given charge density decreased.

With times not exceeding 5–10 s, linear sections in the coordinates, criterion for diffusion-limited processes were observed (Fig. 2b). A similar situation observed for pure silver and its alloys with gold allowed the authors of the study [19] to draw a conclusion about the solid-phase-diffusion control of the anode process. It should be assumed that on silver-zinc alloys, the anode process is controlled by mass transfer along the phase of the growing oxide as well.

In the general case, the recorded current and charge characterize not only the formation of Ag_2O oxide

$$2Ag + 2OH^- = Ag_2O + H_2O + 2\,e^-, \tag{3}$$

but also the transition of silver ions into the solution:

$$Ag + 2OH^- = Ag(OH)_2^- + e^-. \tag{4}$$

In addition, zinc oxidation, accompanied by the formation of an oxide or hydroxide film on the

---

[*] Centre for the Collective Use of Scientific Equipment of VSU.

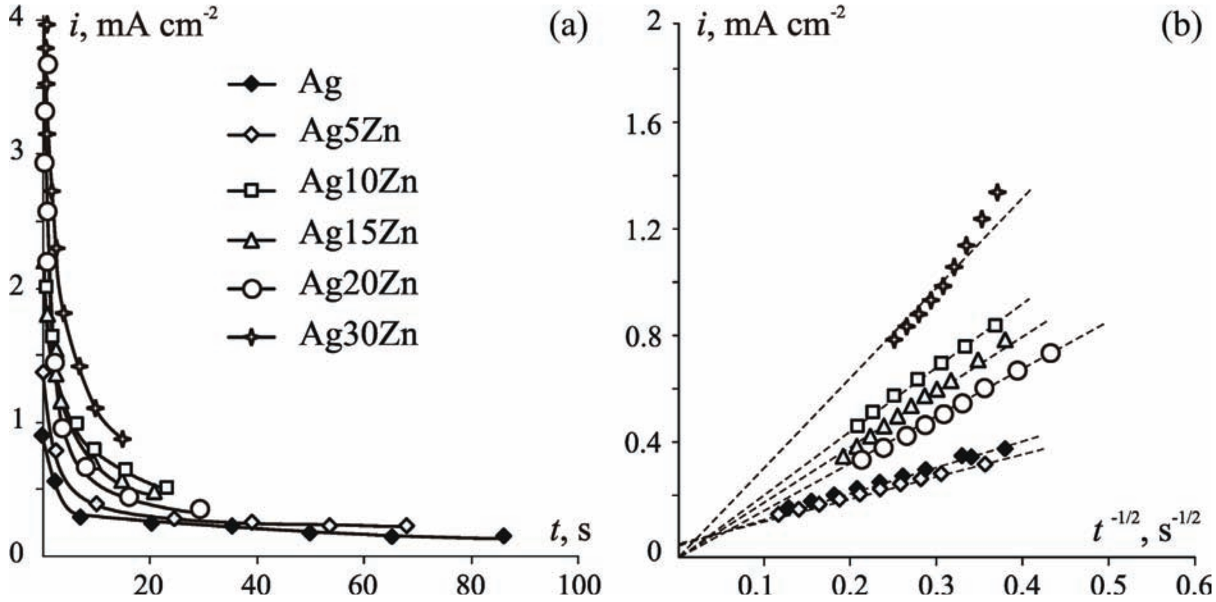

Fig. 2. Current transients of silver and Ag-Zn alloys in original (a) and Cottrell coordinates (b) in 0.1 M KOH at $E_a = 0.56$ V

surface of the electrode and ions in the electrolyte solution is possible:

$$Zn + 2OH^- = ZnO + H_2O + 2e^-; \quad (5)$$

$$Zn + 2OH^- = Zn(OH)_2 + 2e^-; \quad (6)$$

$$Zn + 4OH^- = Zn(OH)_4^{2-} + 2e^-. \quad (7)$$

In solutions with a high pH value (> 10), soluble products are formed:

$$ZnO + OH^- + H_2O = Zn(OH)_3^-; \quad (8)$$

$$ZnO + 2\,OH^- + H_2O = Zn\,(OH)_4^{2-}. \quad (9)$$

3.2. Measurement of open-circuit potential

Certain information regarding the nature and electrochemical behaviour of the oxide or hydroxide phase formed in 0.1 M KOH can be obtained using chronopotentiometry in open-circuit mode, carried out after the end of potentiostatic polarization (Fig. 3). When $N_{Zn} \leqslant 10$ at.% the open-circuit potential E_0 of oxidized alloys varies slightly over time and remains close to the values characteristic of Ag(I) oxide formed on silver. When concentration of zinc in the alloy increases, the potential E_0 shifts to less positive values. At the same time, a rather sharp decrease of potential over time was observed. Chemical dissolution of Ag(I) oxide can be the reason for a decrease in E_0:

$$Ag_2O + 2\,OH^- + H_2O = 2\,Ag\,(OH)_2^-. \quad (10)$$

The possibility of this process on silver and its alloys with gold was confirmed by the results of the photopotential measurement experiments [20–22].

3.3. Selective dissolution of Ag-Zn alloys

Chronoamperograms obtained on Ag15Zn and Ag30Zn alloys in 0.01 M HNO_3 + 0.09 M KNO_3 at various E^{SD} potentials had a similar shape. Typical current transients are shown in Fig. 4*a* for Ag15Zn alloy. During the anodic polarization, the current dropped to almost zero, reflecting the almost

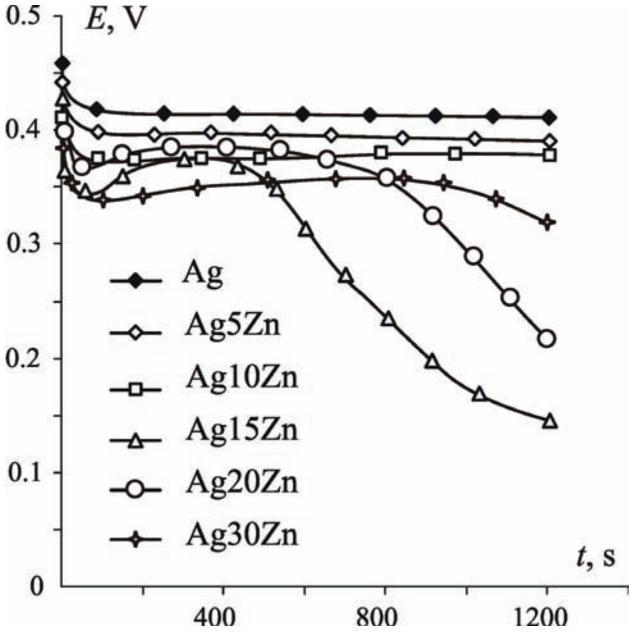

Fig. 3. Potential transients of silver and Ag-Zn alloys after the anodic oxidation in 0.1 M KOH

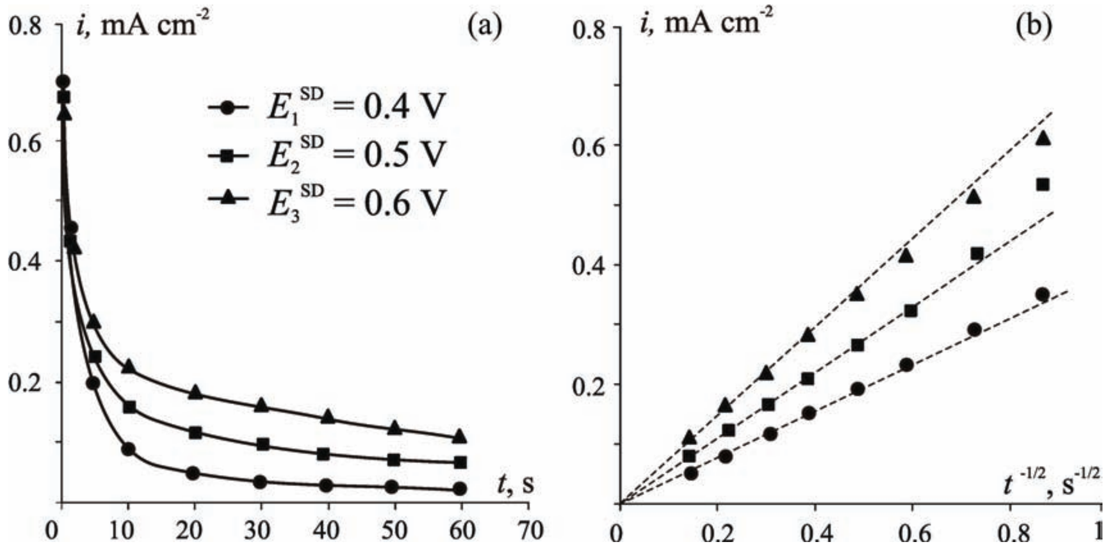

Fig. 4. Current transients of Ag15Zn in original (a) and Cottrell coordinates (b) at different E^{SD} in 0.01 M HNO_3 + 0.09 M KNO_3

complete dezincification of the surface layer of the alloy. The presence of linear sections in the Cottrell coordinates (Fig. 4*b*) allows applying SD chronoamperometry theory for the calculation of the diffusion coefficient and concentration of vacancies [15, 16]:

$$I(t) = \frac{z_A F N_A D_A^{1/2} S_g}{V_m \pi^{1/2} t^{1/2}} \left[1 - e^{-\frac{z_A F}{RT}\eta} \right]. \qquad (11)$$

Here: I – current, t – time, z_A – the number of electrons involved in the oxidation of the electronegative component, N_A – volume concentration of atoms of component A in the alloy, $D_A = D_v N_v$ – diffusion coefficient of the atoms of component A in the surface layer of the alloy, D_v – diffusion coefficient of vacancies, N_v – concentration of vacancies, S_g – geometric surface area of the electrode, V_m – molar volume of the alloy, R = 8.314 J K^{-1} mol^{-1} – universal gas constant, T = 298 K – temperature, η – overvoltage.

The values of equilibrium vacancy concentrations equal to $2.55 \cdot 10^{-5}$ and $1.05 \cdot 10^{-5}$ at.% in Ag15Zn and Ag30Zn alloys, respectively, were obtained by thermodynamic calculations using data on the vacancy formation energy and their diffusion coefficients in individual metals [16].

Zinc diffusion coefficients D_A calculated according to (11) from the slopes $i,t^{-1/2}$-dependencies for each of the alloys increased with increase in E^{SD} (Table 2). According to the solid-phase-diffusion mechanism of SD, the reason for this is an increase in the concentration of superequilibrium vacancies (Table 2), e.g., the concentration of vacancy defects in the surface layer.

3.4. Anodic oxidation of Ag-Z**n** *alloys after selective dissolution*

Chronoamperograms obtained in 0.1 M KOH on alloys with different concentration of vacancy defects in the surface layer were similar in shape to chronoamperograms obtained on alloys without preliminary SD (not shown in the figures). Linear sections were also preserved in the criterion coordinates, indicating the transport nature of the limitations of the anode process in

Table 2. Diffusion coefficients of zinc D_A and concentration of superequilibrium vacancies N_v in the surface layer of Ag-Zn alloys at different potentials E^{SD}

Alloy	E^{SD}, V	D_A 10^{18}, cm^2 s^{-1}	N_v 10^4, at%
Ag15Zn	0.40	3.8	1.0
	0.50	8.1	2.1
	0.60	12.2	3.2
Ag30Zn	0.40	0.7	0.09
	0.50	1.1	0.1
	0.60	2.7	0.4

an alkaline environment. Most likely, the nature of the anodically formed products did not undergo significant changes during the transition from alloys without SD to alloys after SD.

3.5. The cathodic reduction of insoluble products of alloys oxidation

The cathodic voltammograms obtained on silver and alloys with an equilibrium concentration of vacancies after the end of anodic oxidation and change of solution in the cell are shown in Fig. 5a.

Considering the equilibrium potentials of processes (3)–(7), we can conclude that the maximum cathode current at potentials $E_{Ag(I)}$ = 0.32–0.36 V corresponds to the reduction process of Ag(I) oxide. A sharp increase in the cathode current associated with the onset of hydrogen emission was observed at potentials near –1.0 V, which was significantly higher than the equilibrium potentials of formation/reduction of zinc oxide or hydroxide (~ –1.3 V). Thus, if the products of zinc oxidation were also present in the oxide film on the alloys, then it was impossible to detect their presence using cathodic voltammograms.

When the cathodic reduction was preceded by a 20-minute stage of potential measurement in open-circuit mode, then the shape of voltammograms in general did not change (Fig. 5b). However, the peak of reduction of the Ag(I) oxide sharply decreased in amplitude, and it was absent on the Ag20Zn and Ag30Zn alloys. Indeed, on these alloys E_0 value was below $E_{Ag(I)}$ potentials of the reduction of Ag_2O. It should be assumed that the major volume of the formed oxide was already chemically dissolved according to (10) over the period of recording of the open-circuit potential.

If anodic oxidation was preceded by SD of alloys (stages 1′ and 2′), then E_0 and $E_{Ag(I)}$ potentials on cathodic voltammograms were shifted to more positive values characteristic for pure silver (Fig. 5c). The cathodic peak of reduction of the Ag(I) oxide was reliably fixed, and the absolute values of the maximum current were much higher than on alloys not subjected to preliminary SD.

5.6. The current efficiency of the anodic formation of Ag(I) *oxide*

The results of calculating the current efficiency according to (1) and the thickness of the Ag_2O films corrected to this value by (2) formed on silver and alloys of the Ag-Zn system after various stages of research are summarized in Tables 3 and 4. Cathodic charge Q_c characterizing the reduction of Ag(I) oxide was calculated according to the results of cathodic voltammetry (Fig. 5a, b, c) in the potential region from E_0 up to E = 0.20 V.

The current efficiency of anodic oxide formation on alloys without SD (Table 3) was lower than on silver, and decreased with increasing zinc concentration in the alloy. Accordingly, the thickness of the Ag(I) oxide also decreased from 32 to 5.8 nm during the transition from Ag to Ag30Zn. The decrease in current efficiency with increasing zinc concentration can be explained by an increase in the porosity of the oxide film. As a result, the possibility of dissolution of silver through the pores increased, the fraction of the current used for the formation of silver ions entering the solution

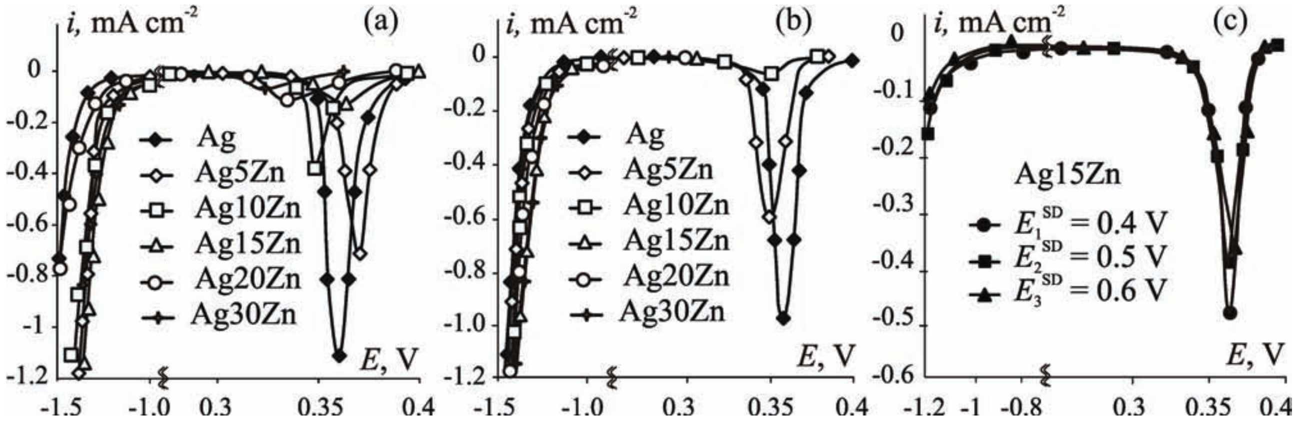

Fig. 5. Cathodic voltammograms of silver and Ag-Zn alloys after the anodic polarization at E_a = 0.56 V and change of the solution: (a) without an open-circuit stage; (b) after the open-circuit stage and after the preliminary selective dissolution of Ag15Zn (c)

Table 3. Current efficiency Ψ and thickness L of Ag(I) oxide, anodically formed on silver and alloys without preliminary SD

N_{Zn}, at. %	Without an open-circuit stage		After the open-circuit stage	
	Ψ, %	L, nm	Ψ*, %	L*, nm
0	94.4	32.0	89.1	30.3
5	70.7	24.0	65.5	22.3
10	39.4	13.0	28.7	9.6
15	28.0	9.5	28.2	9.6
20	24.6	8.4	8.1	2.8
30	16.2	5.8	5.4	1.8

Table 4. Current efficiency Ψ^{SD} and thickness L^{SD} of Ag(I) oxide, anodically formed on Ag15Zn and Ag30Zn after the preliminary SD

N_{Zn}, at. %	E^{SD}, V	Ψ^{SD}, %	L^{SD}, nm
15	0.4	53.2	18.1
	0.5	47.9	16.3
	0.6	43.3	14.7
30	0.4	12.4	4.2
	0.5	8.1	2.8
	0.6	3.5	1.7

increased, and the fraction of the current used for the formation of the film decreased.

After a 20 min exposure in open circuit mode, the current efficiency values of Ψ* calculated from (1) and oxide thickness L* determined by (2) further decreased (Table 3), which confirms the assumption of the chemical dissolution of silver oxide in an alkaline medium.

The current efficiency of anodic oxide formation on alloys subjected to preliminary SD (Table 4) was lower than that on silver, but higher than that on alloys without preliminary SD. As the potential of SD increased, i.e., increased concentration of vacancy defects in the surface layer of the alloy, the current efficiency and thickness of the Ag(I) oxide decreased.

3.7. Morphology of anodically formed films

Comparison of the results of energy-dispersive microanalysis conducted on the alloys before the start of their anodic oxidation and after its completion demonstrated an increase in the oxygen concentration in the surface layer (Table 5), which confirms the presence of an oxide layer on the surface.

The thickness of the oxide intended for SEM was increased to 120 nm, taking into account the obtained current efficiency values. Typical SEM images of the oxidized surface for Ag15Zn and Ag30Zn without SD (Fig. 6a, b) and for the same alloys, but subjected to preliminary SD at the potential E_2^{SD} (Fig. 6 c, d) are presented. On the surface of all alloys, individual particles of the oxide phase can be observed; the particle shape was close to spherical. Depending on the initial concentration of zinc in the alloy and the conditions for preparing the surface for oxidation, the particles size and quantity on the unit of the electrode surface changed.

On alloys not subjected to preliminary SD, a decrease in the particle diameter of the formed

Table 5. The composition (at.%) of the alloy samples before and after the anodic oxidation

Stage	Element	Alloy				
		Ag5Zn	Ag10Zn	Ag15Zn	Ag20Zn	Ag30Zn
Before oxidation	Ag	93.77	89.32	85.99	77.84	71.36
	Zn	6.23	10.68	14.01	22.16	28.64
After oxidation	Ag	54.23	61.66	52.45	38.50	40.27
	Zn	2.90	8.30	7.81	11.23	15.86
	O	42.87	30.03	39.74	50.27	43.87

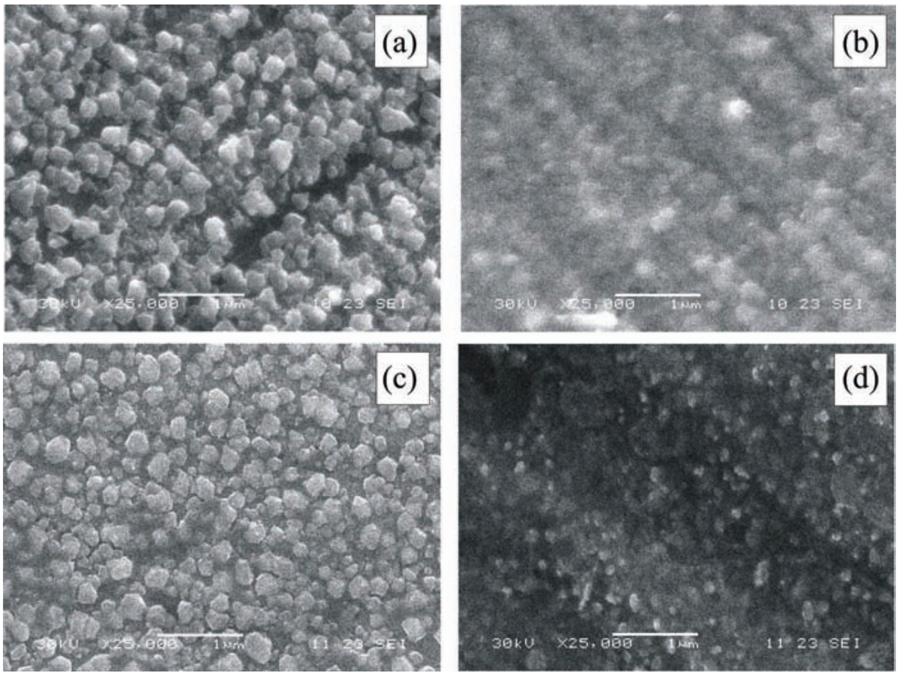

Fig. 6. SEM images of Ag(I) oxide, anodically formed on Ag15Zn (a), (c) and Ag30Zn (b), (d) in 0.1 M KOH at E_a = 0.56 V without SD (a), (b) and after preliminary SD at E_2^{SD} = 0.50 V (c), (d)

oxide with increasing zinc concentration was revealed (Table 6). Probably this situation was associated with a decrease in the interatomic distance of Ag-Ag from 0.409 to 0.403 nm with increasing N_{Zn} from 0 to 30 at.% [23]. At the same time, an increase in the oxide particles quantity on the unit of the electrode surface was observed.

Upon transition to alloys subjected to preliminary SD, the particles diameter decreased, and the particles quantity on the unit of the electrode surface increased (Table 6). In this case, a decrease in the particle size of the Ag(I) oxide probably was associated with an increase in the concentration of vacancy defects in the surface layer of alloys. It is not possible to trace a clear trend of decreasing oxide particles diameter or increasing their quantity on the unit of the electrode surface with increasing zinc concentration on alloys after SD.

4. Conclusions

1. Ag(I) oxide is the main product of the anodic dissolution in an aqueous alkaline medium of homogeneous polycrystalline alloys of the Ag-Zn system (α-phase), as well as these alloys, but subjected to preliminary selective dissolution of zinc from their surface layer in an acidic medium.

2. Silver-zinc alloys with enriched to almost pure silver, but with a structurally-disordered surface layer, are characterized by increased current efficiency of the anodic oxide formation process, as well as a higher thickness of Ag(I)

Table 6. Diameter *d* of Ag_2O particles and their quantity *P* on the unit of the electrode surface

Stage	Parameter	Electrode					
		Ag	Ag5Zn	Ag10Zn	Ag15Zn	Ag20Zn	Ag30Zn
Without SD	*d*, nm	350	200	170	180	200	170
	P, μm⁻²	13	13	13	21	28	21
E_1^{SD}	*d*, nm	–	95	100	90	90	100
	P, μm⁻²	–	111	44	101	68	79
E_2^{SD}	*d*, nm	–	160	110	110	120	100
	P, μm⁻²	–	44	59	59	87	70
E_3^{SD}	*d*, nm	–	90	100	95	90	95
	P, μm⁻²	–	70	70	71	67	60

oxide in comparison with equilibrium alloys of the same chemical composition. At the same time, these characteristics turn out to be noticeably lower in comparison with compact polycrystalline silver.

3. Ag(I) oxide, anodically formed on silver and silver-zinc alloys (α-phase) of not only the initial composition, but also after the selective dissolution of zinc from their surface layer, is chemically unstable in an alkaline medium.

4. The diameter of the anodically formed Ag(I) oxide particles decreases, and their quantity on the unit of the electrode surface increases with an increase in the concentration of vacancy defects in the surface layer of the alloy.

Acknowledgments

The results of the research were obtained using the Centre for the Collective Use of Scientific Equipment of Voronezh State University. URL: http://ckp.vsu.ru

Conflict of interests

The authors declare that they have no known competing financial interests or personal relationships that could have appeared to influence the work reported in this paper.

References

1. Gao X.-Y., Wang S.-Y., Li J., Zheng Y.-X., Zhang R.-J., Zhou P., Yang Y.-M., Chen L.-Y. Study of structure and optical properties of silver oxide films by ellipsometry, XRD and XPS methods. *Thin Solid Films*. 2004;455-456: 438-442. DOI: https://doi.org/10.1016/j.tsf.2003.11.242

2. Mehdi H. E., Hantehzadeh M. R., Valedbagi Sh. Physical properties of silver oxide thin film prepared by DC magnetron sputtering: effect of oxygen partial pressure during growth. *J. Fusion Energy*. 2013;32(1): 28–33. DOI: https://doi.org/10.1007/s10894-012-9509-5

3. Ferretti A. M., Ponti A., Molteni G. Silver(I) oxide nanoparticles as a catalyst in the azide–alkyne cycloaddition. *Tetrahedron Letters*. 2015;56(42): 5727-5730. DOI: https://doi.org/10.1016/j.tetlet.2015.08.083

4. Klingshirn C. F., Meyer B. K., Waag A., Hoffmann A., Geurts J. *Zinc oxide. From fundamental properties towards novel applications*. Berlin: Springer; 2010. 374 p.

5. Wei J., Lei Y., Jia H., Cheng J., Hou H., Zheng Z. Controlled in situ fabrication of Ag_2O/AgO thin films by a dry chemical route at room temperature for hybrid solar cells. *Dalton Trans*. 2014;43(29): 11333–11338. DOI: https://doi.org/10.1039/C4DT00827H

6. Shuaishuai M., Jinjuan X., Yuming Z., Zewu Z. Photochemical synthesis of ZnO/Ag_2O heterostructures with enhanced ultraviolet and visible photocatalytic activity. *J. Mater. Chem. A*. 2014;2(20): 7272–7280. DOI: https://doi.org/10.1039/C4TA00464G

7. Shahriary L., Athawale A. A. Electrochemical deposition of silver/silver oxide on reduced graphene oxide for glucose sensing. *J. Solid State Electrochem*. 2015;19(8): 2255–2263. DOI: https://doi.org/10.1007/s10008-015-2865-0

8. Istomina O. V., Evstropiev S. K., Kolobkova E. V., Trofimov A. O. Photolysis of diazo dye in solutions and films containing zinc and silver oxides. *Optics and Spectroscopy*. 2018;124(6): 774–778. DOI: https://doi.org/10.1134/S0030400X18060097

9. Xiang Q., Meng G., Zhang Y., Xu J., Xu P., Pan Q., Yu W. Ag nanoparticle embedded-ZnO nanorods synthesized via a photochemical method and its gas-sensing properties. *Sens. Actuators B*. 2010 ;143(2): 635–640. DOI: https://doi.org/10.1016/j.snb.2009.10.007

10. Meng F., Hou N., Jin Z., Sun B., Guo Z., Kong L., Xiao X., Wu H., Li M., Liu J. Ag-decorated ultra-thin porous single-crystalline ZnO nanosheets prepared by sunlight induced solvent reduction and their highly sensitive detection of ethanol. *Sens. Actuators B*. 2015;209: 975–982. DOI: https://doi.org/10.1016/j.snb.2014.12.078

11. Kaesche H. *Corrosion of metals*. Berlin: Springer-Verlag; 2012. 594 p.

12. McCafferty E. *Introduction to corrosion science*. New York: Springer; 2010. 583 p.

13. Marcus P. *Corrosion mechanisms in theory and practice*. New York: Marcel Dekker; 2002. 729 p.

14. Marshakov I. K., *Termodinamika i korroziya splavov* [Thermodynamics and corrosion of alloys]. Voronezh: VSU Publishing House; 1983. 166 p. (In Russ.)

15. Marshakov I. K., Vvedensky A.V., Kondrashin V. Yu., Bokov G. A. *Anodnoe rastvorenie i selektivnaya korroziya splavov* [Anodic dissolution and selective corrosion of alloys]. Voronezh: VSU Publishing House; 1988. 402 p. (In Russ.)

16. Kozaderov O. A., Vvedensky A. V. *Massoperenos i fazoobrazovanie pri anodnom selektivnom rastvorenii gomogennykh splavov* [Mass transfer and phase formation during anodic selective dissolution of homogeneous alloys]. Voronezh: Nauchnaya kniga; 2004. 288 p. (In Russ.)

17. Vvedenskii A. V., Kozaderov O. A. Linear voltammetry of anodic selective dissolution of homogeneous metallic alloys. In: Saito Y., Kikuchi T. (eds.) *Voltammetry: theory, types and applications*. New York: Nova Science Publishers, Inc.; 2014. 363 p.

18. Murtazin M. M., Nesterova M. Yu., Grushevskaya S. N., Vvedensky A. V. Silver(I) oxide on silver-zinc alloys: anodic formation and properties. *Electrochemistry*. 2019;55(7): 873–884. DOI: https://doi.org/10.1134/S0424857019070089 (In Russ.)

19. Vvedenskii A., Grushevskaya S., Kudryashov D., Kuznetsova T. Kinetic peculiarities of anodic dissolution of silver and Ag-Au alloys under the conditions of oxide formation. *Corrosion Science*. 2007;49: 4523–4541. DOI: https://doi.org/10.1016/j.corsci.2007.03.046

20. Kudryashov D. A., Grushevskaya S. N., Vvedensky A. V. *Fotopolyarizatsiya v anodnom okside Ag2O na serebre pri UF-obluchenii* [Photopolarization in anodic oxide Ag_2O on silver under UV irradiation]. *Kondensirovannye sredy i mezhfaznye granitsy = Condensed Matter and Interphases*. 2005;7(2): 141–149. Available at: http://www.kcmf.vsu.ru/resources/t_07_2_2005_006.pdf (In Russ.)

21. Kudryashov D. A., Grushevskaya, S. N., Vvedenskii A. V. Determining some structure-sensitive characteristics of nano-sized anodic Ag(I) oxide from photopotential spectroscopy. *Protection of Metals*. 2007;43: 591–599. DOI: https://doi.org/10.1134/S0033173207060124

22. Kudryashov D. A., Grushevskaya S. N., Olalekan O., Kukhareva N. V., Vvedenskii A. V. Effect of orientation of crystal face of silver and its alloying with gold on properties of thin anodic Ag(I) oxide films: II. Photopotential. *Protection of Metals and Physical Chemistry of Surfaces*. 2010;46(1): 32–39. DOI: https://doi.org/10.1134/S2070205110010041

23. Pearson W. B. *A Handbook of lattice spacing sand structures of metals and alloys*. London: Pergamon Press; 1958. 1044 p.

Information about the authors

Svetlana N. Grushevskaya – PhD in Chemistry, Associate Professor, Department of Physical Chemistry, Voronezh State University, Voronezh, Russian Federation; e-mail: sg@chem.vsu.ru. ORCID iD: https://orcid.org/0000-0002-7083-1438.

Aleksander V. Vvedenskii, DSc in Chemistry, Professor, Department of Physical Chemistry, Voronezh State University, Voronezh, Russian Federation; e-mail: alvved@chem.vsu.ru. ORCID iD: https://orcid.org/0000-0003-2210-5543.

Valeria O. Zaitseva, 5th year student of the Faculty of Chemistry, Voronezh State University, Voronezh, Russian Federation; e-mail: valera.zaytseva.00@mail.ru.

All authors have read and approved the final manuscript.

Translated by Valentina Mittova.
Edited and proofread by Simon Cox.

Condensed Matter and Interphases
(Kondensirovannye sredy i mezhfaznye granitsy)

Original articles

DOI: https://doi.org/10.17308/kcmf.2020.22/2529 eISSN 2687-0711
Received 30 January 2020
Accepted 15 March 2020

X-ray Diffraction Analysis of Thin Metal Films with Magnetic Layers of Fe-Cr-Co Alloy

© 2020 V. S. Zayonchkovskiy✉,[a], I. A. Antoshina[b], Aung Kyaw Kyaw[a], E. I. Isaev[b], I. M. Milyaev[c]

[a] *Kaluga branch of Bauman Moscow State Technical University (national research university),
2 Bazhenova str., Kaluga 248000, Russian Federation*

[b] *Obninsk Institute for Nuclear Power Engineering (OINPE) – a branch of National Research Nuclear University MEPhI,
1 Studgorodok, Obninsk 249040, Kaluga region, Russian Federation*

[c] *Baikov Institute of Metallurgy and Materials Science, RAS, 49 Leninsky prospekt, Moscow 119334, Russian Federation*

Abstract

The aim of this study was to determine the phase composition of the structures of permanent magnet films with layers of a Fe-Cr-Co alloy of micron range thickness, also known as the Kaneko alloy. The information about the phase composition is necessary for the development of physical and technical approaches for the production of optimal structures with permanent magnet films on single-crystal silicon wafers, the films being based on a dispersion-hardened alloy with the magnetization vector in the plane of the silicon substrate.

Three-layer metal films were obtained by magnetron sputtering on a silicon wafer: a dispersion-hardened alloy layer based on the Fe-Cr-Co system (3600 nm thick),), a compensating copper layer (3800 nm), and a vanadium adhesion barrier layer (110 nm). Multilayer films formed on a silicon wafer were subjected to one-minute of annealing in a high vacuum in the temperature range of 600–650 °C. A qualitative phase analysis of the structures obtained by magnetron sputtering and subjected to a single-stage thermal treatment was performed using X-ray diffraction.

It was determined that high-vacuum “rapid” one-minute of annealing of the Fe-Cr-Co dispersion-hardened alloy layer in the temperature range of 600–650 °C does not result in the formation of oxides of the main components or the σ-phase. At the temperature of 630 °C, the maximum intensity of the X-ray diffraction line (110) of the α-phase is observed, which indicates the formation of a predominantly α-solid solution and serves as a basis for the correct implementation of the subsequent annealing stages for the spinodal decomposition of this phase.

Keywords: magnetron sputtering, thin films, coercive force, vacuum annealing, phase composition.

For citation: Zayonchkovskiy V. S., Antoshina I. A., Aung Kyaw Kyaw, Isaev E. I., Milyaev I. M. X-ray diffraction analysis of thin metal films with magnetic layers of Fe-Cr-Co alloy. *Kondensirovannye sredy i mezhfaznye granitsy = Condensed Matter and Interphases*. 2020;22(1): 58–65. DOI: https://doi.org/10.17308/kcmf.2020.22/2529

1. Introduction

Bulk permanent magnets are produced from various materials. However, permanent magnet films used in microelectronics can only be made from materials which are suitable for use with integrated circuit technology. Permanent magnet films are used to bias magnetically soft active layers of magnetoresistors of magnetoresistive integrated circuits (MIC) on silicon substrates [1–4]. Such MICs are used to produce contactless current sensors and read/write heads of disk drives. The in-plane bias of magnetoresistors is created in order to neutralise the Barkhausen effect. The high-quality magnet films described in [4] were based on precious metals, which increased the cost of such magnets significantly. An alternative to using precious metals is to create magnets using dispersion-hardened alloys (DHA) based on the Fe-Cr-Co system with micron range thickness, also known as the Kaneko alloy

---

✉ Vyacheslav S. Zayonchkovskiy,
e-mail: zajonc4340@gmail.com

[1, 5], and the Al-Ni-Co system [6]. The properties of these alloys depend on the properties of phases formed in them after spinodal decomposition, as well as the mode of thermal treatment. The formation of σ- and γ-paramagnetic phases has a destructive effect on magnetic properties of the materials in the two systems [4,5]. Bulk Fe-Cr-Co alloys have better mechanical properties than Al-Ni-Co alloys. Furthermore, the only way to produce Al-Ni-Co ingots used as targets for magnetron sputtering is by moulding. Fe-Cr-Co alloys can be mechanically shaped or cut. The production of Fe-Cr-Co based magnets involves thermal treatment in a magnetic field, during which crystalline anisotropy of the α_1-phase develops, which results in high coercivity [7]. The higher the magnetic field during the annealing in a magnetic field, the higher the coercivity during the subsequent stepped annealing [8]. In order to produce high-quality magnets from these materials, their phase states at various stages of thermal treatment should be carefully analysed.

[2, 3] describe the properties of Fe-Cr-Co alloy-based films formed on silicon wafers. Coercivity H_C is the most important property of hard magnetic materials. Its value in the submicron thick layers of DHA-based films is high enough for them to be used in magnetoresistive MICs. The H_C of the films with multi-micron thick layers of DHA is significantly lower [9]. For the H_C of the multi-micron thick layers to be optimal, it is necessary to control the spinodal decomposition of the body-centered α-phase of the uniform solid solution of chromium in iron in the absence of γ- and σ-phases. This can be done by analysing the phase composition of the layers of the above mentioned films.

The aim of this study was to determine the phase composition of the layers of DHA in order to develop physical and technical approaches for the production of an optimal heterostructure with a permanent magnet film based on dispersion-hardened alloy of Fe-Cr-Co of micron range thickness with a magnetization vector in the plane of the silicon substrate.

2. Experimental

2.1. The method of obtaining films

Thin metal films were produced using magnetron sputtering conducted in a modernized vacuum unit UVN-71P3, with three thermal evaporation sources having been replaced with three planar magnetrons. The fore-vacuum pressure was created using a 2NVR-5D rotary vacuum pump, and high vacuum conditions were created using an NBT-950 turbomolecular pump. In order to ensure the high quality of the residual gases, the lid of the vacuum chamber and the substrate holder were heated. The pressure of the residual gases in the vacuum chamber before the introduction of the plasma-forming gas (highly pure argon 5.5) did not exceed $5\cdot10^{-4}$ Pa. The substrate temperature prior to the deposition of the adhesion layer (vanadium) was 200 °C. The temperature was controlled by means of a temperature sensitive resistor with a sliding contact. The sputtering targets were vanadium, copper, and Fe-Cr-Co alloy disks with a diameter of 90 mm. The magnetrons were operating with the plasma current of up to 3 A. In order to reach a highly effective state, rapid thermal processing (rapid annealing) was performed in a vacuum furnace with vacuum created by an oil-diffusion pump. The residual gas pressure did not exceed 10^{-3} Pa. After the oil-diffusion pump was applied, the atmosphere in the furnace was reducing.

2.2. Measuring equipment

X-ray phase analysis was performed by a DRON-7M diffractometer using copper radiation with the wavelength $\lambda_{K\alpha m}$ = 0.154186 nm [10].

The scanning was performed in step scan mode with the angular step size of 0.05°, the X-ray tube current of 30 kV, the anode current of 15 mA, and the exposure time of 5 sec. The angular scan range was 10–110°.

2.3. Film structures

The article presents the results of the study of structures obtained on single-crystal double side polished silicon wafers KDB-10 with (111) spatial orientation. For the X-ray analysis square samples were used with 15 mm sides. First, a 100 nm vanadium layer was deposited on the wafers. They were then covered with a 3800 nm copper layer followed by a 3600 nm Fe-Cr-Co layer. The thickness of the layers was measured by a confocal microscope NanoFocus,μ-Surf modification [11], based on the patterns obtained by means of photolithography with subsequent wet etching.

Concentrations of the main components of the target (Cr 25wt% and Co 12wt%) were determined by a X-ray fluorescence portable spectrometer MetExpert [12]. In our study, we used a target produced from Fe-Cr-Co alloy in order to obtain layers of DHA. The bulk alloy based on the Fe-Cr-Co system was subjected to basic thermal treatment, which, however, yielded comparatively low magnetic parameters.

It is possible to sputter a single layer DHA film on silicon within a wide thickness range (80–3.800 nm). However, with thicker DHA layers the bending strain of the round single-crystal silicon wafer becomes stronger. To reach high coercivity (HC) values annealing had to be performed, as it allowed for spinodal decomposition of the supersaturated solid solution of chromium in iron. The process was accompanied by partial decomposition of DHA layers, which became separated from the underlying layers.

In order to preserve the structure of the film, a compensating copper layer was introduced, which has a large deformation range due to the higher δ percent elongation ($\delta_{\text{max Cu}} = 45$ %) [13]. However, this layer has low adhesion to single-crystal silicon, which is why we also added an adhesion vanadium layer. This layer provides poor compensation for the modulation of the crystal lattice of DHA layers ($\delta_{\text{max V}} = 17$ %), [14], but it has high adhesion to single-crystal silicon [15] and is compatible with the copper layer [16]. This happens because vanadium does not form any intermetallic compounds with copper. The vanadium layer also serves as a diffusion barrier for copper, preventing direct contact between copper and silicon.

Most often, when manufacturing bulk magnets based on various DHA types by means of high-temperature homogenization and subsequent quenching, it is necessary to prevent the formation of undesirable γ- and σ-phases, which occur during the cooling of ingots in air at temperatures over 600 °C [17]. However, for the composition needed for our experiment (Fe – 25 wt % Cr –12 wt %Co) this requirement was optional [18]. The method we used allowed us to deposit the films by magnetron sputtering with the temperature of the wafers not exceeding 200 °C, which is enough for the melting of DHA layers.

3. Results and discussion

Fig. 1 shows an X-ray diffraction pattern of the metal film deposited on a (111)-oriented silicon wafer. Very intense (111) and (333) peaks of the silicon wafer are observed. The maximal peaks of the sputtered film layers are practically not visible at this resolution.

To analyse the three-layer metal film we used X-ray diffraction patterns recorded within an angle range of 40–94° in order to rule out highly intense peaks of the wafer (Fig. 2). The scanning step was 0.05°. In this range of angles 2θ a weak silicon peak (222) is observed. The presence of peaks of various intensity of reflection (111) complies with the International Centre for Diffraction Data PDF-2 (card No. 03-065-1060 ICDD PDF-2).

The diffraction pattern shows peaks corresponding to the α-phase of the solid solution FeCrCo (cards No. 03-065-4664 and 00-034-0396 ICDD PDF-2). Peak (110) (Fig. 2) was used to calculate the lattice constant of the α-phase $a = 0.2858$ nm, which corresponds to the lower bound of the range $a = (0.286–0.289)$ nm, according to [21].

Copper peaks were indexed (Fig. 2). Copper has a face-centred cubic lattice with the lattice parameter $a = 0.36148$ nm [23]. According to [22], Fe-Cr-Co alloys may contain a γ-phase with a face-centred cubic lattice and the lattice constant $a = (0.357–0.361)$ nm. The lattice parameters of copper and γ-phase are very similar. It was, therefore, impossible to separate the copper and γ-phase peaks within our study. The peaks may be separated, for example, by means of neutron diffraction.

High coercivity values for bulk samples were obtained only when the annealing temperature was within the range of 500–700 °C [17]. In order to determine the phase composition of the DHA layers after the thermal treatment, we used samples composed of a single silicon wafer with a metal film sputtered over it. The samples were annealed in a vacuum furnace for 1 minute at a temperature of 600–650 °C [17].

Before comparing the diffraction patterns of the annealed samples, we needed to make sure, that they had been recorded under identical conditions. In order to do this we needed to identify a diffraction peak that did not depend on the conditions of the annealing. This was

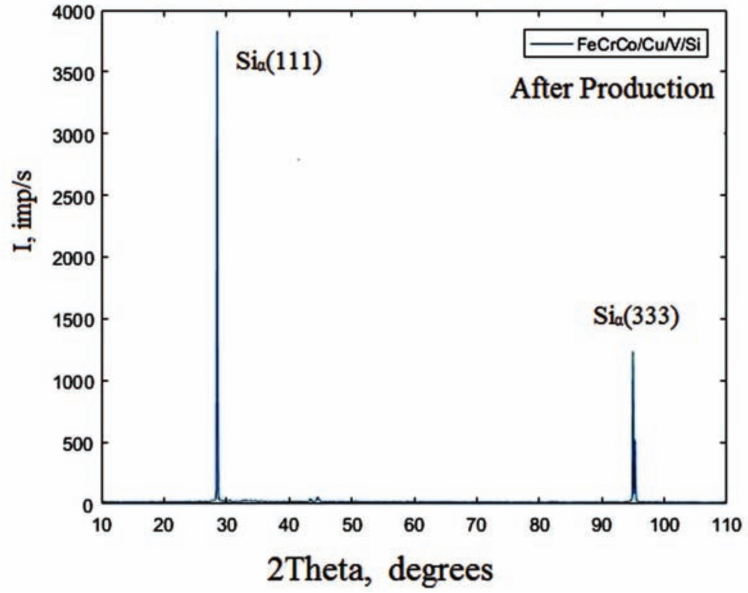

Fig. 1. Diffraction pattern of the three-layer metal film on a (111)-oriented single crystal silicon wafer. Scanning step 0.1°, recording interval (10–110)°

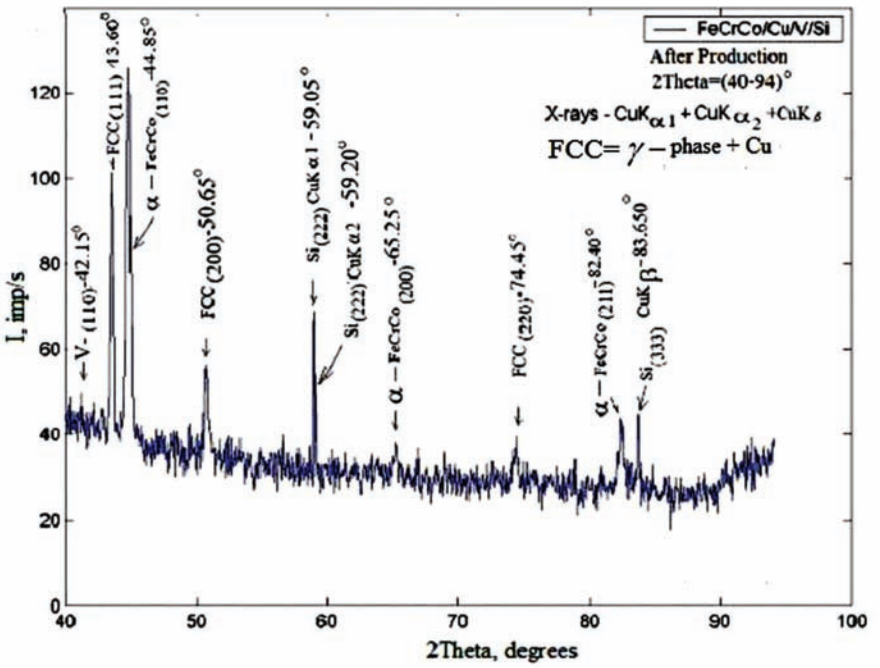

Fig. 2. Diffraction pattern of the three-layer metal film on a (111)-oriented single crystal silicon wafer. Scanning step 0.1°, recording interval (40–94)°

the (222) double peak, resulting from the X-rays going through the deposited thee-layer metal film and being reflected by the silicon wafer (Fig. 3). Figure 3 demonstrates the maximal peak (222) of the silicon wafer for the samples after the film sputtering and after the subsequent annealing at the temperatures of 600, 630, and 650 °C. The intensity of the peak stayed constant, which proves that the speed of photon counting during the scanning sessions was the same with a precision of up to 5 %.

Having established the stability of the recordings, we could analyse the alterations in the α-phase composition based on the difference in the intensity of the diffraction maximal peak (110). Figure 4 shows that line (110) has the maximal integral intensity. This line is present in the sample annealed at 630 °C.

The profiles of the diffraction line (111) of the γ-phase + Cu in the samples after the film deposition and subsequent annealing at the temperatures of 600, 630, and 650 °C are presented in Fig. 5.

A characteristic feature of the conducted experiments was the dependence of the intensity of diffraction maximal peaks of line (110) of the α-phase and line (111) of the γ-phase + Cu on the annealing temperature (Fig. 6) The maximal intensity of line (110) of the α-phase is observed in the sample annealed at 630 °C. At the same time, line (111) of the γ-phase + Cu reaches its minimum. The thickness of the copper layer stays constant during the annealing within the chosen temperature range. Therefore, the

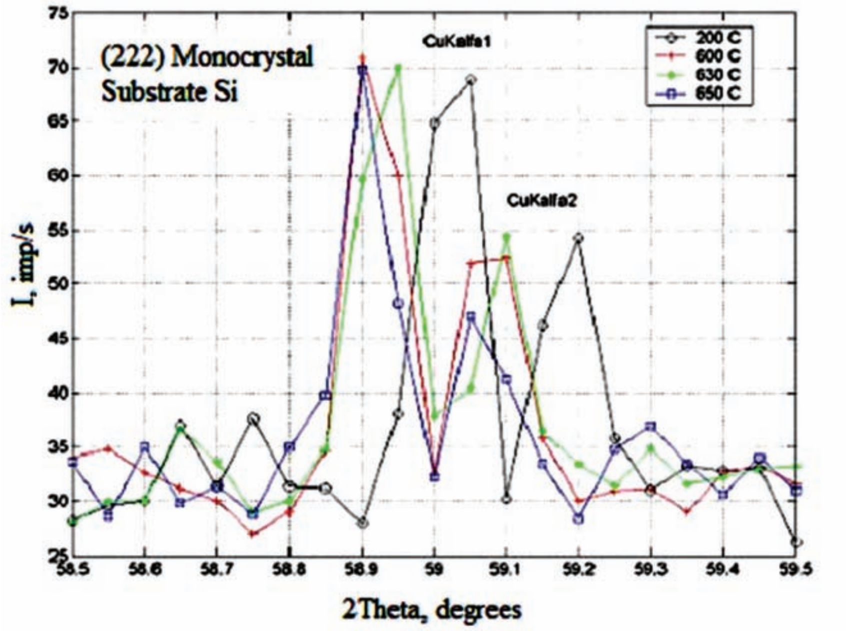

Fig. 3. The intensity of the X-ray diffraction peak (222) of silicon for the samples after sputtering and after one-minute of isochronous annealing at 600, 630, and 650 °C

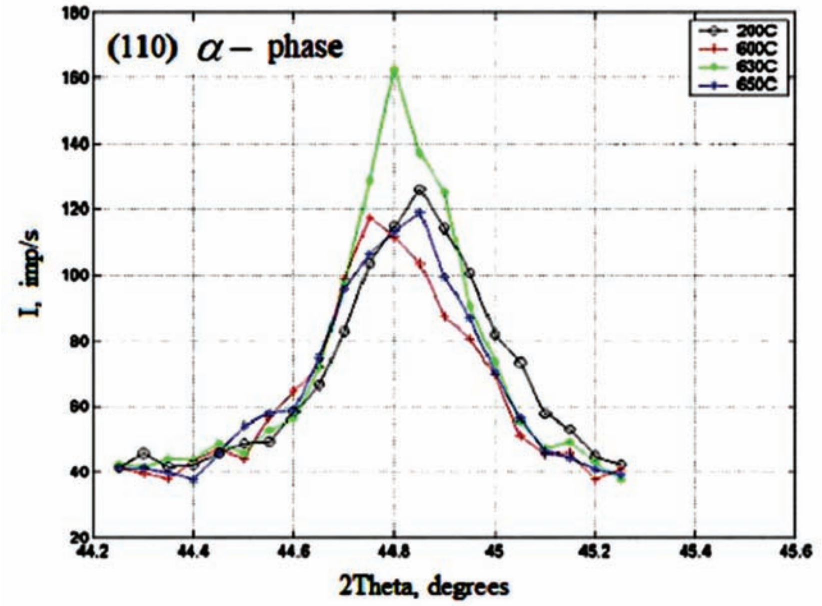

Fig. 4. The intensity of the X-ray diffraction peak (110) of the α-phase for the samples after sputtering and after one-minute of isochronous annealing at 600, 630 and 650 °C

alterations in line (111) of the γ-phase + Cu result from the difference in the concentration of the γ-phase. The intensity of this line is maximal for the sample annealed at 630 °C. This means that annealing at 630 °C yields the minimal concentration of the γ-phase and the maximal concentration of the α-phase. When the annealing time is long, the α-phase decomposes into phases α_1 and α_2, which results in higher coercivity values of the studied films [1].

The σ-phase is often present in bulk samples of Fe-Cr-Co alloys, which dramatically decreases the magnetic characteristics of these alloys. According to [21], this phase constitute up to 59% of the sample. For this phase, the most intense are the diffraction peaks (411) and (410) reflected from the σ-phase planes [24]. The diffraction

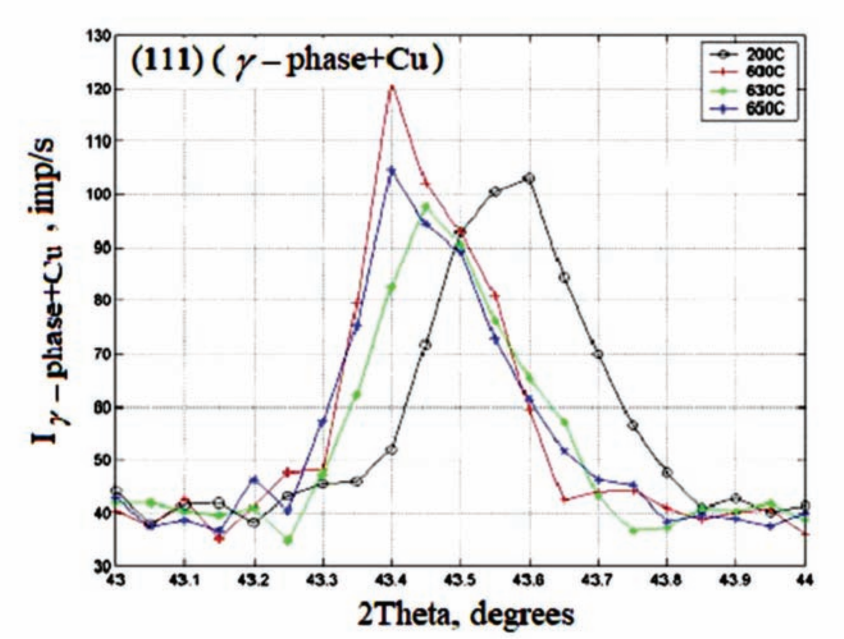

Fig. 5. The intensity of the X-ray diffraction peak (111) of the γ-phase + Cu for the samples after sputtering and after one-minute of isochronous annealing at 600, 630 and 650 °C

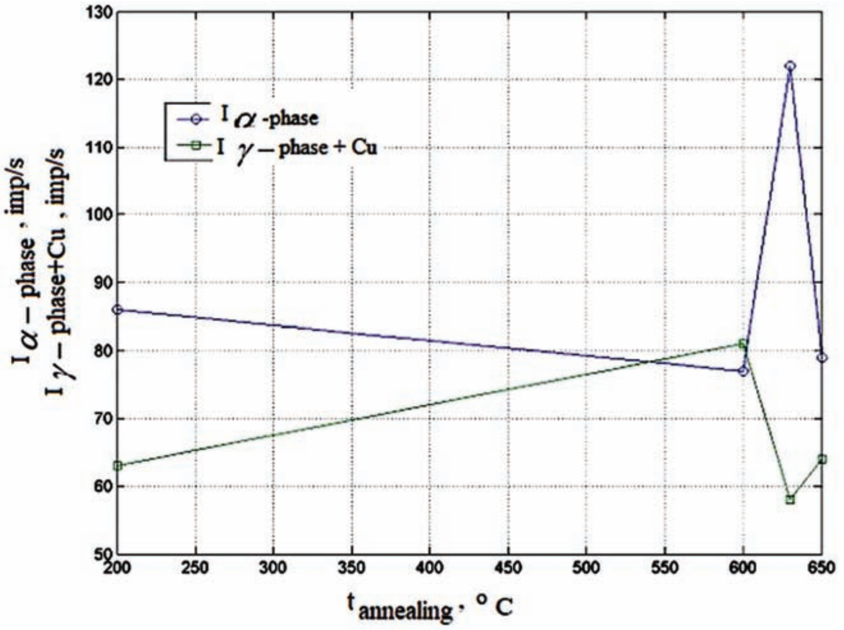

Fig. 6. Dependence of the intensity of the X-ray diffraction lines (110) of the α-phase, and (111) of the γ-phase + Cu on the annealing temperature, without taking into account the noise rate of 40 imp/s

patterns of all samples recorded before and after the annealing do not show any peaks of the σ-phase with a tetragonal β-uranium lattice. According to card No. 01-089-4790 ICDD PDF-2 [24], peaks (411) and (410) are the most intense for this structure. According to [21], the lattice parameters of the σ-phase are within the range: a = (0.8794–0.881) nm, c = (0.4552–0.458) nm. The calculations based on this data demonstrated that in CuK_α radiation the location of the maximal peaks (411) and (410) should correspond to the range of angles 2θ (46.91–47.05)° and (41.34–42.29)° respectively. Peaks of the σ-phase were observed in the same angular range in [5]. The diffraction patterns obtained in our experiment do not show these peaks, which allows us to state that the concentration of the σ-phase in the DHA layers is below the limit that can be detected using the method described in this article.

The absence of peaks at the angles 2θ = 49.5° and 2θ = 54.2° demonstrates the absence of the oxide of the main component of the films' surface layer – iron oxide Fe_2O_3.

4. Conclusions

1. Indexed diffraction patterns of the heterostructure of the permanent magnet film on a single-crystal silicon wafer with a magnetic layer of Fe-Cr-Co dispersion-hardened alloy demonstrated the presence of the α-phase whose concentration reaches its maximum during the one-minute of rapid annealing at 630 °C.

2. The study determined that the DHA layers of the composition Fe – 25wt % Cr –12 wt % Co obtained by magnetron sputtering do not contain the σ-phase. This phase is also not formed after one-minute of high vacuum annealing at 600–650 °C.

3. It was also determined that the heterostructure obtained by means of magnetron sputtering does not contain oxides of the main iron component either before, or after one-minute of high vacuum annealing at 600–650 °C.

Conflict of interests

The authors declare that they have no known competing financial interests or personal relationships that could have influenced the work reported in this paper.

References

1. Kaneko H., Homma M., Nakamura K. New ductile permanent magnet of Fe-Cr-Co system. *AJP Conference Proceedings*. 1972;5: 1088–1092. DOI: https://doi.org/10.1063/1.2953814

2. Tsung-Shune Chin, Kou-Her Wang, Cheng-Hsiung Lin. High coercivity Fe-Cr-Co thin films by vacuum evaporation. *Japanese Journal of Applied Physics*. 1991;30(8): 1652–1695. DOI: https://doi.org/10.1143/jjap.30.1692

3. Chang H. C., Chang Y. H., Yao S. Y. The magnetic properties and microstructures of Fe-Cr-Co thin films obtained by ion beam sputtering. *Materials Science and Engineering B*. 1996; 39(2): 87–94. DOI: https://doi.org/10.1016/0921-5107(95)01428-4

4. Masahiro Kitada, Yoshihisa Kamo, Hideo Tanabe. Magnetoresistive thin-film sensor with permanent magnet biasing film. *Journal of Applied Physics*. 1985;58(4): 1667–1670. DOI: https://doi.org/10.1063/1.336058

5. Rastabi R. A., Ghasemi A., Tavoosi M., Ramazani M. Magnetic features of Fe-Cr-Co alloys with tailoring chromium content fabricated by spark plasma sintering. *Magnetic Materials*. 2017;426(15): 742–752. DOI: https://doi.org/10.1016/j.jmmm.2016.10.132

6. Zubair Ahmad, Zhongwu Liu, A. ul Haq. Synthesis, magnetic and microstructural properties of Alnico magnets with additives. *Journal of Magnetism and Magnetic Materials*. 2017;428: 125–131. DOI: https://doi.org/10.1016/j.jmmm.2016.12.023

7. Jin Y., Zhang W., Kharel P. R., Valloppilly S. R., Skomski R., Sellmyer D. J. Effect of boron doping on nanostructure and magnetism of rapidly quenched Zr2Co11-based alloys. *AIP Adv*. 2016;6(5): 056002. DOI: https://doi.org/https://doi.org/10.1063/1.4942556

8. Lin Zhang, Zhaolong Xiang, Xiaodi Li, Engang Wang. Spinodal decomposition in Fe-25Cr-12Co alloys under the influence of high magnetic field and the effect of grain boundary. *Nanomaterials (Basel)*. 2018;8(8): 578. DOI: https://doi.org/10.3390/nano8080578

9. Zayonchkovskiy V., Kyaw A. K., Milyaev, I., Perov N., Prokhorov I., Klimov A., Andreev A. Thin metal films with dispersion-hardening magnetic layers of Fe–Cr–Co alloy. *Kondensirovannye Sredy i Mezhfaznye Granitsy = Condensed Matter and Interphases*. 2019;21(4): 505–518. DOI: https://doi.org/10.17308/kcmf.2019.21/2362 (In Russ., abstract in Eng.)

10. Mirkin L. I. *Spravochnik po rentgenostrukturnomu analizu polikristallov* [Polycrystal X-ray Analysis Handbook]. Moscow: Fizmatgiz Publ.; 1961. 863 p. (in Russ.)

11. *NanoFocus website*. Available at: https://m.nanofocus.de/en/ (in Russ.)

12. *OOO "GEO-NDT" website*. Available at: https://www.geo-ndt.ru/pribor-6855-rentgenoflyorescentnii-analizator-metekspert.htm (in Russ.)

13. *Spravochnik po cvetnym metallam* [Handbook of non-ferrous metals]. Available at: https://libmetal.ru/index.htm (in Russ.)

14. *Website "All About Metallurgy"*. Available at: http://metal-archive.ru/vanadiy/955-mehanicheskie-svoystva-vanadiya.html (in Russ.)

15. Gromov D. G. Mochalov A. I., Sulimin A. D., Shevyakov V. I. *Metallizaciya ul'trabol'shih integral'nyh skhem* [Ultra-Large Integrated Circuit Metallization]. Moscow: BINOM Publ.; 2012. 277 p. (In Russ.)

16. Lyakishev N. P., Bannyh O. A., Rohlin L. L. *Diagrammy sostoyaniya dvojnyh metallicheskih sistem: Spravochnik v trekh tomah* [State Charts of double metal systems: A Handbook in three volumes]. Moscow: Mashinostroenie Publ.; 1997. 872 p. (In Russ.)

17. Kekalo I. B., Samarin B. A. *Fizicheskoe metallovedenie precizionnyh splavov. Splavy s osobymi magnitnymi svojstvami* [Physical metallurgy of precision alloys. Special magnetic alloys]. Moscow: Metallurgiya Publ.; 1989. 496 p. (In Russ.)

18. GOST 24897-81. *Materialy magnitotverdye deformiruemye* [Solid magnetic deformed materials. Marks]. Moscow: Izdatel'stvo standartov Publ.; 1981. 21 p. (In Russ.)

19. Bragg W. L. The diffraction of short electromagnetic waves by a crystal. Proceedings of the Cambridge Philosophical Society, 17, 43–57 (1913). Communicated by Professor Sir J. J. Thomson. Read 11 November 1912. In: *X-ray and Neutron Diffraction*. Elsevier; 1966. p. 19–125. DOI: https://doi.org/10.1016/b978-0-08-011999-1.50015-820.

20. *Kremnij. Fizicheskaya enciklopediya. Gl. red. A. M. Prohorov*. [Silicon. Physical encyclopedia. A. M. Prokhorov (ed.)]. Moscow: Sovetskaya enciklopediya Publ.; 1990. 704 p. (In Russ.)

21. Vompe T. N., D'yakonova N., Milyaev I., Prutskov M. Kinetics of y-phase formation in a strain aging hard magnetic Fe-33% Cr-12% Co-2% Cu alloy. *Russian Metallurgy (Metally)*. 2012;(1): 55–57. DOI: https://doi.org/10.1134/s0036029512010168

22. Generalova K. N., Ryaposov I. V., Shacov A. A. The powder alloys of Fe-Cr-Co system heat-treated in the "ridge" region. *Letters on Materials*. 2017; 7(2): 133–136. DOI: https://doi.org/10.22226/2410-3535-2017-2-133-136 (In Russ., abstract in Eng.)

23. *Med'. Fizicheskaya enciklopediya* [Copper. Physical Encyclopedia]. Moscow: Sovetskaya enciklopediya Publ.; 1992. 672 p. (In Russ.)

24. *International Centre for Diffraction Data (ICDD)*. Available at: www.icdd.com

25. Kozvonin V. A., Shacov A. A., Ryaposov I. V. Kozvonin V. A., Shatsov A. A., Ryaposov I. V. Multicomponent concentration-inhomogeneous alloys of Fe-Cr-Co-Si-B with high density. *Bulletin PNRPU. Mechanical engineering, materials science*. 2016. 18(4): 188–202. DOI: https://doi.org/10.15593/2224-9877/2016.4.14 (In Russ., abstract in Eng.)

Information about the authors

Vyacheslav S. Zayonchkovskiy, PhD in Physics and Mathematics, Associate Professor, Department of Materials Science and Chemistry, Kaluga branch of Bauman Moscow State Technical University (national research university), Kaluga, Russian Federation; e-mail: zajonc4340@gmail.com. ORCID iD: https://orcid.org/0000-0002-6519-6003

Irina A. Antoshina, PhD in Physics and Mathematics, Associate Professor, Institute of Laser and Plasma Technologies, Obninsk Institute for Nuclear Power Engineering (OINPE) - a branch of the National Research Nuclear University MEPhI, Obninsk, the Kaluga region, Russian Federation; e-mail: antoshina_irina@mail.ru. ORCID iD: https://orcid.org/0000-0001-9143-2404.

Aung Kyaw Kyaw, postgraduate student, Kaluga branch of Bauman Moscow State Technical University (national research university), Kaluga, Russian Federation; ORCID iD: https://orcid.org/0000-0001-8427-3046.

Evgenij I. Isaev, PhD in Physics and Mathematics, Associate Professor, Institute of Laser and Plasma Technologies, Obninsk Institute for Nuclear Power Engineering (OINPE) - a branch of National Research Nuclear University MEPhI, Obninsk, the Kaluga region, Russian Federation; e-mail: e.isaev87@gmail.com. ORCID iD: https://orcid.org/0000-0002-1777-5342.

Igor' M. Milyaev, DSc in Physics and Mathematics, leading research fellow, Baikov Institute of Metallurgy and Materials Science, RAS, Moscow, Russian Federation.

All authors have read and approved the final manuscript.

Translated by Yulia Dymant.
Edited and proofread by Simon Cox.

Condensed Matter and Interphases
(Kondensirovannye sredy i mezhfaznye granitsy)

Original articles

DOI: https://doi.org/10.17308/kcmf.2020.22/2530 eISSN 2687-0711
Received 30 January 2020
Accepted 15 February 2020

Synthesis and Hydration Properties of the Superabsorbent "Solid water"

© 2020 A. V. Zenishcheva✉, V. N. Semenov, V. A. Kuznetsov, P. O. Kuschev

Voronezh State University, 1 Universitetskaya pl., Voronezh 394018, Russian Federation

Abstract

Global warming has posed a number of challenges for agriculture. The key problem is water retention in soil. Existing irrigation methods are costly and ineffective. To solve this problem, a synthesis of a rare-cross-linked hydrophilic polymer material with the properties of a pectin-based superabsorbent was conducted.

The paper considers the structure and moisture absorption of the polymer material "Solid water". The hydration properties of the superabsorbent in its original state and after contact with pectins were determined using IR spectroscopy. Our research showed that the water-adsorbing ability is ensured by the presence of short-sized acrylamide residues, fragments with residues of carboxyl groups and polysaccharide units in the structure. The superabsorbent with pectin as a biodegradable component is able to retain a portion of water of hydration even during prolonged drying. The effect of the pH of the medium on the water absorption capacity and swelling of the superabsorbent "Solid water" was shown. This superabsorbent can be used in different types of soils, as confirmed by the studies conducted in distilled water, as well as in alkaline and acidic media. The polymer is characterised by the highest swelling values in an alkaline medium due to the electrostatic repulsion of dissociated carboxyl groups, formed as a result of the hydrolysis of acrylamide. This makes it suitable for use in leached soils, such as leached black soil (Chernozem) in the Voronezh region.

IR spectroscopy showed the presence of the superabsorbent's functional groups that form supramolecular structures including bound water molecules with no additional coordinate covalent bonds present. Thus, the reactions can be characterised as processes with the elements of system self-organisation.

Keywords: superabsorbent, hydration properties, water absorption, pectin, IR spectra.

Funding: The study was supported by the Fund for Promotion of Innovations "The Foundation for Assistance to Small Innovative Enterprises in Science and Technology" (grant agreement No. 2598GS/41289).

For citation: Zenishcheva A. V., Semenov V. N., Kuznetsov V. A., Kuschev P. O. Synthesis and Hydration Properties of the Superabsorbent "Solid water". *Kondensirovannye sredy i mezhfaznye granitsy = Condensed Matter and Interphases.* 2020;22(1): 66–74. DOI: https://doi.org/10.17308/kcmf.2020.22/2530

1. Introduction

Abrupt climatic changes of the past few years have led to global warming, which caused the expansion of dry regions and increased the agricultural risk in these areas. Therefore, one of the key objectives of contemporary agriculture is maintaining the required level of moisture and soil fertility for high harvest yields. Irrigation and application of mineral fertilisers, microelements, and microorganisms are the methods used to solve these problems. However, hydro-amelioration methods applied in the areas with insufficient freshwater resources are sophisticated, costly, and inefficient. The application of a large amount of fertilisers leads to irreversible changes in soil pH, the risk of soil salinisation and exhaustion and the pollution of underground water with derivatives of nitric and phosphoric acids, which negatively affects the state of the plants that consume such water [1].

A promising solution of the above-mentioned problems is the use of new composite organic

---

✉ Anna V. Zenishcheva, e-mail: anvitz@mail.ru

hydrophilic polymer materials capable of multiple absorption and slow release of the absorbed water into the soil without changing their properties [2]. Such polymers can be used as water reservoirs for maintaining the required level of moisture and various additives in a wide range of temperatures over a period of several years.

Previously, a synthesis of a rare-cross-linked hydrophilic polymer material with the properties of a superabsorbent was conducted with addition of biodegradable fragments to its structure. When used in the soil, these fragments decompose, increasing moisture capacity and saturating the soil with nitrogen required for the normal vegetation of plants [3]. Pectin was used as one of these fragments.

The aim of this work was the development of synthesis of polymer biodegradable composites with the properties of a superabsorbent and the study of hydration properties of the original material "Solid water".

2. Experimental

The first stage of synthesis was preliminary preparation of the solution of the biodegradable component in a glass reactor at 40 °C and the redox initiator system H_2O_2+$Fe_2(SO_4)_3$ for the initiation of radical polymerisation. This mixture was vigorously stirred for 30 minutes and then the solution of acrylamide and the crosslinking agent was added to the reactor. The second stage of synthesis involved stirring for 5 hours at the temperature of 40 °C.

The obtained rare-cross-linked superabsorbents with different content of biodegradable components and specific additives were dried in the flow of warm air, and water surplus was removed using acetone or isopropyl alcohol. The dried polymer material was ground and used for tests [3].

Water absorption by the polymer was determined according to the following method. Equal samples (0.2 g) of the superabsorbent were weighed and put into small organza bags. Water can permeate through this fabric, but is practically not absorbed by it. Each bag with a polymer sample was placed in a separate glass with 500 ml of water. Then the glass was tightly closed and sealed, and 24 hours later the bags with the samples were removed from the glasses. The volume of the remaining water was measured using a measuring cylinder, and the volume of water absorbed by the sample was calculated as the difference between the original and the remaining volume. After that, the calculations were made taking into account the water adsorption of 1 kg of the polymer.

IR spectroscopy of the powder samples fixed by a holder on the sensitive surface of the prism was conducted on the Bruker Vertex 70v vacuum FTIR spectrometer using a "Platina" single-pass ATR adapter.

3. Results and discussion

The specific feature of the structure of the supersorbent "Solid water" is the result of choosing special monomers for the synthesis and developing the conditions of the synthesis itself. Fig.1 shows one of the possible schematic structures of the superabsorbent which demonstrates that water-adsorbing ability is secured by the presence of short-sized acrylamide residues, fragments with residues of carboxyl groups and polysaccharide units in the structure. A necessary condition of

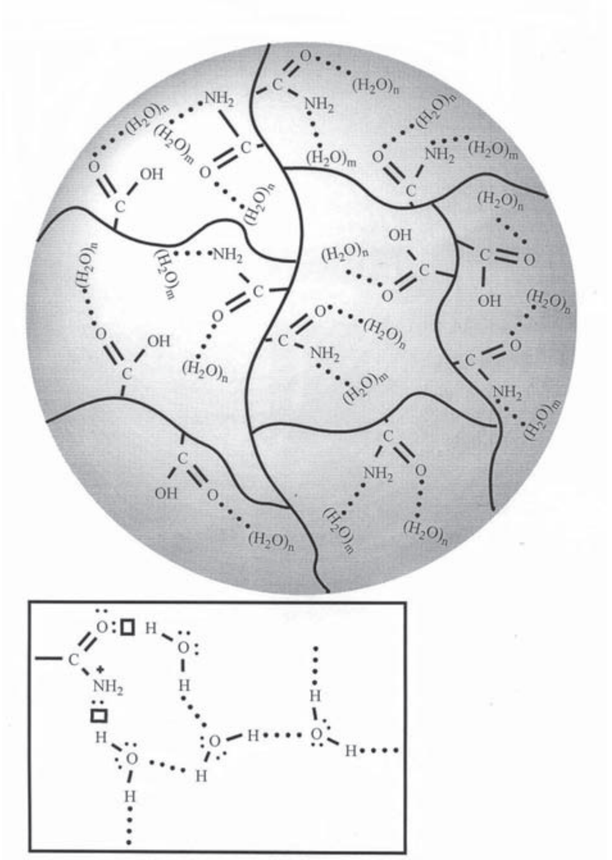

Fig. 1. Scheme of the polymer

a considerable amount of water absorbed by a sorbent is mechanical stability of polyelectrolyte chains in the processes of association and reassociation of the solvent molecules.

In this case, one may talk of common properties of polyelectrolyte chains of the superabsorbent and intracellular membranes which are able to ensure smooth transport of water molecules (Fig. 2).

$R–COOH + H_2O = R–COO^-H_3O^+$
$R–COO^- H_3O^+ + nH_2O = [R–COO^-H_3O^+][H_2O]_n$
$R–N(CH_3)_2 + H_2O = R–N^+H–(CH_3)_2–OH^-$
$R–N^+H_2–(CH_3)_2–OH^- + nH_2O = [R–NH–(CH_3)_2–][H_2O]_{n+2}$

Fig. 2. General scheme of water absorption by sorbents

The integrity of exceptionally thin structures is maintained in polyelectrolyte chains in the "Solid water", as for biomembranes, due to polar interactions and variance relationships. There is no data indicating the presence of covalent and coordination bonds between successive molecules of lipids and between adjacent lipid and protein molecules in membranes. A similar effect was observed during the interaction of polyelectrolyte chains in the "Solid water" polymer with amide and –COOH-groups of neighbouring chains. The difference in the considered case is that intracellular membranes are based on phospholipids while the chains of "Solid water" are based on polysaccharide residues [4].

It should be noted that polysaccharide chains in the "Solid water" as well as biomembranes are capable of self-assembly, which corresponds to the minimum of free energy in the systems [6, 7]. Pectins play a certain role in the processes of self-assembly and self-organisation of supramolecular structures in the superabsorbent.

It is known that pectin substances include polyuronides contained in soluble or insoluble forms in all land plants and in most algae. Water-insoluble (at t = 5–15 °C) pectin components of plants are called protopectin. In fact, pectin substances are a mixture, and it was possible to separate its soluble part (25–30 %) from the insoluble one by water evaporation and further dissolution of the dried powder in 70° ethanol [8, 9]. The dissolved component belongs to polysaccharides (arabanes) (which hydrolise to 1-arabinose when heated in diluted acids). Pectin substances that are not dissolved in 70° ethanol are actually called pectin. The main monosaccharide forming a part of pectin is D-galacturonic acid (Fig. 4)

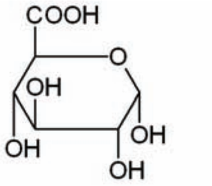

Fig. 4. D-galacturonic acid

In effect, pectin is partially etherified, that is containing $[–O–CH_3]$ groups, polygalacturonic acid. Similar to cellulose, as the authors in [8, 9] believe, pectin has chain structure (Fig. 5).

However, such a widespread opinion may be considered somewhat simplified. In a number of cases, pectin chains can be branched (Fig. 6).

The core of the branched molecule (6) has glycosidic linkage α (1→5) in the branching point and α (1→4) in the branches.

To confirm the scheme presented in Fig. 1, IR spectra of the original superabsorbent from pectin and the superabsorbent after supplementary interaction with polysaccharide

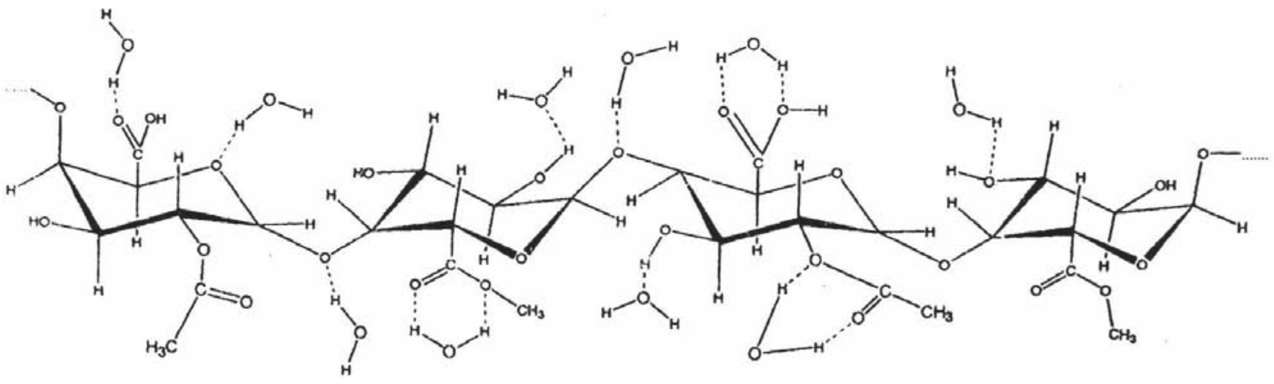

Fig. 3. The scheme of water and pectin interaction [5]

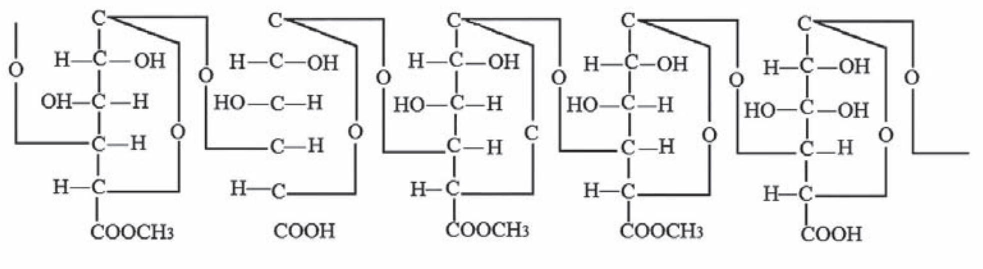

Fig. 5. Structure of pectin

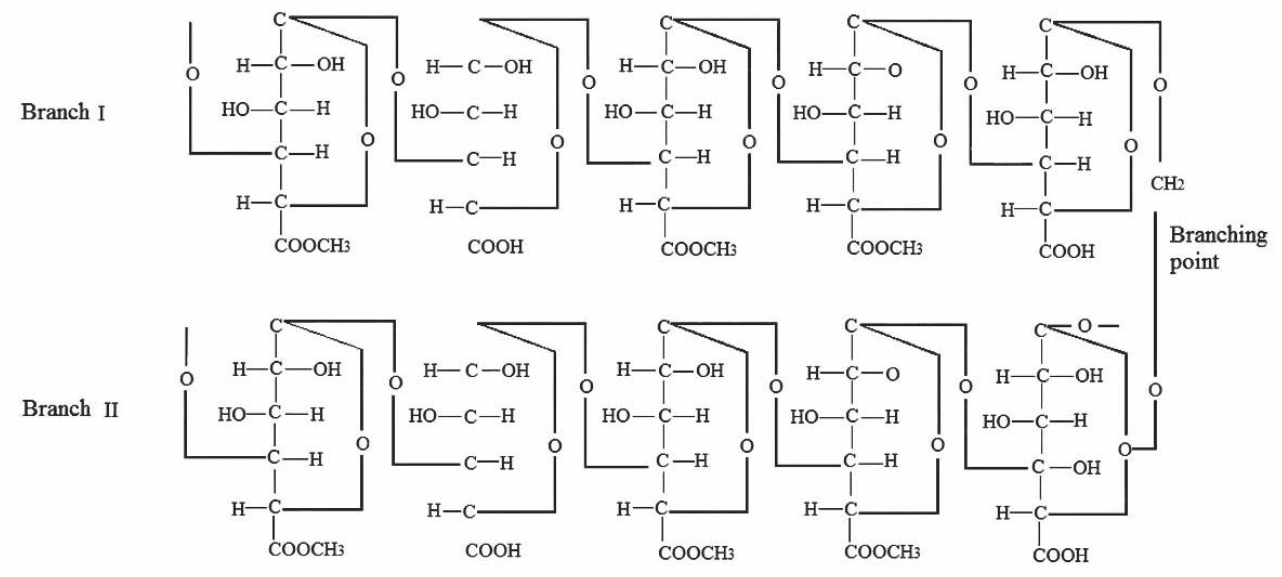

Fig. 6. Branched pectin chains

were obtained (Fig. 7–9). The obtained results are presented in Table 1. It was confirmed that amides play a significant role in the formation of short-chain fragments in the "Solid water" polymer. Notably, such effect for the original pectin-based polymer is confirmed not only by the presence of amide I absorption bands (3322, 3260, 3185 cm^{-1}) in IR spectra but also by the presence of maximums typical for (C-N and σ_s NH_2 in amides) amide II (1641, 1610, 1464 cm^{-1}) and amide III (750, 669, 550 cm^{-1}) [7, 10–12].

After the interaction with pectin, peaks are observed in the IR spectra of the superabsorbent. These peaks are typical for 6-membered pyranose rings of D-galacturonic acid (1117 cm^{-1}) [7, 10–12].

In the IR spectra of the polymer material there are absorption bands at 1653 and 1609 cm^{-1} corresponding to stretching vibrations of the C=O group (amide I) and combined frequency of deformation vibrations and the C–N NH group (amide II) of amide fragments [13]. Wide absorption bands at 3184–3332 cm^{-1} indicate the presence of OH and NH_2 groups of the biodegradable component [11, 14–16]. On the other hand, the superabsorbent (SA) can be characterised as a polymer expressing a bipolar function in the neutral pH region [15–17]. In this case, the polymer network of a "Solid water" sample, formed from polysaccharide units and acrylamide residues, will contain carboxyl groups forming hydration structures with water (ν 3206 cm^{-1}, δ 1653 cm^{-1} – stretching and deformation vibrations of the OH groups respectively) [15, 16]. Also, short-chain fragments of the "Solid water" polymer contain the residues of –COOH groups not associated with each other or functioning as dimers (1735, 1309, 1240 cm^{-1}) respectively [10, 12].

As for the the supersorbent "Solid water", plausible guesses can be made about the influence of the pH of medium on water-absorption capacity and swelling of the polymers. The polymer network of "Solid water" samples is formed by polysaccharide units and acrylamide residues, responsible for the presence of amide

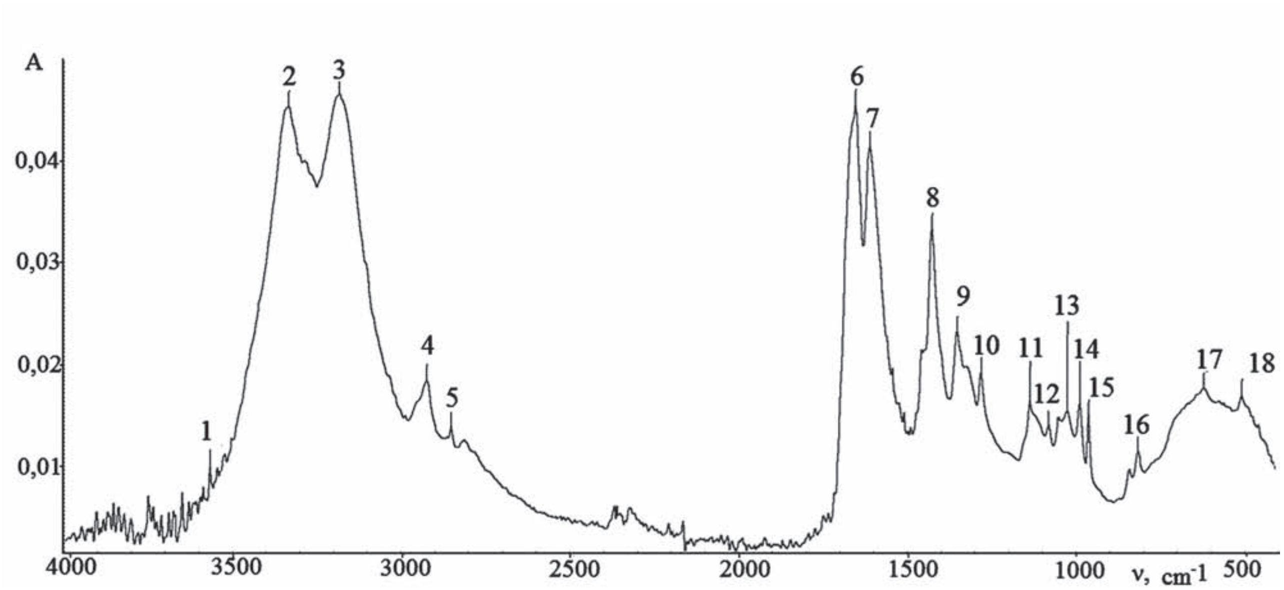

Fig. 7. IR spectra of the original superabsorbent (starch+acrylamide+2% crosslinking agent) (1 – 3566; 2 – 3332; 3 – 3184; 4 – 2924; 5 – 2852; 6 – 1653; 7 – 1609; 8 – 1426; 9 – 1351; 10 – 1280; 11 – 1135; 12 – 1080; 13 – 1025; 14 – 988; 15 – 961; 16 – 815; 17 – 621; 18 – 508 cm^{-1})

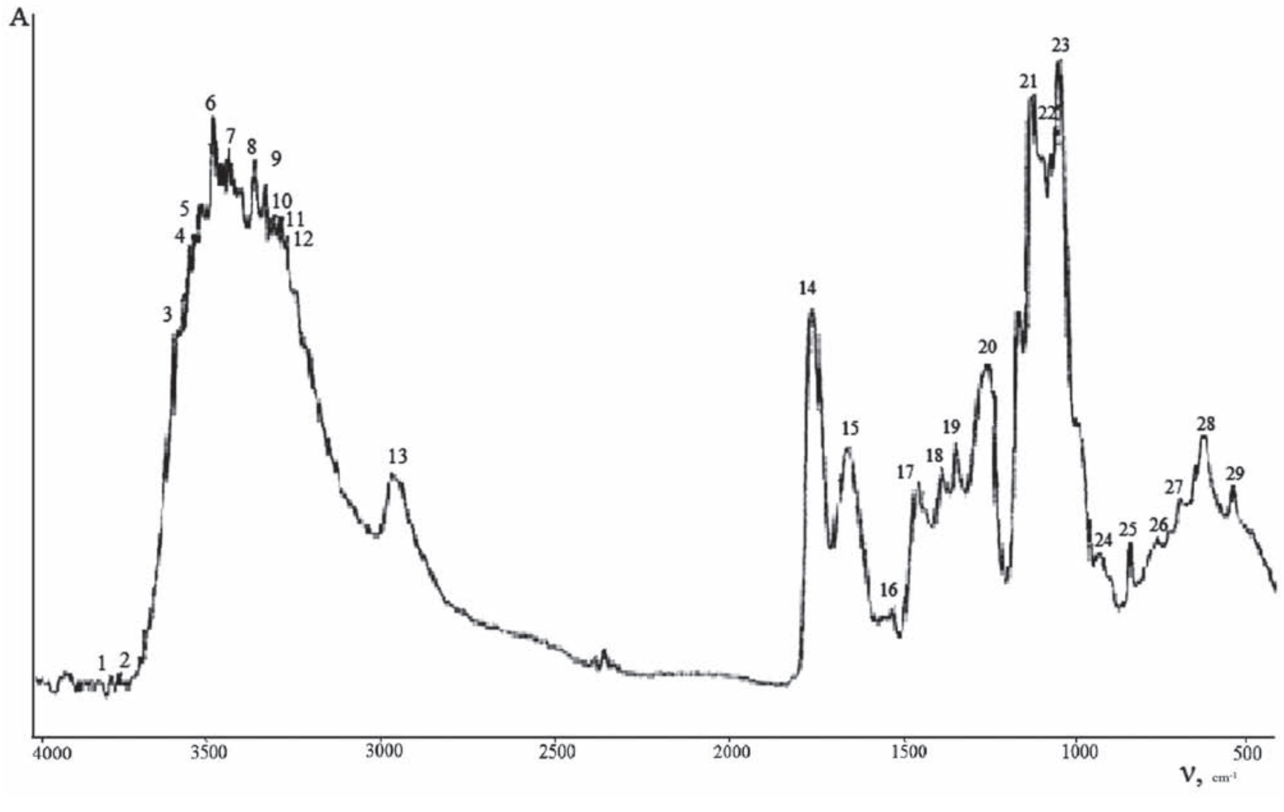

Fig. 8. IR spectrum of alcohol-precipitated beet pectin [5] (1 –3756; 2 – 3736; 3 – 3663; 4 – 3524; 5 – 3492; 6 – 3452; 7- 3411; 8 – 3399; 9 – 3307; 10 – 3268; 11 – 3263; 12 – 3253; 13 – 2948; 14 – 1739; 15 – 1640; 16 – 1618; 17 – 1441; 18 – 1370; 19 – 1329; 20 – 1236; 21 – 1148; 22 – 1102; 23 – 1049; 24 – 1023; 25 – 918; 26 – 831; 27 – 751; 28 – 684; 29 – 620; 30 – 666 cm^{-1})

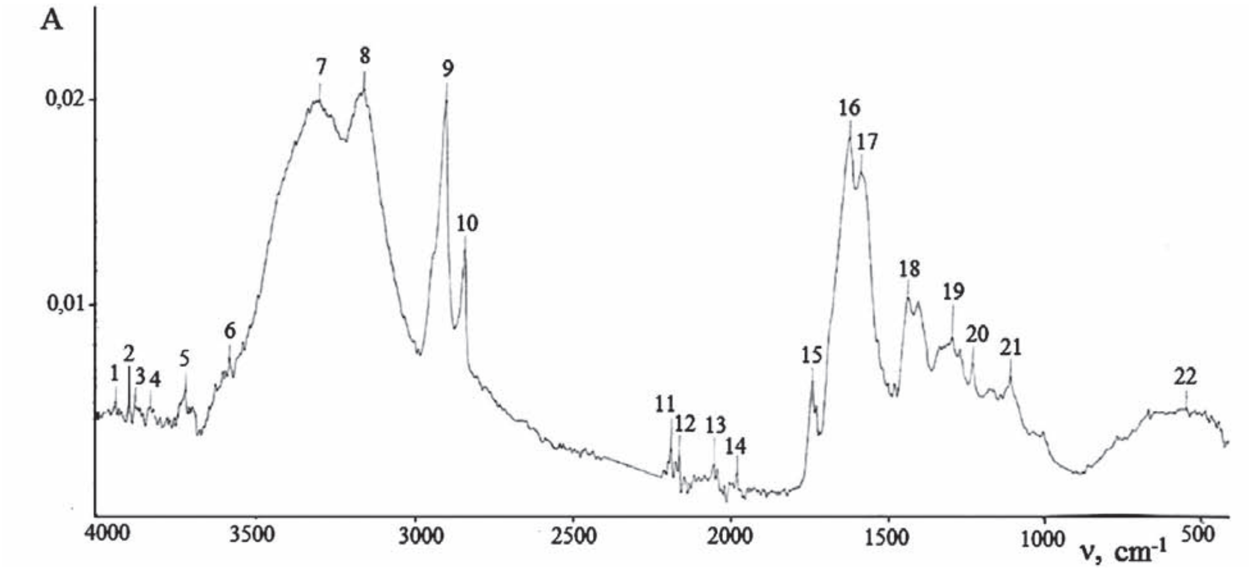

Fig. 9. IR spectra of the superabsorbent "Solid water" (pectin + acrylamide + 2 % crosslinking agent), held at 50 °C for 72 hours (1 – 3943; 2 – 3900; 3 – 3881; 4 – 3833; 5 – 3725; 6 – 3587; 7 – 3322; 8 – 3184; 9 – 2924; 10 – 2853; 11 – 2189; 12 – 2162; 13 – 2052; 14 – 1979; 15 – 1744; 16 – 1648; 17 – 1610; 18 – 1454; 19 – 1307; 20 – 1240; 21 – 1117; 22 – 550 cm^{-1})

Табл. 1. Attribution of absorption bands in the IR spectra of a rare-cross-linked polymer material with superabsorbent and pectin properties

ν, cm^{-1}			Attribution of absorption bands
The original polymer	Pectin	Исходный полимер + пектин	
–	–	3587	$\nu_s NH_2$ free in amides; $\nu_s OH_2\cdots H_2O$ $\nu_s OH_2\cdots H_2O$
–	3450	–	
–	3403	–	
3362	3346	–	$\nu_s NH_2$ linked in primary amides; $\nu_s OH_2\cdots O{=}C$ assoc. in primary amides (amide I), $\nu_s OH_2\cdots O{=}C$ assoc. with COOH groups
–	3318	3322	
3285	3261	3260	
3180	3185	3185	
2928	2941	2928	$\nu_{as} CH_2$; $\nu_s CH_2$;
2852	–	2853	
2322	2340	–	–OH в COOH (linked)
–	–	2189	
–	1735	1735	ν C=O in COOH
1641	–	1648	ν C-N and σ_s NH in amides (amide II); $\nu_{as} H_2O$
1605	1617	1610	
–	1518	1464	
1406	1419	1406	Amide III; σ-OH of pyranose rings;
1380	1371	–	
–	1330	1309	Fan-shaped CH_2; –COOH in dimers;
1277	1238	1240	Pendulum σ_sCH, with –COOH at the end;
–	1146	1152	
1106	1102	1117	$\nu_s OH_2$ в 6-membered rings
–	1023	–	
962	962	979	
–	930	–	
–	831	815	$(CH_2)_n$ – pendulum
–	–	750	Amide III; σ_s CH in rings
–	687	669	
–	617	–	
–	536	550	

and carboxyl groups (Fig. 3). The influence of the OH groups of polysaccharide groups on the formation of hydration structures allows considering moisture absorption as the process of disordering (destruction) of "water-water" associates in all the areas of concentration.

However, in case of maximum moisture absorption, the water structure has to be considered homogeneous, i.e. water molecules are in a single frame with partially filled voids [12, 16]. The presence of carboxyl and amine groups allows considering superabsorbents as ampholytes [15, 16] that can exist in cationic (acidic medium), bipolar (pH = 7), and anionic forms (scheme 1):

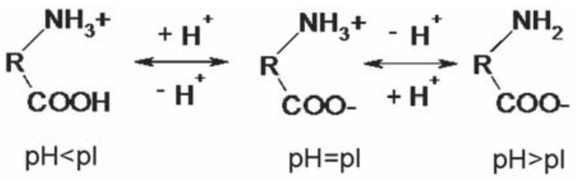

(1)

где pI – изоэлектрическая точка.

The use of the superabsorbent for water retention in different types of soils requires the knowledge of their swelling properties depending on the pH of the medium. For this reason, the ultimate swelling capacity of the samples of various superabsorbents, studied in distilled water (pH = 6.8±0.2) as well as in acid and alkaline media, was determined. Such choice of the condition was due to the fact that soils in which these sorbents may be used are also characterised by a wide range of pH values. The results of the study are presented in Table 2.

Table 2. Degree of swelling of the superabsorbent sample

Superabsorbent	Degree of swelling, ω, %		
	Distilled water	0.1 M HCl	0.1 M NaOH
Solid water, type I	98.90	97.10	112.86

The presented data shows that all the studied samples have almost the same values of the degree of swelling (ω). However, the value ω for the sorbent "Solid water" is slightly lower in acidic and alkaline environments as compared to the value obtained in distilled water. In this case, water structure is influenced by non-electrolytes (hydroxyl groups of polysaccharide units) and electrolytes ($-COO^-$, Na^+, $-NH_3^+$, Cl^-) [17, 18]. Among the obtained samples of the sorbents "Solid water", the best results in swelling were achieved with a sample of "Solid water", synthesised using a hydrophilic crosslinking agent N,N-Methylene-*bis*-acrylamide. This sample is characterised by the highest values ω in an alkaline medium, which is accounted for by electrostatic repulsion of disassociated carboxyl groups formed as a result of the acrylamide hydrolysis. This makes it suitable for use in leached soils, such as the black soil (Chernozem) in the Voronezh region.

Transition from one ionic form to another occurs with the participation of water molecules and is accompanied by the formation of the first hydration layer (short-range hydration) [18] (scheme 2):

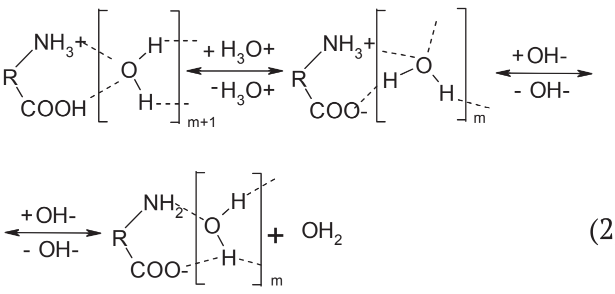

(2)

Further water absorption by the sorbent (long-range hydration) occurs due to the formation of H-bonds between the solvent molecules.

One of the possible options of the formation of the polymer frame of the superabsorbent "Solid water" can be related to the formation of SAC-like macromolecules of the complex polysaccharide-acrylamide (AA). If we indicate branch I in the Fig. 10. as X and branch II as Y, the formation of "polysaccharide (pectin)-acrylamide " can be schematically presented in the following way:

The suggested scheme explains to some extent the superabsorbent's capacity for hydration and absorption of considerable in weight amounts of water [19].

It is confirmed by IR spectra of the original superabsorbent (pectin + acrylamide + 2 % of crosslinking agent) presented in Fig. 9. The specified sample was dried for 72 hours at the temperature of 50 °C. After such a long heat treatment, there are absorption bands 3587; 3322; 3184 cm^{-1} present in the IR spectra that are typical for stretching vibrations of the OH

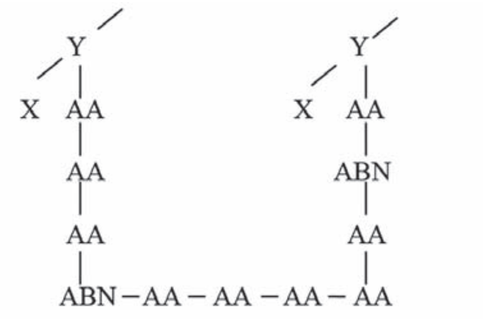

where ABN is N,N-Methylene-bis-acrylamide

Fig. 10. Schematic formation of a "polysaccharide (pectin)-acrylamide"

groups in hydration structures $H_2O \cdots H_2O$ (with weak hydrogen bonds); $H_2O \cdots HN$ (with acrylamide fragments) and $H_2O \cdots HOOC$ (D-polygalacturonic acid) respectively [20, 21]. The maximum of 1744 cm^{-1} shows the vibrations C=O in non-dissociated –COOH groups [11, 15, 16, 21, 22], which is indicative of incomplete deprotonation of carboxyl groups in pectin.

Therefore, the superabsorbent with pectin as the biodegradable component can retain a portion of hydration water even during prolonged drying.

4. Conclusions

1. The samples of the superabsorbent "Solid water" based on acrylamide and N,N-Methylene-bis-acrylamide with addition of pectin were synthesised. One of the options of the formation of macropores in superabsorbents explaining the maximum water absorption was considered.

2. The influence of the content and nature of the crosslinking agent on the product swelling was studied. It was shown that the synthesised polymer material can reversibly absorb up to 500 ml of water per one gram of the product, and the swelling decreases as the degree cross-linking grows. The superabsorbent with pectin as a biodegradable component is able to retain a portion of water of hydration even during prolonged drying.

3. Plausible guesses can be made about the influence of the pH of the medium on water-absorption capacity and swelling of the superabsorbent "Solid water". The values of the degree of swelling (ω) are almost the same, however, the value ω for the sorbent is slightly lower in acidic environments as compared to the value obtained in distilled water. This polymer is also characterised by the highest values ω in an alkaline medium, which is accounted for by electrostatic repulsion of disassociated carboxyl groups formed as a result of the acrylamide hydrolysis. This makes it suitable for use in leached soils, such as the black soil (Chernozem) in the Voronezh region.

4. IR spectroscopy allowed determining the presence of functional groups of the superabsorbent participating in the formation of supramolecular structures containing linked water molecules. As a result, this leads to the self-organisation elements of the system.

Acknowledgements

The results of the IR spectroscopic study were obtained using the equipment of the Centre for Collective Use of Scientific Equipment of Voronezh State University.

Conflict of interests

The authors declare that they have no known competing financial interests or personal relationships that could have appeared to influence the work reported in this paper.

References

1. Sharma J., Sukriti, Kaith B. S., Bhatti M. S. Fabrication of biodegradable superabsorbent using RSM design for controlled release of KNO_3. *Journal of Polymers and the Environment*. 2018;26(2): 518–531. DOI: https://doi.org/10.1007/s10924-017-0959-8

2. Rojas-Oviedo I., Rodríguez-Hernández S., Cárdenas J., Rivas-Ojeda J. C., Gaviño R. Synthesis, characterization and in vitro application of pH/temperature sensitive superabsorbent hydrogel of phosphated co-polymer of methacrylic acid and methyl methacrylate ester. *Journal of Porous Materials*. 2016;23(6): 1495–1505. DOI: https://doi.org/10.1007/s10934-016-0210-3

3. Kuznetsov V. A., Selemenev V. F., Semenov V. N., Bakalova M. V. Method of obtaining a hydrophilic crosslinked polymer with superabsorbent properties. *Patent No. 2574722 RF.* Publ. 02.10.2016. Bull. No. 4.

4. Gennis R. B. (ed.). *Biomembranes. Molecular Structure and Function*. New York: Springer Science+Business Media; 1989.

5. Lukin A. L., Kotov V. V., Myazin N. G. *Sveklovichnyi pektin: ot polya do konechnogo produkta* [Beet pectin: from the field to the final product] Monograph. V. V. Kotova (ed.). Voronezh: Istoki Publ.; 2005. 176 p. (In Russ.)

6. Shtykov S. N. Lyuminestsentnyi analiz v organizovannykh sredakh [Luminescent analysis in

organised environments]. In: *Luminescent analysis* [Lyuminestsentnyi analiz]. V. 19. Moscow: Nauka Publ.; 2015. p. 121–154. (In Russ.)

7. Selemenev V. F., Rudakov O. B., Slavinskaya G. V., Drozdova N. V. *Pigmenty pishchevykh proizvodstv (Melanoidiny)* [Pigments of food industries (Melanoidins)]. Moscow: Deli Print Publ.; 2008. 246 p. (In Russ.)

8. Silin P. M. *Tekhnologiya sakhara* [Sugar technology]. Moscow: Pishchevaya promyshlennost’ Publ.; 1967. 625 p. (In Russ.)

9. Gordon A., Ford R. *Sputnik khimika. Fiziko-khimicheskie svoistva, metodiki, bibliografiya* [Companion chemist. Physico-chemical properties, methods, bibliography] Moscow: Mir Publ.; 1967. 541 p. (in Russ.)

10. Pimentel G. C. and McClellan A. L. *The Hydrogen Bond.* San Francisco: W. H. Freeman and Co.; 1960.

11. Kazitsyna L. A., Kupletskaya N. B., *Primenenie UF, IK- i YaMR-spektroskopii v organicheskoi khimii* [The use of UV, IR, and NMR spectroscopy in organic chemistry]. Moscow: Vysshaya shkola Publ.; 1971. 264 p. (In Russ.)

12. Uglyanskaya V. A., Chikin G. A., Selemenev V. F., Zav’yalova T. A. *Infrakrasnaya spektroskopiya ionoobmennykh materialov* [Infrared spectroscopy of ion-exchange materials.]. Voronezh: Voronezh State University Publ.; 1989. 207 p. (In Russ.)

13. Shtokkhauzen D., Khartan Kh.-G., Brem G., Ionas G., Messner B., Pflyuger K. Absorbiruyushchie zhidkost’ polimery i sposob ikh polucheniya. *Patent No 2193045 RF.* Publ. 1996; MKP C08F 220/06, A61L 15/60.

14. Bykovskii D. V., Kuznetsov V. A., Sorokin A. V., Lavlinskaya M. S. The effect of the side azole substitutes on extraction ability of the copolymers based on N-vinylamides. *Sorbtsionnye i Khromatograficheskie Protsessy.* 2017;17(5): 804–811. DOI: https://doi.org/10.17308/sorpchrom. 2017.17/442 (In Russ., abstract in Eng.)

15. Bellamy L. J. *The infrared spectra of complex molecules.* London: Methuen; New York, Wiley; 1963. 300 p.

16. Nakanishi K. *Infrakrasnye spektry i stroenie organicheskikh soedinenii* [Infrared spectra and structure of organic compounds]. Moscow: Mir Pub; 1965. 269 p. (In Russ.)

17. Zhdankovich E. L., Annenkova V. Z., Annenkova V. M., Erofeeva L. G., Vladimirov V. A., Vladimirov D. V. Troinoi sopolimer akrilovoi kisloty, ammoniinoi soli akrilovoi kisloty i stirola v kachestve superabsorbenta. *Patent No 2128191 RF.* Publ. 1996; MKP C08F 220/06. (In Russ.)

18. Herth G., Dannehl M., Steiner N. Water-soluble or water-swellable polymers, particularly water-soluble or water-swellable copolymers made of acrylamide and at least one ionic comonomer having a low residual monomer concentration. *Patent No 7973095 US.* 2006; MKP C08F 2/48; C08F 2/04; C08F 2/16; C08F 220/56

19. Kuznetsov V. A., Lavlinskaya M. S., Ostankova I. V., Selemenev V. F., Semenov V. N., Lukin A. A. Water sorption ability of rare cross-linked polymeric material with superabsorbent properties. *Sorbtsionnye i Khromatograficheskie Protsessy.* 2017;17(3); 484–489. DOI: https://doi.org/10.17308/sorpchrom.2017.17/404 (In Russ., abstract in Eng.)

20. Slavinskaya G. V., Selemenev V. F. *Ful’vokisloty prirodnykh vod* [Fulvic acids of natural waters]. Voronezh: Voronezh State University Publ.; 2001. 165 p. (In Russ.)

21. Selemenev V. F., Rudakov O. B., Slavinskaya G. V., Drozdova N. V. *Pigmenty pishchevykh proizvodstv (melanoidiny)* [Food production pigments (melanoidins)]. Moscow: Da Li print Publ.; 2008. 246 p. (In Russ.)

22. Selemenev V. F. Chekin G. A., Khokhlov V. Yu. Interionic and intermolecular interactions in ion-exchange and sorption systems involving physiologically active substances. In: Ion-exchange. New York: Marsel Dekker; 2000(1). p. 851–925. DOI: https://doi.org/10.1201/9780203908341.ch10

Information about the authors

Anna V. Zenishcheva, graduate student of the Department of General and Inorganic Chemistry, Voronezh State University, Voronezh, Russian Federation; e-mail: anvitz@mail.ru. ORCID iD: https://orcid.org/0000-0003-4227-3261.

Victor. N. Semenov, DSc in Chemistry, Full Professor, Head of the Department of General and Inorganic Chemistry, Voronezh State University, Voronezh, Russian Federation; e-mail: semenov@chem.vsu.ru. ORCID iD: https://orcid.org/0000-0002-4247-5667.

Vyacheslav. A. Kuznetsov, DSc in Chemistry, Professor, Department of High-Molecular Compounds and Colloid Chemistry, Voronezh State University, Voronezh, Russian Federation e-mail: dr.v.kuznetsov@gmail.com. ORCID iD: https://orcid.org/0000-0002-0072-2025.

Petr O. Kuschev, PhD in Chemistry, Lecturer at the Department of High-Molecular Compounds and Colloid Chemistry, Voronezh State University, Voronezh, Russian Federation e-mail: peter.kuschev@gmail.com

All authors have read and approved the final manuscript.

Translated by Marina Strepetova.
Edited and proofread by Simon Cox.

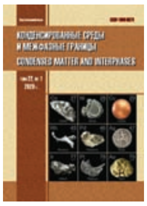

Condensed Matter and Interphases
(Kondensirovannye sredy i mezhfaznye granitsy)

Original articles

DOI: https://doi.org/10.17308/kcmf.2020.22/2507 eISSN 2687-0711
Received 24 January 2020
Accepted 15 February 2020

The Composition and Structure of Phases, Formed in the Thermolysis of Substitutional Solid Solutions $H_2Sb_{2-x}V_xO_6{\cdot}nH_2O$

© 2020 L. Yu. Kovalenko✉, V. A. Burmistrov, D. A. Zakhar'evich

Chelyabinsk State University,
129 Bratiev Kashirinykh str., Chelyabinsk 454001, Russian Federation

Abstract

In compounds, crystallized within the pyrochlore-type structure (sp.gr. Fd3m) of the $A_2B_2X_6X'$ general formula, there could be doubly or triply charged ions in the place of A cations, quadruply or quintuply charged ions in the place of B cations. Most works are devoted to the formation of these structures, depending on the nature and sizes of A and B cations, while little attention has been paid to determining the temperature ranges of their stability. The aim of this work was to study the thermolysis of substitutional solid solutions $H_2Sb_{2-x}V_xO_6{\cdot}nH_2O$ in the range of 25–700 °C and the determination of the influence of the nature of B (Sb, V) cation on the stability of pyrochlore-type structures during heating.

Substitutional solid solutions have been obtained by the co-precipitation method. The samples, containing 0; 5 ($x = 0.10$); 15 ($x = 0.30$); 20 ($x = 0.40$); 24 ($x = 0.48$) at% of vanadium have been chosen as subjects of the present research. The changes in the proton hydrate sublattice in samples, containing different amounts of V^{+5} were analysed by IR spectroscopy. The modelling of the thermolysis process and determination of the phase compositions at each stage was possible using X-ray phase and thermogravimetric analysis of the samples

It was shown that at temperatures of 25–400 °C, proton-containing groups are removed from the hexagonal channels of the pyrochlore-type structure. The increase in number of V^{+5} ions in solid solutions changed the proton-binding energy with oxygen ions $[BO_3]^-$-octahedron, which led to the shift of stage boundaries: oxonium ions and water molecules were removed at higher temperatures, while hydroxide ions were removed at lower temperatures. An increase in temperature to over 500 °C led to the structure destruction due to the oxygen removal from $[BO_3]^-$-octahedrons. The model for the atomic filling of crystallographic positions in the pyrochlore-type structure for phases, formed during $H_2Sb_{2-x}V_xO_6{\cdot}nH_2O$ thermolysis at 25–400 °C, has been proposed.

According to the thermogravimetric analysis, the structural formulas of solid solutions under the air-dry condition has been determined. $(H_3O)Sb_{2-x}V_xO_5(OH){\cdot}nH_2O$, where $0 < x \leq 0.48$, $0 < n \leq 1.1$. It has been shown that the temperature ranges of thermolysis stages were affected by the proton-binding energy with oxygen ions $[BO_3]^-$-octahedron temperature ranges, where B = V, Sb, forming the structural frame. It has been found that the studied solid solutions are stable up to 400 °C within the framework of the pyrochlore-type structure.

Keywords: pyrochlore-type structure, antimony compounds, polyantimonic acid, substitutional solid solutions, thermal analysis, phase transformations.

Funding: The study was financially supported by the Russian Foundation for Basic Research (Grant no. 18-33-00269) and the Foundation for the Support of Young Scientists of Chelyabinsk State University.

For citation: Kovalenko L. Yu., Burmistrov V. A., Zakhar'evich D. A. The composition and structure of phases, formed in the thermolysis of $H_2Sb_{2-x}V_xO_6{\cdot}nH_2O$ substitutional solid solutions. *Kondensirovannye sredy i mezhfaznye granitsy = Condensed Matter and Interphases*. 2020;22(1): 75–83. DOI: https://doi.org/10.17308/kcmf.2020.22/2507

✉ Liliya Yu. Kovalenko, e-mail: LKovalenko90@mail.ru

1. Introduction

Compounds crystallizing in pyrochlore-type structures with a general formula of $A_2B_2X_6X'$ have attracted the attention of scientists for more than fifty years [1–6]. The reason for this is elemental diversity. In the place of A cations there can be doubly or triply charged ions, in place of cations quadruply or quintuply charged ions, and as a result, the variety of properties of the pyrochlores: magnetic [7, 8], photocatalytic [9, 10], dielectric [11] and others. The authors have paid a lot of attention to the study of the formation of the structure depending on the radii of the ions and their arrangement in crystallographic site occupancies [1, 12, 13]. Thus, it was shown that such a structural type for compounds is preferable when the ratio of the radii A and B cations is: $1.46 \le r(A)/r(B) \le 1.61$ [12, 14]. For oxide systems in which oxygen atoms are located at site X, the most important in determining whether a pyrochlore-type structure will form are characteristics of $[BO_3]^-$-octahedrons [15]. However, little attention has been paid to studying the stability of compounds crystallizing in a pyrochlore-type structure during heating. The features of thermolysis were studied only for a few compounds [16–20].

In this work, we selected samples of polyantimonic acid (PAA) doped with vanadium ions, with $H_2Sb_{2-x}V_xO_6{\cdot}nH_2O$ composition as a model system. When atoms are distributed over crystallographic site occupancies of a pyrochlore-type structure, the 8b positions remain vacant, in place of A cations, protons and oxonium ions are located, and Sb^{+5}, V^{+5} ions act as B cations [21]. As a result, a skeletal plane of a defective structure is formed, consisting of $[BO_3]^-$-octahedrons connected by apexes and having hexagonal channels in which protons, oxonium ions, and water molecules are located. Doping of PAA with V^{+5} ions leads to a change in the binding energy of protons with $[BO_3]^-$ and, as a consequence, an increase in proton conduction [22].

According to studies [23–25], proton-containing groups located in the channels of the structure have a significant influence on the stabilization of the PAA phase at high temperatures. Therefore, the doping of PAA with V^{+5} ions should change the phase stability during heating. Therefore, the aim of this work was to study the thermolysis of $H_2Sb_{2-x}V_xO_6{\cdot}nH_2O$ substitutional solid solutions in the temperature range of 25–700 °C, the determination of the composition and structure of phases at each stage of thermolysis, the determination of the influence of the nature of B (Sb, V) cation on the stability of pyrochlore-type structure during heating.

2. Experimental

Samples were synthesized by coprecipitation of solutions of sodium vanadate and antimony trichloride, pre-oxidized with nitric acid, in an excess of distilled water according to the procedure described in the study [21]. The resulting precipitate was separated from the mother liquor, washed with distilled water until the negative reaction of filtrate to chlorine ions, dried in air, and kept at room temperature for a long time under normal conditions (T = 25 °C, RH ≈ 60 %). All chemicals used were of analytical grade.

Ratios of vanadium and antimony (at%) in the samples were determined based on the data of ARL QuanT'X X-ray fluorescence spectrometer, device sensitivity <1 ppm.

In previous studies [21, 26], it was shown that, within the framework of the pyrochlore type structure, a substitutional solid solution $H_2Sb_{2-x}V_xO_6{\cdot}nH_2O$ is formed at $0 < x \le 0.48$. Therefore, finely dispersed powders containing according to elemental analysis 0; 5 ($x = 0.10$); 15 ($x = 0.30$); 20 ($x = 0.40$); 24 ($x = 0.48$) at% vanadium were selected as objects of study.

The IR absorption spectra of the samples were recorded on a Nicolet 380 IR Fourier spectrometer in the frequency range from 500 to 4000 cm^{-1}. For this, the samples were mixed with KBr powder and pounded to a finely dispersed state, followed by pressing the mixture in a compressing mould. As the result, a translucent tablet was obtained.

Phase samples at different stages of thermolysis were obtained by prolonged heat treatment of solid solutions in air at temperatures 400 and 650 °C.

Structural studies of the initial and heat treated samples were performed on a Rigaku Ultima IV X-ray diffractometer (filtered Cu$K\alpha$-radiation) in the range of diffraction angles $10 \le 2\theta \le 70$ deg.

Thermal studies of the samples were carried out using Netzsch STA 449F5 Jupiter synchronous thermal analyser in air. We recorded the change in the mass of the sample and rate of its change during heating at 10 °C/min in the temperature range 24–700 °C, the balance sensitivity was 100 mg. Samples were weighed on an analytical balance with an accuracy of 0.0001 g before and after heating.

For a quantitative assessment of the thermal decomposition of the samples, the relative mass change was found $\Delta\mu_{T\Gamma}$:

$$\Delta\mu_{T\Gamma} = \frac{\Delta m_i}{\Delta m_k}, \qquad (1)$$

where Δm_i – mass change at the given thermal decomposition stage, Δm_k – mass of the final product.

Based on the amount of removed products at each stage, the process of thermolysis of solid solutions was simulated. For the validation of the selected model, the relative mass change of the samples was found $\Delta\mu_T$:

$$\Delta\mu_T = \frac{\Delta M_{ri}}{\Delta M_{rk}}, \qquad (2)$$

where ΔM_{ri} – change in the molecular mass of the thermolysis product at given stage of thermal decomposition, ΔM_{rk} –molecular mass of the final decomposition product - a mixture of two phases $Sb_2O_{4.3(4)}$ and $VSbO_4$ taking into account the given V/Sb ratio. The model was selected in a way, that the discrepancy between $\Delta\mu_{T\Gamma}$ and $\Delta\mu_T$ was the lowest.

3. Results and discussion

Substantial doping of PAA crystallizing in the pyrochlore type structure should lead to a change in the structure of the protohydrate sublattice while maintaining the charge of the main frame [21, 22].

On the IR spectra of PAA and doped forms, a wide complex absorption band in the region of 3700–2700 cm^{-1} (Fig. 1) can be distinguished, which corresponds to the vibrations of hydroxide ions and water molecules involved in the νO–H hydrogen bond [24, 27, 28]. Two maxima can be detected in this region (Fig. 1): at 3400 cm^{-1}, which is attributed to the vibrations of molecules of loosely bound water, and 3250 cm^{-1} responsible for the vibrations of hydroxide ions and water molecules perturbed by the surface field of the crystal lattice [29–31].

The absorption band at 3250 cm^{-1} with an increasing amount of V^{+5} shifts to the region of lower frequencies (Fig. 1). Thus, for the saturated solid solution (x = 0.48) the maximum band has a value of 3200 cm^{-1} (Fig. 1). According to studies [28, 32, 33], the shift of the frequency of stretching vibrations of hydroxide ions to the low frequencies (red shift of collective symmetric vibrations) upon formation of hydrogen bond was due to a decrease in the force constant of the O–H bond itself. Therefore, doping of PAA with V^{+5} ions reduces the energy of interaction of protons with oxygen anions of $[BO_3]^-$-octahedron and, as a result, leads to the weakening of hydrogen bonds in the hexagonal channels of the structure.

In the region of deformation vibrations, intense absorption bands were recorded on the spectra at 1400, 1640 cm^{-1}, corresponding to deformation

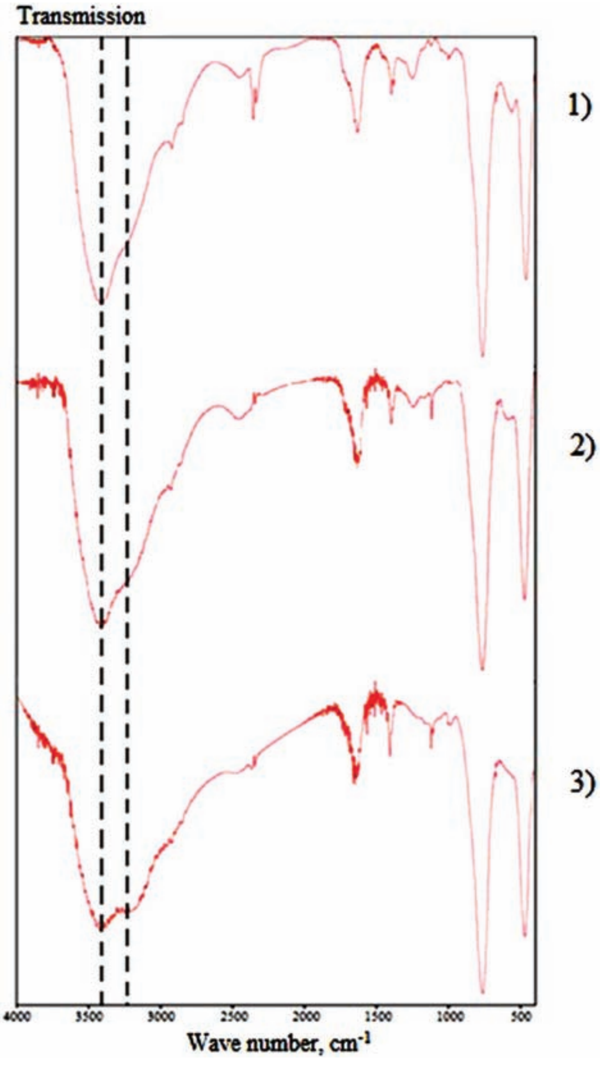

Fig. 1. IR spectra of samples $H_2Sb_{2-x}V_xO_6{\cdot}nH_2O$, where x: 0 (*1*); 0.10 (*2*); 0.48 (*3*)

vibrations δ (Sb^{+5}-OH) and deformation vibrations of water molecules, respectively (Fig. 1) [24, 27]. Band intensity at 1700 cm^{-1}corresponding to deformation vibrations of oxonium ions with increasing amount of V^{+5} decreases. The region of deformation vibrations was less sensitive to the formation of hydrogen bonds of different strengths than the region of stretching vibrations; therefore, a shift of the bands of deformation vibrations to the low-frequency region was not observed (Fig. 1) [28, 34].

Absorption bands at 770 and 450 cm^{-1} corresponded to the stretching vibrations of ν (Sb^{+5}–O). For doped forms, the appearance of additional absorption bands corresponding to V–O bonds was not observed [35]. The absence of additional bands confirms the similarity of the fingerprint region of V–O and Sb–O bonds in complex oxides.

According to thermogravimetric analysis of $H_2Sb_{1.52}V_{0.48}O_6{\cdot}nH_2O$ sample, broad maxima can be distinguished on the mass change rate curve at temperatures of 140 (stages I and II), 280 (stage III) and 560 (stage V) °C (Fig. 2). According to published data [24], in the 100 °C region, during the thermolysis of hydrated oxides and acids adsorbed water molecules should be removed (stage I), and at higher temperatures (100–200 °C) water molecules located near the crystal lattice (stage II) should be removed. It was believed that the first broad maximum reflects the superposition of stages I and II (Fig. 2). With an increase in the amount of V^{+5} in solid solution, the maximum in the mass change rate curve at 400 °C shifted to the region of lower temperatures, its intensity decreased (Fig. 3). However, according to the TG curve (Fig. 2), mass loss was observed in this temperature range (stage IV). For the clarification of the thermolysis stages, an X-ray phase analysis of samples heat treated at temperatures of 400 and 650 °C was carried out.

On the X-ray diffraction patterns of $H_2Sb_{1.52}V_{0.48}O_6{\cdot}nH_2O$ sample after heat treatment at 400 °C (Fig. 4), the lines became of low-intensity, however, the position of the reflections coincided with the initial X-ray diffraction pattern.

Reflections with odd indices extinguished and it was also observed for the undoped PAA sample [24], and indicated the dehydration of compounds and the rearrangement of the structure [23, 24, 34]. In the temperature range 500–600 °C, the decomposition of compounds and the formation of two phases, one of which was $Sb_2O_{4.3(4)}$, the other – $VSbO_4$ phase with the crystal structure of the rutile type (sp. gr. $P4_2/mnm$) was observed [36, 37].

According to the data of a full-profile X-ray analysis [26] carried out for $H_2Sb_{2-x}V_xO_6{\cdot}nH_2O$, $0 < x \leq 0.48$ solid solutions, Sb^{+5} and V^{+5} ions and were statistically located at the 16c positions and formed [BO_3]-octahedrons with oxygen anions and hydroxyl groups occupying the 48f positions. Oxonium ions and water molecules statistically

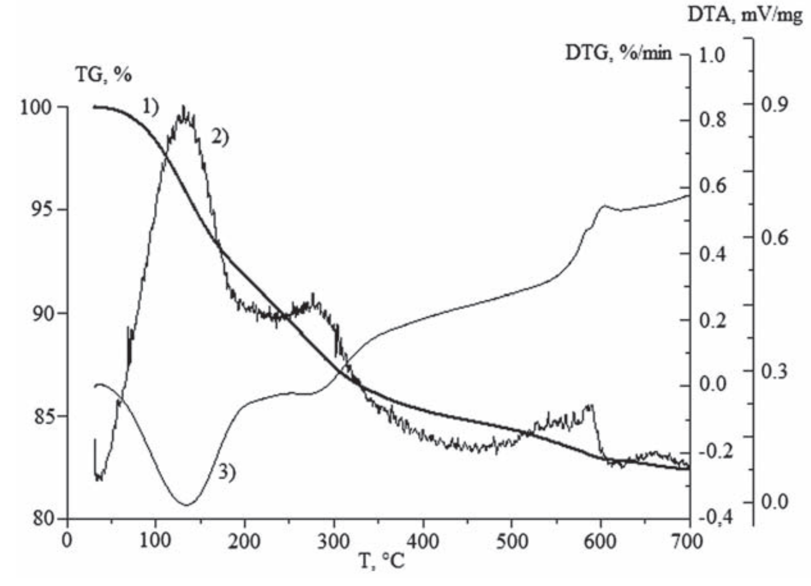

Fig. 2. Dependences of the change in mass – TG (*1*), the rate of change in mass – DTG *(2)* and the change in heat flux – DTA (*3*) of the $H_2Sb_{1.52}V_{0.48}O_6{\cdot}nH_2O$ sample on temperature

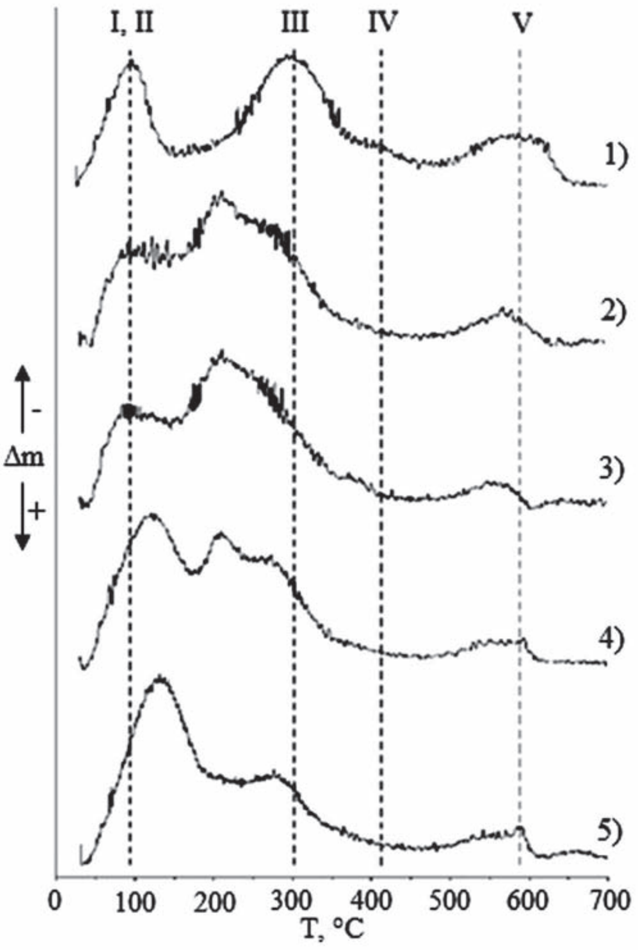

Fig. 3. Dependences of the rate of change of mass (DTG) on the temperature of samples $H_2Sb_{1.52}V_{0.48}O_6{\cdot}nH_2O$, in which x: 0 (*1*); 0.10 (*2*); 0.30 (*3*); 0.40 (*4*); 0.48 (*5*); Roman numerals I–V indicate stage numbers

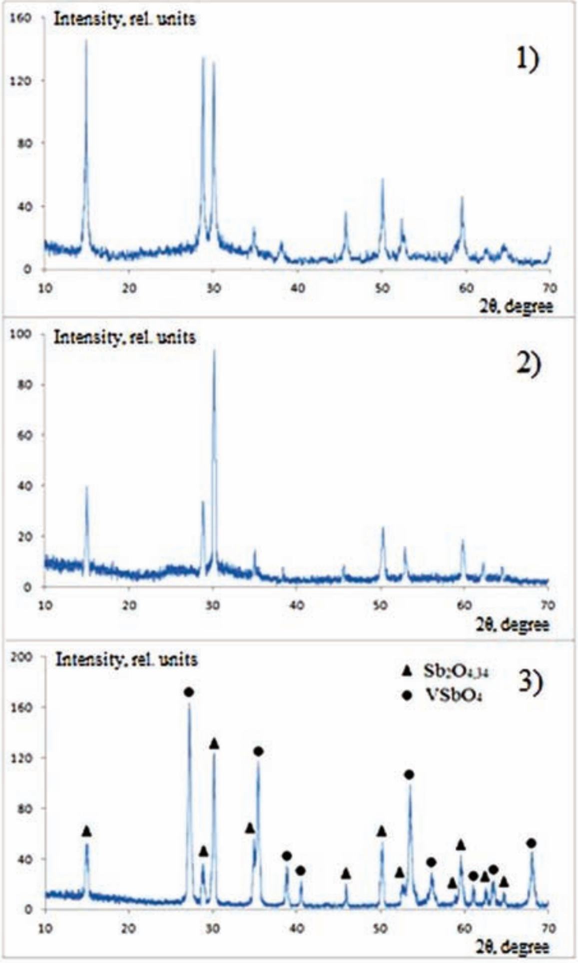

Fig. 4. X-ray diffraction patterns of $H_2Sb_{1.52}V_{0.48}O_6{\cdot}nH_2O$ (*1*) and phases formed after heating at 400 °C (*2*) and 650 °C (*3*)

filled the 16d positions and were located in hexagonal channels. The change in the X-ray pattern at temperatures above 500 °C was due to the removal of protons from the 16d positions of the structure and the transition of Sb^{+5} and V^{+5} ions from octahedral into cubic positions [24]. Thus, the substitutional solid solutions $H_2Sb_{2-x}V_xO_6{\cdot}nH_2O$ within the pyrochlore-type structure were stable up to 400 °C.

For the determination of the phase composition at different stages of thermolysis, we used the following assumption [24]: during thermal transformations, the number of antimony and vanadium atoms does not change, water and oxygen molecules are removed in different temperature ranges. According to mass spectrometry data [24], in the temperature range 24 - 500 °C water molecules (18 a.m.u.) were removed, and in the range of 500 - 700 °C oxygen molecules (32 a.m.u.) were removed. The calculations of the relative mass change were carried out using equations 1 and 2, the results are presented in Table 1.

The experimental and calculated values of the mass loss were in good agreement (Table 1) indicating a correct description of the thermolysis stages. Thus, we were able to determine the initial composition of the solid solution $(H_3O)Sb_{1.52}V_{0.48}O_5(OH){\cdot}0.4H_2O$, its formation temperature and phase composition at each stage of thermolysis. The model of the distribution of atoms over the crystallographic site occupancies of a pyrochlore-type structure for phases formed at temperatures 25-400 °C is presented in Table 2. Water molecules, weakly bound to the structure, were statistically located at 8b positions.

During stages I and II of thermolysis, adsorbed water and water molecules were removed from the

Table 1. The stages of thermolysis of $(H_3O)Sb_{1.52}V_{0.48}O_5(OH)\cdot 0.4H_2O$, according to the proposed model, where $\Delta\mu_t$ – relative changes in the mass of the doped sample; $\Delta\mu_{TG}$ – experimental mass values according to the TG data, relative to the final mass of the sample; temperature ranges ΔT of the stages of phase formation

Stage no.	Reaction	Stage temperature range ΔT, °C	$\Delta\mu_T$, %	$\Delta\mu_{TG}$, %
I–II	$(H_3O)Sb_{1.52}V_{0.48}O_5(OH)\cdot 0.4H_2O = (H)Sb_{1.52}V_{0.48}O_5(OH) + 1.4H_2O$	24–190	9.11	9.37
III	$(H)Sb_{1.52}V_{0.48}O_5(OH) = Sb_{1.52}V_{0.48}O_{4.5}(OH) + 0.5H_2O$	200–300	3.25	3.16
IV	$Sb_{1.52}V_{0.48}O_{4.5}(OH) = Sb_{1.52}V_{0.48}O_5 + 0.5H_2O$	300–360	3.25	3.48
V	$Sb_{1.52}V_{0.48}O_5 = 0.52Sb_2O_{4.3(4)} + 0.48VSbO_4 + 0.41O_2$	520–600	4.74	4.57
	TOTAL:	24–600	20.35	20.58

Table 2. The distribution of atoms according to the crystallographic positions of a pyrochlore type structure for $(H_3O)Sb_{1.52}V_{0.48}O_5(OH)\cdot 0.4H_2O$ and phases formed upon heating (number of formula units Z = 8)

Stages	Formation temperature , °C	Structural formula	16d	16c	48f	8b
–	25	$(H_3O)_8Sb_{12}V_4O_{40}(OH)_8\cdot 3.2H_2O$	$8H_3O^+$	$12Sb^{+5}$, $4V^{+5}$	$40\ O^{-2}$ $8\ OH^-$	$3.2H_2O$
I–II	190	$(H)_8Sb_{12}V_4O_{40}(OH)_8$	$8H^+$	$12Sb^{+5}$, $4V^{+5}$	$40\ O^{-2}$ $8\ OH^-$	–
III	260	$(Sb^{+5})_2Sb_{12}V_4O_{40}(OH)_8$	$2Sb^{+5}$	$12Sb^{+5}$, $4V^{+5}$	$40\ O^{-2}$ $8\ OH^-$	–
IV	360	$(Sb^{+5})_4Sb_{12}V_4O_{48}O_2$	$4Sb^{+5}$	$12Sb^{+5}$, $4V^{+5}$	$48\ O^{-2}$	$2O^{-2}$

16d positions. In the resulting $(H)_8Sb_{12}V_4O_{40}(OH)_8$ phase the $[BO_3]^-$ negative charge was compensated by protons located in the 16d positions. Further heating led to the destruction of the octahedrons due to the interaction of protons located in the 16d positions with part of the oxygen anions of the $[BO_3]^-$-octahedron. In this case, part of the Sb^{+5} ions passed from the 16c into the 16d positions (Table 2). In the phase forming during stage III $(Sb^{+5})_2Sb_{12}V_4O_{40}(OH)_8$ Sb^{+5} ions are compensated by the charge of $[BO_3]^-$-octahedrons. During stage IV, hydroxyl groups were removed in the form of water molecules, octahedrons were further destroyed, and further transitions of Sb^{+5} ions from the 16c into the 16d positions occurred. The $(Sb^{+5})_4Sb_{12}V_4O_{48}O_2$ phase was stable due to Sb^{+5} ions located in the 16d positions. At temperatures above 500 °C, the removal of oxygen began, which indicated the reduction of part of the Sb^{+5} ions into Sb^{+3} and the destruction of the structure.

The removal of proton-containing groups during stages I–III was characterized by endo-effects, the minima of which in the curves of the heat flux (DTA) were fixed at 140 and 290 °C (Fig. 2). With further heating, a small maximum at 320 °C was recorded: the formation of the $(Sb^{+5})_4Sb_{12}V_4O_{48}O_2$ phase was accompanied by heat production. At 600 °C, the exo-effect was associated with the formation of two new phases, $Sb_2O_{4.3(4)}$ and $VSbO_4$.

For solid solutions in which $x < 0.48$, the same number of stages was fixed during thermolysis (Fig. 3), the mass loss was from 18 to 22 % relative to the final decomposition products. With an increase in the amount of vanadium, a substitutional solid solution $(H_3O)Sb_{2-x}V_xO_5(OH)\cdot nH_2O$ contained lower amount of water in an air-dry state. Thus, according to thermogravimetric analysis, $n = 0.4$ for the saturated substitutional solid solution ($x = 0.48$), $n = 1.1$ for PAA [24].

On the mass change rate curves (DTG) of the doped samples, the shift of the stage maxima with an increase in the amount of dopant was recorded (Fig. 3). The maxima of I and II stages were shifted to the region of high temperatures, for the saturated solid solution from 95 to 140 °C. The maxima of stages III and IV, on the contrary, shifted to the low-temperature region. The shift from 300 to 270 °C and 400 to 370 °C respectively was revealed for the saturated solid solution. The shift of stages I and II was probably due to the removal of proton-containing groups at higher temperatures and the higher bonding force of the protonhydrate lattice with the crystal lattice.

The shift of the maxima of stages III and IV into the low temperature region was a common characteristic of doped oxides and heteropoly acids. Probably, the introduction of vanadium facilitates the transition of neighbouring atoms or ions from the main positions into the excited state, according to the order-disorder theory, lowers the decomposition temperature [38].

Stage shifts were also recorded on the curves of heat flux (DTA curves). With an increase in the amount of V^{+5}, the removal of oxonium ions from the 16d positions (stage I and II) occurred at higher temperatures and was accompanied by high energy costs, as was evidenced by the large minimum area at temperatures of 100–150 °C (Fig. 5). The transition of Sb^{+5} ions from the 16c to 16d positions, on the contrary, was more beneficial (Fig. 5, stages III and IV). Thus, the endothermic minimum of stage III (300 °C) shifted to the lower temperature region and its area decreased. The exothermic maximum (370 °C), indicating the formation of the $Sb_{2-x}V_xO_5$ phase shifted to the low-temperature region with an increasing amount of V^{+5} in the solid solution. In the high-temperature region, an exothermic peak (600–630 °C) of high intensity appeared, associated with the formation of two new phases – $Sb_2O_{4.3(4)}$ and $VSbO_4$.

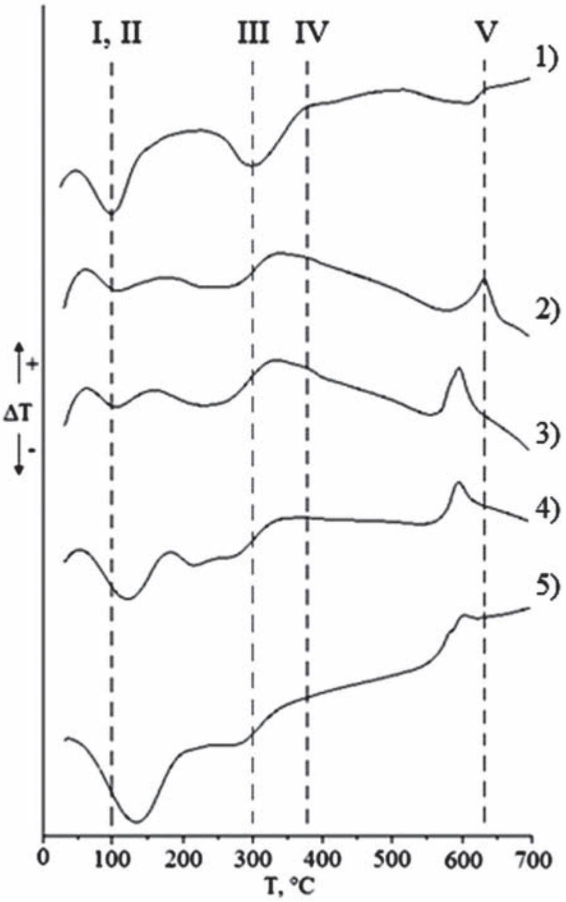

Fig. 5. Dependences of the change in heat flux (DTA) on the temperature of samples $H_2Sb_{2-x}V_xO_6\cdot nH_2O$, where x: 0 (*1*); 0.10 (*2*); 0.30 (*3*); 0.40 (*4*); 0.48 (*5*)

Due to the electronic structure of the vanadium ion, the O–V bond is less covalent than the O–Sb bond [39]; therefore, the proton must form a stronger bond with the oxygen ion of the $[VO_3]^-$ octahedron, which was confirmed by the DTG and DTA data, which showed the shift of stages I and II to the high-temperature region (Fig. 3, Fig. 5). Changes in the binding energy between protons located in hexagonal channels and oxygen ions of $[BO_3]^-$-octahedrons affected the transport of protons between electronegative atoms. As a result, the distance between protons and oxygen ions of $[SbO_3]^-$-octahedrons increased, and the red shift of νO–H vibrations of hydroxide ions and water molecules was recorded on the IR-spectra (Fig. 1). High proton mobility led to an increase in proton conductivity with an increase in the amount of vanadium in the samples [22].

4. Conclusions

It was found that the resulting solid solutions have the structural formulas $(H_3O)Sb_{2-x}V_xO_5(OH)\cdot nH_2O$, where $0 < x \le 0.48$, $0 < n \le 1.1$. Doping leads to a change in the proton-binding with oxygen ions $[BO_3]^-$-octahedrons, where B = V, Sb, forming the structural frame, changing the temperature ranges of the thermolysis stages. It has been shown that substitutional solid solutions $H_2Sb_{2-x}V_xO_6\cdot nH_2O$ within a framework of the pyrochlore-type structure were stable up to 400 °C. The model describing the sequence of phase transformations during the thermolysis of substitutional solid solutions $H_2Sb_{2-x}V_xO_6\cdot nH_2O$ in the temperature range 25–400 °C was proposed, the composition of the phases during each thermolysis stage was established.

Acknowledgements

The study was supported by the Foundation for the Support of Young Scientists of Chelyabinsk State University.

Conflict of interests

The authors declare that they have no known competing financial interests or personal relationships that could influence the work reported in this paper.

References

1. Subramanian M. A., Aravamudan G., Rao G. V. S. Oxide pyrochlores – A review. *Progress in Solid State Chemistry*. 1983;15(2): 55–143. DOI: https://doi.org/10.1016/0079-6786(83)90001-8

2. Krasnov A. G., Piir I. V., Koroleva M. S., Sekushin N. A., Ryabkov Y. I., Piskaykina M. M., Sadykov V. A., Sadovskaya E. M., Pelipenko V. V., Eremeev N. F. The conductivity and ionic transport of doped bismuth titanate pyrochlore $Bi_{1.6}M_xTi_2O_{7-\delta}$ (M – Mg, Sc, Cu). *Solid State Ionics*. 2017;302: 118–125. DOI: https://doi.org/10.1016/j.ssi.2016.12.01.019

3. Cherednichenko L. A., Moroz Ya. A. Catalytic properties of heteropolytungstates with 3d elements and their thermolysis products. *Kinetics and Catalysis*. 2018;59(5): 572–577. DOI: https://doi.org/10.1134/S0023158418050038

4. Krasnov A. G., Kabanov A. A., Kabanova N. A., Piir I. V., Shein I. R. Ab initio modeling of oxygen ion migration in non-stoichiometric bismuth titanate pyrochlore $Bi_{1.5}Ti_2O_{6.25}$. *Solid State Ionics*. 2019;335: 135–141. DOI: https://doi.org/10.1016/j.ssi.2019.02.023

5. Farlenkov A. S., Khodimchuk A. V., Eremin V. A., Tropin E. S., Fetisov A. V., Shevyrev N. A., Leonidov I. I., Ananyev M. V. Oxygen isotope exchange in doped lanthanum zirconates. *Journal of Solid State Chemistry*. 2018;268: 45–54. DOI: https://doi.org/10.1016/j.jssc.2018.08.08.022

6. Rejith R. S., Thomas J. K., Solomon S. Structural, optical and impedance spectroscopic characterizations of $RE_2Zr_2O_7$ (RE = La, Y) ceramics. *Solid State Ionics*. 2018;323: 112–122. DOI: https://doi.org/10.1016/j.ssi.2018.05.025

7. Egorysheva A. V., Ellert O. G., Gaitko O. M., Berseneva A. A., Maksimov Y. V., Dudkina T. D. Magnetic properties of $Pr_{2-x}Fe_{1+x}SbO_7$ and $Bi_{2-x}Ln_xFeSbO_7$ (Ln = La, Pr) pyrochlore solid solutions. Inorganic Materials. 2016;52(10): 1035-1044. DOI: https://doi.org/10.1134/S0020168516100071

8. Rau J. G., Gingras M. J. P. Frustrated quantum rare-earth pyrochlores. *Annual Review of Condensed Matter Physics*. 2019;10(1): 357–386. DOI: https://doi.org/10.1146/annurev-conmatphys-022317-110520

9. Lomanova N. A., Tomkovich M. V., Sokolov V. V., Ugolkov V. L. Formation and thermal behavior of nanocrystalline $Bi_2Ti_2O_7$. *Russian Journal of General Chemistry*. 2018;88(12): 2459–2464. DOI: https://doi.org/10.1134/s1070363218120010

10. Liu X., Huang L., Wu X., Wang Z., Dong G., Wang C., Liu Y., Wang L. $Bi_2Zr_2O_7$ nanoparticles synthesized by soft-templated sol-gel methods for visible-light-driven catalytic degradation of tetracycline. *Chemosphere*. 2018;210: 424–432. DOI: https://doi.org/10.1016/j.chemosphere.2018.07.040

11. Weller M. T., Hughes R. W., Rooke J., Knee Ch. S., Reading J. The pyrochlore family - a potential panacea for the frustrated perovskite chemist. *Dalton transactions*. 2004;19: 3032–3041. DOI: https://doi.org/10.1039/B401787K

12. Knop O., Brisse F., Meads R. E., Brainbridge J. Pyrochlores. IV. Crystallographic and Mossbauer studies of A_2FeSbO_7 pyrochlores. *Canadian Journal of Chemistry*. 1968;46: 3829–3832. DOI: https://doi.org/10.1139/v68-635

13. Sadykov V. A., Koroleva M. S., Piir I. V., Chezhina N. V., Korolev D. A., Skriabin P. I., Krasnov A. V., Sadovskaya E. M., Eremeev N. F., Nekipelov S. V., Sivkov V. N. Structural and transport properties of doped bismuth titanates and niobates. *Solid State Ionics*. 2018;315: 33–39. DOI: https://doi.org/10.1016/j.ssi.2017.12.00.008

14. Egorysheva A. V., Popova E. F., Tyurin A. V. Khoroshilov A. V., Gajtko O. M., Svetogorov R. D. Complex rare-earth tantalates with pyrochlore-like structure: synthesis, structure, and thermal properties. *Russian Journal of Inorganic Chemistry*. 2019;64: 1342–1353. DOI: https://doi.org/10.1134/S0036023619110056

15. McCauley R. A. Structural characteristics of pyrochlore formation. *Journal of Applied Physics*. 1980;51(1): 290–294. DOI: https://doi.org/10.1063/1.327368

16. Lupitskaya Y. A., Burmistrov V. A. Phase formation in the K_2CO_3-Sb_2O_3-WO_3 system on heating. *Russian Journal of Inorganic Chemistry*. 2011;56(2): 290–292. DOI: https://doi.org/10.1134/S0036023611020173

17. Piir I. V., Koroleva M. S., Korolev D. A., Chezina N. V., Semenov V. G., Panchuk V. V. Bismuth iron titanate pyrochlores: Thermostability, structure and properties. *Journal of Solid State Chemistry*. 2013;204: 245–250. DOI: https://doi.org/10.1016/j.jssc.2013.05.031

18. Lupitskaya Y. A., Kalganov D. A., Klyueva M. V. Formation of compounds in the Ag_2O–Sb_2O_3–MoO_3 system on heating. *Inorganic materials*. 2018;54(3): 240–244. DOI: https://doi.org/10.1134/S0020168518030081

19. Lomakin M. S., Proskurina O. V., Danilovich D. P., Panchuk V. V., Semenov V. G., Gusarov V. V. Hydrothermal synthesis, phase formation and crystal chemistry of the pyrochlore/Bi_2WO_6 and pyrochlore/α-Fe_2O_3 composites in the Bi_2O_3–Fe_2O_3–WO_3 system. *Journal of Solid State Chemistry*. 2020,282: 121064 DOI: https://doi.org/10.1016/j.jssc.2019.121064

20. Yang J., Han Y., Shahid M., Pan W., Zhao M., Wu W., Wan C. A promising material for thermal barrier coating: Pyrochlore-related compound Sm_2FeTaO_7. *Scripta Materialia*. 2018;149: 49–52. DOI: https://doi.org/10.1016/j.scriptamat.2018.02.005

21. Kovalenko L. Yu., Burmistrov V. A., Lupitskaya Yu. A., Kovalev I. N., Galimov D. M. Synthesis of

the solid solutions $H_2Sb_{2-x}V_xO_6 \cdot nH_2O$ with the pyrochlore-type structure *Butlerovskie soobshhenija = Butlerov Communications*. 2018;55(8): 24–30. ROI: jbc-01/jbc-01/18-55-8-24 (In Russ., abstract in Eng.)

22. Kovalenko L. Yu., Burmistrov V. A. Dielectric relaxation and proton conductivity of polyantimonic acid doped with vanadium ions. *Kondensirovannye sredy i mezhfaznye granitsy = Condensed Matter and Interphases*. 2019;21(2): 204–214. DOI: https://doi.org/10.17308/kcmf.2019.21/758 (In Russ., abstract in Eng.)

23. Trofimov V. G., Sheinkman A. I., Kleshchev G. V. About antimony pentoxide in a crystalline state. *Journal of Structural Chemistry*. 1973;14(2): 275–279. (In Russ.)

24. Kovalenko L. Yu., Yaroshenko F. A., Burmistrov V. A., Isaeva T. N., Galimov D. M. Thermolysis of Hydrated Antimony Pentoxide. *Inorganic Materials*. 2019;55(6): 586–592. DOI: https://doi.org/10.1134/S0020168519060086

25. Chen J., Chen Z., Zhang X., Li X., Yu L., Li. D. Antimony oxide hydrate ($Sb_2O_5 \cdot 3H_2O$) as a simple and high efficient photocatalyst for oxidation of benzene. *Applied Catalysis B: Environmental*. 2018;210: 379–385. DOI: https://doi.org/10.1016/j.apcatb.2017.04.004

26. Kovalenko L. Yu., Burmistrov V. A., Lupitskaya Yu. A., Yaroshenko F. A., Filonenko E. M., Bulaeva E. A. Ion exchange of H^+/Na^+ in polyantimonic acid, doped with vanadium ions. *Pure and Applied Chemistry*. 2019. DOI: https://doi.org/10.1515/pac-2019-0112

27. Yukhnevich G. V. Advances in the use of infrared spectroscopy for the characterization of OH bonds. *Russian Chemical Reviews*. 1963;32(11): 619–633. DOI: https://doi.org/10.1070/RC1963v032n11ABEH001370

28. Tarasova N. A., Animitsa I. E. The influence of the nature of halogen on the local structure and intercalation of water in oxyhalides Ba_2InO_3X (X = F, Cl, Br). *Optics and Spectroscopy*. 2018;124: 163. DOI: https://doi.org/10.1134/S0030400X18020170

29. Deryagin B. V., Churaev N. V., Ovcharenko F. D., Tarasevich Ju. I., Bukin V. A., Sarvazjan A. P., Harakoz D. P., Saushkin V. V. *Water in disperse systems*. Moscow: Chemistry Publ.; 1989. 288 p. (In Russ.)

30. Ferapontov N. B., Vdovina S. N., Gagarin A. N., Strusovskaja N. L., Tokmachev M. G. Water properties in hydrophylic polymer gels. *Kondensirovannye sredy i mezhfaznye granicy = Condensed Matter and Interphases*. 2011;13(2): 208–214. Available at: http://www.kcmf.vsu.ru/resources/t_13_2_2011_015.pdf (In Russ.)

31. Frenkel L. S. Nuclear magnetic resonance method for determining the moisture holding capacity of cation exchange resins as a function of temperature. *Analytical Chemistry*. 1973;45(8): 1570–1571. DOI: https://doi.org/10.1021/ac60330a052

32. Kargovsky A. V. Water clusters: structures and optical vibrational spectra. *Izvestiya VUZ. Applied nonlinear dynamics*. 2006;14(5): 110–119. DOI: https://doi.org/10.18500/0869-6632-2006-14-5-110-119 (In Russ., abstract in Eng.)

33. Eisenberg D., Kauzmann W. *The Structure and properties of water*. Oxford: Oxford University Press; 1969. 296 p.

34. Yu T., Zhang H., Cao H., Zheng G. Understanding the enhanced removal of Bi(III) using modified crystalline antimonic acids: creation of a transitional pyrochlore-type structure and the Sb(V)–Bi(III) interaction behaviors. *Chemical Engineering Journal*. 2019;360: 313–324. DOI: https://doi.org/10.1016/j.cej.2018.11.209

35. Nakamoto K. *Infrared and raman spectra of inorganic and coordination compounds: Part A: Theory and applications inorganic chemistry* (Sixth ed.). New York: John Wiley & Sons; 2009. 419 p. DOI: https://doi.org/10.1002/9780470405840

36. Birchall T., Sleight A. W. Oxidation states in vanadium antimonate (“$VSbO_4$”). *Inorganic chemistry*. 1976;15(4): 868–870. DOI: https://doi.org/10.1021/ic50158a026

37. Guerrero-Pérez M. O. V-containing mixed oxide catalysts for reduction – oxidation-based reactions with environmental applications: A short review. *Catalysts*. 2018;8(11): 564. DOI: https://doi.org/10.3390/catal8110564

38. Yaroslavtsev A. B., Kotov V. Yu. Proton mobility in hydrates of inorganic acids and acid salts. *Russian Chemical Bulletin*. 2002;51(4): 555–568.

39. Pauling, L. The nature of the chemical bond – an introduction to modern structural chemistry. (3rd Edition). New York: Cornell University Press, Ithaca; 1960.

Информация об авторах

Liliya Yu. Kovalenko, Senior Lecturer of the Department of Solid State Chemistry and Nanoprocesses, Chelyabinsk State University, Chelyabinsk, Russian Federation, e-mail: lkovalenko90@mail.ru. ORCID iD: https://orcid.org/0000-0002-9187-6934.

Vladimir A. Burmistrov, DSc in Physics and Mathematics, Professor, Dean of Chemical Department, Chelyabinsk State University, Chelyabinsk, Russian Federation; e-mail: burmistrov@csu.ru. ORCID iD: https://orcid.org/0000-0002-7862-6017.

Dmitrii A. Zakhar’evich, PhD in Physics and Mathematics, Associate Professor, Acting Dean of Physical Department, Chelyabinsk State University, Chelyabinsk, Russian Federation; e-mail: dmzah@csu.ru. ORCID iD: https://orcid.org/0000-0003-1184-9571.

All authors have read and approved the final manuscript.

Translated by Valentina Mittova.
Edited and proofread by Simon Cox.

Condensed Matter and Interphases
(Kondensirovannye sredy i mezhfaznye granitsy)

Original articles

DOI: https://doi.org/10.17308/kcmf.2020.22/2531 eISSN 2687-0711
Received 29 November 2019
Accepted 15 February 2020

NEXAFS and XPS Studies of Cr/MWCNT Composites

based on the materials of the XXIII All-Russian Conference with International Participation "X-ray and electron spectra and chemical bonds" (Voronezh, October 1–4, 2019)

© 2019 S. V. Nekipelov[✉,a,b], A. E. Mingaleva[a,c], O. V. Petrova[a], D. V. Sivkov[a,c], A. M. Ob'edkov[d], B. S.Kaverin[d], D. V. Bogachuk[a], R. N. Skandakov[a], V. N. Sivkov[a,b]

[a]*Federal Research Centre "Komi Science Centre of the Ural Branch of the Russian Academy of Sciences",*
24 ul. Kommunisticheskaya, Syktyvkar 167982, Russian Federation

[b]*Pitirim Sorokin Syktyvkar State University, 55 Oktyabrsky prospekt, Syktyvkar 167000, Russian Federation*

[c]*Saint Petersburg State University 7-9 Universitetskaya naberehnaya, Saint Petersburg 199034, Russian Federation*

[d]*G. A. Razuvaev Institute of Organometallic Chemistry of Russian Academy of Sciences,*
49 ul. Tropnina, Nizhny Novgorod 603137, Russian Federation

Abstract

Nanocomposites obtained by MOCVD through deposition of pyrolytic chromium layers of different thickness on the outer surface of multi-walled carbon nanotubes (MWCNTs) using the "Barkhos" chromium-organic liquid were studied.. These pyrolytic Cr coatings have high microhardness, heat resistance, hydrophobicity, and chemical resistance to hydrochloric and sulphuric acids and alkali melt.

The unique physical properties of chromium coatings as well as chemical resistance in a wide temperature range and large external surface of MWCNTs offer great opportunities for the possible applications of the studied nanocomposites. An important problem in this case is the determination of the mechanisms of chromium adhesion to the chemically inert surface of MWCNTs.

A promising method of studying the interface between the MWCNT surface and the coating layer is ultra-soft X-ray spectroscopy in the NEXAFS 1s carbon ionization threshold region. However, there are practically no publications on such studies for chromium compounds due to the superposition of the structure of NEXAFS Cr2p absorption spectra on the NEXAFS C1s ionization threshold region. In the present paper, nanocomposites were studied by the total electron yield method using the unique technique of suppressing and measuring the contribution of multiple orders near the C1s absorption edge.

The studies of the nanocomposite (pyrolytic Cr)/MWCNT performed by NEXAFS and XPS methods showed: (i) the initial MWCNT features are preserved in the composite spectrum; (ii) there is no significant destruction of the outer layers of MWCNTs; (iii) the interface between the MWCNT and the pyrolytic chromium coating is a multilayer structure. This structure includes the outer surface of the MWCNT, the atoms of which form C–O and C–Cr bonds with the pyrolytic chromium coating, chromium carbide monolayer, and the chromium oxide (Cr_2O_3) coating layer. The effective thickness of the chromium oxide and chromium carbide coating layers is 1.5 and 0.3 nm respectively, were determined for the studied samples.

Keywords: multi-walled carbon nanotube, absorption cross section, photoelectron output depth, metal coating, NEXAFS, XPS, MOCVD.

Funding: The reported study was funded by the Russian Foundation for Basic Research (Grant No. 19-32-50062, No. 19-32-60018, and No. 18-33-00776), the bilateral program RGBL at BESSY II, and the governmental order for IOMC RAS (topic No. 45.8).

For citation: Nekipelov S. V., Mingaleva A. E., Petrova O. V., Sivkov D. V., Ob'edkov A. M., Kaverin B. S., Bogachuk D. V., Skandakov R. N., Sivkov V. N. NEXAFS and XPS Studies of Cr/MWCNT Composites *Kondensirovannye sredy i mezhfaznye granitsy = Condensed Matter and Interphases.* 2020;22(1): 84–88. https://doi.org/10.17308/kcmf.2020.22/2531

✉ Sergey V. Nekipelov, e-mail: NekipelovSV@mail.ru

1. Introduction

Composites based on multi-walled carbon nanotubes (MWCNTs) with a metal containing coating offer great opportunities for use in various scientific and technical applications. The most common methods of composite synthesis are the electrochemical reduction of metallic salts using the sol-gel method, metal organic chemical vapor deposition (MOCVD), and physical deposition (electron-beam sputtering, thermal spraying, etc.). In our earlier studies, it was shown that MOCVD, due to its technological characteristics, is the most appropriate method for the synthesis of MWCNT composites with a metal containing coating [1–4].

The present paper is devoted to the investigation of an MWCNT composite with a pyrolytic Cr coating. Unlike pure Cr, pyrolytic Cr coatings have high microhardness, heat resistance, hydrophobicity, and chemical resistance to hydrochloric and sulphuric acids and alkali melt. Therefore, they can be used in the aviation (friction joints in aircraft control systems), petrochemical (anticorrosive coatings highly resistant to aggressive environments high in hydrogen sulphide), and steel (foundry and pressing equipment, thermocouple protection tubes) industries.

The chemical composition of the MWCNT outer surface, pyrolytic chromium coating, and the interface between the coating and the MWCNT surface was studied using NEXAFS (Near Edge X-ray Absorption Fine Structure) and XPS (X-ray Photoelectron Spectroscopy) methods.

2. Experimental

The initial MWCNTs were synthesized by MOCVD through thermal decomposition of the mixtures of ferrocene with toluene in a quartz reactor in a argon flow at atmospheric pressure. Deposition of pyrolytic chromium coatings on the MWCNT surface was also performed by the MOCVD method using as a precursor the “Barkhos” chromium-organic liquid, consisting of a mixture of bis-arene chromium compounds. The details of the preparation technique of the studied samples are described in the following works [1, 3, 4].

The study of the initial MWCNT surface, the chemical composition, and measurement of Cr coating thickness as well as the study of the Cr/MWCNT interface were conducted by NEXAFS spectroscopy using a a synchrotron radiation of Russian and German source at BESSY II [5]. Spectral dependence of absorption cross section in a wide energy range of 250–900 eV and near the C1s and Cr2p absorption edges of initial MWCNTs, Cr/MWCNT composite, and chromium oxide Cr_2O_3 were measured in the Total Electron Yield (TEY) mode. The studied samples were prepared by rubbing MWCNT powder and Cr/MWCNT composite into the pure surface of a Cu plate. An additional thin-film Ti filter with a thickness of 160 nm installed on an Au grid in front of the sample in the path of incident radiation was used for the suppression and estimation of the radiation reflected from a diffraction grating in multiple diffraction orders and long-wave diffuse background radiation [6]. The tracking of the contribution of background radiation is especially important for the Cr/MWCNT composite as the structure near the Cr/MWCNT composite absorption edge of the Cr coating in the second order diffraction is applied to a thin structure near the NEXAFS C1s absorption edge of the MWCNT.

XPS measurements of the Cr/MWCNT composite were performed using the equipment of the Center for Studies in Surface Science of Research park of St.Petersburg State University – Combined Auger, X-ray and Ultraviolet Photoelectron spectrometer Thermo Fisher Scientific ESCALAB 250Xi with an ion-electron system for charge compensation. An X-ray tube with an Al-anode was used as a source of radiation. Energetic positions of all peaks were calibrated against the C1s peak at 284.6 eV

3. Results and discussion

The analysis of NEXAFS C1s spectra (Fig. 1a) shows that the structures (π^* and σ^* resonances) typical for a initial MWCNT are preserved in the spectrum of the Cr/MWCNT composite, which indicates the absence of significant destruction of the outer layers of MWCNTs. However, an additional structure A (287.1 eV), B (287.7 eV), C (288.4 eV), and D (290.4 eV) was observed in an intermediate region between the π^* and σ^* resonances. The positions of these peaks are in good agreement with the energetic positions of the elements of NEXAFS C1s absorption spectrum of graphite oxide [7] corresponding to the ordinary (C–O, band A), epoxide (C–O–C, band B), and double (C=O, band C) bonds and the carbonate group $[CO_3]^{2-}$ [8]. It should be noted that in the quantum energy 285–287 eV range there may be a structure related to the possible formation of carbides [9], absorption transition in these compounds may make a contribution to A and B peak intensity in the C1s-spectra.

The presence of the elements typical for Cr_2O_3 (Fig. 1b) in the NEXAFS Cr2p edge allows assuming that the layer of chromium deposited on the surface is oxidised completely due to contact with atmospheric oxygen.

According to the data of the NEXAFS C1s spectra of MWCNT and the Cr/MWCNT composite, the effective thickness of the oxide coating (Cr_2O_3) was assessed according to the ratio:

$$d_{\text{eff}} = \lambda \ln\left(\frac{S_1}{S_2}\right), \qquad (1)$$

λ = 1 nm photoelectron escape depth from the surface of Cr_2O_3 [10]; S_1 and S_2 – areas under the spectral dependence of absorption cross section of MWCNTs, and the composite Cr/MWCNT, respectively ($S_1/S_2 = 2.6$); $d_{\text{eff}} = 0.96$ nm.

Photoelectron studies are traditionally used for examining the phase composition of nanocomposites, in particular they can be used to determine the presence of the chromium carbide layer on the MWCNTs surface as well as to assess the characteristic thickness of the layers of chromium compounds covering the nanotubes. Fig. 2 shows XPS spectra in the C1s and Cr2p ionization thresholds region, both for the studied composite and for the initial nanotubes. The comparison of integral intensities of bands A in the carbon spectra of the initial MWCNT and the composite Cr/MWCNT ($S_1/S_2 = 1.91$) also allowed assessing the thickness of the Cr_2O_3 coating that equalled $d_{\text{eff}} = 1.5$ nm (in this case the free path was $\lambda = 1.89$ nm [11]), which agrees with the above-mentioned assessment according to the NEXAFS spectra data. The appearance of additional B bands, both in 1s carbon spectra and 2p chromium spectra, should be noted while examining the XPS spectra of the composite. Their energetic position correlates well with the ionization thresholds in chromium carbides [12–13], which allows assuming that the carbon atoms of the nanotube interact with the chromium atoms and Cr-C chemical bonds are formed. At the same time, taking into account the free path of photoelectrons in the MWCNT layer $\lambda = 3.11$ nm [11], the ratio of bands A and B in the XPS C1s spectra of the composite allows assessing the thickness of the carbide layer as $d_{\text{eff}} = 0.3$ nm. Thus, the chromium atoms coating formation process on the nanotube surface is as follows: at the initial stage, during the process of MOCVD, chromium atoms form a chemical bond with carbon atoms on the MWCNT surface forming a thin layer of chromium carbide that is covered with a layer of metal oxidised to Cr_2O_3 when the composite is subsequently exposed to the air.

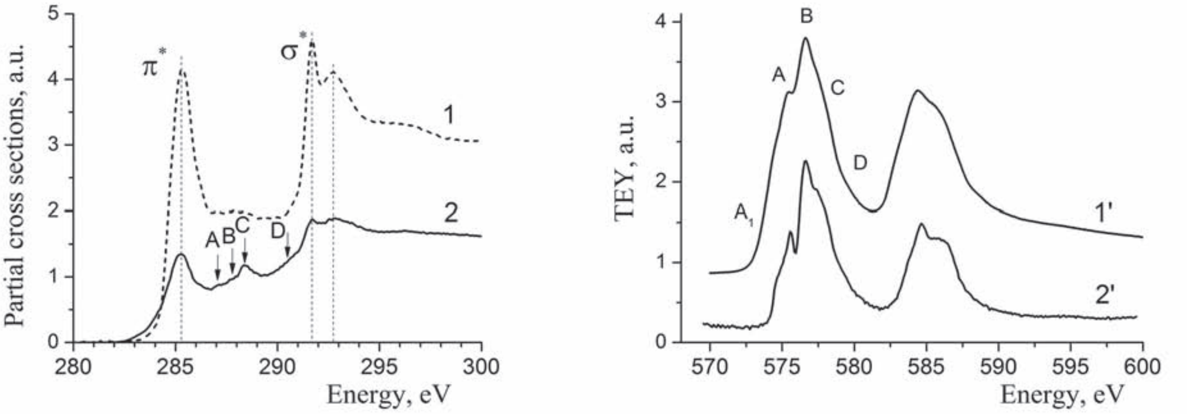

a b

Fig. 1. Spectral dependences of a) the partial absorption cross sections of MWCNTs (*1*) and the Cr/MWCNT composite (*2*) in the NEXAFS region of the C1s absorption edge; b) TEY signals of the Cr/MWCNT (*1'*) and Cr_2O_3 (*2'*) composite in the NEXAFS region of the Cr2p absorption edge

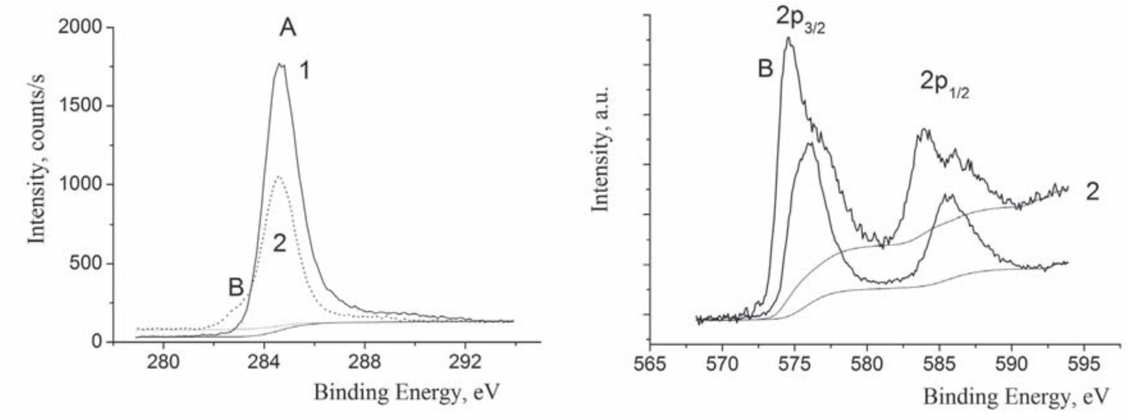

a b

Fig. 2. XPS spectra a) in the region of the C1s edge of the ionization of the initial MWCNTs (*1*) and the Cr/MWCNT composite (*2*) and b) in the region of the Cr2p edge of the ionization of Cr_2O_3 (*1*) and the Cr/MWCNT composite (*2*)

4. Conclusions

The analysis of the data obtained by NEXAFS and XPS methods allowed establishing that, as a result of the interaction of chromium atoms with the outer surface of MWCNT, a multilayer structure is formed, consisting of the outer surface layer of MWCNT, a thin layer of chromium carbide covered with the of chromium oxide Cr_2O_3 layer with an effective thickness 0.3 and 1.5 nm respectively.

Acknowledgements

The authors are grateful to Prof. A. Vinogradov for their useful counsel during the preparation of this article.

Conflict of interests

The authors declare that they have no known competing financial interests or personal relationships that could have influenced the work presented in this paper.

References

1. Ob'edkov A. M., Kaverin B. S., Gusev S. A., Ezerskii A. B., Semenov N. M., Zaytsev A. A., Egorov V. A., Domrachev G. A. MOCVD modification of the surface of multiwalled carbon nanotubes to impart to them the necessary physicochemical properties. *Journal of Surface Investigation*. 2009; 3(4): 554–558. DOI: https://doi.org/10.1134/S1027451009040120

2. Kirillov A. I., Ob'edkov A. M., Egorov V. A., Domrachev G. A., Kaverin B. S., Semenov N. M., Lopatina T. I., Gusev S. A., Mansfeld A. D. Sozdanie s pomoshch'yu MOCVD-tekhnologii nanostrukturirovannykh kompozitsionnykh materialov na osnove mnogostennykh uglerodnykh nanotrubok [Creation of nanostructured composite materials based on multi-walled carbon nanotubes using MOCVD] *Nanotekhnika [Nanotechnology]* 2011; 1(25): 72–78. (In Russ.)

3. Sivkov V. N., Ob'edkov A. M., Petrova O. V., Nekipelov S. V., Kremlev K. V., Kaverin B. S., Semenov N. M., Gusev S. A. X-ray and synchrotron investigations of heterogeneous systems based on multiwalled carbon nanotubes. *Physics of the Solid State*. 2015;57(1): 197–204. DOI: https://doi.org/10.1134/S1063783415010291

4. Petrova O. V., Nekipelov S. V., Mingaleva A. E., Sivkov V. N., Obiedkov A. M., Kaverin B. S., Kremlev K. V., Ketkov S. Yu., Gusev S. A., Vyalikh D. V., Molodtsov S. L. Study of composite MWCNT/pyrolytic Cr interface by NEXAFS spectroscopy. *Journal of Physics: Conference Series*. 2016;741(1): 012038. DOI: https://doi.org/10.1088/1742-6596/741/1/012038

5. Fedoseenko S. I., Iossifov I. F., Gorovikov S. A., Schmidt J., Follath R., Molodtsov S. L., Adamchuk V. K., Kaindl G. Development and present status of the Russian-German soft X-ray beamline at BESSY II. *Nucl. Instr. and Meth. A*. 2001;470: 84–88. DOI: https://doi.org/10.1016/S0168-9002(01)01032-4

6. Kummer K., Sivkov V. N., Vyalikh D. V., Maslyuk V. V., Bluher A., Nekipelov S. V., Bredow T., Mertig I., Mertig M., Molodtsov S. L. Oscillator strength of the peptide bond π*-resonances at all relevant x-ray absorption edges. *Physical Review B*. 2009;80: 155433–155438. DOI: https://doi.org/10.1103/PhysRevB.80.155433

7. Jeong H.-K., Noh H.-J., Kim J.-Y., Jin M. H., Park C. Y., and Lee Y. H. X-ray absorption spectroscopy of graphite oxide. *Europhysics Letters*. 2008;82: 67004-1–5. DOI: https://doi.org/10.1209/0295-5075/82/67004

8. Madix R. J., Solomon J. L., and Stцhr J. The orientation of the carbonate anion on Ag(110). *Surf. Sci*. 1988;197: L253–L259. DOI: https://doi.org/10.1016/0039-6028(88)90624-3

9. Chen J. G. NEXAFS investigations of transition metal oxides, nitrides, carbides, sulfides and other interstitial compounds. *Surface Science Report*. 1997;30: 1–152. DOI: https://doi.org/10.1016/S0167-5729(97)00011-3

10. Ruihua Cheng B. Xu., Borca C. N., Sokolov A., Yang C.-S., Yuan L., Liou S.-H., Doudin B., Dowben P. A. Characterization of the native Cr_2O_3 oxide surface of CrO_2. *Appl. Phys. Letters*. 2001;79: 3122–3124. DOI: https://doi.org/10.1063/1.1416474

11. NIST Standard Reference Database 71. *NIST Electron Inelastic-Mean-Free-Path Database: Version 1.2*. Available at: www.nist.gov/srd/nist-standard-reference-database-71

12. Teghil R., Santagata A., De Bonis A., Galasso A., Villani P. Chromium carbide thin films deposited by ultra-short pulse laser deposition. *Applied Surface Science*. 2009; 255: 7729–7733. DOI: https://doi.org/10.1016/j.apsusc.2009.04.151

13. Zhao D., Jiang X., Wang Y., Duan W., Wang L. Microstructure evolution, wear and corrosion resistance of Cr-C nanocomposite coatings in seawater. *Applied Surface Science*. 2018;457: 914–924. DOI: https://doi.org/10.1016/j.apsusc.2018.06.248

Information about the authors

Sergey V. Nekipelov, PhD in Physics and Mathematics, Head of the Laboratory, Federal Research Centre “Komi Science Centre of the Ural Branch of the Russian Academy of Sciences”; Associate Professor, Pitirim Sorokin Syktyvkar State University, Syktyvkar, Russian Federation; e-mail: NekipelovSV@mail.ru. ORCID iD: https://orcid.org/0000-0001-6749-738X.

Alena E. Mingaleva, Junior Researcher, Federal Research Centre “Komi Science Centre of the Ural Branch of the Russian Academy of Sciences”, Syktyvkar, Russian Federation; Trainee, Saint Petersburg State University, Saint Petersburg, Russian Federation; e-mail: amingaleva@gmail.com.

Olga V. Petrova, PhD in Physics and Mathematics, Researcher, Federal Research Centre “Komi Science Centre of the Ural Branch of the Russian Academy of Sciences”, Syktyvkar, Russian Federation; e-mail: teiou@mail.ru. ORCID iD: https://orcid.org/0000-0003-0398-3113.

Danil V. Sivkov, PhD in Physics and Mathematics, Researcher, Federal Research Centre “Komi Science Centre of the Ural Branch of the Russian Academy of Sciences”, Syktyvkar, Russian Federation; Researcher, Saint Petersburg State University, Saint Petersburg, Russian Federation; e-mail: d.sivkov@spbu.ru. ORCID iD: https://orcid.org/0000-0002-5324-1209.

Dmitry V. Bogachuk, postgraduate student, Federal Research Centre “Komi Science Centre of the Ural Branch of the Russian Academy of Sciences”, Syktyvkar, Russian Federation; e-mail: bogachuk108@gmail.com.

Roman N. Skandakov, postgraduate student, Federal Research Centre “Komi Science Centre of the Ural Branch of the Russian Academy of Sciences”, Syktyvkar, Russian Federation; e-mail: scanick@yandex.ru.

Anatoly M. Ob’edkov, PhD in Chemistry, Head of the Laboratory, G.A. Razuvaev Institute of Organometallic Chemistry of Russian Academy of Sciences, Nizhny Novgorod, Russian Federation; e-mail: amo@iomc.ras.ru.

Boris S. Kaverin, PhD in Physics and Mathematics, Leading Researcher, G. A. Razuvaev Institute of Organometallic Chemistry of Russian Academy of Sciences, Nizhny Novgorod, Russian Federation; e-mail: kaverin@iomc.ras.ru.

Viktor N. Sivkov, DSc in Physics and Mathematics, Senior Researcher, Federal Research Centre “Komi Science Centre of the Ural Branch of the Russian Academy of Sciences”; Professor, Pitirim Sorokin Syktyvkar State University, Syktyvkar, Russian Federation; e-mail: SVN@dm.komisc.ru. ORCID iD: https://orcid.org/0000-0001-9916-1514.

All authors have read and approved the final manuscript.

Translated by Marina Strepetova.
Edited and proofread by Simon Cox.

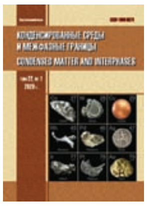

Condensed Matter and Interphases
(Kondensirovannye sredy i mezhfaznye granitsy)

Original articles

DOI: https://doi.org/10.17308/kcmf.2020.22/2532 eISSN 2687-0711
Received 6 March 2020
Accepted 15 March 2020

Spectromicroscopic Studies of Porous Silicon Oxide on Silicon Using Synchrotron Radiation

© 2020 E. V. Parinova✉,[a], D. Marchenko[b], A. K. Fedotov[c], D. A. Koyuda[a], Yu. A. Fedotova[c], R. Ovsyannikov[b], S. Yu. Turishchev[a]

*[a]Voronezh State University,
1 Universitetskaya pl., Voronezh 394018, Russian Federation*

*[b]Helmholtz Zentrum Berlin,
15 Albert Einstein str., Berlin 12489, Germany*

*[c]Institute for Nuclear Problems,
Belarusian State University, 11 Bobruiskaya str., Minsk 220030, Belarus*

Abstract

This work is dedicated to microscopic synchrotron studies of the morphology, atomic, and electronic structure of an array of submicron-sized pores in a SiO_2 layer on silicon formed with the use of ion-track technology in combination with chemical etching after irradiation. The research method was photoemission electron microscopy using high-intensity synchrotron radiation. The method was used in two modes. The use of chemically selective electron microscopy allowed obtaining morphological information about the studied array of pores. The X-ray spectroscopy mode of the synchrotron radiation of X-rays absorption near-edge fine structure spectroscopy allowed us to obtain information about the specificity of the local surrounding of the given atoms from microscopic regions of nanometer and submicron areas of the obtained microscopic images. The pores had rather sharp boundaries, without a transition layer. The bottom of the pores was a substrate - a crystalline silicon wafer covered with a natural 2-3 nm thick oxide layer. Ion irradiation and chemical etching did not significantly affect the structural and phase characteristics of the porous silicon oxide matrix. There was no significant disordering in the silicon atoms available at the bottom of individual pores. There was no technological contamination. The efficiency of using ion-track technology in combination with chemical etching after irradiation for the formation of isolated pores arrays with close submicron range sizes was shown. The obtained results demonstrated the efficiency of the photoemission electron microscopy method using high-intensity synchrotron radiation for the high accuracy microscopic scale study of a wide range of objects with the composite structure-phase nature of the surface.

Keywords: silicon dioxide, submicron pores, atomic and electronic structure, synchrotron radiation, XANES, Photoemission Electron Microscopy, local atomic surrounding.

Funding: The reported study was funded by Russian Foundation for Basic Research according to the research project No 18-32-01046 and partially supported by the Ministry of Education and Science of the Russian Federation as the part of the state task for high education institution in the field of scientific activity for 2017-2020 – project No 16.8158.2017/8.9 (general XANES studies and results calibration).

For citation: Parinova E. V., Marchenko D., Fedotov A. K., Koyuda D. A., Fedotova Yu. A., Ovsyannikov R., Turishchev S. Yu. Spectromicroscopic studies of porous silicon oxide on silicon using synchrotron radiation. *Kondensirovannye sredy i mezhfaznye granitsy = Condensed Matter and Interphases*. 2020;22(1): 89–96. DOI: https://doi.org/10.17308/kcmf.2020.22/2532

✉ Elena V. Parinova, e-mail: parinova@phys.vsu.ru

1. Introduction

Arrays of porous silicon dioxide on silicon can be used as effective matrices in a variety of technological solutions [1–2]. The semiconductor substrate allows the effective control of the porous layer formation itself and various composite structures based on it [3–4]. Such structures (templates) can be used in a wide range of areas from semiconductor magnetic composite devices [5] to optical sensors based on surface-enhanced Raman scattering [6]. Chemical and electrochemical processes of nanostructures synthesis in separate pores and the formation of self-organized particles in the pores require careful selection of the method for the formation of the porous layer and the control of its composition and structure. The ion-track technology of swift heavy ions in combination with subsequent chemical etching is a promising technology for the formation of a porous template [4–6]. Being relatively simple, this method has a number of advantages, for example, the ability to effectively control the density and geometric parameters of pores according to studies [1–6].

The method of scanning electron microscopy is particularly effective in the primary morphology diagnostic of the formed pores arrays. This method has previously been repeatedly demonstrated with high resolution, including for template structures [7]. However, this method is not always sensitive to the phase composition and does not allow the effective study of the structure and the specifics of the local atomic surrounding specificity in the porous layer. Such studies are important considering the developed surface which is accessible to external influences and may also be subjected to internal reconstruction. X-ray and electron spectroscopy is an indispensable tool for accurate and qualitative studies of the physical and chemical state of a porous layer as a morphologically complex object with a pronounced surface and potentially numerous boundaries [8–11]. The use of synchrotron radiation sources in the X-ray spectral range allows increasing the accuracy of experiments for objects of small sizes and low intensities of a useful signal [8, 10]. X-ray photoelectron spectroscopy [10] and XANES – X-ray absorption near edge structure [8–11] are in demand for studying the atomic and electronic structure of developed surfaces and accessible interfaces between micro- and nanostructured objects.

X-ray and electron spectroscopy experiments are usually conducted independently of microscopic ones, which often complicates the research. In addition, despite the sensitivity to the local atomic surrounding, the area of the surface from which the spectrum is recorded is, at best, hundreds of micrometres [12]. The real microscopic approach in terms of obtaining information about the morphology of small studied objects and their physical and chemical state as well as their atomic and electronic structure in a "micropoint" is implemented in spectromicroscopy methods [13, 14]. Such methods include photoemission electron microscopy (PEEM – PhotoEmission Electron Microscopy), including PEEM with the use of high intensity synchrotron (undulator) radiation in the soft X-ray range. Earlier, we demonstrated the effectiveness of using the PEEM method in the XANES spectrum registration mode for effective studies of the morphology, specificity of the atomic and electronic structure, composition and structure of objects of micron, submicron, and nanometer sizes in a single experiment [14–17]. However, the studies were conducted for structures mainly consisting of different sorts of atoms, e.g. nickel structures in porous silicon dioxide matrix with etched tracks [16, 17].

This work presents the results of PEEM studies of the morphology, atomic and electronic structure of an array of submicron pores in a SiO_2 layer on silicon by synchrotron photoemission electron microscopy. The array of submicron pores was obtained using ion-track technology and subsequent chemical etching.

2. Experimental

SiO_2 layer with the thickness ~ 500 nm was obtained by thermal oxidation of c-Si crystalline silicon wafers of the KDB 40 (100) type (100) in an O_2 atmosphere (purity 99.9999 vol. %, 1100 °C, 10 hours). The formation of swift heavy ion tracks in the SiO_2 dielectric layer on Si was carried out at the Hahn-Meitner Institute (Berlin, Germany) accelerator by irradiating the silicon dioxide layer with $197Au^+$ ions with an energy of 350 MeV. For the formation of pores, latent tracks formed after irradiation of a silicon oxide layer were etched at 20 °C room temperature in a diluted aqueous solution of hydrofluoric acid (the mass fraction of the acid was 1.35 %). The ion fluence during irradiation was $1\cdot10^{8}$ cm^{-2}, and the etching time was 80 minutes.

In this work the por-SiO_2/Si structures were studied by the PEEM method using high-intensity synchrotron (undulator) radiation from the BESSY II Helmholtz-Zentrum-Berlin storage ring (Berlin, Germany). For PEEM studies, a UE56-2 PGM2 radiation beamline was used, and the SurICat beamline was additionally used for XANES measurements of reference spectra in the "standard" (non-microscopic) mode. PEEM studies were performed using the Scienta Omicron Focus PEEM microscope. PEEM data were obtained by recording the electronic yield in the region of silicon $L_{2,3}$ X-ray absorption near edge structure (XANES Si $L_{2,3}$) The measurements were carried out at room temperature and the instrumental broadening upon recording the XANES spectra was ~ 0.1 eV.

XANES spectra in the "standard" mode were registered using sample compensation (drain) current technique in the mode of the total electron yield (TEY) detection. The vacuum in the working chambers of all synchrotron analytical stations was 10^{-10} Torr. When registering Si $L_{2,3}$ XANES spectra, the analysis depth was about 5 nm according to [18]. Standard procedures for calibration and normalization of all spectra obtained using a pure gold foil signal were used. The reference objects were: a source crystalline silicon wafer (c-Si) and an amorphous silicon film (a-Si) on silicon wafer covered by 2 nm layer of natural SiO_2 oxide, as well as thermal SiO_2 film of 20 nm on silicon wafer.

The XANES method allows obtaining information about the distribution of the local partial density of free electronic states in the conduction band according to [19, 20]. This makes the XANES spectroscopy data extremely sensitive to the specificity of the local atomic surrounding, which has been demonstrated many times before [8–11].

PEEM (XANES) data for the por-SiO_2/Si structure were recorded using fields of view from 100 to 10 μm. Spectra near the $L_{2,3}$ silicon absorption edge from regions up to several hundred nanometres in diameter were considered for obtaining microscopic data on the local atomic and electronic structure.

3. Results and discussion

XANES spectra registered in the standard way for a set of reference samples are shown in Fig. 1. These are the top three spectra. It is easy to see the presence of a low-energy absorption edge in the range from 100 to 105 eV of the reference spectra of crystalline silicon and an amorphous silicon film. In the first case, the specified absorption edge was characterized by a fine structure with two groups of A and A' maxima (Fig. 1) corresponding to the spin-orbital splitting of core Si $L_{2,3}$ level [21, 22]. A fine structure was not observed for the amorphous film [21, 22] due to the smearing of the density of states in the conduction band. The fine structure of c-Si and

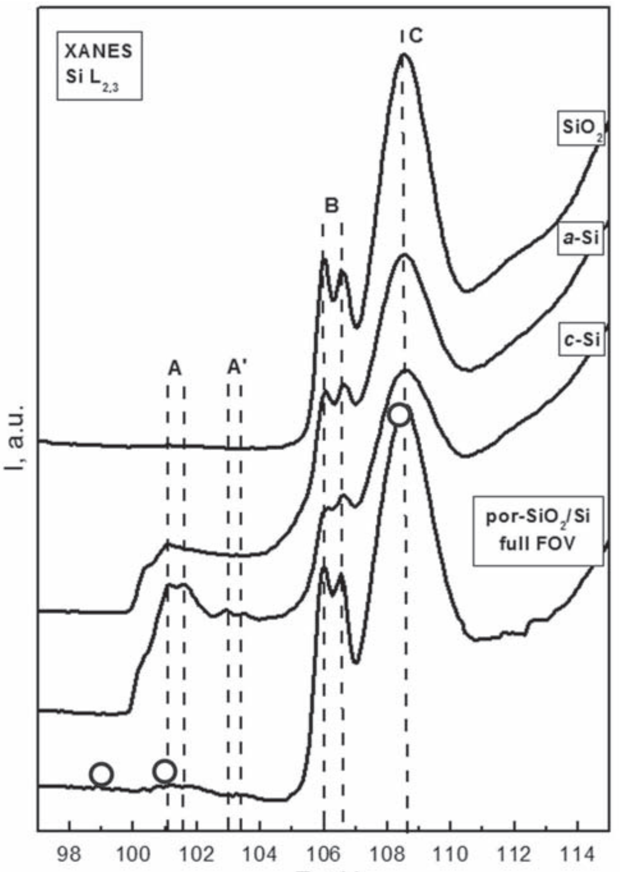

Fig. 1. Synchrotron XANES Si $L_{2,3}$ spectra of references: crystalline silicon c-Si, amorphous silicon a-Si, silicon dioxide SiO_2, together with the spectrum extracted from the 10 μm microscopic field of view. Dashed lines highlight the characteristic regions of the spectra fine structure: A and A' for "elementary" silicon; B and C for silicon dioxide. Circles show the quantum energies at which high-resolution images were recorded

a-Si reference samples was almost equivalent to the SiO_2 reference sample at synchrotron radiation quantum energies exceeding 105 eV (Fig. 1). Sufficiently long-term storage of the crystalline silicon wafer and a structure with a film of amorphous silicon under the laboratory conditions led to the formation of a natural SiO_2 oxide layer with a thickness of ~ 2 nm, the absorption edge from which we observed. For the SiO_2 reference sample the fine structure of this edge was more pronounced (Fig. 1), especially near the first double maximum of 106–106.6 eV (maxima group B) of the molecular orbital σ^* a_1 (transitions from $2p_{1/2,3/2}$ level to 3*s* state) [23]. The main peak for the SiO_2 reference sample was maximal at $h\nu$ ~ 108.6 eV (molecular orbital σ^* t_2, transition from $2p_{1/2,3/2}$ level to 3*p* state), indicated in Fig. 1 as C. It was also more pronounced compared to the natural oxide on c-Si and a-Si. The high intensity of the characteristic maxima of the spectrum of silicon dioxide ($h\nu$ > 105 eV) was obvious since it corresponded to a denser package of the main structural unit of silicon dioxide, the SiO_4 tetrahedron for the thermal oxide film (middle order), compared with a more “loose” layer of natural oxide [23].

The fourth curve in Fig. 1 corresponds to the XANES Si $L_{2,3}$ spectrum obtained integrally, which was extracted for only 10 μm of the field of view (FoV) of the microscopic image of the surface area (shown in Fig. 2). The following characteristic features of this spectrum can be easily seen. A small “influx” in the region of A and A’ maxima indicates a weak X-ray spectral signal from silicon atoms, which are not bound to oxygen atoms and possibly present in an ordered state (A’ “influx”). The oxide part of the spectrum according to the position of the main spectral features (B and C), as well as the distribution of their relative intensities, indicates that the surface layer was mainly silicon dioxide, close to the thermal dioxide based on the package density. This is certain, since the original film was obtained by thermal oxidation. Thus, damage caused by irradiation with gold ions and subsequent chemical etching did not affect, at least “macroscopically”, the nature of the local atomic structure and the electron-energy spectrum of the oxide film.

The electron microscopy images of the studied surface area from which the XANES Si $L_{2,3}$ spectrum (shown in Fig. 1) was obtained are shown in Fig. 2. Three images were obtained with high resolution in the X-ray spectral region of synchrotron (undulator) quantum energies preceding the absorption edge of “elementary” silicon (99 eV, the “background” part of the XANES spectrum), after the specified absorption edge (101 eV), and in the region of the main silicon dioxide peak (108.2 eV).

In all three images, the observed picture was practically identical. This result is quite understandable, since images using the PEEM method are formed due to different electronic work function leaving the surface layer of the sample during excitation by quanta of the corresponding energies [13]. In our case, these energies are close, since in addition to the morphology studies, we were interested in the specifics of the local silicon atoms surrounding (see below). According to the X-ray spectral characteristic of the entire

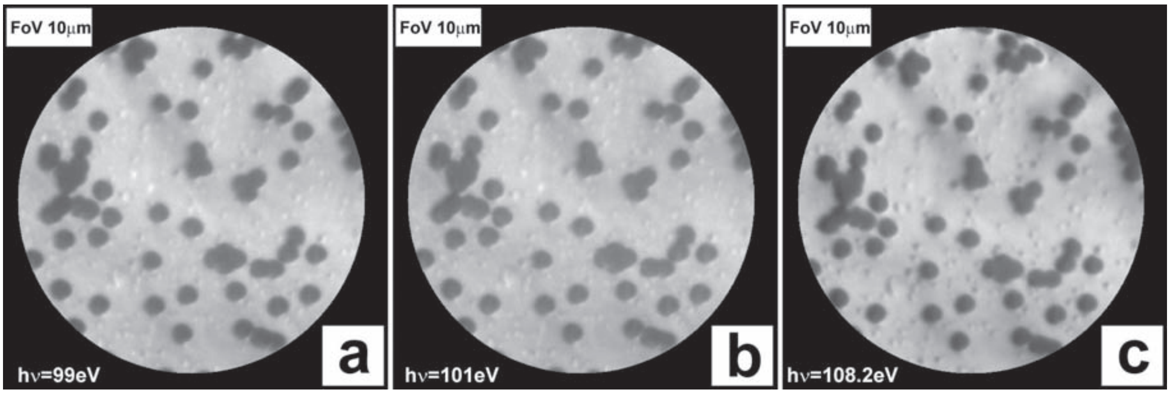

Fig. 2. PEEM electron microscopic images of the por-SiO_2/Si sample surface recorded at different quantum energies of synchrotron (undulator) radiation in three characteristic X-ray spectral regions: a – ($h\nu$ = 99 eV); b – ($h\nu$ = 101 eV) and c – ($h\nu$ = 108.2 eV). The field of view was 10 μm

field of view (Fig. 1) for quantum energies before the edge of "elementary" silicon absorption and immediately after this edge (99 and 101 eV, respectively), the increase in intensity was barely noticeable. At the same time, the relative intensity variation for the edge of "elementary" silicon and SiO_2 was quite significant (Fig. 1, lower spectrum). Therefore, the image shown in Fig. 2 (c) is, in our opinion, characterized by higher sharpness. However, it should be noted, that the main features of the surface morphology of the studied area were preserved in all three images.

The surface contained an array of spherical objects with close diameter values of ~ 300 nm. Presumably, these objects are voids or pores, which follows from the lower signal intensity from these areas (dark shades), and the fact that the etching mode assumed reaching the wafer. The edges of the pores were sharp, which indicates an extremely small difference in pore width at the base and at the top, as well as an almost unchanged surface morphology around the pore, even due to a noticeable "etching" of the SiO_2 film surface. Mainly separated pores were formed. However, individual cases of the merging of 2–4 pores and the formation of voids of several micrometres in size can be noted. This distribution was not accidental and it was a consequence of the selected etching mode (etching reagent composition, etching time) and the inhomogeneous distribution of $197Au^+$ ions. However, with the fluence used, despite the arbitrary nature of the distribution of latent tracks, etching of the irradiated silicon dioxide film practically did not lead to pore fusion.

Finally, a separate formations of random location with sizes less than 100 nm were observed on residual, non-etched SiO_2 surface areas. This distribution pattern may indicate that the observed features correspond to the intrinsic defects of the original thermal SiO_2 film. Such defects were characterized by sizes smaller than the latent ion track and therefore were less susceptible to etching.

Before proceeding to the real "micropoint" spectra, extracted from surface regions of interest (ROI) of submicron sizes, the following should be noted. We used the PEEM method in the XANES Si $L_{2,3}$ spectroscopy mode for morphology studies with simultaneous reference to the analysis of the local surrounding of silicon atoms in the "micropoint". Here, the registration of the XANES spectrum using the PEEM method involves the accumulation of a set of images for each specified quantum energy value in the detecting spectral range. In our case, this range was 95–115 eV, at 0.1 eV increment step. Extraction of the XANES spectrum from the image ROI area (desired surface part) occurs by recalculating the relative intensity of the signal from the desired ROI from the entire sequence of the registered microscopic images stack in a single scale.

A set of characteristic individual surface areas not exceeding a diameter of 250 nm each is shown in Fig. 3a. In the same figure (Fig. 3b), we present the XANES Si $L_{2,3}$ spectra extracted from each of the designated ROI. The first two sections, ROI1 and ROI2, respectively, were selected outside the pores and provide an idea about the surface property of the residual, non-etched thermal SiO_2 film. ROI3 is a surface region selected in the centre of a massive surface part of several merged pores. ROI4 corresponds to the centre of a three merged pores region with the common external boundary. Finally, ROI5 represents the inner part of a single pore.

The character of the main features distribution of the ROI1 and ROI2 spectra suggests their complete coincidence, as well as their similarity to the reference spectrum of the SiO_2 thermal film. Thus, the surface of the film that was not affected by the collision with the ion and subsequent chemical etching did not undergo noticeable transformations with respect to the local surrounding of Si atoms. The relatively weak signal characteristic of all ROIs was particularly noticeable on the pre-edge background and it was a result of the low spectrum extraction area dimensions (~ 250 nm).

XANES Si $L_{2,3}$ spectra extracted from the ROI3–ROI5 sections differed from the fine structure of the ROI1 and ROI2 spectra. In the quantum energies range above ~ 100 eV, a pronounced absorption edge was observed, indicating the presence of silicon atoms not bound with oxygen atoms. The fine structure was indistinguishable due to the low intensity, however, the flatter shape of A–A' regions was closer to the c-Si reference. This result confirms that pores in silicon dioxide were formed down to the wafer, the corresponding

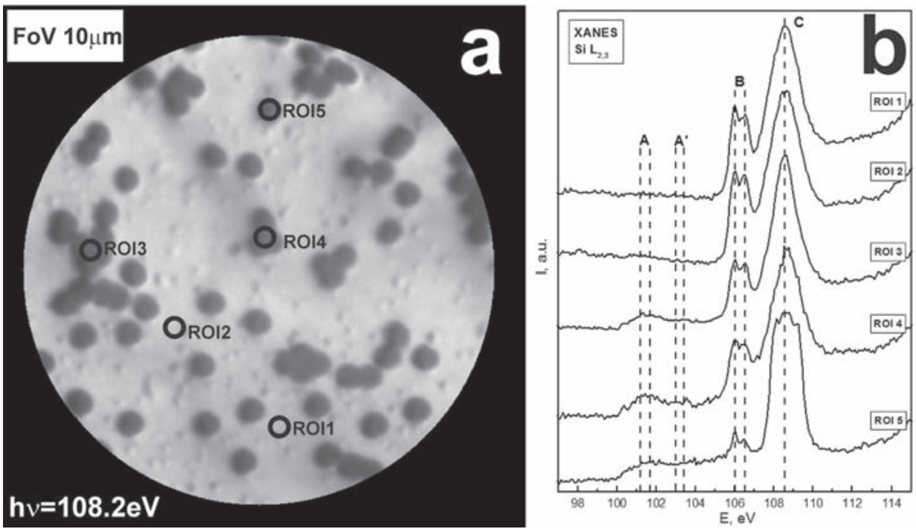

Fig. 3. a – PEEM image of the studied surface area with a field of view of 10 microns, registered at the energy of synchrotron (undulator) radiation quanta *h*ν = 108.2 eV with designated spectra extraction ROI with a diameter of ~ 250 nm. b – Synchrotron XANES Si $L_{2,3}$ spectra of individual submicron surface regions from the ROI indicated on the microscopic image. The characteristic fine structure maxima identical to the XANES Si $L_{2,3}$ spectra of the reference samples are shown

area of which provides such X-ray spectral signal. The presence of B and C features indicates a natural oxidation of the silicon surface at the bottom of the pores. The shape of the observed features in the "oxide" region corresponds to the reference spectra for ROI3 and ROI4. In the case of ROI5, the maxima were deformed, possibly due to a noticeable local redistribution of the potential within the area near the pore that had a pronounced surface relief. This redistribution of the surface potential, obviously, affects the signal statistics, causing deviations in the form of the registered (extracted) absorption edge fine structure. Nevertheless, all the main features peculiar to "elementary" silicon and its dioxide were observed. The ratio of the relative intensities of these edges, according to data [18], and the dip in the energy region between the features B and C, suggest the natural origin of the oxide layer with thickness ~ 2–3 nm on the surface of the bottom of individual pores. Thus, even individual SiO_2 pores in their array in the por-SiO_2/Si structure had sharp vertical boundaries separating the silicon oxide walls from the bottom of the silicon wafer pore. We did not find any traces of transition layers or other transformations of the physical and chemical state of the studied structure of the array of spherical pores formed in a layer of thermal silicon dioxide on a c-Si wafer.

4. Conclusions

For the first time, in a single experiment, the morphology and atomic and electronic structure of porous silicon oxide on silicon formed by irradiating the SiO_2 film with 197Au+ ions with an energy of 350 MeV and its subsequent chemical etching were studied. The PEEM method with the use of high-intensity synchrotron (undulator) radiation in two complementary modes: physicochemically selective electron microscopy and spectroscopy of the X-ray absorption near edge fine structure with high lateral and energy resolution was used for studies.

It was shown that the pores formed in the por-SiO_2/Si structure had rather sharp and almost vertical borders, without a transition layer. At the bottom of the pores was a substrate – a crystalline silicon wafer covered by a natural oxide with a thickness of ~ 2–3 nm. Despite the conducted ion irradiation and subsequent chemical etching the porous silicon oxide matrix did not undergo noticeable structural-phase transformations. Significant disordering and technological contamination were not revealed for the silicon wafer atoms at the bottom of the pores. Thus, ion-track technology in combination with irradiation followed by chemical etching is effective for obtaining arrays of the isolated submicron range pores of identical sizes. Por-

SiO_2/Si structures can be used as a convenient matrix for further controlled functionalization of the developed surface.

The extremely high efficiency of the PEEM photoemission electron microscopy method for study of a wide range of the objects characterized by composite structural-phase state of the surface layer with high accuracy and on a microscopic scale was demonstrated.

Acknowledgements

The reported study was funded by Russian Foundation for Basic Research according to the research project No 18-32-01046 and partially supported by the Ministry of Education and Science of the Russian Federation as the part of the state task for high education institution in the field of scientific activity for 2017-2020 – project No 16.8158.2017/8.9 (general XANES studies and results calibration).

The authors are grateful to the director and administration of the Helmholtz Zentrum Berlin, as well as to the Coordinators of the Russian-German laboratory and beamlines of the Helmholtz Zentrum Berlin BESSY II synchrotron.

Conflict of interests

The authors declare that they have no known competing financial interests or personal relationships that could have influenced the work reported in this paper.

References

1. Sinha D., Petrov A., Fink D., Fahrner W. R., Hoppe K., and Chandra A. Tempos structures with gold nanoclusters. *Radiation Effects and Defects in Solids*. 2004;159(8-9): 517–533. DOI: https://doi.org/10.1080/10420150412331304187

2. Kaniukov E. Yu., Ustarroz J., Yakimchuk D. V., Petrova M., Terryn H., Sivakov V., Petrov A. V. Tunable nanoporous silicon oxide templates by swift heavy ion tracks technology. *Nanotechnology*. 2016;27(11): 115305. DOI: https://doi.org/10.1088/0957-4484/27/11/115305

3. Ivanou D. K., Streltsov E. A., Fedotov A. K., Mazanik A. V., Fink D., Petrov A. Electrochemical deposition of PbSe and CdTe nanoparticles onto p-Si(100) wafers and into nanopores in SiO_2/Si(100) structure. *Thin Solid Films*. 2005;490(2): 154–160. DOI: https://doi.org/10.1016/j.tsf.2005.04.046

4. Ivanova Yu. A., Ivanou D. K., Fedotov A. K., Streltsov E. A., Demyanov S. E., Petrov A. V., Kaniukov E. Yu., Fink D. Electrochemical deposition of Ni and Cu onto monocrystalline n-Si(100) wafers and into nanopores in Si/SiO_2 template *J. Materials Science*. 2007;42(22): 9163-9169. DOI: https://doi.org/10.1007/s10853-007-1926-x

5. Fink D., Alegaonkar P. S., Petrov A. V., Wilhelm M., Szimkowiak P., Behar M., Sinha D., Fahrner W. R., Hoppe K., Chadderton L. T. Electrochemical deposition of Ni and Cu onto monocrystalline n-Si(100) wafers and into nanopores in Si/SiO_2 template. *Nucl. Instr. Meth B*. 2005;236(1–4): 11–20. DOI: https://doi.org/10.1016/j.nimb.2005.03.243

6. Mosier-Boss P. Review of SERS substrates for chemical sensing. *Nanomaterials*. 2017;7(6): 142. DOI: https://doi.org/10.3390/nano7060142

7. Jahn M., Patze S., Hidi I. J., Knipper R., Radu A. I., Muhlig A., Yuksel S., Peksa V., Weber K., Mayerhofer T., Cialla-May D., Popp J. Plasmonic nanostructures for surface enhanced spectroscopic methods. *Analyst*. 2016;141(3): 756–793. DOI: https://doi.org/10.1039/c5an02057c

8. Turishchev S. Yu., Parinova E. V., Pisliaruk A. K., Koyuda D. A., Yermukhamed D., Ming T., Ovsyannikov R., Smirnov D., Makarova A., Sivakov V. Surface deep profile synchrotron studies of mechanically modified top-down silicon nanowires array using ultrasoft X-ray absorption near edge structure spectroscopy. *Scientific Reports*. 2019;9(1): 8066. DOI: https://doi.org/10.1038/s41598-019-44555-y

9. Liu L., Sham T. K. The effect of thermal oxidation on the luminescence properties of nanostructured silicon. *Small*. 2012;8(15): 2371–2380. DOI: https://doi.org/10.1002/smll.201200175

10. Barranco A., Yubero F., Espinos J.P., Groening P., Gonzalez-Elipe A. R. Electronic state characterization of SiOx thin films prepared by evaporation. *J. Appl. Phys*. 2005;97(11): 113714. DOI: https://doi.org/10.1063/1.1927278

11. Parinova E. V., Fedotov A. K., Koyuda D. A., Fedotova J. A., Streltsov E. A., Malashchenok N. V., Ovsyannikov R., Turishchev S. Yu. The composite structures based on nickel rods in the matrix of silicon dioxide formation peculiarities study using synchrotron XANES in the electrons and photons yield registration modes. *Kondensirovannye sredy i mezhfaznye granitsy = Condensed Matter and Interphases*. 2019;21(1): 116–125. Available at: https://journals.vsu.ru/kcmf/article/view/726 (In Russ., abstract in Eng.)

12. Kleineberg U., Haindl G., Hutten A., Reiss G., Gullikson E.M., Jones M.S., Mrowka S., Rekawa S. B., Underwood J. H. Microcharacterization of the surface oxidation of Py/Cu multilayers by scanning X-ray absorption spectromicroscopy. *Appl. Phys. A*. 2001;73(4): 515–519. DOI: https://doi.org/10.1007/s003390100801

13. Schmahl G., Rudolph D. (eds) *X-Ray Microscopy*. Springer Series in Optical Sciences, vol 43. Berlin,

Heidelberg: Springer: 1984. DOI: https://doi.org/10.1007/978-3-540-38833-3_1

14. Polishchuk I., Bracha A. A., Bloch L., Levy D., Kozachkevich S., Etinger-Geller Y., Kauffmann Y., Burghammer M., Giacobbe C., Villanova J., Hendler G., Chang-Yu Sun, Giuffre A. J., Marcus M. A., Kundanati L., Zaslansky P., Pugno N. M., Gilbert G. P., Katsman A., Pokroy B. Coherently aligned nanoparticles within a biogenic single crystal: a biological prestressing strategy. *Science*. 2017;358(6368): 1294–1298. DOI: https://doi.org/10.1126/science.aaj2156

15. Kalegowda Y., Chan Y-L., Wei D-H., Harmer S. L. X-PEEM, XPS and ToF-SIMS characterisation of xanthate induced chalcopyrite flotation: Effect of pulp potential. *Surface Science*. 2015;635: 70–77. DOI: https://doi.org/10.1016/j.susc.2014.12.012

16. Turishchev S. Yu., Parinova E. V., Kronast F., Ovsyannikov R., Malashchenok N. V., Streltsov E. A., Ivanov D. K. and Fedotov A. K. Photoemission electron microscopy of arrays of submicron nickel rods in a silicon dioxide matrix. *Physics of the Solid State*. 2014;56(9): 1916–921. DOI: https://doi.org/10.1134/S1063783414090297

17. Turishchev S. Yu., Parinova E. V., Fedotova J. A., Mazanik A. V., Fedotov A. K., Apel P. Yu. Submicron Ni rods massives distributed in silicon dioxide matrix microscopic characterization. *Kondensirovannye sredy i mezhfaznye granitsy = Condensed Matter and Interphases*. 2013;15(1): 54–58. Available at: https://journals.vsu.ru/kcmf/article/view/878 (In Russ., abstract in Eng.)

18. Kasrai M., Lennard W. N., Brunner R. W., Bancroft G. M., Bardwell J. A., Tan K. H. Sampling depth of total electron and fluorescence measurements in Si L- and K-edge absorption spectroscopy. *Appl. Surf. Science*. 1996;99(4): 303–312. DOI: https://doi.org/10.1016/0169-4332(96)00454-0

19. Zimkina T. M., Fomichev V. A. *Ul'tramyagkaya rentgenovskaya spektroskopiya* [Ultrasoft X-Ray Spectroscopy]. Leningrad: LGU Publ.; 1971. 132 p. (In Russ.)

20. Stohr J. *NEXAFS Spectroscopy*. Berlin: Springer; 1996, 403 p.

21. Brown F. C., Rustgi O. P., Extreme ultraviolet transmission of crystalline and amorphous silicon. *Phys. Rev. Let.* 1972;28(8): 497–500. DOI: https://doi.org/10.1103/PhysRevLett.28.497

22. Turishchev S. Yu., Terekhov V. A., Parinova E. V., Korolik O. V., Mazanik A. V., Fedotov A. K. Surface modification and oxidation of Si wafers after low energy plasma treatment in hydrogen, helium and argon. *Materials Science in Semiconductor Processing*. 2013;16(6): 1377–1381. DOI: https://doi.org/10.1016/j.mssp.2013.04.020

23. Domashevskaya E. P., Terekhov V. A., Turishchev S. Yu., Khoviv D. A., Parinova E. V., Skryshevskii V. A., Gavril'chenko I. V. Peculiarities of electron-energy structure of surface layers of porous silicon formed on *p*-type substrates. *Inorganic Materials*. 2012;48(14): 1291–1297. DOI: https://doi.org/10.1134/S0020168512140063

Information about the authors

Elena V. Parinova, PhD in Physics and Mathematics, Researcher of the Joint Laboratory “Electronic Structure of Solids”, Voronezh State University, Voronezh, Russian Federation; e-mail: parinova@phys.vsu.ru. ORCID iD: https://orcid.org/0000-0003-2817-3547.

Dmitry Marchenko, PhD in Physics and Mathematics, Researcher of the Helmholtz Zentrum Berlin, Berlin, Germany; e-mail: marchenko.dmitry@gmail.com.

Aleksander K. Fedotov, DSc in Physics and Mathematics, Professor, Belarusian State University, Minsk, Belarus; e-mail: fedotov@bsu.by.

Dmitry A. Koyuda, Researcher Associate of the Joint Laboratory “Electronic Structure of Solids”, Voronezh State University, Voronezh, Russian Federation; e-mail: koyuda@phys.vsu.ru.

Julia A. Fedotova, DSc in Physics and Mathematics, Deputy Head, Institute for Nuclear Problems, Belarusian State University, Minsk, Belarus; e-mail: julia@hep.by. ORCID iD: https://orcid.org/0000-0002-4471-0552.

Ruslan Ovsyannikov, PhD, Scientist of the Helmholtz Zentrum Berlin, Berlin, Germany; e-mail: ovsyannikov@helmholtz-berlin.de. ORCID iD: https://orcid.org/0000-0001-6311-5516.

Sergey Yu. Turishchev, DSc in Physics and Mathematics, Associate Professor of the Solid State Physics and Nanostructures Department, Voronezh State University, Voronezh, Russia; e-mail: tsu@phys.vsu.ru. ORCID iD: https://orcid.org/0000-0003-3320-1979.

All authors have read and approved the final manuscript.

Translated by Valentina Mittova.
Edited and proofread by Simon Cox.

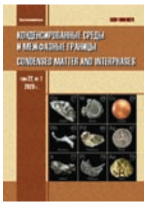

Condensed Matter and Interphases
(Kondensirovannye sredy i mezhfaznye granitsy)

Original articles

DOI: https://doi.org/10.17308/kcmf.2020.22/2533 eISSN 2687-0711
Received 11 February 2020
Accepted 15 March 2020

Study of the Thermal Conductivity of PbS, $CuFeS_2$, ZnS

© 2020 P. A. Popov[a], S. V. Kuznetsov[a], A. A. Krugovykh[a], N. V. Mitroshenkov[a], S. S. Balabanov[b], P. P. Fedorov✉,[c]

[a]*Bryansk State Academician I. G. Petrovski University,*
14 Bezhitskaya str., Bryansk 241036, Russian Federation

[b]*Devyatykh Institute of Chemistry of High Purity Substances of the Russian Academy of Sciences,*
49 ul. Tropinina, Nizhniy Novgorod 603137, Russian Federation

[c]*Prokhorov General Physics Institute of the Russian Academy of Science of the Russian Academy of Sciences,*
38 Vavilov str., Moscow 119991, Russian Federation

Abstract

It is necessary to know the values of the thermal conductivity coefficient of a semiconductor material to assess the possibility of its application as a thermoelectric. The thermal conductivity of natural minerals of galena (PbS), chalcopyrite ($CuFeS_2$), and ZnS ceramics was studied using the absolute stationary method of longitudinal heat flux in the range of 50–300 K.

The samples were homogeneous, had low impurity content (the chemical composition of the samples was controlled by the X-ray fluorescence method) and were characterized by high electrical resistivity ($\rho > 9\cdot10^{-2}$ Ohm·m at room temperature). It corresponds to the electronic component of the thermal conductivity $k_e < 1\cdot10^{-4}$ W/(m·K). The results of the thermal conductivity measurements are presented graphically and in tabular form. All the dependences are shown to be decreasing. The thermal conductivity values (W/(m·K)) at 50 K amount to 10.9 for PbS, 62 for $CuFeS_2$, and 73-98 for ZnS. At 300 K the values are 2.48, 10.5 and 18.6 – 18.8 W/(m·K), respectively.

All the studied materials have much worse thermal conductivity than pyrite (FeS_2). The obtained data was compared to the data available in literary sources. The temperature dependence of the thermal conductivity of galena is low, its low thermal conductivity is favourable for thermoelectric applications.

The thermal conductivity of chalcopyrite, which was detected in this study, appeared to be the highest among the corresponding literature data. The high thermal conductivity of zinc sulphide correlates to its wide variability depending on the structural features of the material. The temperature dependences of the mean free path of phonons were calculated. The values of this characteristic, estimated for the melting temperature, for PbS and for ZnS, in particular, significantly exceed the size of an elementary crystal cell, which is unusual.

Keywords: mineral, galena, chalcopyrite, ceramics, zinc sulphide, thermal conductivity, temperature dependence.

Funding: The study was carried out in the framework of and financially supported by State Assignment no. 3.8326.2017/8.9 and performed using the equipment provided by the Centre for Collective Use of Bryansk State University

For citation: Popov P. A., Kuznetsov S. V., Krugovykh A. A., Mitroshenkov N. V., Balabanov S. S., Fedorov P. P. Study of the thermal conductivity of PbS, $CuFeS_2$, ZnS. *Kondensirovannye sredy i mezhfaznye granitsy = Condensed Matter and Interphases.* 2020;22(1): 97–105. DOI: https://doi.org/10.17308/kcmf.2020.22/2533

✉ Pavel P. Fedorov, e-mail: ppfedorov@yandex.ru

1. Introduction

Sulphides are a vast class of compounds with a semiconductor nature of electrical conductivity [1]. It is necessary to know the values of the thermal conductivity coefficient to determine the scope of application of a solid material, including its application as a thermoelectric [2]. The feature of this characteristic is its considerable variability depending on temperature, impurity composition, and structural features of the material. The existing theoretical concepts of heat transfer processes do not allow reliable and accurate a priori estimates of thermal conductivity, and the experimental method is the only reliable way to determine it.

So far, a number of experimental studies researching the thermal conductivity of pyrite (FeS_2) [3], galena (PbS) [4–9], chalcopyrite ($CuFeS_2$) [10–14], and zinc sulphide [15–19] are known. The results obtained in these studies vary greatly in the absolute value of thermal conductivity as well as in the nature of its temperature dependence.

The aim of this study was to conduct an independent research of temperature dependence of the thermal conductivity of the natural minerals of galena and chalcopyrite (Ural region), and also of synthetic zinc sulphide ceramics.

2. Experimental

Thermal conductivity in the range of 50–300 K was measured using the absolute stationary method of longitudinal heat flux. The experimental equipment and methods are described in [20]. PbS and $CuFeS_2$ samples were about 9×9×24 mm in size, see Fig. 1, 2, ZnS – 5×5×40 mm. The measurement error for the value of thermal conductivity was no more than ± 5 %.

The chemical composition of the samples was controlled using the X-ray fluorescence method on “SUR-01 Renom”. The X-ray tube had copper anode, its voltage was 30 kV, and its current amounted to 4800 μA. A vanadium filter (100 μm) was used.

X-ray phase analysis was performed using the DRON-7 diffractometer with cobalt anode of the tube (λ_m = 1.79021 Å).

The PbS sample was cut from a homogeneous, monolithic piece of galena (see the photo on Fig. 1) with a mass of about 0.5 kg. The study of its chemical composition did not reveal any impurities with an accuracy of 0.01 wt. % with respect to Pb. In this regard, the resistivity measured at room temperature turned out to be $\rho = 9\cdot10^{-2}$ Ohm·m. This is a sufficiently high value that, using the Wiedemann-Franz-Lorentz law, the electronic component of thermal conductivity $k_e < 1\cdot10^{-4}$ W/(m·K) can be considered negligible compared to the experimentally determined.

The $CuFeS_2$ sample (see the photo on Fig. 2) was cut from a homogeneous, monolithic piece of chalcopyrite. The X-ray powder diffraction pattern of this sample is given in Fig. 3. It is almost identical to the diffraction patterns obtained in [13].

The results of the chalcopyrite sample chemical composition study are given in Table 1. The probes were taken from different parts of the sample.

Fig. 1. Photo of a galena monolith with a piece cut off for a sample

Fig. 2. Photo of a chalcopyrite monolith with a piece cut off for a sample

Table 1. Content (wt%) of chemical elements in the chalcopyrite sample

Element	Probe number			
	1	2	3	4
Fe	35.03	40.29	39.97	38.09
Cu	60.61	59.48	59.71	60.98
Zn	0.00	0.00	0.00	0.359
Ar	0.213	0.107	0.325	0.338
Mn	0.151	0.117	0.00	0.280

We can see little deviation in the chemical composition in terms of homogeneity and the low impurity content. The resistivity and electronic component of the thermal conductivity at room temperature were close to those determined for galena.

One of the zinc sulphide samples (OOO PromLab, Nizhniy Novgorod, Russia) was obtained using the method of chemical deposition from the gas phase by the reaction between zinc vapour and hydrogen sulphide. The sample carved for the thermal conductivity measurement was 5×5×40 mm in size, its major axis was perpendicular to the growth direction of the material. Zinc sulphide of the FLIR grade is a highly purified material (its chemical purity of metal impurities is 6N), its electrical conductivity is, consequently, very low. The average grain size is about 10 µm, the density is more that 99.99 % of the theoretical value. The material is suitable for optical applications in IR equipment and its transparency is in the range of 1–13 µm. In the visible range, ZnS scatters radiation due to the presence of an insignificant share of the hexagonal wurtzite phase alongside with the cubic sphalerite phase.

The second sample of zinc sulphide was submitted by A.G. Soldatov. (Minsk, Belarus, Scientific Production Centre of Material Studies) After fabrication for the measurement, it had dimensions of 8×6×20 mm. Its electrical conductivity was negligibly low.

3. Results and discussion

In Fig. 4 there is a temperature dependence graph of the thermal conductivity $k(T)$ of the galena sample. For comparison, the results obtained by the authors of other studies are also given (the coordinates of the $k(T)$ points were obtained by the method of digitization of the shown graphs).

It can be seen that in the region of nitrogen temperatures our $k(T)$ values are close to those obtained for one of the few synthesized single crystals in [9]. However, they are significantly lower than those given in [4]. Low-temperature thermal conductivity is known [21] to be particularly sensitive to various structural features of the material. It should be noted that extrapolation of our data to the T > 600 K area (dotted line in

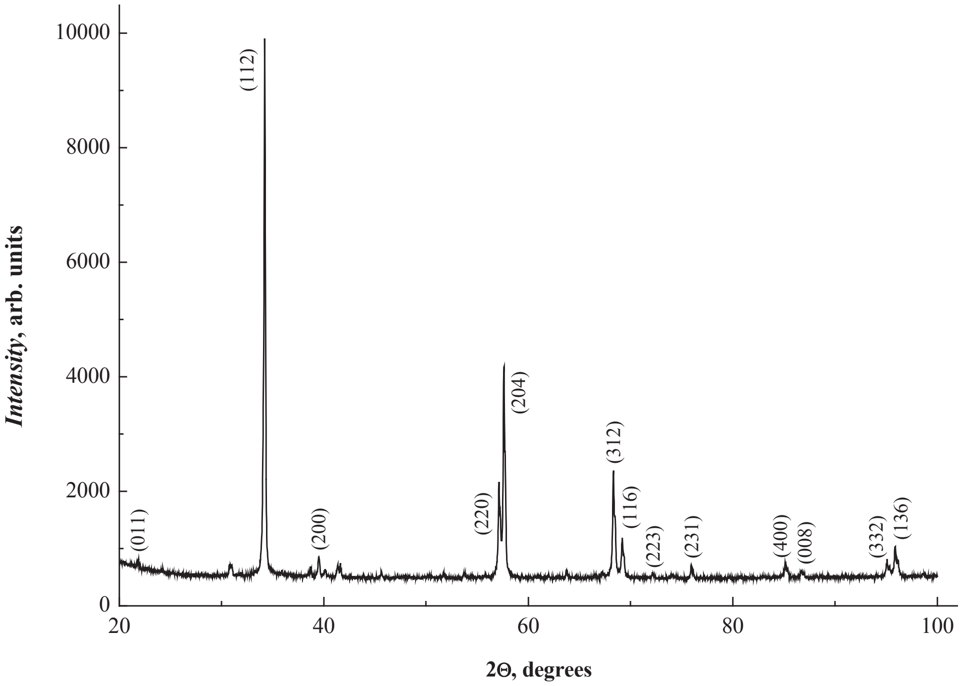

Fig. 3. Powder diffraction pattern of the chalcopyrite sample

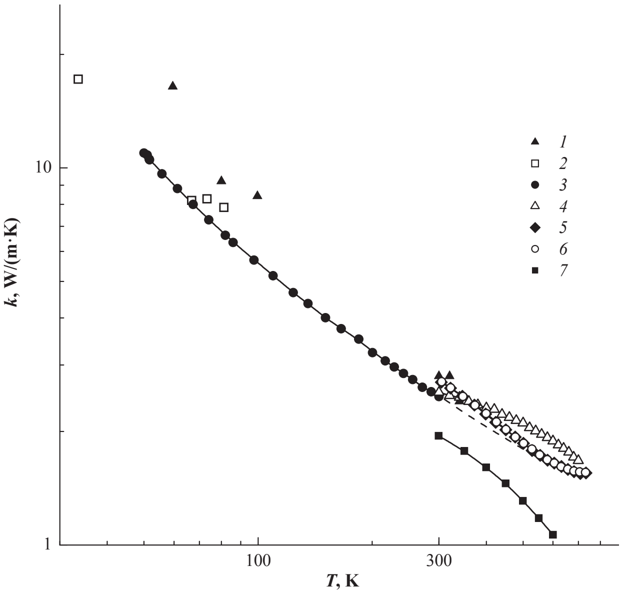

Fig. 4. Temperature dependence of the thermal conductivity of galena: (*1*) [4], (*2*) [9], our data (*3*), (*4*) [8], (*5*) [6], (*6*) [5], (*7*) [7]

Fig. 4) almost matches the data in [5, 6]. This allows us to evaluate the latter as common to the PbS crystalline matrix.

The $k(T)$ curve, obtained in [7], turns down. And in the sector of the highest temperatures when describing the behaviour of thermal conductivity by $k(T) \sim T^n$ function, the parameter value is $n > 1.1$, which seems doubtful, especially taking into consideration the very low values of thermal conductivity. In the aforementioned study the thermal conductivity was determined from the temperature conductivity using the temperature dependence of the heat capacity, calculated by Debye's theory. However, it is well known that actual behaviour of thermal conductivity of many compounds differs significantly from that of Debye's theory. Indeed, as shown in [22, 4], the PbS thermal conductivity increases sharply when the temperature reaches room values and continues to increase until the melting point [23].

The authors [8] used their own heat capacity data to define the behaviour of thermal conductivity, which, in our opinion, are in doubt. We associate the $k(T)$ downward curve, obtained in this study, with this circumstance.

In Fig. 5 there is a graph of temperature conductivity of the mean free path of phonons $l(T)$ in galena. It was determined from Debye's expression

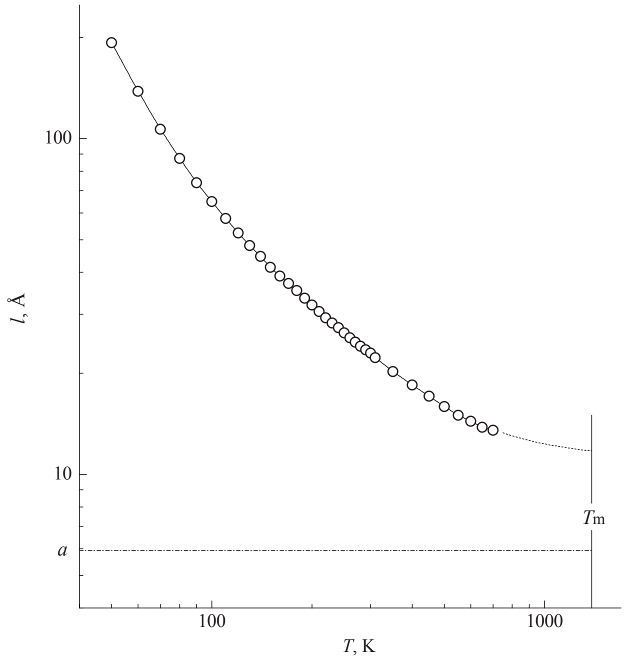

Fig. 5. Temperature dependence of the mean free path of phonons in PbS

$$k = C{\cdot}v{\cdot}l/3, \qquad (1)$$

where C is the thermal conductivity of a volume unit, v is the mean free path of phonons (sound). The phonon thermal conductivity model can be provisionally used not only for monocrystals but also for significantly disordered media. We used our data regarding thermal conductivity, their extrapolation to the area of high temperatures, thermal conductivity data from [4] and [23] for our calculations. The value $v = 2040$ m/s from [5] was taken as the average speed of sound.

It can be observed that the temperature dependence $l(T)$ is relatively low. In the 50–300 K temperature range the l value changes by only one order of magnitude. Such behaviour of $l(T)$ indicates a significant manifestation of phonon scattering, which is characteristic for the polycrystalline compound of the material. In the range of melting temperature, the value l, obtained by extrapolation, is 2 times higher than the parameter of the PbS crystal cell. Note that for many monocrystals with different matrix chemical compositions and structures, the minimum value of l, determined similarly, is close to the cell parameter or comparable to the average interstitial distance in the crystal [24, 25]. It seems to be difficult to explain the obtained large value of $l_{\min}$ for galena. As follows from the equation (1), the restrictions on the choice of heat capacity components effective for heat transfer can only lead to an increase in the calculated values of *l*. Bipolar contribution to the measured PbS conductivity noted in [5,6] in the context of our sample with small impurity content should be negligibly low.

The results of the thermal conductivity measurements of chalcopyrite are presented in Fig. 6. For comparison there are also given the data of other authors (the coordinates of the *k*(*T*) points were obtained by the digitization of the graphs in the figures).

It can be seen that the current data regarding the thermal conductivity of chalcopyrite varies significantly. The thermal conductivity of the natural sample examined at temperatures below room temperature is significantly higher (Fig. 6, curve *1*) than that of the synthesized samples. Taking into account the small impurity content it clearly indicates a lesser degree of disorder in the structure. The temperature behaviour of our graph *k*(*T*) is close to that defined in [12] (curve *4*).

Slowing down of the *k*(*T*) dependency decrease, revealed in [11] (curve *2*) is, apparently, due to the non-lattice contribution to the thermal conductivity. In study [13] the chalcopyrite sample synthesized by melting-annealing-sintering process was studied, which had Fe/Cu atomic ratio of 1.005. We used the heat capacity (Const(*T*) defined using Dulong–Petit law to calculate the thermal conductivity from the measured temperature conductivity. In fact, the heat capacity of chalcopyrite increases with temperature. According to the data in [26] it is close to the limit value of $3R×4 = 100$ (J/(mol·K) already at room temperature, which is far from melting temperature, and it continues to increase. These data were in good agreement with the high temperature results obtained in [27]. This is probably why the *k*(*T*) graph of the authors [13] (curve *6*) in our Fig. 6 with the selected scale has an unusual shape, in that it bends sharply downwards. In the range of room temperature, the exponent n in the expression $k(T) \sim T^{-n}$ is more than one and for the highest temperatures $n > 2$.

The results of the thermal conductivity measurement of the sample of $Cu_{25.43}Fe_{25.66}S_{48.91}$ [14] (curve *5*) are the closest to the data in [13]. In that study the authors took into account the experimentally determined temperature dependence of heat capacity. However, no numerical heat capacity data are given in that article.

A possible explanation for the great decrease in high temperature heat conductivity reported in [13, 14] may be the proximity to the Neel temperature $T_N = 823$ K [28, 29].

The authors of study [10] examined a polycrystal that did not undergo a complete annealing procedure after synthesis. The glass-like nature of the temperature dependence of its thermal conductivity (curve *3*)) is associated with the inhomogeneity of the sample. But the positioning of the two *k*(*T*) points close to room temperature raises questions about possible changes in the experimental method or the quality of the sample, and also about the shape of a part of the graph which can be extrapolated to the sector of elevated temperatures.

In Fig. 7 there is a graph of temperature dependence of the mean free path of phonons in the studied chalcopyrite sample in accordance with expression (1). The calorimetric data from [26, 27] were taken into account. The value

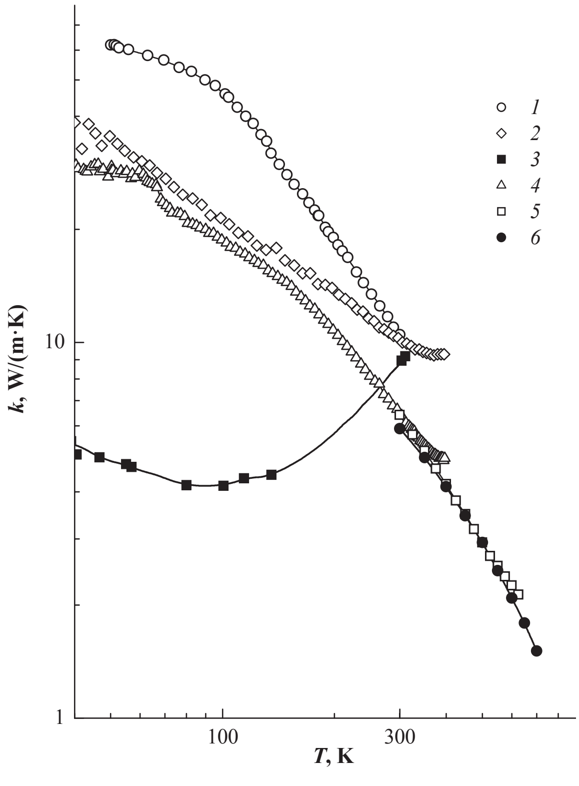

Fig. 6. Temperature dependence of the thermal conductivity of chalcopyrite: (*1*) our data, (*2*) [11], (*3*) [10], (*4*) [12], (*5*) [14], and (*6*) [13]

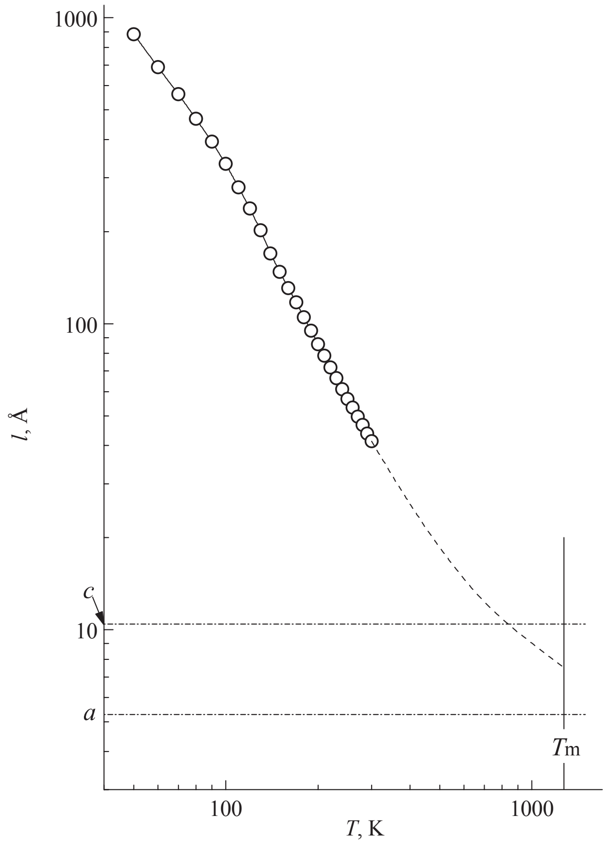

Fig. 7. Temperature dependence of the mean free path of phonons in chalcopyrite

v = 2040 m/s determined in [13] was taken as the average speed of phonons.

A slowdown of the growth of $l(T)$ in condition of the decrease in temperature from T = 100 K demonstrates the manifestation of phonon-defect scattering. In the range of room temperature, the $l(T)$ value decreases rapidly, namely in proportion to $T^{-1.6}$. Extrapolation of the graph to the melting temperate range of $CuFeS_2$ gives us the l_{min} value, which is an intermediate between the values of a and c parameters of the crystalline lattice of this compound.

The results of the thermal conductivity measurements of two ZnS samples are presented in Fig. 8. The zinc sulphide thermal conductivity data of other authors were also presented there (the numerical data of [16,17] were used, in other cases the coordinates of the $k(T)$ points were obtained by digitization of the curves presented in the figures in the articles).

Significant differences in the given graphs indicate strong sensitivity of the ZnS thermal conductivity to the impurity composition and structural features of the material. The $k(T)$ curves of monocrystalline ZnS samples studied in [15,18] are given above the other ones. Based on a slightly higher thermal conductivity in the sector of the lowest studied temperatures, it can be argued that the Luguevs [18] sample (Fig. 8, curve *1*) had the most perfect structure. Moreover, the polycrystalline ZnS sample [18] also demonstrates (curve *2*) a higher thermal conductivity at low temperatures than Slack's monocrystal [15] (curve *3*). In this regard, we note that phonon scattering at the boundaries of crystalline grains with cubic symmetry may be insignificant even at sub nitrogen temperatures [30]. In study [16] the object of the research was the natural mineral of sphalerite, which can explain the features of the obtained $k(T)$ dependence.

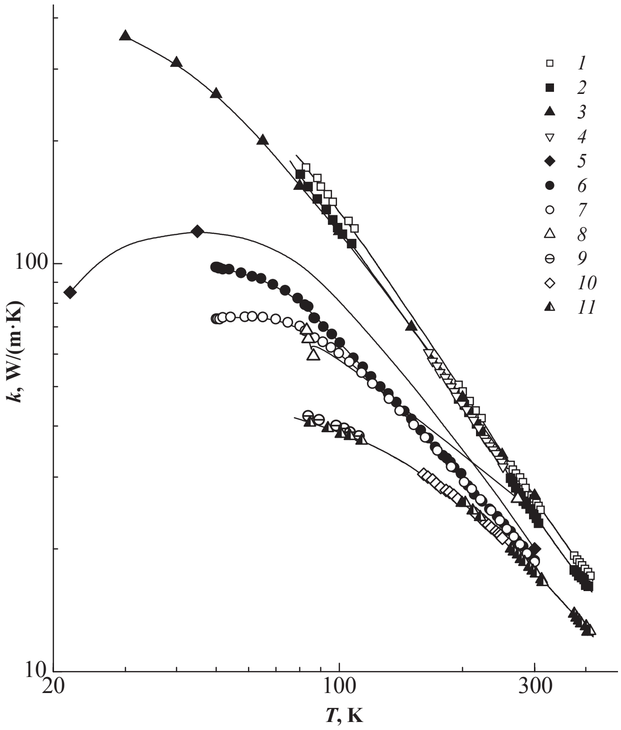

Fig. 8. Temperature dependence of the thermal conductivity of ZnS: (*1*), (*2*), (*4*), (*9*), (*10*), (*11*) [18], (*3*) [15], (*5*) [17], (*6*) and (*7*) our data, and (*8*) [16]

As for our samples, their $k(T)$ curves are located between the graphs for a monocrystal studied by Krueger [17] (curve *5*) and porous polycrystals from [18] (curves *9*, *10*, *11*). The $k(T)$ graphs that we obtained have indications of their reaching the low temperature maximum. It is known that with an increase in the structure defectiveness, this maximum decreases and usually shifts toward higher temperatures [21].

The lesser low temperature thermal conductivity of the sample by OOO PromLab (curve *7*), taking into consideration its chemical purity, can be explained by phonon scattering due to the presence of the hexagonal wurtzite phase in it.

In Fig. 9 there is a graph of temperature conductivity of the mean free path of phonons $l(T)$ in this sample. The calorimetric data from [31] were taken into account, the value of $v = 2.86$ km/s calculated using the elastic modules from [32] was taken as the average speed of sound.

It can be observed that in the temperature range of 100–300 K the obtained dependence is satisfactory described by the power function $T^{-1.61}$. Moreover, in the room temperature range, the value of l remains significant (~ 102 Å). Note that it is 2 times smaller than the l value determined in [18] by another method, provided that the difference in thermal conductivity is only ~ 1.5 times. Extrapolating our $l(T)$ graph to the ZnS melting temperature range gives us the value of $l_{\min}$ which is almost 4 times higher than the lattice parameter a. This circumstance seems to indicate the features of the phonon-phonon interaction in this compound.

The data presented in Table 2 demonstrate a contrasting difference in the values of the thermal conductivity coefficient of the studied compounds. We should note the high value of the thermal conductivity of chalcopyrite, which indicates the ordered arrangement of cations in the lattice. The very low thermal conductivity of galena attracts attention, being unusual for compounds with a simple lattice (such as sodium chloride). This property means it is favourable for the development of thermoelectric materials. The high thermal conductivity of zinc sulphide favours its use in photonics.

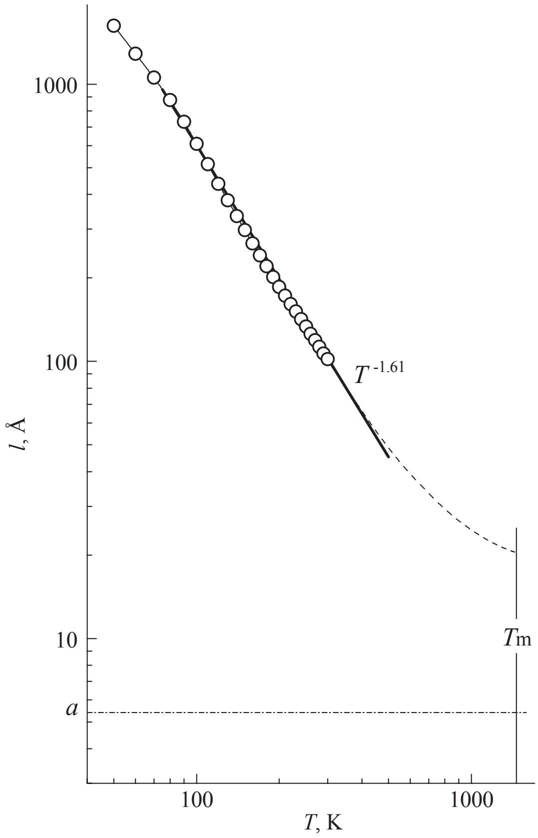

Fig. 9. Temperature dependence of the mean free path of phonons in the ZnS sample

4. Conclusion

Thus, experimental data were obtained that substantially complement the concepts of the thermal conductivity of the natural minerals of chalcopyrite and galena, as well as synthetic ceramics of zinc sulphide. These data indicate the fundamental prospects of natural sources of raw materials for instrument engineering. The low thermal conductivity of galena means its use is favourable for thermoelectric applications. On the other hand, the wide variability of the thermal conductivity coefficient of these compounds depending on the state of the material was revealed. In the future, it is planned to expand the

Table 2. Thermal conductivity values of the studied sulphides at different temperatures

T, K	PbS	$CuFeS_2$	ZnS PromLab	ZnS (Minsk)	FeS_2 [3]
50	10.9	62	73.2	98	900
100	5.6	46.5	60.0	64	207
150	4.02	27.8	40.9	41.6	106
200	3.27	18.8	29.5	30.0	73
250	2.79	13.6	23.1	23.3	58
300	2.48	10.5	18.6	18.8	48

research into the thermal conductivity of natural sulphide minerals from various deposits.

Acknowledgements

The authors are grateful to A. G. Soldatov for providing a sample of ZnS for the research.

Conflict of interests

The authors declare that they have no known competing financial interests or personal relationships that could have influenced the work reported in this paper.

References

1. Samofalova T. V., Semenov V. N., Nituta A. N., Zvyagina O. V., Proskina E. Yu. Synthesis and properties of the CdS–ZnS films doped by copper ions. *Kondensirovannye sredy i mezhfaznye granitsy = Condensed Matter and Interphases*. 2018;20(3): 452–459. DOI: https://doi.org/10.17308/kcmf.2018.20/582 (In Russ., abstract in Eng.)

2. Ioffe A. F., Ioffe A. V. Teploprovodnost' tverdykh rastvorov poluprovodnikov [Thermal conductivity of solid solutions of semiconductors]. *Physics of the Solid State*. 1960;2(5): 781–792. Available at: http://books.e-heritage.ru/book/10085074 (In Russ.)

3. Popov P. A., Kuznetsov S. V., Fedorov P. P. Thermal conductivity of FeS_2 pyrite crystals in the temperature range 50–300 K. *Crystallography Reports*. 2013;58(2): 319–321. DOI: https://doi.org/10.1134/S1063774513020223

4. Wei L., Chen J.-F., He Q.-Y., Teng W. Study of lattice thermal conductivity of PbS. *Journal of Alloys and Compounds*. 2014;584: 381–384. DOI: https://doi.org/10.1016/j.jallcom.2013.09.081

5. Pei Y.-l., Liu Y. Electrical and thermal transport properties of Pb-based chalcogenides: PbTe, PbSe, and PbS. *Journal of Alloys and Compounds*. 2012;514: 40–44. DOI: https://doi.org/10.1016/j.jallcom.2011.10.036

6. Zhao L. D., Lo Sh., He J., Li H., Biswas K, Androulakis J., Wu C.-I., Hogan T. P., Chung D.-Y., Dravid V. P., Kanatzidis M. G. High performance thermoelectrics from earth-abundant materials: enhanced figure of merit in PbS by second phase nanostructures. *J. Am. Chem. Soc.* 2011;133: 20476–20487. DOI: https://doi.org/10.1021/ja208658w

7. Zhang H., Wang H., Zhu H., Li H., Su T., Li Sh., Hu M., Fan H. Hydrothermal synthesis and thermoelectric properties of PbS. *Materials Science-Poland*. 2016;34(4): 754–759 DOI: https://doi.org/10.1515/msp-2016-0098

8. El-Sharkawy A. A., Abou El-Azm A. M., Kenawy M. I., Hillal A. S., Abu-Basha H. M. Thermophysical properties of polycrystalline PbS, PbSe, and PbTe in the temperature range 300–700 K. *Int. J. Thermophys*. 1983;4(3): 261–269. DOI: https://doi.org/10.1007/BF00502357

9. Greig D. Thermoelectricity and thermal conductivity in the lead sulfide group of semiconductors. *Phys. Rev.* 1960;120(2): 358–365. DOI: https://doi.org/10.1103/PhysRev.120.358

10. Popov V. V., Kizhaev S. A., Rud' Y. V. Magnetic and thermal properties of $CuFeS_2$ at low temperatures. *Physics of the Solid State*. 2011;53(1): 71–75. DOI: https://doi.org/10.1134/S1063783411010240

11. Tsujii N., Mori T. High thermoelectric power factor in a carrier-doped magnetic semiconductor $CuFeS_2$. *Appl. Phys. Express*. 2013;6(4): 043001-4. DOI: https://doi.org/10.7567/APEX.6.043001

12. Tsujii N. Possible enhancement of thermoelectric properties by use of a magnetic semiconductor: carrier-doped chalcopyrite $Cu_{1-x}Fe_{1+x}S_2$. *J. Electron. Mater.* 2013;42(7): 1974–1977. DOI: https://doi.org/10.1007/s11664-013-2485-3

13. Li Y., Zhang T., Qin Y., Day T., Snyder G. J., Shi X., Chen L. Thermoelectric transport properties of diamond-like $Cu_{1-x}Fe_{1+x}S_2$ tetrahedral compounds. *Journal of Applied Physics*. 2014;116: 203705-8. DOI: https://doi.org/10.1063/1.4902849

14. Xie H., Su X., Yan Y., Liu W., Chen L., Fu J., Yang J., Uher C., Tang X. Thermoelectric performance of $CuFeS_{2+2x}$ composites prepared by rapid thermal explosion. *NPG Asia Mater.* 2017;9: e390(12). DOI: https://doi.org/ 10.1038/am.2017.80

15. Slack G. A. Thermal conductivity of II–VI compounds and phonon scattering by Fe^{2+} Impurities. *Physical Review*. 1972;6(10): 3791–3800. DOI: https://doi.org/10.1103/PhysRevB.6.3791

16. Eucken A., Kuhn G. New Measurement of heat of conductivity of solid crystalline substances at 0° and – 190 °C. *Z. Physik. Chem., A*. 1928;134(1): 193–219. DOI: https://doi.org/ 10.1515/zpch-1928-13416

17. Krüger R. Wärmeleitfähigkeit und spezifische Wärmekapazität von ZnS und CdS im Temperaturbereich von 20 K bis 300 K. *Thesis*. Tecnische Universitat Berlin; 1969. 93 p. (in German).

18. Lugueva N. V., Luguev S. M. The influence of structural features on the thermal conductivity of polycrystalline zinc sulfide. *Physics of the Solid State*. 2002;4(2): 260–265. DOI: https://doi.org/10.1134/1.1451010

19. Lugueva N. V., Luguev S. M. The effect of structural defects on the thermal conductivity of ZnS, ZnSe, and CdTe polycrystals. *High Temperature*. 2004;42: 54–59.DOI: https://doi.org/10.1023/B:HITE.0000020091.31679.b0

20. Popov P. A., Sidorov A. A., Kul'chenkov E. A., Anishchenko A. M., Avetisov I. Sh., Sorokin N. I., Fedorov P. P. Thermal conductivity and expansion of PbF_2 single crystal. *Ionics*. 2017;23(1): 233–239. DOI: https://doi.org/10.1007/s11581-016-1802-2

21. Berman R. *Thermal Conduction in Solids*. Oxford: Clarendon; 1976. 193 p.

22. Parkinson D. H., Quarrington J. E. The molar heats of lead sulphide, selenide and telluride in the

temperature range 20°K to 260°K. *Proceedings of the Physical Society. Section A*. 1954;67(7): 569–579. DOI: https://doi.org/ 10.1088/0370-1298/67/7/301

23. Blachnik R., Igel R. Thermodynamische eigenschaften von IV–VI-verbindungen: bleichalkogenide/Thermodynamic properties of IV–VI-compounds: Leadchalcogenides. *Z. Naturforsch*. 1974;29B: 625–629. DOI: https://doi.org/ 10.1515/znb-1974-9-1012

24. Popov P. A., Matovnikov A. V., Moiseev N. V., Buchinskaya I. I., Karimov D. N., Sorokin N. I., Sul'yanova E. A., Sobolev B. P., Krutov M. A. Thermophysical characteristics of $Pb_{0.679}Cd_{0.321}F_2$ solid-solution crystals. *Crystallography Reports*. 2015;60(1): 111–115. DOI: https://doi.org/10.1134/S1063774515010174

25. Popov P. A. Teploprovodnost' tverdotel'nykh opticheskikh materialov na osnove neorganicheskikh oksidov i ftoridov [Thermal conductivity of solid-state optical materials based on inorganic oxides and fluorides]. *Diss. DSc in physics and mathematics*. Moscow: Bauman MSTU Publ.; 2015. 532 p. Available at: https://elibrary.ru/download/elibrary_25834920_35812051.pdf (In Russ.)

26. Robie R. A., Wiggins L. B., Barton P. B., Hemingway B.S. Low-temperature heat capacity and entropy of chalcopyrite ($CuFeS_2$): estimates of the standard molar enthalpy and Gibbs free energy of formation of chalcopyrite and bornite (Cu_5FeS_4). *J. Chem., Thermodynamics*. 1985;17(5): 481–488. DOI: https://doi.org/ 10.1016/0021-9614(85)90147-8

27. Pankratz L. B., King E. G. *High-temperature enthalpies and entropies of chalcopyrite and bornite*. U.S. Bur. Mines: Rep Investig 7435: 1–10.

28. Berthebaud D., Lebedev O. I., Maignan A. Thermoelectric properties of *n*-type cobalt doped chalcopyrite $Cu_{1-x}Co_xFeS_2$ and *p*-type eskebornite $CuFeSe_2$. *J. Materiomics*. 2015;1(1): 68–74. DOI: https://doi.org/10.1016/j.jmat.2015.03.007

29. Sato K., Harada Y., Taguchi M., Shin S., Fujimori A. Characterization of Fe 3d states in $CuFeS_2$ by resonant X-ray emission spectroscopy. *Phys. Stat. Solid. A*. 2009;206: 1096–1100. DOI: https://doi.org/10.1002/pssa.200881196

30. Popov P. A., Dukel'skiy K. V., Mironov I. A., Smirnov A. N., Smolyanskiy P. L., Fedorov P. P., Osiko V. V., Basiev T. T. Thermal conductivity of CaF_2 optical ceramic. *Doklady Physics*. 2007;52(1): 7–9. DOI: https://doi.org/10.1134/S1028335807010028

31. *Tablitsy fizicheskikh velichin* [Tables of physical quantities]. Handbook / ed. I. K. Kikonin. Moscow, Atomizdat; 1976 1008 p. (In Russ.)

32. Khenata R., Bouhemadou A., Sahnoun M., Reshak A. H., Baltache H., M. Rabah M. Elastic, electronic and optical properties of ZnS, ZnSe and ZnTe under pressure. *Computational Materials Science*. 2006;38(1): 29–38. DOI: https://doi.org/10.1016/j.commatsci.2006.01.013

Information about the authors

Pavel A. Popov, DSc in Physics and Mathematics, Professor, Bryansk State Academician I.G. Petrovski University, Bryansk, Russian Federation, e-mail: tfbgubry@mail.ru. ORCID iD: https://orcid.org/0000-0001-7555-1390.

Sergey V. Kuznetsov, PhD in Chemistry, Head of Chemistry Department, Bryansk State Academician I. G. Petrovski University, Bryansk, Russian Federation, e-mail: passivoxid@mail.ru. ORCID iD: https://orcid.org/0000-0002-6885-6433.

Alexander A. Krugovykh, postgraduate student, Bryansk State Academician I. G. Petrovski University, Bryansk, Russian Federation, e-mail: aleksander,kru@yandex.ru. ORCID iD: https://orcid.org/0000-0002-3063-4552.

Nikolay V. Mitroshenkov, PhD in Physics and Mathematics, senior lecturer, Bryansk State Academician I. G. Petrovski University, Bryansk, Russian Federation, e-mail:weerm@yandex.ru. ORCID iD: https://orcid.org/0000-0002-4418-9613.

Stanislav S. Balabanov, PhD in Chemistry, leading research fellow, Devyatykh Institute of Chemistry of High Purity Substances of the Russian Academy of Sciences, Nizhniy Novgorod, Russian Federation, e-mail: balabanov@ihps,nnov.ru. ORCID iD: https://orcid.org/0000-0003-1920-9894.

Pavel P. Fedorov, DSc in Chemistry, Professor, Chief Researcher at the Prokhorov General Physics Institute of the Russian Academy of Science, Moscow, Russian Federation; e-mail: ppfedorov@yandex.ru. ORCID iD: https://orcid.org/0000-0002-2918-3926.

All authors have read and approved the final manuscript.

Translated by Anastasiia Ananeva.
Edited and proofread by Simon Cox.

Condensed Matter and Interphases
(Kondensirovannye sredy i mezhfaznye granitsy)

Original articles

DOI: https://doi.org/10.17308/kcmf.2020.22/2534 eISSN 2687-0711
Received 02 February 2020
Accepted 15 February 2020

Phase Equilibria in the Sn–As–Sb System with Tin Concentrations of Less than 50 mol%

© 2019 T. P. Sushkova✉, G. V. Semenova, A. V. Sheveljukhina, S. V. Kannykin, E. Yu. Proskurina, A. V. Nerushev

Voronezh State University 1 Universitetskaya pl., Voronezh 394018, Russian Federation

Abstract

Tin- and antimony-based alloys, including SnSb and other compounds of the $A^{IV}B^{V}$ type, are used for the production of anodes for Li^+- and Na^+ion batteries. Multicomponent solid solutions allow varying the properties of the material and improve the technical characteristics of the anodes. There is very little information in the literature about solid phase solubility in the Sn–As–Sb system, and the phase diagram of the system has not been studied yet. The aim of this paper was to study the polythermal sections SnAs–Sb and SnAs–SnSb using the X-ray diffraction analysis (XRD) and differential thermal analysis (DTA), as well as to construct a phase equilibria scheme for the Sn–As–Sb system with the range of tin concentrations of less than 50 mol%.

The alloys of the polythermal sections SnAs–Sb and SnAs–SnSb were obtained from pre-synthesized binary compounds and then subjected to homogenizing annealing. The obtained powdered samples were then investigated using differential thermal analysis (DTA) and X-ray diffraction analysis (XRD).

The XRD results showed that all the studied alloys were heterophase mixtures of solid solutions (SnAs), (SnSb) and α', where α' is a solid solution of tin in the $As_{1-x}Sb_x$ phase. The concentration range of solid solutions based on binary compounds at room temperature was below 10 mol %. The DTA demonstrated that in several alloys of the two sections the first endothermic effect was observed at the same temperature (393 ± 2 °C). This temperature corresponds to the peritectic process involving the above-mentioned phases: $L + \alpha' \leftrightarrow (SnAs) + (SnSb)$.

Using the DTA method and the XRD data, T–x diagrams of polythermal sections SnAs–Sb and SnAs–SnSb were constructed. The coordinates of the invariant peritectic equilibrium $L + \alpha' \leftrightarrow (SnAs) + (SnSb)$ were determined; a scheme of phase equilibria in the Sn–As–Sb system with the range of tin concentrations of less than 50 mol % was proposed. To construct a complete scheme of phase equilibria in the ternary system, it is necessary to further investigate the SnAs–Sn_4Sb_3 and Sn_4As_3–Sn_4Sb_3sections.

Keywords: Sn–As–Sb system, solid solutions, phase equilibria.

For citation: Sushkova T. P., Semenova G. V., Sheveljuhina A. V., Kannykin S. V., Proskurina E. Yu., Nerushev A. V. Phase equilibria in the system Sn–As–Sb with tin concentrations of less than 50 mol%. *Kondensirovannye sredy i mezhfaznye granitsy = Condensed Matter and Interphases*. 2020; 22(1): 106–115. DOI: https://doi.org/10.17308/kcmf.2020.22/2534

1. Introduction

The latest technological advancements stimulate the research and development of new high-energy, reliable, and long lifespan devices for energy conversion and storage. Owing to their natural abundance, low cost, and environmental benignity, sodium- and potassium-ion batteries are a promising alternative to commonly used lithium-ion batteries [1–3]. However, the low energy density and poor life cycle stability limit their commercial applications [2, 4]. The development of high-performance electrode materials is one of the key issues in the production of next-generation alkali-ion batteries.

Anodes based on alloys including Si, Ge, Sn, P, As, Sb, and Bi, have been actively investigated over the past few years [2, 4–22]. The intermetallic compound SnSb is one of the best materials for the production of anodes for Li^+-ion batteries and is a

---

✉ Tatiana P. Sushkova, e-mail: sushtp@yandex.ru

promising material for the production of Na^+-ion batteries [4–10]. There are two reasons for this. First, SnSb contains two elements active toward Li. Hence, the uptake and release of lithium ions occurs in the presence of two lithium phases. The formation of a more stable compound of lithium and antimony Li_3Sb results in an increase in volume, which is buffered by the ductile phase of tin. This prevents any significant alterations in the volume that may lead to the decomposition of the anode material [5–7]. Second, the SnSb phase has a layered crystalline structure (rhombohedral lattice, space group R-3m) [23, 24], which allows for easy intercalation of of ions of alkali metals into the interlayer space.

Some other compounds of type $A^{IV}B^{V}$ also have layered structures [25–27], and were tested as anode materials and intercalates [11–22, 28]. For instance, tin phosphide Sn_4P_3 has the same crystal lattice [26] as SnSb, and is one of the best anode materials for Li^+- and Na^+-ion batteries [11–16].

One of the ways to enhance the technical characteristics of anodes is to increase the number of elements in the system and to use solid solutions based on pure compounds, rather than the compounds themselves. Modifying the composition of a solid solution we can significantly extend the functional characteristics of the material. This means that it is important to analyse the nature of phase equilibria in multicomponent systems. It was determined that a continuous series of solid solutions Sn_4P_3–Sn_4As_3 and substitutional bounded solid solutions based on SnAs and SnP_3 [29–32] is formed in the system Sn–As–P. Taking into account that Sn_4P_3, Sn_4As_3, Sn_4Sb_3 and SnSb have identical crystal lattices [24–26], while phosphorus, arsenic, and antimony are electronic analogues, and the atoms of As and Sb are close in size (the system As–Sb demonstrates complete miscibility [33]), we can expect the formation of ternary solid solutions in the system Sn–As–Sb as well.

To date the phase diagram of this system has not been well studied. [34] mentions that the earliest study, published in 1919, suggested the possibility of existence of a ternary chemical compound, but its crystalline structure was not determined; later studies did not confirm this suggestion but indicated high miscibility of rhombohedral SnSb and cubic SnAs. It is therefore important to study the phase equilibria in the ternary system Sn–As–Sb.

The binary systems limiting the ternary system Sn–As–Sb, contain four chemical compounds. Arsenide Sn_4As_3 decomposes peritectically, while SnAs melts congruently [35]. The composition and structure of the two intermediate phases of the system Sn–Sb still cause a lot of controversy. All the previously published versions of the phase diagram of Sn–Sb are thoroughly analysed in [23]. In this study, we used the phase diagram described in [24], which is based on a rigorously conducted experiment using a set of modern research methods. According to [24], SnSb and Sn_4Sb_3 have incongruently melting phases with wide homogeneity regions. Therefore, none of the sections of the studied ternary system can be quasi-binary.

The aim of this paper was to study the polythermal sections SnAs–Sb and SnAs–SnSb using X-ray phase analysis (XRD) and differential thermal analysis (DTA) and to construct a phase equilibria scheme for the Sn–As–Sb system with the range of tin concentrations of less than 50 mol%.

2. Experimental

The alloys whose compositions correspond to the polythermal sections SnAs–Sb and SnAs–SnSb were obtained in two stages. The binary phases were preliminary obtained by means of direct melting of simple chemical substances: Sn-5N tin (99.999 %), As-5N arsenic (99.9997 %), and Sb-000 antimony (99.99%). Arsenic was preliminary purified from oxides by vacuum sublimation. The samples were weighed using electronic scales AR2140 (measurement error $\pm 1 \cdot 10^{-3}$ g). The alloys were synthesized in quartz ampoules vacuumed to the residual pressure of $5 \cdot 10^{-4}$ hPa. The three-component samples underwent homogenizing annealing at 300 °C for 150 hours. The samples were then cooled in the furnace.

X-ray phase analysis was performed using an ARLX’TRA diffractometer with Bragg–Brentano Θ–Θ focusing geometry. The source of radiation was an X-ray tube with a copper anode which had the following characteristics: maximum capacity – 2200 W; $\lambda(\text{Cu-}K_{\alpha1}) = 0.1541$ nm; $\lambda(\text{Cu-}K_{\alpha2}) = 0.1544$ nm. The X-ray patterns were made with a step size of 0.04° and a counting time of 3 seconds per step. The error for determining the interplanar distances d_{hkl} was below $5 \cdot 10^{-4}$ nm. The obtained patterns were interpreted using the Powder Diffraction File of the International Centre for Diffraction Data (ICDD PDF-2, 2012).

Differential thermal analysis (DTA) was performed using a furnace with a programmed heating rate of 5 deg./min and chromel-alumel thermocouples. The signal received from the thermocouples was digitized and processed by the MasterSCADA software package. The reference sample was calcined aluminium oxide placed in a Stepanov quartz vacuumed vessel of approximately the same size as the quartz ampoules containing the studied substances.

The calibration benchmarks for the system were pure substances: tin (232.1 °C), tellurium (449.7 °C), and antimony (630.9 °C) [36]. The error for temperature measurement was below ±2°. Since the alloys of the studied system have a tendency to undercool, the temperature of phase transformations was determined by the heating curves.

3. Results and discussion

Fig. 1 demonstrates X-ray powder diffraction patterns of certain alloys of the polythermal section SnAs–Sb. When the concentrations of antimony in the samples are low, the diffractograms show peaks attributable to three phases: solid solutions based on tin monoseride (SnAs) and antimony monoseride (SnSb), and tin solid solution in the phase $As_{1-x}Sb_x$ (α′). Since the alloy containing 10 mol% of Sb was not single-phase (Fig. 1a), we can conclude that the concentration range of the SnAs-based solid solution along the section SnAs–Sb at room temperature is below 10 mol%.

The peak shift occurring due to the alteration of the alloy compositions indicates the formation of a SnAs-based solid solution. It is even better demonstrated by the increase in the interplanar distances and the cubic lattice parameter (Table 1). The samples with antimony concentrations of less than 50 % demonstrated few (SnAs) peaks which were of very low intensity, since (SnAs) is formed in these alloys only during secondary or tertiary crystallization and in very small quantities.

The lines corresponding to the solid solution (SnSb) and shifted toward greater angles as a result of substitution of antimony atoms with smaller arsenic atoms, were observed in the X-ray powder diffraction patterns of all the samples.

For all the samples, the 100% intensity line corresponded to the solid solution α′. The number of peaks of this phase increased with higher concentrations of antimony in the alloys. A significant shift of the lines following the alteration of the composition of the samples indicated a significant difference in the composition of this phase. This resulted from the change in the direction of the connodes connecting the melting point and the composition of the crystallised α′-phase.

Table 1. Interplanar distances (*d*, nm) and the lattice parameter (*a*, nm) of the SnAs-based solid solution present in the alloys of the section SnAs–Sb

SnAs		The composition (mol. f. Sb) of the alloys of the section SnAs– Sb				
hkl	*d*	0.10	0.20	0.30	0.40	0.50
111	0.3306	0.3308				
200	0.2862	0.2869				
220	0.2024	0.2042	0.2054	0.2045	0.2045	
311	0.1726	0.1730	0.1749	0.1752		
222	0.1652	0.1655		0.1686		
400	0.1431	0.1433	0.1470		0.1473	0.1474
331	0.1312	0.1319	0.1332	0.1332	0.1332	0.1349
420	0.1280	0.1281		0.1299		
422	0.1168	0.1170	0.1198	0.1198	0.1196	
511	0.1101	0.1102	0.1113	0.1134		
Lattice parameter, *a*	0.5725	0.5735	0.5799	0.5824	0.5900	0.5977

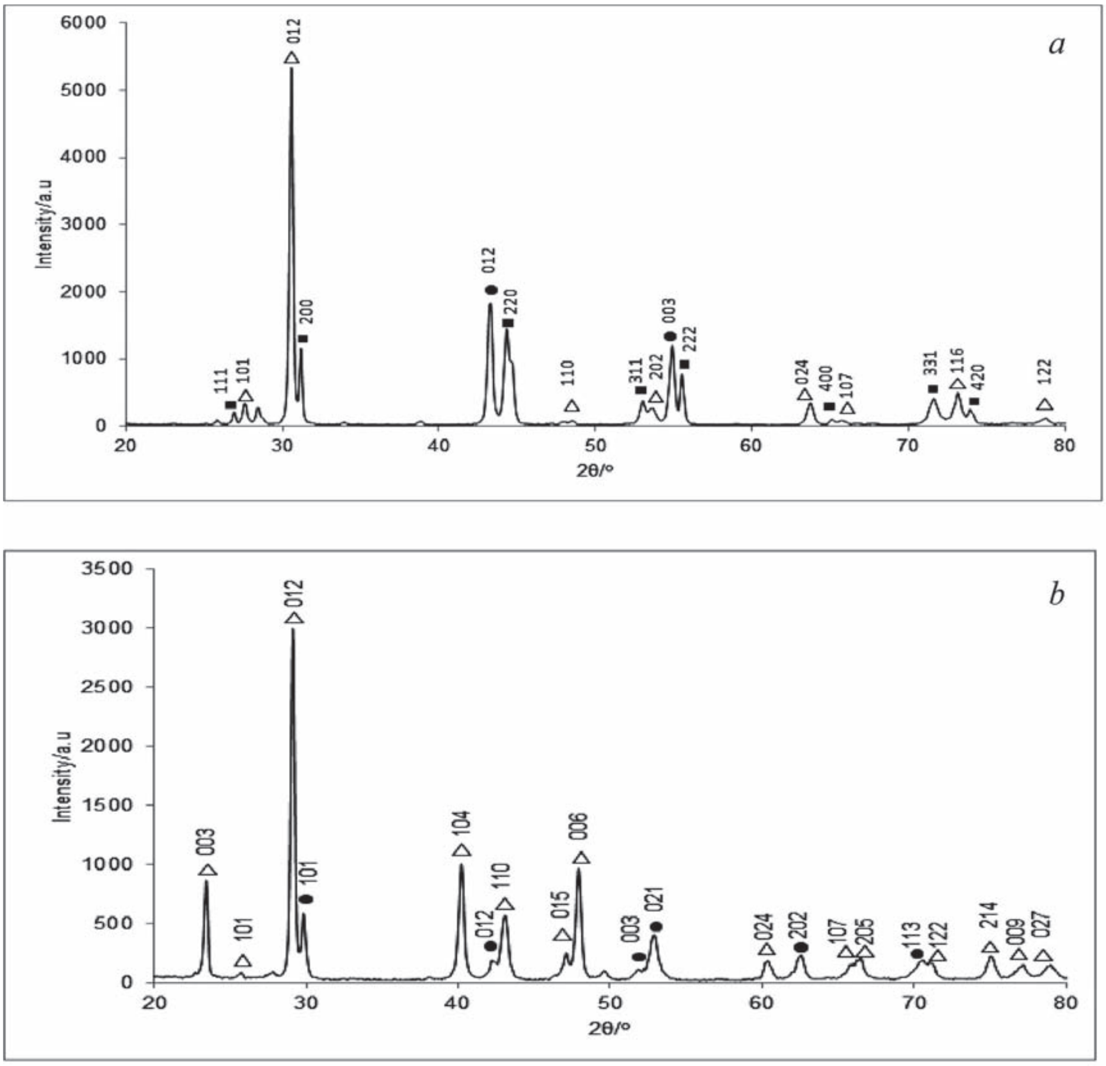

Fig. 1. X-ray powder diffraction patterns of the polythermal section SnAs–Sb: a – 0.10, b – 0.70 mol.f. Sb. Designations: ● – (SnSb), ■ – (SnAs), Δ – α′

The study of the second polythermal section SnAs–SnSb by means of XRD analysis demonstrated that the samples also contained three solid solutions: (SnAs), (SnSb), and α′ (Fig. 2). (SnAs) peaks were dominant in the samples with less then 20 mol% of SnSb (Fig. 2a). Then their number and intensity decreased, and the most intense lines corresponded to the solid solution (SnSb) (Fig. 2b). Table 2 presents the calculations of the lattice parameters of the solid solution based on tin monoseride. It is impossible to evaluate the composition of the solid solution using Vegard's law, since SnAs and SnSb have crystal lattices of different types.

The peaks of phase α′ are present in the X-ray powder diffraction patterns of all the samples, but their number and intensity are relatively small. Judging by the absence of single-phase alloys, we can conclude that the solid phase solubility along the section SnAs–SnSb at room temperature is below 5 mol%.

Differential thermal analysis demonstrated that in several samples of the studied sections the first endothermic effect was observed at nearly the same temperature of 393±2 °C (Fig. 3). In order to interpret the experimental results of the DTA correctly and construct *T-x* diagrams of the sections, we analysed the crystallization processes of the alloys.

Fig. 4 shows the representation of the *T-x-y* diagram of the ternary system limited by binary systems. The polythermal section SnAs–Sb intersects the fields of primary crystallization of the SnAs-based solid solution and the solid solution α′. For the alloys whose compositions correspond to the *ab*segment,

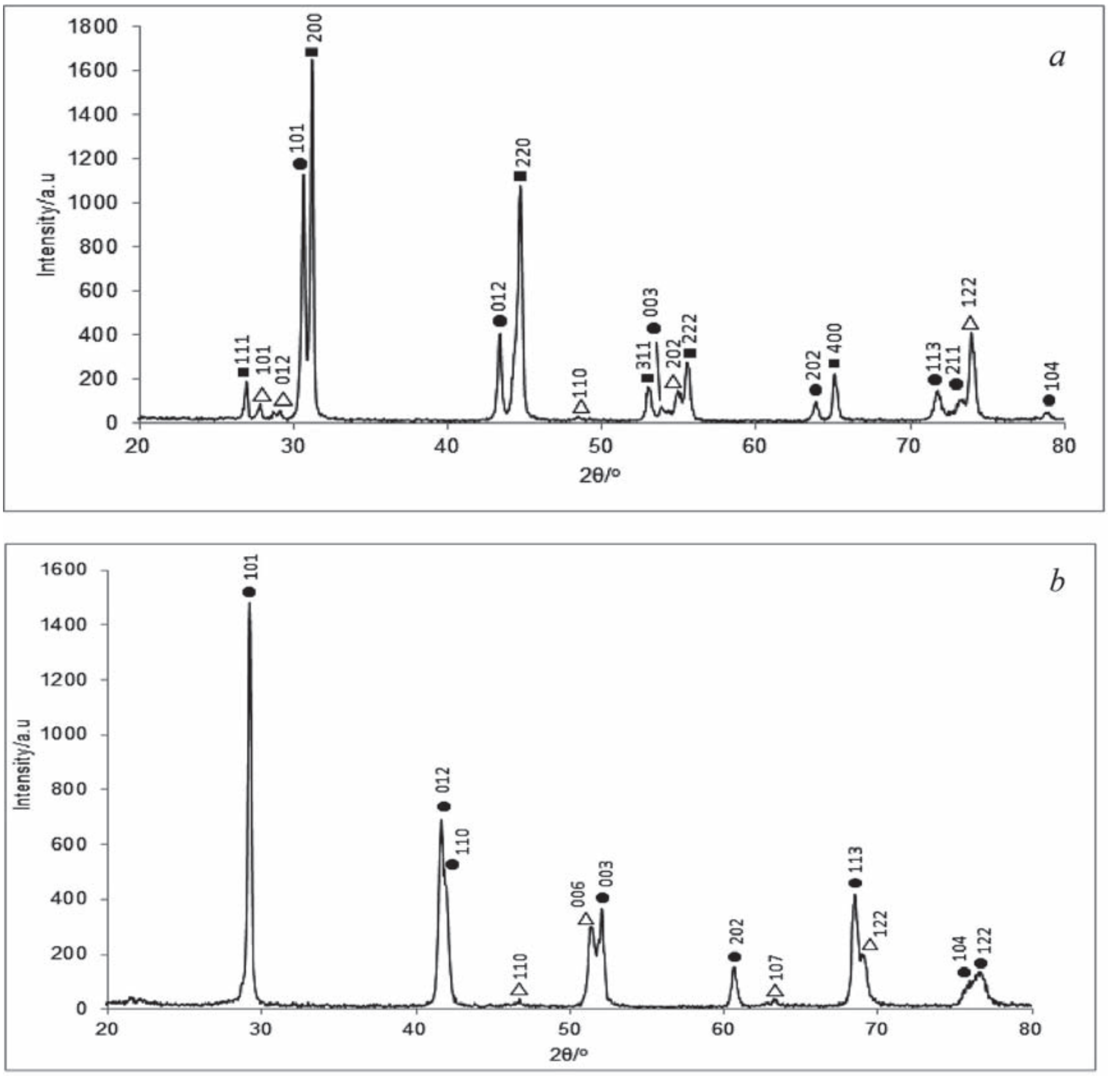

Fig. 2. X-ray powder diffraction patterns of the polythermal section SnAs–SnSb: a – 0.05; b – 0.90 mol.f. SnSb. Designations: ● – (SnSb), ■ – (SnAs), Δ – α′

Table 2. Interplanar distances (*d*, Å) and the lattice parameter (*a*, Å) of the SnAs-based solid solution present in the alloys of the section SnAs–SnSb

SnAs		The composition (mol. f. SnSb) of the alloys of the section SnAs – SnSb					
hkl	*d*	0.05	0.10	0.20	0.30	0.40	0. 60
111	0.3306	0.3306	0.3306				
200	0.2862	0.2865	0.2866	0.2876			
220	0.2024	0.2026	0.2029	0.2028	0.2040	0.2043	
311	0.1726	0.1728		0.1729	0.1740	0.1753	0.1758
222	0.1652	0.1654	0.1654			0.1680	0.1687
400	0.1431	0.1433	0.1434	0.1437	0.1437	0.1439	
331	0.1313	0.1316	0.1317				
Lattice parameter, *a*	0.5725	0.5730	0.5732	0.5742	0.5780	0.5829	0.5909

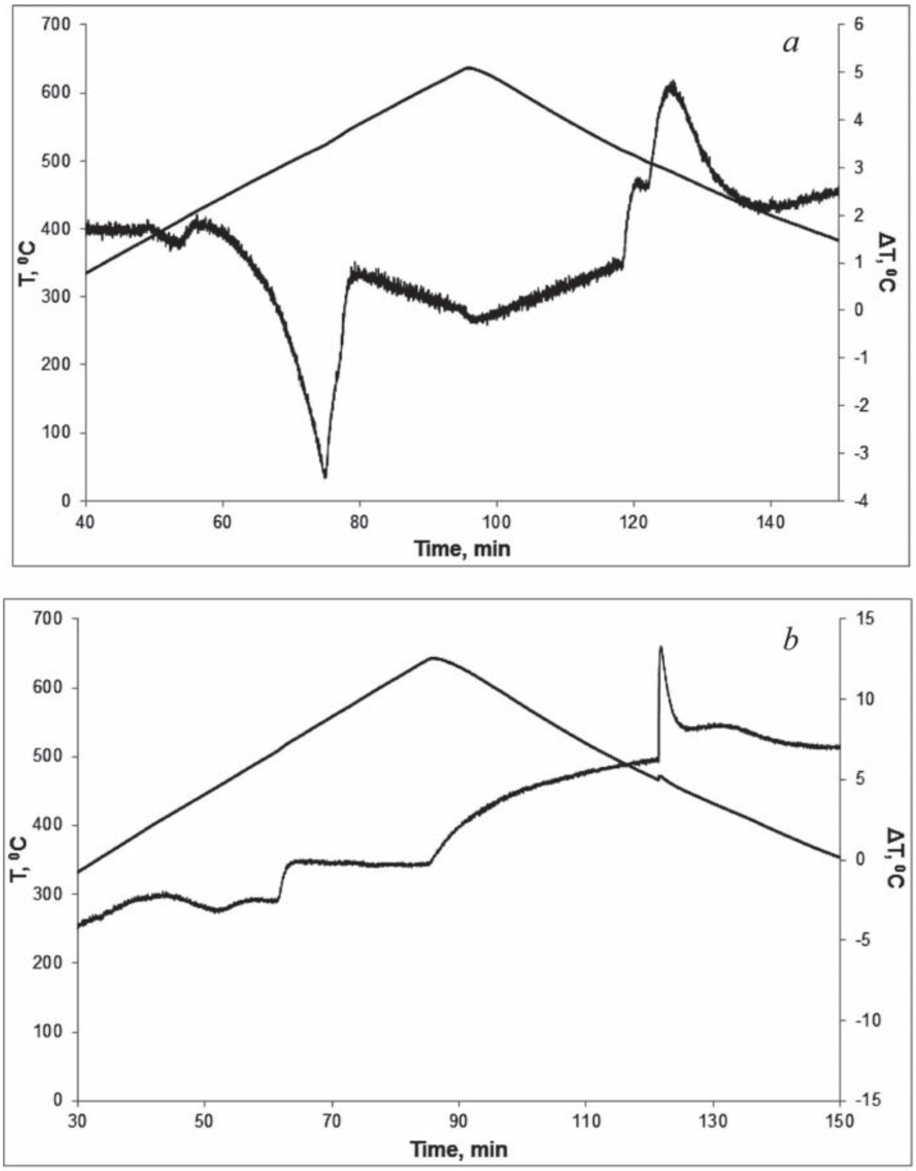

Fig. 3. Thermograms of alloys $(SnAs)_{0.6}Sb_{0.4}$ (a) and $(SnAs)_{0.4}(SnSb)_{0.6}$ (b)

primary crystallization is carried out according to the $L \leftrightarrow$ (SnAs) scheme; secondary crystallization corresponds to line e_1U_1 ($L \leftrightarrow$ (SnAs) + α'); the process ends at U_1. For the alloys whose compositions correspond to the *bc*segment, primary crystallization occurs in the solid solution α' (its composition is different for different alloys); then the figurative melting point falls either on the curve e_1U_1, or the curve p_2U_1, along which the peritectic process $L+ \alpha' \leftrightarrow$ (SnSb) occurs. For one of the compositions, secondary crystallization does not occur, and the figurative point falls directly on U_1.

Thus, for all the alloys of the section SnAs–Sb the crystallization process ends at U_1, which lies outside the trapezium As–SnAs–SnSb–Sb. It is at this point that the temperature is 393±2 °C, which allows for the peritectic transformation $L + \alpha' \leftrightarrow$ (SnAs) + (SnSb). On the *T*-*x* diagrams of the polythermal sections (Fig. 5) U_1 corresponds to the horizontal, below which there are only solid phases.

The polythermal section SnAs–SnSb also intersects the fields of primary crystallization of solid solutions (SnAs) and α'. The sequence of the crystallization processes of the alloys whose compositions correspond to segments *ad* and *df* is the same as that of the alloys corresponding respectively to segments *ав* and *вс* on the section SnAs–Sb. The*T*-*x* diagram of the section SnAs–

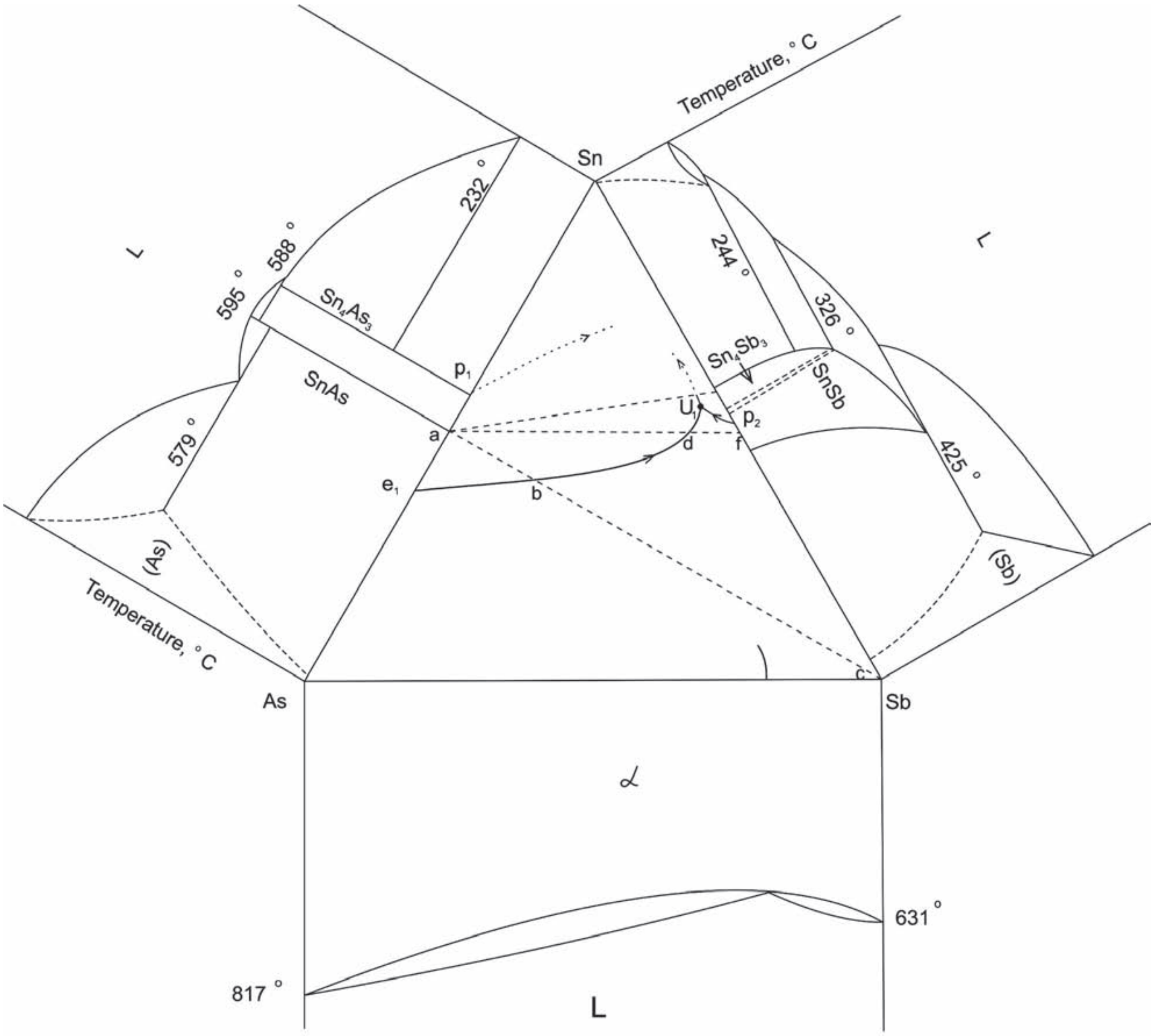

Fig. 4. Scheme of phase equilibria in the Sn–As–Sb ternary system

SnSb is shown in Fig. 5b. The second horizontal at the temperature of 408±2 °C is accounted for by the fact that after primary crystallization of (SnAs) the figurative melting point falls at the same point (*d*) on the monovariant curve e_1U_1, and secondary crystallization of several alloys begins at the same temperature.

The triple points on *T*-*x* diagrams of the sections (Fig. 5b) correspond to points *b* and *d* on the curve e_1U_1 (Fig. 4). Thus, the results of the DTA allow to determine the coordinates of the monovariant equilibrium line e_1U_1. This curve intersects the section SnAs–Sb at the temperature of 500±2 °C and the composition $(SnAs)_{0.70}Sb_{0.30}$. It intersects the section SnAs–SnSb at the temperature of 408±2 °C and the composition $(SnAs)_{0.10}(SnSb)_{0.90}$.

The line starting at U_1 (Fig. 4) separates the fields of primary crystallization of phases (SnAs) and (SnSb). The eutectic process $L \leftrightarrow$ (SnAs)+(SnSb) occurs along this line. This process should end at a four-phase equilibrium point. But in order to determine the character of this equilibrium we need to analyse the polythermal sections SnAs–Sn_4Sb_3 and Sn_4As_3–Sn_4Sb_3.

Assuming that a continuous solid solution is formed between Sn_4As_3 and Sn_4Sb_3 (which is quite probable, since they have the same crystalline structure and similar lattice parameters), we can suggest that the second four-phase equilibrium

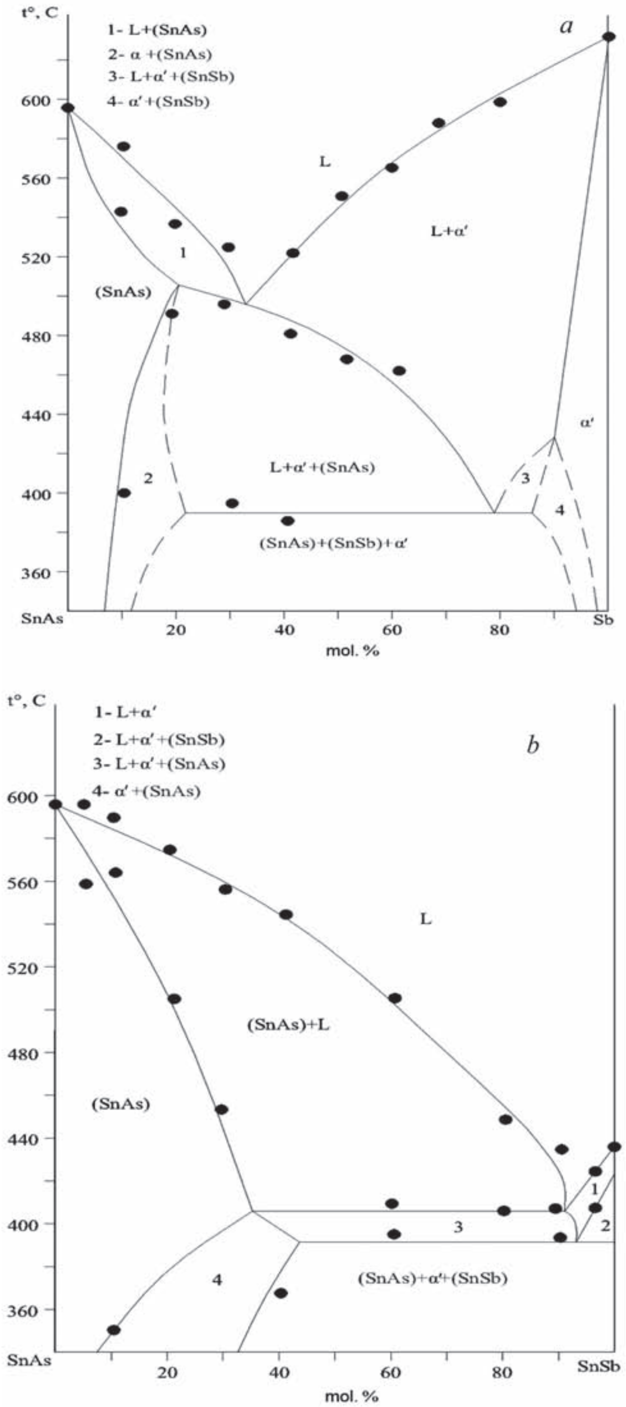

Fig. 5. *T-x* diagrams of the polythermal sections SnAs – Sb (a) and SnAs – SnSb (b)

point U_2 corresponds to the peritectic process L + (SnAs) ↔ $(Sn_4As_3)_{1-x}(Sn_4Sb_3)_x$ + (SnSb).

4. Conclusions

The analysis of polythermal sections SnAs–Sb and SnAs–SnSb by X-ray phase analysis demonstrated that all the alloys include three phases, specifically solid solutions based on SnAs and SnSb, and a solid solution of tin in phase $As_{1-x}Sb_x$ (α′). The concentration range of the solid solution based on tin monoarsenide along the section SnAs–Sb at room temperature is below 10 mol%; the solid phase solubility along the section SnAs–SnSb is below 5 mol% on both sides. Using the results of the differential thermal analysis and the XRD data *T-x* diagrams of polythermal sections SnAs–Sb and SnAs–SnSb were constructed. It was determined that at a temperature of 393±2 °C the invariant peritectic equilibrium L + α′ ↔ (SnAs) + (SnSb) is present in the ternary system Sn–As–Sb. To construct a complete scheme of phase equilibria in the ternary system, further investigation of the SnAs–Sn_4Sb_3 and Sn_4As_3–Sn_4Sb_3sections is necessary.

Acknowledgements

The X-ray phase analysis was carried out using the equipment of the Centre for the Collective Use of Scientific Equipment of Voronezh State University.

Conflict of interests

The authors declare that they have no known competing financial interests or personal relationships that could have influenced the work reported in this paper.

References

1. Hu Y., Lu Y. 2019 Nobel Pprize for the Li-ion batteries and new opportunities and challenges in Na-ion batteries. *ACS Energy Letters*. 2019;4(11): 2689–2690. DOI: https://doi.org/10.1021/acsenergylett.9b02190

2. Song K., Liu C., Mi L., Chou S., Chen W., Shen C. Recent progress on the alloy-based anode for sodium-ion batteries and potassium-ion batteries. *Small*. 2019;334: 1903194. DOI: https://doi.org/10.1002/smll.201903194

3. Kulova T. L., Skundin A. M.. From lithium-ion to sodium-ion battery. *Russian Chemical Bulletin*. 2017;66(8): 1329–1335. DOI: 10.1007/s11172-017-1896-3

4. Jing W. T., Yang C. C., Jiang Q. Recent progress on metallic Sn- and Sb-based anodes for sodium-ion batteries. *Journal of Materials Chemistry A*. 2020; Advance Article. DOI: https://doi.org/ 10.1039/C9TA11782B

5. Kamali A. R., Fray D. J. Tin-based materials as advanced anode materials for lithium ion batteries: a review. *Reviews on Advanced Material Science*. 2011;27: 14–24. Available at: http://194.226.210.10/e-journals/RAMS/no12711/kamali.pdf

6. Wachtler M., Winter M., Besenhard J.O. Anodic materials for rechargeable Li-batteries. *Journal of Power Sources*. 2002;105: 151–160. DOI: https://doi.org/10.1016/S0378-7753(01)00934-X

7. Wachtler M., Besenhard J. O., Winter M. Tin and tin-based intermetallics as new anode materials for lithium-ion cells. *Journal of Power Sources*. 2001;94: 189–193. DOI: https://doi.org/10.1016/S0378-7753(00)00585-1

8. Xie H., Tan X., Luber E. J., Olsen B. C., Kalisvaart W. P., Jungjohann K. L., Mitlin D., Buriak J. M. β-SnSb for sodium ion battery anodes: phase transformations responsible for Eenhanced cycling stability revealed by in situ TEM. *ACS Energy Letters*. 2018;*3*(7): 1670–1676. DOI: https://doi.org/10.1021/acsenergylett.8b00762.

9. Li H., Wang Q., Shi L., Chen L., Huang X. Nanosized SnSb Alloy Pinning on hard non-graphitic carbon spherules as anode materials for a Li-ion battery. *Chemistry of Materials*. 2002;14(1): 103–108. DOI: https://doi.org/10.1021/cm010195p

10. Huang B., Pan Z., Su X., An L. Tin-based materials as versatile anodes for alkali (earth)-ion batteries. *Journal of Power Sources*. 2018;*395*: 41–59. DOI: https://doi.org/10.1016/j.jpowsour.2018.05.063.

11. Zhang W., Pang W., Sencadas V., Guo Z. Understanding high-energy-density Sn_4P_3 anodes for potassium-ion batteries. *Joule*. 2018;2(8): 1534–1547. DOI: https://doi.org/10.1016/j.joule.2018.04.022

12. Jung S. C., Choi J., Han Y. The origin of excellent rate and cycle performance of Sn_4P_3 binary electrodes for sodium-ion batteries. *Journal of Materials Chemistry A*. 2018;6(4): 1772–1779. DOI: https://doi.org/10.1039/C7TA07310K

13. Domi Y., Usui H., Nakabayashi E., Yamamoto T., Nohira T., Hiroki Sakaguchi H. Potassiation and depotassioation Pproperties of Sn_4P_3 electrode in an ionic-liquid electrolyte. *Electrochemistry*. 2019;87(6): 333-335. DOI: https://doi.org/10.5796/electrochemistry.19-00052

14. Saddique J., Zhang X., Wu T., Su H., Liu S., Zhang D., Zhang Y., Yu H. Sn_4P_3-induced crystalline/amorphous composite structures for enhanced sodium-ion battery anodes. *Journal of Materials Science & Technology*. 2019. In Press. DOI: https://doi.org/10.1016/j.jmst.2019.05.032

15. Zhang J., Wang W., Li B. Effect of particle size on the sodium storage performance of Sn_4P_3. *Journal of Alloys and Compounds*. 2019;771: 204–208. DOI: https://doi.org/10.1016/j.jallcom.2018.08.271

16. Lan D., Li Q. Sn_4P_3/SbSn nanocomposites for anode application in sodium-ion batteries. *ChemElectroChem*. 2018;*5*(17): 2383–2386. DOI: https://doi.org/10.1002/celc.201800639

17. Lee K. Synthesis and characterization of tetrel pnictides and compounds in the lithium-tetrel-arsenic system. *Dissertation*. University of California, Davis; 2016. 136 p. Available at: https://search.proquest.com/openview/6c5577b9817fa2c2864fdeda33e2acfb/1?pq-origsite=gscholar&cbl=18750&diss=y

18. Usui H., Domi Y., Yamagami R., Fujiwara K., Nishida H., Sakaguchi H. Sodiation–desodiation reactions of various binary phosphides as novel anode materials of Na-ion battery. *ACS Applied Energy Materials*. 2018;*1*(2): 306–311. DOI: https://doi.org/10.1021/acsaem.7b00241

19. Liu S., Zhang H., Xu L., Ma L., Chen X. Solvothermal preparation of tin phosphide as a long-life anode for advanced lithium and sodium ion batteries. *Journal of Power Sources*. 2016;304: 346–353. DOI: https://doi.org/10.1016/j.jpowsour.2015.11.056

20. Liu J., Wang S., Kravchyk K., Ibáñez M., Krumeich F., Widmer R., Nasiou D., Meyns M., Llorca J., Arbiol J., Kovalenko M. V., Cabot A. SnP nanocrystals as anode materials for Na-ion batteries. *Journal of Materials Chemistry A*. 2018;6(23): 10958–10966. DOI: https://doi.org/10.1039/C8TA01492B

21. Liu C., Yang X., Liu J., Ye X. Theoretical Prediction of Two-Dimensional SnP_3 as a Promising Anode Material for Na-Ion Batteries. *ACS Applied Energy Materials*. 2018;*1*(8): 3850–3859. DOI: https://doi.org/10.1021/acsaem.8b00621

22. Saddique J, Zhang X., Wu T, Wang X., Cheng X., Su H., Liu S., Zhang L., Li G., Zhang Y., Yu H. Enhanced Silicon Diphosphide-Carbon Composite Anode for Long-Cycle, High-efficient sodium ion batteries. *ACS Applied Energy Materials*. 2019;2(3): 2223–2229. DOI: https://doi.org/10.1021/acsaem.8b02242

23. Schmetterer C., Polt J., Flandorfer H. The phase equilibria in the Sb-Sn system. Part I: Literature review. *Journal of Alloys and Compounds*. 2017;728: 497–505. DOI: https://doi.org/10.1016/j.jallcom.2017.08.215

24. Schmetterer C., Polt J., Flandorfer H. The phase equilibria in the Sb-Sn system. Part II: Experimental results. *Journal of Alloys and Compounds*. 2018;743: 523–536. DOI: https://doi.org/10.1016/j.jallcom.2017.11.367

25. Kovnir K. A., Kolen'ko Yu. V., Baranov A. I., Neira I. S., Sobolev A. V., Yoshimura M., Presniakov I. A., Shevelkov A. V. A Sn_4As_3 revisited: Solvothermal synthesis and crystal and electronic structure. *Journal of Solid State Chemistry*. 2009;182(3): 630–639. DOI: https://doi.org/10.1016/j.jssc.2008.12.007

26. Kovnir K. A., Kolen'ko Yu. V., Ray S., Li J., Watanabe T., Itoh M., Yoshimura M., Shevelkov A. V. A facile high-yield solvothermal route to tin phosphide Sn_4P_3. *Journal of Solid State Chemistry*. 2006;179(12): 3756–3762. DOI: https://doi.org/10.1016/j.jssc.2006.08.012

27. Semenova G. V., Goncharov E. G. *Tverdye rastvory v trojnyh sistemah s uchastiem jelementov pjatoj gruppy [Solid solutions involving elements of the fifth group]*. Moscow: MFTI Publ.; 2000. 160 p. (in Russ.)

28. Woo K. E., Dolyniuk J., Kovnir K. Superseding van der Waals with electrostatic interactions: intercalation of Cs into the interlayer space of $SiAs_2$. *Inorganic Chemistry*.2019;58(8): 4997–5005. DOI: https://doi.org/10.1021/acs.inorgchem.9b00017

29. Semenova G. V., Kononova E. Yu., Sushkova T. P. Polythermal section Sn_4P_3–Sn_4As_3. *Russian Journal of Inorganic Chemistry*. 2013;58: 1242–1245. DOI: https://doi.org/10.7868/S0044457X13090201

30. Kononova E. Yu., Semenova G. V., Sinyova S. I., Sushkova T. P. Phase equilibria in the Sn–As–Ge and Sn–As–P systems. *Journal of Thermal Analysis and Calorimetry*. 2014;117(3): 1171–1177. DOI: https://doi.org/10.1007/s10973-014-3883-3

31. Sushkova T. P, Semenova G. V., Naumov A. V., Proskurina E. Yu. Solid solutions in the system Sn-As-P. *Vestnik VGU. Serija: Himija. Biologija. Farmacija = Proceedings of Voronezh State University. Series: Chemistry. Biology. Pharmacy.* 2017;3: 30–36. Available at: http://www.vestnik.vsu.ru/pdf/chembio/2017/03/2017-03-05.pdf (In Russ., abstract in Eng.)

32. Semenova G. V., Sushkova T. P., Zinchenko E. N., Yakunin S. V. Solubility of phosphorus in tin monoarsenide. *Kondensirovannye sredy i mezhfaznye granitsy = Condensed Matter and Interphases*. 2018;20(4): 644–649. DOI: https://doi.org/10.17308/kcmf.2018.20/639

33. Okamoto H., Subramanian P. R., Kacprzak L., Massalski T. B. *Binary Alloy Phase Diagrams*, *Second Edition*. Ohio: ASM International, Materials Park; 1990. 810 p.

34. Allen W. P., Perepezko J. H. Solidification of undercooled Sn-Sb peritectic alloys: Part 1. Microstructural evolution. *Metallurgical Transactions A*. 1991;22: 753–764. DOI: https://doi.org/10.1007/BF02670298

35. Gokcen N. A. The As-Sn (Tin-Arsenic) system. *Bulletin of alloy phase diagrams*. 1990;11(3): 271–278. DOI: https://doi.org/10.1007/bf03029298

36. Emsli Dzh. *Elementy*. Moscow: Mir Publ; 1993. 256 c. (in Russ.)

Information about the authors

Tatiana P. Sushkova, PhD in Chemistry, Associate Professor, Department of General and Inorganic Chemistry, Voronezh State University, Voronezh, Russian Federation; e-mail: sushtp@yandex.ru. ORCID iD: https://orcid.org/0000-0003-1969-7082.

Galina V. Semenova, DSc in Chemistry, Professor, Department of General and Inorganic Chemistry, Voronezh State University, Voronezh, Russian Federation; e-mail: semen157@chem.vsu.ru. ORCID iD: https://orcid.org/0000-0003-3877-985X.

Aleksandra V. Sheveljuhina, postgraduate student, Department of General and Inorganic Chemistry, Voronezh State University, Voronezh, Russian Federation; e-mail: alexandrashevelyuhina@yandex.ru. ORCID iD: https://orcid.org/0000-0002-0146-315X.

Sergey V. Kannykin, PhD in Physics and Mathematics, Associate Professor, Department of Materials Science and Nanosystems Technologies, Voronezh State University, Voronezh, Russian Federation; e-mail: svkannykin@gmail.com. ORCID iD: https://orcid.org/0000-0001-8756-5722.

Elena Yu. Proskurina, PhD in Chemistry, Assistant, Department of General and Inorganic Chemistry, Voronezh State University, Voronezh, Russian Federation; e-mail: helko7@yandex.ru. ORCID iD: https://orcid.org/0000-0002-6149-1398.

Alexey V. Nerushev, MSc student, Faculty of Chemistry, Voronezh State University, Voronezh, Russian Federation; e-mail: alex.nerushew@yandex.ru. ORCID iD: https://orcid.org/0000-0001-6285-3058.

All authors have read and approved the final manuscript.

Translated by Yulia Dymant.
Edited and proofread by Simon Cox.

Condensed Matter and Interphases
(Kondensirovannye sredy i mezhfaznye granitsy)

DOI: https://doi.org/10.17308/kcmf.2020.22/2535 eISSN 2687-0711
Received 26 January 2020
Accepted 15 February 2020

Influence of Nanoscale Layers of the $Mn_3(P_{0.1}V_{0.9}O_4)_2$ Chemostimulator-Modifier on the Process of Thermal Oxidation of GaAs, its Composition, and Morphology of the Resulting Films

© 2020 E. V. Tomina✉[a,*] B. V. Sladkopevtsev[a], A. I. Dontsov[a,b], L. I. Perfileva[b], I. Ya. Mittova[a]

Voronezh State University,
1 Universitetskaya pl., Voronezh 394018, Russian Federation

Voronezh State Technical University,
14 Moskovsky av., Voronezh 394026, Russian Federation

Abstract
Chemostimulated thermal oxidation is one of the approaches to the formation of functional nanoscale films on an $A^{III}B^{V}$ surface. In order to obtain the desired result, it is necessary to reasonably choose an object that can act as a chemostimulator of the process or a modifier of the structure and properties of films formed as a result of oxidation. The use of complex compounds capable of combining both of these functions seems to be effective. The purpose of the study was an investigation into the effect of nanoscale layers of the $Mn_3(P_{0.1}V_{0.9}O_4)_2$ chemostimulator-modifier on the process of thermal oxidation of GaAs, its composition, and morphology of the formed films.

The object of study was gallium arsenide (100) with nanosized layers of manganese vanadate-phosphate $Mn_3(P_{0.1}V_{0.9}O_4)_2$ deposited on its surface. In order to increase the speed of the process and ensure the high chemical homogeneity of the product, it was proposed to use microwave activation of the synthesis of the chemostimulator-modifier $Mn_3(P_{0.1}V_{0.9}O_4)_2$ and its further deposition onto the surface of the semiconductor by the spin-coating method. The formed $Mn_3(P_{0.1}V_{0.9}O_4)_2$/GaAs heterostructures were thermally oxidized in the temperature range 490–550 °C for 60 min in an oxygen stream. The thickness of the growing films (by laser and spectral ellipsometry), their composition (X-ray phase analysis, Auger electron spectroscopy), and surface morphology (atomic force microscopy) were controlled.

Studies of the kinetics of thermal oxidation of $Mn_3(P_{0.1}V_{0.9}O_4)_2$/ GaAs heterostructures showed that the determining process is the solid-phase reaction, limited by diffusion in the solid phase, and the transit character of the chemostimulator without the catalytic effect occurs. It was revealed that manganese vanadate-phosphate promoted an increase in the growth of the formed film by an average of 70–220% compared to the standard oxidation of GaAs, leads to the intensification of secondary interactions of the oxides of the substrate components with the products of thermolysis of $Mn_3(P_{0.1}V_{0.9}O_4)_2$ and the absence of segregation of arsenic in the film in a non-oxidized state.

Thermal oxidation of $Mn_3(P_{0.1}V_{0.9}O_4)_2$/GaAs heterostructures results in the formation of nanoscale (50-200 nm) films with a fairly pronounced relief. Further study of the electrophysical characteristics of the films is necessary, since composition data suggest they possess a dielectric nature. This can be used in practice for the formation of films on the surface of $A^{III}B^{V}$ with functional purposes and with widely varying characteristics.

Keywords: gallium arsenide, manganese vanadate-phosphate, nanoscale films, chemostimulated oxidation, microwave synthesis.

Funding: The study was supported by the Russian Foundation for Basic Research (Grant No. 18-03-00354 A)

For citation: Tomina E. V., Sladkopevtsev B. V., Mittova I. Ya., Perfileva L. I. Influence of nanoscale layers of the $Mn_3(P_{0.1}V_{0.9}O_4)_2$ chemostimulator-modifier on the process of thermal oxidation of GaAs, its composition, and morphology of the resulting films. *Kondensirovannye sredy i mezhfaznye granitsy = Condensed Matter and Interphases*. 2020; 22 (1): 116–123. DOI: https://doi.org/10.17308/kcmf.2020.22/2535

✉ Elena V. Tomina, e-mail: tomina-ev@yandex.ru

1. Introduction

Heterostructures on gallium arsenide are widely used in technologies for the production of microwave integrated circuits, various optoelectronic devices, and field-effect transistors [1–6]. The result of the appearance of gallium arsenide microelectronics was the creation of efficient and powerful injection lasers and LEDs based on GaAs/GaAlAs heterostructures in the wavelength range of 600–900 nm [7–9]. Moreover, the variety of objects formed on the GaAs surface and possessing a wide range of properties is extremely large: quantum dots, one-dimensional nanostructures, and thin films. In the latter case, the application of a wide variety of oxides, sulphides, nitrides, and complex compounds is possible, and now there are a number of physical and chemical methods for the creation of such $A^{III}B^{V}$ based thin-film heterostructures [10–13]. However, the problem of synthesizing functional nanoscale films by relatively simple and technologically advanced methods has not yet been solved.

The formation of functional nanosized films on the GaAs surface by thermal oxidation requires the use of reasonably selected synthesis chemostimulators and film modifiers [14, 15]. Chemostimulators change the semiconductor oxidation mechanism and prevent segregation of arsenic in a free state at the inner boundary of the film. Modifiers in the process of thermal oxidation are embedded in the film, enabling its rapid growth, and a targeted change in its composition and nanostructure.

The use of complex compounds in the process of thermal oxidation of $A^{III}B^{V}$ seems to be effective. Their cationic component includes a chemostimulator. An anionic component can act as a modifier, by being included in the composition of the film (phosphates, sulphates, etc.) as a group, and can also contain a second, additional, chemostimulator (for example, vanadates). In this case, there is an additional opportunity to fine-tune the regulation of the synthesis processes using the combined effects of the chemostimulator-modifier. In this study, manganese vanadate-phosphate $Mn_3(P_{0.1}V_{0.9}O_4)$ was chosen as a chemostimulator-modifier. Manganese oxides are effective chemostimulators of the oxidation processes of $A^{III}B^{V}$ [16]. Vanadate groups VO_4^{3-}, isostructural to arsenate anions AsO_4^{3-} [17], are ready fragments of films formed during the oxidation process. In addition, oxygen compounds of vanadium, are able to exhibit the function of a chemostimulator even in the anionic component [18]. The doping of manganese vanadate with phosphorus ensures the inclusion of phosphate groups PO_4^{3-} exhibiting dielectric properties in the films [19].

The purpose of the study was the investigation of the effect of nanoscale layers of the chemostimulator-modifier $Mn_3(P_{0.1}V_{0.9}O_4)_2$ on the process of thermal oxidation of GaAs and the composition and morphology of the formed films.

2. Experimental

The synthesis reactions of manganese vanadate-phosphate $Mn_3(P_{0.1}V_{0.9}O_4)_2$ from a solution of precursors was carried out under the influence of microwave radiation (operating frequency 2450 MHz, P_{max} of source – 800 W) [20]. Vanadium (V) oxide V_2O_5 (analytical grade, Russian Federation Purity Standard TU 6-09-4093-88) was dissolved in an excess of a 20 % NaOH solution (analytical grade, Russian Federation Purity Standard GOST 432877), which led to the formation of sodium metavanadate $NaVO_3$. $Na_2HPO_4 \cdot 12H_2O$ (analytical grade, Russian Federation Purity Standard GOST 4172-76) and $MnCl_2 \cdot 4H_2O$ (International Purity Standard analytical reagent) solutions were added to a $NaVO_3$ solution for the synthesis of $Mn_3(P_{0.1}V_{0.9}O_4)_2$. Exposure to microwave irradiation of 600 W was performed for 10 min. The resulting suspension was cooled to room temperature and the $Mn_3(P_{0.1}V_{0.9}O_4)_2$ precipitate was separated from it using a vacuum filter. Then the precipitate was washed, dried, and annealed at a temperature of 400 °C for 2 h in a muffle furnace (SNOL 8.2/1100).

The phase composition was determined by X-ray phase analysis (XRDs) using an ARL X'TRA diffractometer in continuous mode. The angular range of the study was in the range from 10 to 80 ° ($CuK_{\alpha 1}$ c $\lambda = 1.540562$ Å) at 25 °C. The size of the coherent scattering regions (CSR) according to X-ray phase analysis (XRD) for the synthesized $Mn_3(P_{0.1}V_{0.9}O_4)_2$ powder was calculated according to the Scherrer equation [21]:

$$D_{hkl} = \frac{kx\lambda}{\beta_{hkl}\cos\theta},$$

where D_{hkl} – average particle size, Å, k – correction factor (for cubic and orthorhombic structure $k = 0.9$), λ – X-ray tube wavelength, θ – the position of the peak maximum, deg., β_{hkl} – intrinsic physical broadening of the diffraction maximum, rad.

Monocrystal (100) gallium arsenide wafers of AGTSCh-1 grade were used as semiconductor substrates. GaAs was doped with zinc, the concentration of the main charge carriers was $11.5\cdot10^{18}–2.5\cdot10^{18}$ cm^{-3}. For the creation of $Mn_3(P_{0.1}V_{0.9}O_4)_2$/GaAs heterostructures with nanosized vanadate phosphate layers, the spin coating method was used [22]. Distilled water was added to the $Mn_3(P_{0.1}V_{0.9}O_4)_2$ powder. Dispersion was then carried out in an ultrasonic bath (VU-09-“Ya-FP”-0) for 15 min. A small amount of gelatine was added for the improvement of the adhesion to the substrate during spin-coating application. The final solution was stirred at 80 °C for 15 min with a magnetic stirrer (Magnetic Stirrer MSH-300).

Before the formation of thin-film heterostructures, the GaAs semiconductor substrates were treated with concentrated HF (49 %) for 10 min [23].

The thermal oxidation of $Mn_3(P_{0.1}V_{0.9}O_4)_2$/GaAs heterostructures was carried out in a flowing quartz reactor of a horizontal resistive heating furnace (MTP-2M-50-500) with temperature control with an error of 1 °C (ARIES TRM-201). The process was carried out in flowing oxygen (medical (99.5 %) GOST 5583-78, National product classification code: 21 1411 0200) with a volumetric flow rate of 30 l /h (linear gas flow rate in the reactor was 10 cm/min). Oxidation of the samples was carried out in the temperature range 490–550 °C for 60 minutes.

The thickness of the deposited layers of vanadate phosphate and films grown by thermal oxidation was measured using a LEF-754 laser ellipsometer (LE, accuracy ± 1 nm) and an Ellipse-1891 spectral ellipsometer (SE) [24]. According to the LE and SE data, the layer thickness of $Mn_3(P_{0.1}V_{0.9}O_4)_2$ on the semiconductor surface was 25±1 nm.

The elemental composition of oxide films on GaAs and the distribution of components based on their thickness were determined by the Auger electron spectroscopy (AES) method using an ESO-3 spectrometer with a DESA-100 analyser, determination accuracy ± 10 %. In this study, the layer-by-layer etching of films by argon ions was used for obtaining information on the distribution of elements along the film depth.

The imaging of the samples was performed by atomic force microscopy (AFM) using a Solver P47 Pro (NT-MDT) scanning probe microscope with the HA_NC Etalon cantilever.

3. Results and discussion

Microwave activation of the synthesis of a chemostimulator modifier $Mn_3(P_{0.1}V_{0.9}O_4)_2$ for a significant increase in the speed of the process and provision of high chemical homogeneity of the product was proposed in studies [25–27].

According to the study [28], decomposition of crystalline hydrates of 3*d*-elements in the microwave field was carried out in several stages to the oxide phase. Initially, crystalline hydrate solutions absorb microwave radiation due to the water of crystallization. At temperatures of 130–180 °C, hydrolysis of salts starts, with the formation of oxo- and hydroxo- compounds as intermediate products. Fine oxide particles that are formed after decomposition of salt compositions are uniformly distributed over the reaction volume and are able to actively interact with each other. A significant contribution is also made by the specific “non-thermal” effect of microwave radiation associated with the generation of ion currents at intercrystalline boundaries, the intensity of which increases significantly in highly dispersed systems.

XRD results of synthesized $Mn_3(P_{0.1}V_{0.9}O_4)_2$ powder in addition to the presence of the target phase showed the presence of impurities in the form of $Mn_3(PO_4)_2$ (d_{hkl} = 2.8745 Å; 1.8610 Å) and V_2O_5 (d_{hkl} = 4.3611 Å; 4.0797 Å; 3.3979 Å; 2.7566 Å). Despite the excess of sodium hydroxide during the synthesis of metavanadate, it was not possible to fully use V_2O_5, which according to the literature [29] can be observed in similar reactions. However, the presence of vanadium (V) oxide in the synthesized nanocrystalline powder is not a drawback, since previously [18] an effective chemostimulating effect of V_2O_5 by the catalytic mechanism was revealed in the processes of thermal oxidation of $A^{III}B^{V}$ semiconductors. The average size of the CSR was 30 nm.

The kinetic characteristics of the oxidation processes of $Mn_3(P_{0.1}V_{0.9}O_4)_2$/GaAs heterostructures processed using the equation $d = (k\tau)^n$, are presented in Table 1.

Table 1. Kinetic parameters of the equation $d = k^n t^n$ for the process of thermal oxidation of $Mn_3(P_{0.1}V_{0.9}O_4)_2$/GaAs heterostructures

Chemostimulator-modifier	Oxidation temperature range, °C	$n_{wed}\pm\Delta n$, $nm^{1/n}min^{-1}$	EAE, kJ/mol	Maximum relative increase of film thickness,%
$Mn_3(P_{0.1}V_{0.9}O_4)_2$/GaAs	490–550	0.39±0.01	156	220
GaAs (standard)	450–550	0.56±0.01	110	–

During the thermal oxidation of $Mn_3(P_{0.1}V_{0.9}O_4)_2$/GaAs heterostructures the value of n_{av} was less than 0.5, indicating that in this temperature range the determining process is the solid-phase reaction, limited by diffusion in the solid phase [16]. The EAE value of the studied process was somewhat higher (156 kJ/mol) compared with the intrinsic thermal oxidation of GaAs (110 kJ/mol). It is typical for a solid-solid reaction without a catalytic effect and indicates the transit nature of the action of the chemostimulator in the considered process [14].

The relative increase in film thickness g during chemically stimulated thermal oxidation of $Mn_3(P_{0.1}V_{0.9}O_4)_2$/GaAs (Table 2) in comparison with the intrinsic oxidation of the semiconductor was calculated by the formula:

$$g = \frac{\Delta d_{Mn_3(P_{0.1}V_{0.9}O_4)_2/GaAs}}{\Delta d_{GaAs}} \cdot 100\ \%,$$

where $\Delta d_{Mn3(P0.1V0.9O4)2/GaAs}$ – change in the thickness of the film formed in the process of thermal oxidation of the studied heterostructures with a deposited chemostimulator layer minus the thickness of the latter, and Δd_{GaAs} – change in the oxide film thickness during intrinsic oxidation of gallium arsenide.

When the chemostimulator-modifier $Mn_3(P_{0.1}V_{0.9}O_4)_2$ was used over the entire temperature–time range, an increase in the growth of the formed film by an average of 70–220 % was revealed compared with the oxidation of GaAs. This, apparently, was due to both the incorporation of ready isostructural phosphate and vanadate groups into growing films, and the effective chemostimulating effect of the cationic component of vanadate phosphate and V_2O_5 detected in the initial powder.

Films formed by the oxidation of $Mn_3(P_{0.1}V_{0.9}O_4)_2$/GaAs heterostructures contained $MnAsO_4$, $Mn_3(VO_4)_2$, $Mn_3(PO_4)_2$, GaAs, $GaAsO_4$ (Table 3). With an increase in the oxidation temperature, the intensities of the reflections of gallium arsenate and manganese arsenate were observed, confirming the intensification of the secondary interactions of the oxides of the substrate components with the products of thermolysis of the chemostimulator.

The analysis of the distribution profiles of elements along the depth of the film formed by the oxidation of $Mn_3(P_{0.1}V_{0.9}O_4)_2$/GaAs heterostructure in the regime of 510 °C, 60 min, demonstrated (Fig. 1) that the film was enriched with oxygen (up to 50-60 %) over the entire thickness. This indicates the absence of segregation of arsenic in the film in an unoxidized state (which is an attribute of the process of intrinsic thermal oxidation of gallium arsenide), and hence the effective chemostimulating effect of manganese vanadate-phosphate. The presence of gallium and arsenic on the film surface confirms their significant diffusion into the chemostimulator layer. Phosphorus in the film was practically not fixed, which was probably associated with its small amount due to evaporation in the form of oxides and the detection limit of elements

Table 2. Relative increase in oxide film thickness during thermal oxidation of $Mn_3(P_{0.1}V_{0.9}O_4)_2$/GaAs heterostructures in comparison with the GaAs standard

Образец	Relative increase in thickness as a function of oxidation time, %						
	T, °C/t, min	10	20	30	40	50	60
$Mn_3(P_{0.1}V_{0.9}O_4)_2$/GaAs	530	68	83	84	82	83	90
	550	69	90	115	190	196	220

Table 3. Composition of films formed by the thermal oxidation of $Mn_3(P_{0.1}V_{0.9}O_4)_2$/GaAs heterostructures (XRD data [30])

Heterostructure, thermal oxidation mode	d_{hkl}, Å	Angle 2θ, degrees	Phase
$Mn_3(P_{0.1}V_{0.9}O_4)_2$/GaAs, 500 °C, 60 min	1.7829	51.195	$MnAsO_4$
	1.3898	67.320	$Mn_3(VO_4)_2$
	3.5777; 2.7806	24.867; 32.166	$Mn_3(PO_4)_2$
	3.2541	27.386;	GaAs
	1.6299; 2.0674	56.406; 43.752	$GaAsO_4$
$Mn_3(P_{0.1}V_{0.9}O_4)_2$/GaAs, 530 °C, 60 min	1.7909	24.823	$MnAsO_4$
	3.2542	27.385	GaAs
	3.5840; 2.774	24.823; 32.204	$Mn_3(PO_4)_2$
	2.0679	43.739	$GaAsO_4$

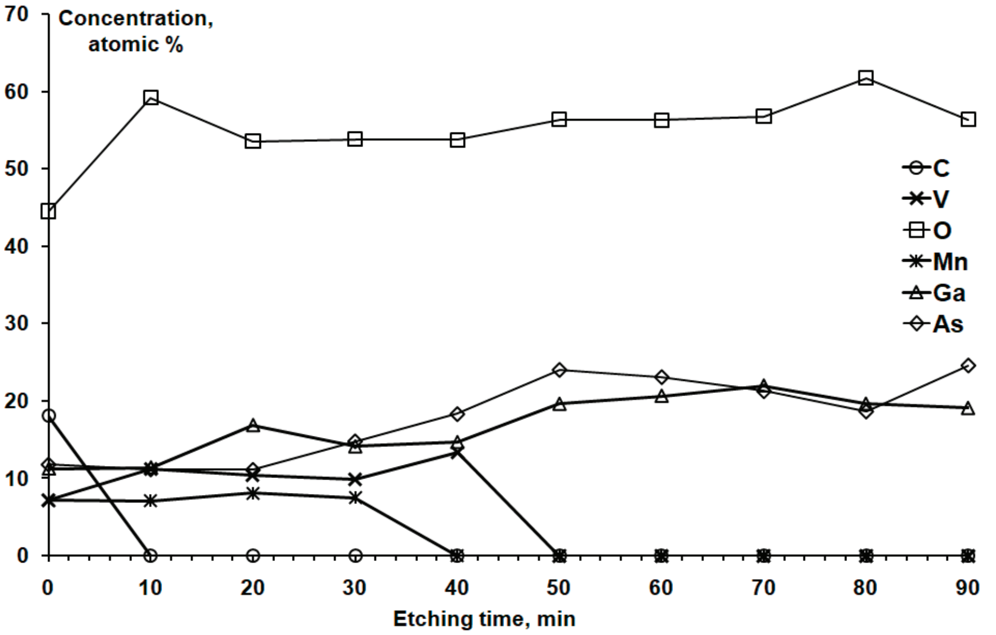

Fig. 1. Auger profiles of the distribution of elements in the film formed by the oxidation of an $Mn_3(P_{0.1}V_{0.9}O_4)_2$/GaAs heterostructure at 510 °C, 60 min

by the Auger electron spectroscopy method. With further propagation into the film, oxidized gallium and arsenic exist in the form of gallium arsenate, which correlates with XRD data.

According to AFM data for a non-oxidized $Mn_3(P_{0.1}V_{0.9}O_4)_2$/GaAs heterostructure, the average difference in the relief height was about 15 nm (Fig. 2). For $Mn_3(P_{0.1}V_{0.9}O_4)_2$/GaAs heterostructure, oxidized at 490 °C for 60 min, the difference in the relief height decreased to 8–10 nm. The average grain size was within 200 nm (Fig. 3a, b) With an increase in the oxidation temperature to 550 °C, the films had more expressed relief (Fig. 3c, d) The height difference increased to 20–25 nm, the average grain size increased to 300 nm.

Thus, nanoscale (thickness range of 50–200 nm) films with a fairly expressed relief were formed during the thermal oxidation of $Mn_3(P_{0.1}V_{0.9}O_4)_2$/GaAs heterostructures. As the oxidation temperature increased, the grain structure of the films became more expressed.

4. Conclusions

The chemically stimulated oxidation of gallium arsenide with a nanoscale layer of

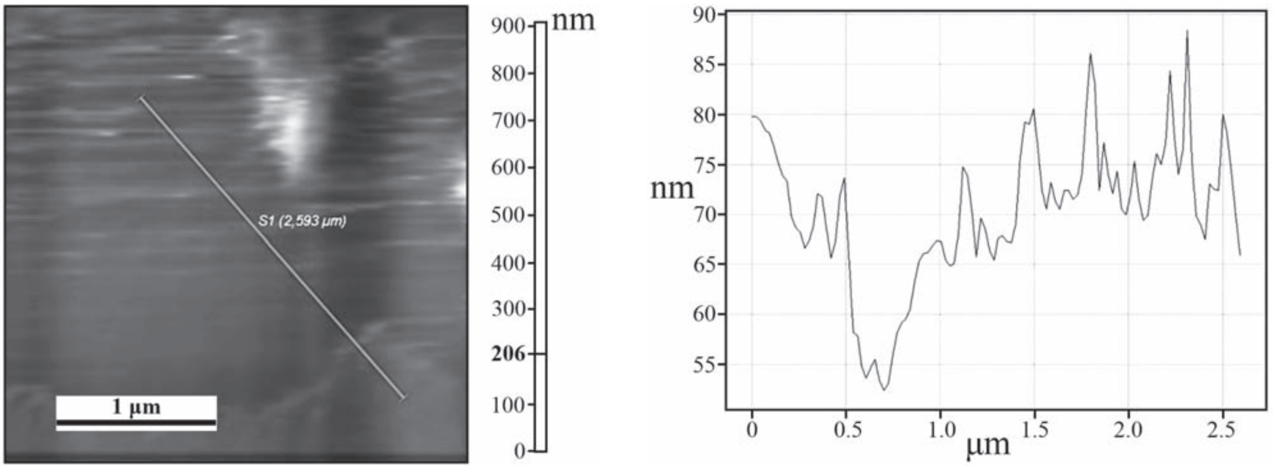

a b

Fig. 2. AFM image of the surface of a non-oxidized $Mn_3(P_{0.1}V_{0.9}O_4)_2$/GaAs heterostructure: a) topography; b) profile. The size of the scanning area 3×3 μm^2

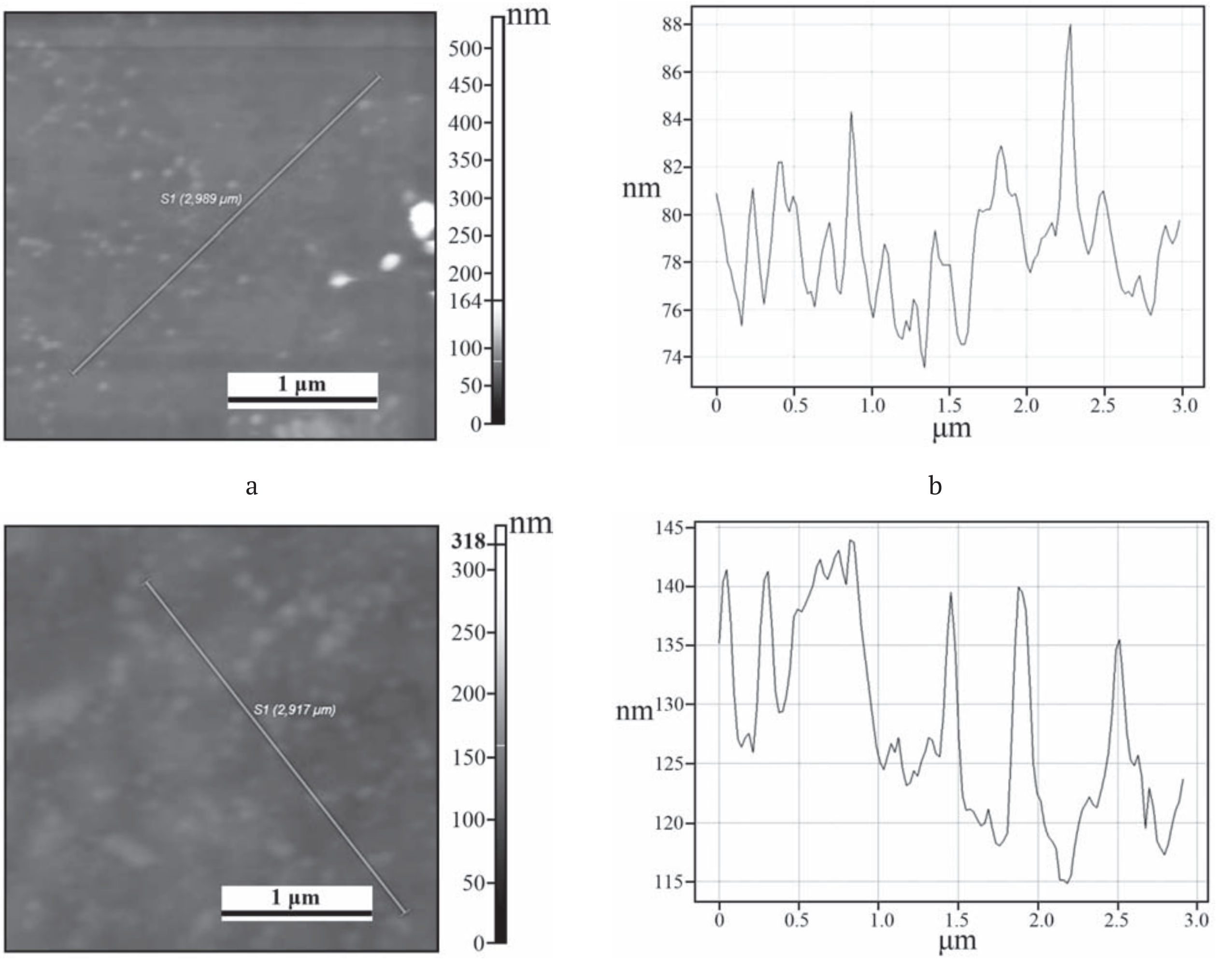

a b

c d

Fig. 3. AFM images of the films surface (a, c) and profile (b, d) formed by the oxidation of $Mn_3(P_{0.1}V_{0.9}O_4)_2$/GaAs heterostructures at 490 °C, 60 min. (a, b) and 550 °C, 60 min. (c, d). The size of the scanning area is 3×3 μm^2

manganese vanadate-phosphate on the surface proceeds via a transit mechanism. This was evidenced by the EAE value of the process (of the order of 156 kJ/mol), which was somewhat higher in comparison with the standard oxidation of GaAs (~ 110 kJ/mol). According to the XRD results, V_2O_5, a chemostimulator with a pronounced catalytic mechanism of action, initially present in the starting vanadate-phosphate was not detected in the films, which confirms the absence of a catalyst regeneration cycle $V_2O_5 \leftrightarrow VO_2$. Films formed by the oxidation of $Mn_3(P_{0.1}V_{0.9}O_4)_2$/GaAs heterostructures were in the thickness range of 50-200 nm. They mainly contained manganese and gallium arsenates and had expressed relief with a grain size in the range of 200-300 nm.

Acknowledgements

The research results were partially obtained using the equipment of the Centre for the Collective Use of Scientific Equipment of Voronezh State University. URL: http://ckp.vsu.ru.

Conflict of interests

The authors declare that they have no known competing financial interests or personal relationships that could have appeared to influence the work reported in this paper.

References

1. Tang M., Park J.-S., Wang Z., Chen S., Jurczak P., Seeds A., Liu H. Integration of III-V lasers on Si for Si photonics. *Progress in Quantum Electronics*. 2019;66: 1–18. DOI: https://doi.org/10.1016/j.pquantelec.2019.05.002

2. Torkhov N. A., Babak L. I., Kokolov A. A. On the application of Schottky contacts in the microwave, extremely high frequency, and THz ranges. *Semiconductors*.2019;53: 1688–1698. DOI: https://doi.org/10.1134/S1063782619160280

3. Lutz J., Schlangenotto H., Scheuermann U., De Doncker R. *Semiconductor power devices. Physics, characteristics, reliability*. Springer-Verlag Berlin Heidelberg; 2018. 714 p. DOI: https://doi.org/10.1007/978-3-319-70917-8

4. Yadav S., Rajan C., Sharma D., Balotiya S. GaAs-SiGe based novel device structure of doping less tunnel FET. In: Sengupta A., Dasgupta S., Singh V., Sharma R., Kumar Vishvakarma S. (eds.) *VLSI Design and Test. VDAT 2019. Communications in computer and information science, vol. 1066*. Singapore: Springer 2019.p. 694–701. DOI: https://doi.org/10.1007/978-981-32-9767-8_57

5. Klotzkin D. J. *Semiconductors as laser materials 1: Fundamentals. In: Introduction to semiconductor lasers for optical communications*. Springer, Cham; 2020. p. 31–52. DOI: https://doi.org/10.1007/978-3-030-24501-6_3

6. Paswan R. K., Panda D. K., Lenka T. R. Dielectric Modulated AlGaAs/GaAs HEMT for label free detection of biomolecules. In: Sharma R., Rawal D. (eds.) *The physics of semiconductor devices. IWPSD 2017*. *Springer proceedings in physics, vol. 215*. Springer, Cham; 2017. p. 709–715. DOI: https://doi.org/10.1007/978-3-319-97604-4_109

7. Eichler H. J., Eichler J., Lux O. Semiconductor lasers. In: *Lasers*. *Springer Series in Optical Sciences, vol. 220*. Springer, Cham; 2018.p. 165–203. DOI: https://doi.org/10.1007/978-3-319-99895-4_10

8. Mikhailova M. P., Moiseev K. D., Yakovlev Y. P. Discovery of III – V semiconductors: physical properties and application semiconductors. *Semiconductors*. 2019;53(3): 273–290. DOI: https://doi.org/10.1134/S1063782619030126

9. Anfertev V. A., Vaks V. L., Reutov A. I., Baranov A. N., Teissier R. Studying the frequency characteristics of THz quantum cascade lasers with using the open optical resonator. *Journal of radioelectronics*. 2018;12:14–24. DOI: https://doi.org/10.30898/1684-1719.2018.12.5 (In Russ.)

10. Pawar S. A., Kim D., Kim A., Park J. H., Shin J. C., Kim T. W., Kim H. J. Heterojunction solar cell based on n-MoS_2/p-InP. *Optical Materials*. 2018;86: 576–581. DOI: https://doi.org/10.1016/j.optmat.2018.10.05.05

11. Sugiyama H., Uchida K., Han X., Periyanayagam G. K., Aikawa M., Hayasaka N., Shimomura K. MOVPE grown GaInAsP/GaInAsP SCH-MQW laser diode on directly-bonded InP/Si substrate. *Journal of Crystal Growth*. 2019;507:93–97. DOI: https://doi.org/10.1016/j.jcrysgro.2018.10.024

12. Sharma S. K., Singh S. P., Kim D. Y. Fabrication of the heterojunction diode from Y-doped ZnO thin films on p-Si substrates by sol-gel method. *Solid State Communications*. 2018;270:124–129. DOI: https://doi.org/10.1016/j.ssc.2017.12.12.010

13. Asalzadeh S., Yasserian K. The effect of various annealing cooling rates on electrical and morphological properties of TiO_2 thin films. *Semiconductors*. 2019;53: 1603–1607. DOI: https://doi.org/10.1134/S1063782619160036

14. Tomina E. V., Mittova I. Ya., Sladkopevtsev B. V., Kostryukov V. F., Samsonov A. A., Tretyakov N. N. Thermal oxidation as a method of formation of nanoscale functional films on $A^{III}B^{V}$ semiconductors: chemostimulated influence of metal oxides overview. *Kondensirovannye sredy i mezhfaznye granitsy = Condensed Matter and Interphases*. 2018;20(2):184-203. DOI: https://doi.org/10.17308/kcmf.2018.20/522 (In Russ., Abstract in Eng.)

15. Liu H. A short review on thermal vapor sulfurization of semiconductor thin films for optoelectronic applications. *Vacuum*. 2018;154; 44–48. DOI: https://doi.org/10.1016/j.vacuum.2018.04.050

16. Mittova I. Ya., Sladkopevtsev B. V., Tomina E. V., Samsonov A. A., Tretyakov N. N., Ponomarenko S. V. Preparation of dielectric films via thermal oxidation of MnO_2/GaAs. *Inorganic Materials*. 2018;54(11): 1085–1092. DOI: 10.1134 / S0020168518110109

17. Housecroft C., Sharpe A.G. *Inorganic Chemistry* (4th ed.). Pearson; 2012. 1213 p.

18. Mittova I. Ya., Tomina E. V., Lapenko A. A., Khorokhordina A. O. Solid-state reactions during thermal oxidation of vanadium-modified GaAs surfaces. *Inorganic Materials*. 2004;40(5): 441-444.

19. Spicer W. E., Lindau I., Skeath P., Su C. Y., Chye P. Unified mechanism for Schottky-barrier formation and III–V oxide inter-face states. *Physical Review Letters*. 1980;44: 420. DOI: https://doi.org/10.1103/PhysRevLett.44.420

20. Tomina E. V., Mittova I. Ya., Burtseva N. A., Sladkopevtsev B. V. A method for the synthesis of a phosphor based on yttrium orthovanadate. *Patent No. 2548089 RF*. Claim 11.12.2013. Publ. 05.20.2015. Byul. No. 2013133382/05.

21. Brandon D., Kaplan W. D. *Microstructural characterization of materials*. John Wiley & Sons Ltd; 1999. 409 p.

22. Popielarski P., Mosinska L., Bala W., Paprocki K., Zorenko Yu., Zorenko T., Sypniewska M. Persistent photoconductivity in ZnO thin films grown on Si substrate by spin coating method. *Optical Materials*. 2019;97: 109343. DOI: https://doi.org/10.1016/j.optmat.2019.109343

23. Feng C., Zhang Y., Liu J., Qian Y., Bai X. Optimized chemical cleaning procedure for enhancing photoemission from GaAs photocathode. *Materials Science in Semiconductor Processing*. 2019;91: 41–46. DOI: https://doi.org/10.1016/j.mssp.2018.11.003

24. Mittova I. Ya., Tomina E. V., Sladkopevtsev B. V., Tret'yakov N. N., Lapenko A. A., Shvets V. A. High-speed determination of the thickness and spectral ellipsometry investigation of films produced by the thermal oxidation of InP and V_XO_Y/InP structures. *Inorganic Materials*. 2013;49(2): 179–184.

25. Kostyukhin E. M. Synthesis of magnetite nanoparticles upon microwave and convection heating. *Russian Journal of Physical Chemistry A*. 2018;92(12): 2399–2402. DOI: https://doi.org/10.1134/S0036024418120233

26. Budin O. N., Budin O. N., Kropachev A. N., Agafonov D. G., Cherepov V. V. Investigation into the carbothermic method of digestion of titanium raw materials by the example of artificially synthesized perovskite. *Russian Journal of Non-Ferrous Metals*. 2018;59(6): 612–616. DOI: https://doi.org/10.3103/S1067821218060020

27. Kuznetsova V. A., Almjasheva O. V., Gusarov V. V. Influence of microwave and ultrasonic treatment on the formation of $CoFe_2O_4$ under hydrothermal conditions. *Glass Physics and Chemistry*. 2009;35(2): 205–209. DOI: https://doi.org/10.1134/S1087659609020138

28. Tretyakov Yu. D. Development of inorganic chemistry as a fundamental for the design of new generations of functional materials. *Russian Chemical Reviews*. 2004;73(9): 831–846. DOI: https://doi.org/10.1070/RC2004v073n09ABEH000914

29. Krasnenko T. I., Samigullina R. F., Rotermel M. V., Nikolaenko I. V., Zaitseva N. A., Onufrieva T. A., Ishchenko A. V. The effect of the synthesis method on the morphological and luminescence characteristics of α-$Zn_2V_2O_7$. *Russian Journal of Inorganic Chemistry*. 2017;62(3):269–274. DOI: https://doi.org/10.1134/S0036023617030111

30. JCPDC PCPDFWIN: *A Windows Retrieval/Display program for Accessing the ICDD PDF - 2 Data base*. International Center for Diffraction Data; 1997.

Information about the authors

Elena V. Tomina, DSc in Chemistry, Associate Professor, Department of Materials Science and Industry of Nanosystems, Voronezh State University, Voronezh, Russian Federation; e-mail: tomina-ev@yandex.ru. ORCID iD: https://orcid.org/0000-0002-5222-0756.

Boris V. Sladkopevtsev, PhD in Chemistry, Associate Professor, Department of Materials Science and Industry of Nanosystems, Voronezh State University, Voronezh, Russian Federation; e-mail: dp-kmins@yandex.ru. ORCID iD: https://orcid.org/0000-0002-0372-1941.

Aleksey I. Dontsov, PhD in Phys.-Math., Associate Professor, Department of Materials Science and Industry of Nanosystems, Voronezh State University; Associate Professor of the Department of Physics, Voronezh State Technical University, Voronezh, Russian Federation; e-mail: dontalex@mail.ru. ORCID iD https://orcid.org/0000-0002-3645-1626.

Lidia I. Perfileva, MSc student, Voronezh State University, Voronezh, Russian Federation; e-mail: stepina-Lidija97@yandex.ru ORCID iD: https://orcid.org/0000-0002-1603-3662.

Irina Ya. Mittova, DSc in Chemistry, Professor, Department of Materials Science and Industry of Nanosystems, Voronezh State University, Voronezh, Russian Federation; e-mail: imittova@mail.ru. ORCID iD: https://orcid.org/0000-0001-6919-1683.

All authors have read and approved the final manuscript.

Translated by Valentina Mittova.
Edited and proofread by Simon Cox.

Condensed Matter and Interphases
(Kondensirovannye sredy i mezhfaznye granitsy)

DOI https://doi.org/10.17308/kcmf.2020.22/2536
eISSN 2687-0711
Received 10 February 2020
Accepted 15 March 2020

Microcone Anodic Oxide Films on Sintered Niobium Powders

© 2020 N. M. Yakovleva✉,[a], A. M. Shulga[a], K. V. Stepanova[a], A. N. Kokatev[a], V. S. Rudnev [b], I. V. Lukiyanchuk[b], V. G. Kuryavyi[b]

*[a]Petrozavodsk State University,
33 Lenina prospect, Petrozavodsk 185910, Republic of Karelia, Russian Federation*

*[b]Institute of Chemistry, Far-Eastern Branch of the Russian Academy of Sciences,
159 prospect 100-letya Vladivostoka, Vladivostok 690022, Russian Federation*

Abstract
Information on the anodizing of sintered powders (SP) of niobium is limited by the study of the growth of barrier-type films. The formation of a nanostructured anodic oxide film (AOF) on the surface of powder particles should lead to a noticeable increase in the specific surface of the sample and an increase in the chemical activity of the material. In view of the above, the study of the anodic nanostructuring of sintered niobium powders is of high importance and offers opportunities for creating new functional nanomaterials. This paper was aimed at the study of the anodizing process of sintered Nb powders in a fluorine-containing aqueous electrolyte 1 M H_2SO_4 + 1 % HF.

The objects of the study were samples of sintered Nb powder with a specific area of S_{spec} = 800 cm^2/g. Anodizing was conducted in a 1 M H_2SO_4 + 1 % HF electrolyte with various values of current density j_a. Surface morphology before and after anodising was investigated by scanning electron microscopy (SEM) and atomic force microscopy (AFM). X-ray diffractometry was used to study the phase composition. Kinetics of the growth of anodic oxide films (AOF) on the surface of sintered Nb powders SP in galvanostatic mode was studied. The optimal conditions were defined for obtaining $U_a(t)$ voltage-time transients, characteristic of the formation of self-organised porous anodic oxide films (AOF). It was established that anodizing at current density values j_a = 0.10–0.20 mA/cm^2 leads to the formation of a Nb_2O_5 oxide film on the surface of sintered powders SP with a regular-porous layer adjacent to metal and a crystalline microcone layer over it. The microcones (up to 0.6 µm high, up to 2 µm in effective base diameter) consist of branched fibrils with a diameter of ~18–30 nm, connected on top.

It was established for the first time that anodizing of sintered niobium powders in a fluorine-containing aqueous electrolyte leads to the formation of an oxide film with an upper crystalline microcone layer on the surface of powder microparticles. The suggested method for surface processing can be used for the development of biocompatible powder implants.

Keywords: sintered niobium powders, anodic oxide films, microcones, crystalline, nanostructured.

Funding: The study was supported by the Flagship University Development Program of the FSFEI HE Petrozavodsk State University for 2017–2021.

For citation: Yakovleva N. M., Shulga A. M., Stepanova K. V., Kokatev A. N., Rudnev V. S., Lukiyanchuk I. V., Kuryavyi V. G. Microcone anodic oxide films on sintered niobium powders. *Kondensirovannye sredy i mezhfaznye granitsy = Condensed Matter and Interphases.* 2020;22(1): 124–134. DOI: https://doi.org/10.17308/kcmf.2020.22/2536

✉ Natalia M. Yakovleva, e-mail: nmyakov@gmail.com

1. Introduction

It is known that the anodizing of Ta, Nb, Al, Ti, and other metals in weak acid water solutions that do not dissolve the oxide film being formed leads to the formation of thick (or barrier-type) anodic oxide films (AOF) with dielectric properties on their surfaces [1]. Self-organised oxide films with regularly located nanosized structural elements (tubes or pores) can also be formed on the surface of metals and alloys by electrochemical anodizing in electrolyte solutions. Self-organised AOFs are usually divided into two groups: porous and tubular with different morphological characteristics [2, 3].

Previous research showed that the synergy of the processes of the oxide film growth and dissolution implemented during the anodizing of niobium in fluorine-containing electrolytes also lead to the formation of self-organised nanoporous anodic oxide films [4–13]. The interest in nanoporous AOFs formed on Nb can be explained by such properties as high specific area, good adhesion to the substrate, biocompatibility, antibacterial, and catalytic activity. Such AOFs can be effectively used in gas sensors, catalysts, electrolytic capacitors, and electrochromic devices as well as in thin-film lithium-ion batteries, etc. [11, 13–17].

According to [15, 18–30], the anodizing of niobium foil in fluorine and phosphate containing aqueous and non-aqueous (organic) electrolytes can also help to obtain oxide films with a surface layer consisting of an ensemble of nanonstructured microcones. The oxide films with such morphology obtained by the anodising of niobium in fluorine-containing aqueous solutions were mentioned for the first time in papers [18, 19]. In a series of articles [21–23], it was shown that microcones can also be obtained by anodizing in a hot glycerine electrolyte with additives K_2HPO_4 and K_3PO_4. It was established that microcones have crystal structure corresponding to orthorhombic T-Nb_2O_5 [29] in contrast to self-organised AOFs that tend to be X-ray amorphous. Specific features of the structure of microcones have not been thoroughly studied yet, although it is shown that they consist of dendritic fibres of nanosized diameter connected on top [28–30]. Their large surface area, morphological regularity, and crystal atomic structure make them appealing for different applications. In particular, new biomedical applications, fabrication of the surfaces with regulated wettability, and the use as photoanodes in dye-sensitised solar cells are considered [28, 29]. The relative lack of information on crystalline microcone anodic niobium oxides provides motivation for the further study of their formation.

There is no agreement on the mechanism of initiation and development of microcones of crystalline Nb_2O_5 during anodizing. Only first model representations, based on the initiation and development of crystalline oxide nuclei on the metal/oxide interface, have been suggested [21, 29]. Most researchers agree that the initiation and growth of microcones of crystallites Nb_2O_5 with the formation of nanostructured microcones occur under a strong electric field in the presence of fluoride ions (with NaF and/or HF in aqueous electrolytes) or phosphate ions (with K_2HPO_4 + K_3PO_4 in organic electrolytes) with a rather long time of anodizing and/or increased temperatures of the electrolyte (T ~ 160 °C).

Previously, the growth of nanoporous and nanotubular AOFs obtained on the surface of metal foil and tin was studied. Exceptions are the works dedicated to the formation of bioactive anodic oxide coatings on the surface of porous titanium [30–32] and sintered powders of TiAl [3, 33–35]. Information available on the anodizing of sintered powders (SP) of niobium is limited by the study of the growth of barrier-type films. The formation of a nanostructured anodic oxide film (AOF) on the surface of powder particles should lead to a noticeable increase in the specific area of the sample and an increase in the chemical activity of the material. In view of the above, the study of the anodic nanostructuring of sintered niobium powders is highly important and offers opportunities for creating new functional nanomaterials.

This paper was aimed at the study of the anodizing process of sintered Nb powders in a fluorine-containing aqueous electrolyte 1 M H_2SO_4 + 1 % HF.

2. Experimental

The objects of the study were samples of sintered powder (SP) of Nb. The pressed niobium powder [36] was sintered at T = 1850 °C for 1 h. As a result, cylindrical samples with specific area of S_{spec} = 800 cm^2/g were obtained.

The samples were preliminarily degreased in acetone and ethanol in an ultrasonic bath, washed in distilled water, and dried in the air at room temperature. Anodizing was conducted at room temperature using a three-electrode cell with a tantalum cathode and platinum counter electrode in the fluorine-containing aqueous electrolyte 1 M H_2SO_4 + 1 % HF. Anodizing was conducted in galvanostatic mode with various values of current density j_a = 0.05, 0.1, 0.15, 0.20 mA/cm^2. The process lasted 1 and 2 hours.

During the growth of the AOF, voltage-time transients $U_a(t)$ were recorded using an electronic recorder "ERBIY-7115" connected to a computer. The detailed description of the anodising technique is presented in the works [33, 37, 38].

Surface morphology of the samples before and after anodising was investigated by scanning electron microscopy (SEM) on high-resolution microscopes Mira (Tescan, Czech Republic) and S-55009 (Hitachi, Japan). Due to the fact that the anodised samples are non-conductive, their surface was preliminarily sputtered with gold.

At the same time, the elemental composition was assessed by energy dispersive X-ray analysis (EDXA) using a Thermo Scientific attachment (USA). The data was collected for 5–10 areas, including those of microscopic size (up to 50×50 μm^2) as well as the "dots" of 50×50 nm^2 and 10×10 nm^2. The areas were chosen according to the previously obtained SEM images of the surface with further quantitative analysis of the elemental composition. The thickness of the oxide films was assessed by SEM images of the samples.

At the same time, atomic force microscopy (AFM) was used to study the structure of the surface of the samples. The studies were conducted in air on a Solver Next (ZAO NT-MDT, Russia) scanning probe microscope (SPM) in tapping mode. High-resolution diamond-like carbon tips (NSG01) with the length of 125 μm, resonance frequency of 87–230 kHz, and curvature radius of the needle of 10 nm were used. The size of the scan area varied in the range from 1 to 25 μm^2 taking into account the inhomogeneous surface relief of the powder samples. Generally, fairly homogeneous areas were selected for surface scanning. From 2 to 5 areas of the surface were scanned. Using the image processing module, Image Analysis P9, of the SPM Solver Next, a primary image processing was conducted (first, filtration using a Gaussian 3×3 0.391 linear filter and a Hybrid Median non-linear filter, then image skew was corrected using the Fit Lines method of Flatten Correction 1-D for colour correction), and size distribution of the image objects (using Grain Analysis) was assessed [39].

X-ray diffractometry was used to study the phase composition. The samples were studied using the X-ray technique before and after anodising on a D8 ADVANCE (Bruker, Germany) automated diffractometer using Cu*K*α radiation in the angular range 2θ = (10–90)^o with 0.02^o step. To identify the phase composition of the AOF, a set of d-spacings, calculated according to the experimental data, was compared to the corresponding values for Nb and crystalline modifications of niobium oxides. For that purpose, a search programme EVA with a PDF-2 (Powder Diffraction File; Kabekkodu, 2007) database was used.

3. Results and discussion

Anodizing of sintered Nb powders in a fluorine-containing aqueous electrolyte was conducted for the first time. Initial conditions for the formation of anodic oxide films (AOF) were chosen using the data, obtained during the study of anodizing of niobium foil. According to [4], in order to obtain nanoporous AOFs in the water solution 1 M (10 wt%) H_2SO_4 with addition of (0.5–2) wt% HF, it is preferable to use the voltstatic mode at the voltage U_a = 20 V, room temperature of the electrolyte $T = T_r$ = (20–25) °C, and the process duration t_a from 30 min to 1 h. The use of such conditions of niobium foil anodising allowed obtaining a self-organised porous AOF with the diameter of open pores d_p ~ 10–30 nm and the thickness δ not exceeding 450–500 nm [12].

Taking into account this information, an electrolyte, 1 M H_2SO_4 +1 % HF, was selected for the anodizing of sintered powders (SP). By varying the current density and anodizing time of the galvanostatic process, it was established that at the current density values in the range of j_a = 0.05–0.20 mA/cm^2 and t_a = 1–2 hours the type of voltage-time transients $U_a(t)$ is typical for the formation of self-organised porous AOFs (Fig. 1). There are successively distinguished sections of $U_a(t)$ curves that correspond to different stages of the formation of oxide films: growth of a barrier layer, initiation and self-organisation of pores, and the steady-state growth of the porous layer [2].

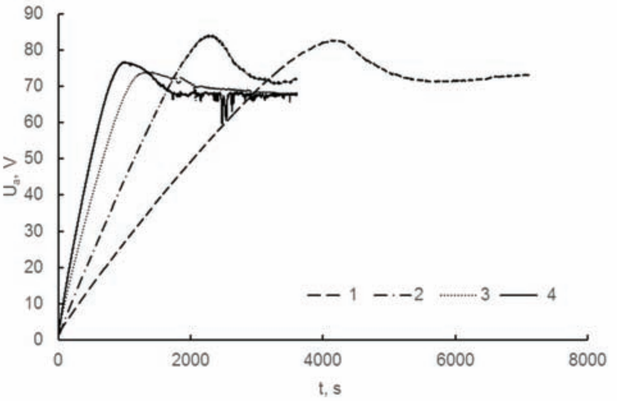

Fig. 1. $U_a(t)$ transients obtained during anodising of sintered Nb powders in the 1 M H_2SO_4 + 1% HF electrolyte with different values of current density j_a: curve 1 – j_a = 0.05 mA/cm^2 (t_a = 2 h) and curves 2, 3, 4 – j_a = 0.1, 0.15, 0.2 mA/cm^2 (t_a = 1 h)

As j_a increases, both the growth rate of voltage at the stage of formation of the barrier layer and the time of transition to steady-state growth increase. For instance, if the time of transition to the stage of steady-state growth is approximately 2 hours with j_a= 0.05 mA/cm^2 (Fig. 1, curve *1*), then with bigger values of j_a it takes from 40 minutes to 1 hour. In all the cases, the value of steady-stage voltage is similar to the value U_a^{stat} ~ 70 V. However, U_a^{stat} tends to decrease slightly with the growth of j_a. It should be noted that the presence of numerous voltage peaks at the stage of the steady-state growth of pores is characteristic of $U_a(t)$ obtained at j_a = 0.20 mA/cm^2 (Fig. 1, curve 4). Such voltage behaviour can be caused by a local breakdown in the barrier layer [21].

During the next stage, a microscopic study of the surface morphology of the samples of sintered Nb powders before and after anodizing at j_a = 0.10 mA/cm^2 (t_a = 1 hour) was conducted using SEM. Fig. 2a shows that the microparticles have irregular shapes with linear dimensions from 10 to 40 µm. The study of the elemental composition using EDXA showed the presence of O in the quantity from 1.8 to 7.0 wt% alongside Nb on all the studied areas.

SEM overview images of sintered Nb powders show that the surface morphology changes after anodizing: a multitude of continuously located microinhomogeneities appear (Fig. 2b). A more detailed study (Fig. 3) revealed that the discovered objects are closely located cone-shaped formations with sizes ranging from 0.4 to 2 µm, the so-called microcones (Fig. 3a). In their turn, microcones consist of branched (dendritic) fibres of nanosized diameter ~18–30 nm (fig. 3b,c) connected on top.

Fig. 3a shows that the AOF on the surface of the particles has a heterogeneous structure. From

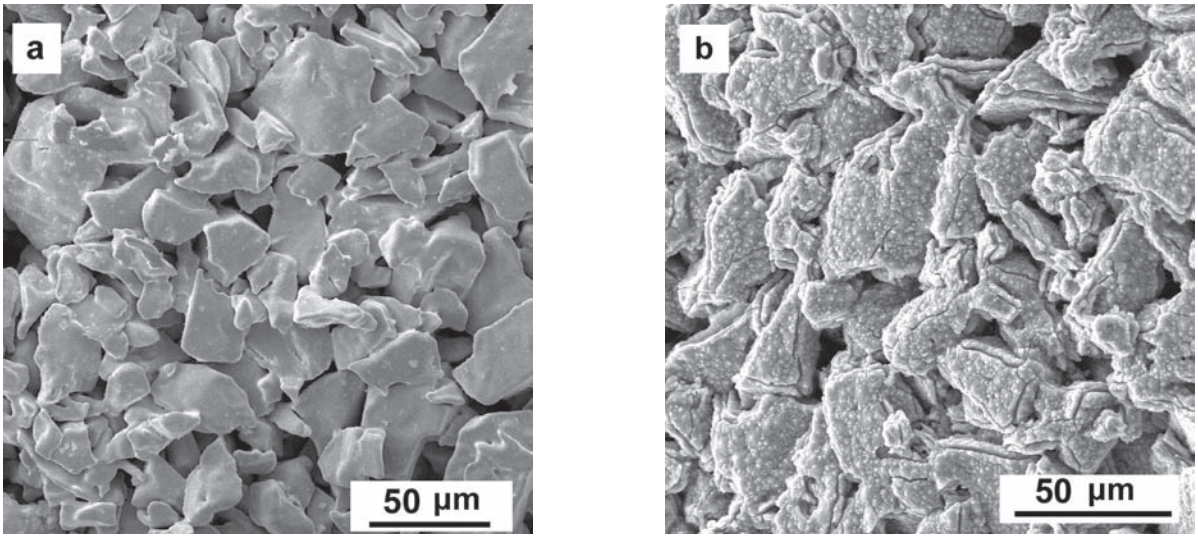

Fig. 2. SEM images of the surface of sintered Nb powder samples before (a) and after anodizing in the 1 M H_2SO_4 + 1 % HF solution for 1 hour with j_a = 0.1 mA/cm^2 (b)

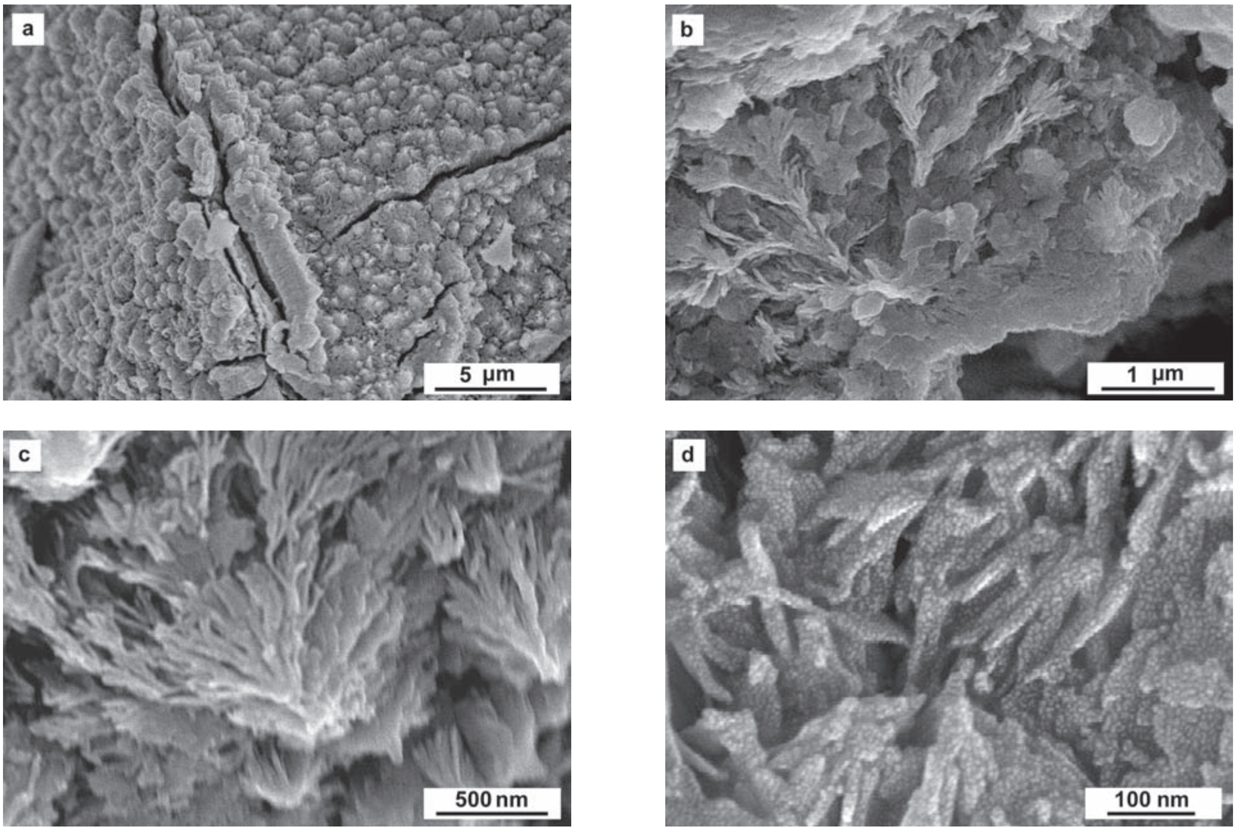

Fig. 3. SEM images of the surface of the anodizing samples of sintered Nb powders obtained at various magnifications. Anodising conditions: $j_a = 0.1$ mA/cm^2, $t_a = 1$ h, $T = T_r$

the side adjacent to the substrate, there is a self-organised porous oxide film of approximately 1 µm consisting of barrier and porous layers. On top of it, there is an inhomogeneous microcone layer. The height of the microcones varies from ~0.1 to 0.6 µm. As Fig. 3d shows, there are round fragments of ~ 2–8 nm in the body of nanofibers that the microcones consist of. Therefore, it can be assumed that the nanofiber has a "fine texture".

Computer processing of the SEM images of the surface area $S \approx 50$ µm^2 (Fig. 4a) allowed assessing the distribution of microcones by size, more specifically by effective base diameter d_o (Fig. 4b). It is evident that there are microcones on the selected surface area with d_o ranging from 0.45 to 1.85 µm. As the type of distribution demonstrates, ~ 40 % of the microcones have d_o in the range of 0.7–0.9 µm and ~ 30 % in the range of 1.0 to 1.3 µm. There are also ~ 30 % of the objects with 0.4 µm < d_o < 0.7 µm. The weighted mean value of the effective base diameter equals $\langle d_o \rangle = 0.85$ µm. Thus, a significant variation of the value d_o is typical for the microcone layer of AOF.

The elemental composition of the AOF was identified by EDXA (depth of analysis up to 1 µm) for the regions of different sizes. Fig. 5 shows the results for the analysed area $S \approx 15$ µm^2. According to the obtained data, Nb and O form a part of the AOF (Fig. 5b). Also, an insignificant amount of F was found in some areas. The presence of F can be caused by the inclusion of fluorine-containing complexes into the porous oxide layer of AOF during its growth [15]. The values of weight percent of the elements $C_{\mathrm{Nb}} \approx 70$ wt%, $C_0 \approx 30$ wt%, (Fig. 5b) show that the composition of the AOF corresponds quite well with Nb_2O_5. The obtained result was close to the EDXA data received during the study of the composition of the microcone layers formed by the anodizing of Nb foil in fluorine-containing aqueous electrolytes [19, 25, 30].

Then, the phase compositions of the samples, before and after anodizing, were studied using the X-ray method. X-ray patterns of all the studied samples after anodizing show a number of low-intensity additional lines in addition to the reflections from the niobium substrate. The identification of diffraction lines on the X-ray

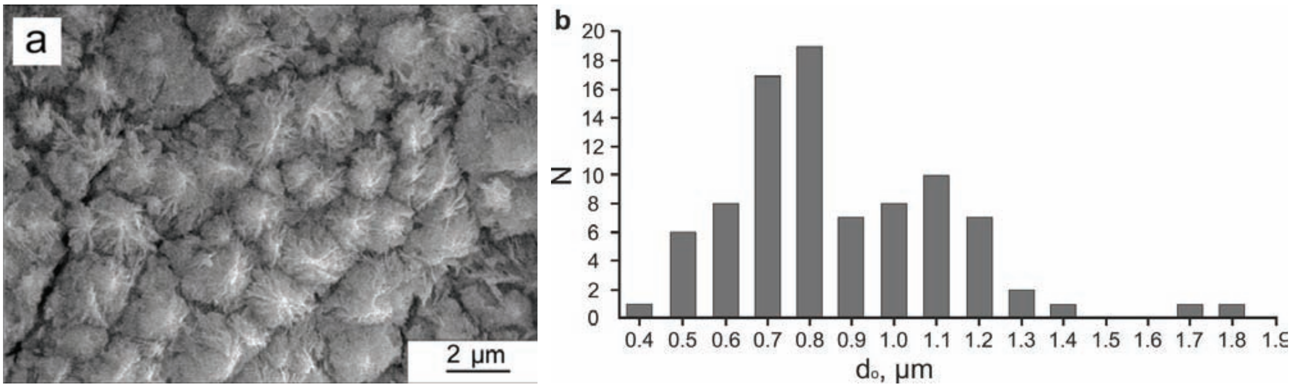

Fig. 4. a) SEM image of the surface area of the anodizing sample of the sintered Nb powder; b) the corresponding distribution of oxide microcones by sizes over effective base diameters of d_o. Anodizing conditions: $j_a = 0.1$ mA/cm^2, $t_a = 1$ h, $T = T_r$

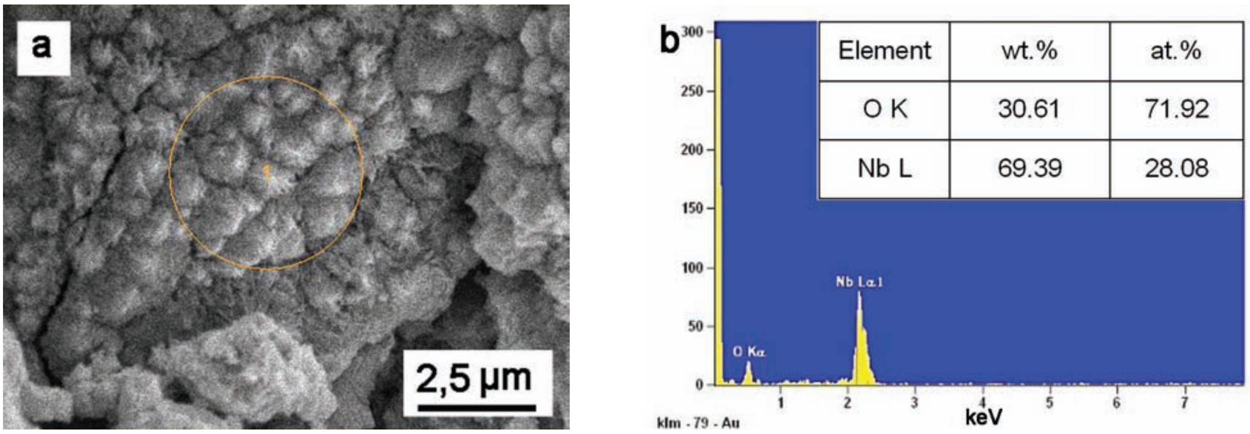

Element	wt.%	at.%
O K	30.61	71.92
Nb L	69.39	28.08

Fig. 5. a) SEM image of the surface area after anodizing; b) EDAX spectrum and composition of the analysed area

patterns of the anodized sintered powders is quite a complicated task, firstly, due to the low intensity of diffraction lines and, secondly, due to the coincident positions of several Bragg reflections for different crystalline phases of niobium oxides. Nevertheless, the comparison of the obtained values of d-spacings with the tabular data allows for the conclusion that the phase composition corresponds to the orthorhombic modification T- Nb_2O_5, which correlates to the results of the comprehensive study of the atomic structure of microcone AOFs on niobium foil in the work [28].

In our previous works [38, 39] it was shown that the AOF formed on the surface of sintered Nb powder possesses super-hydrophilic properties, high corrosion resistance in the solution modelling blood plasma, as well as improved protein adsorption. Therefore, the products made from sintered niobium powder and anodised by the developed technology can be used as biocompatible implants.

At the same time, atomic force microscopy (AFM) was used to study the structure of the surface of the samples before and after anodizing at different values of j_a. The appearance of AFM images of sintered Nb powder demonstrates that the surface has quite a developed relief and is characterised by the presence of elongated (“fibrous”) formations. The width of the “fibres” is in the range from 80 to 160 nm and the length is in the range from 200 to 300 nm. A similar structure of sintered Nb powders is also revealed on SEM images of sintered Nb powders [37]. It appears that such surface morphology can be explained by special aspects of the production of cylindrical samples from sintered niobium powder.

After anodizing for 1 hour at $j_a = 0.05$ mA cm^2, of the surface relief practically does not change, which is likely to be related to the fact that the barrier layer of the AOF is formed during this period of time (Fig. 1, curve 1). When t_a is increased to 2 hours (Fig. 6b), a change in the

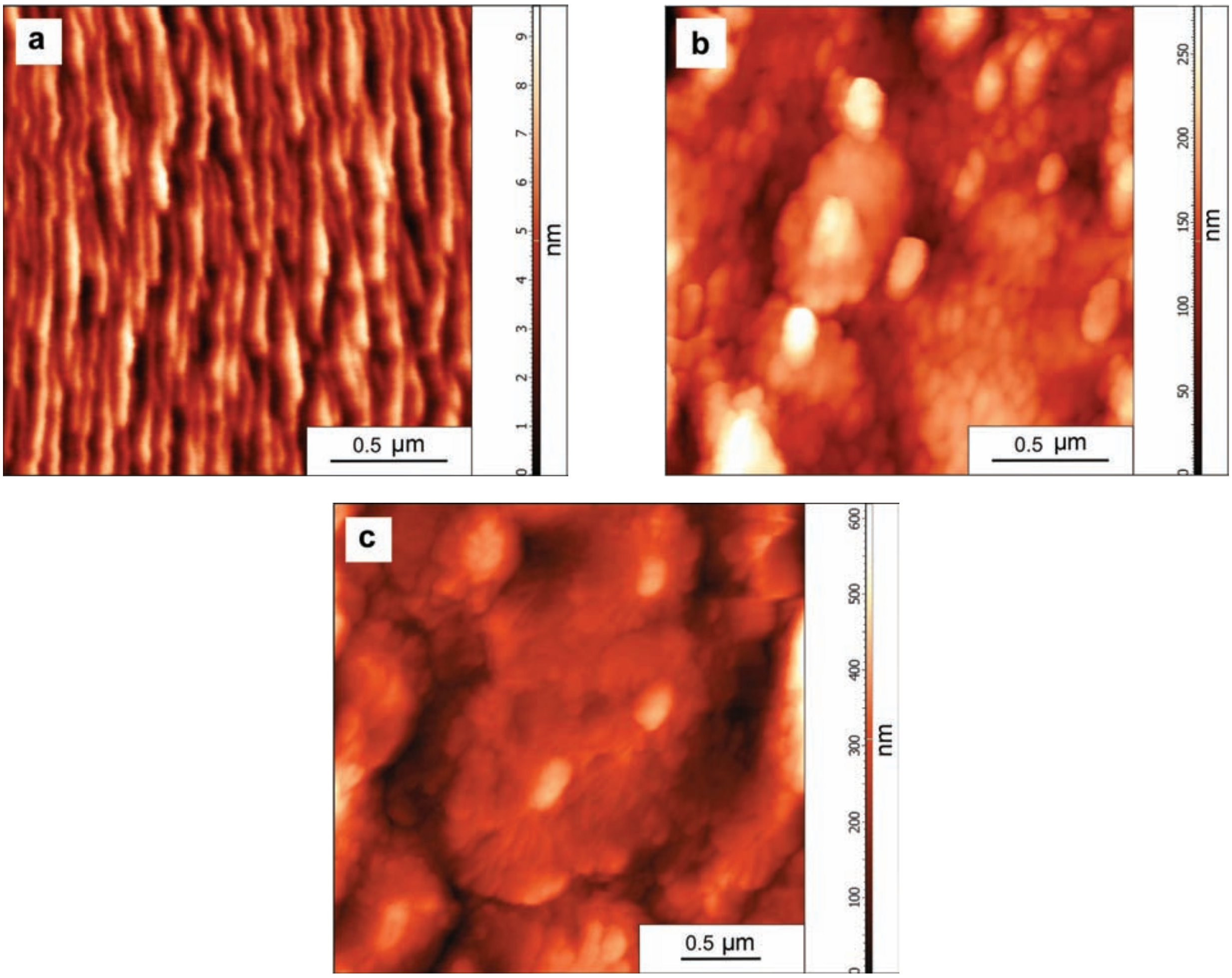

Fig. 6. AFM images of sintered Nb powders before (a) and after anodizing in 1 MH_2SO_4 +1% HF with different values of current density: b) 0.05 mA/cm^2, t_a= 2 h; c) 0.1 mA/cm^2 (t_a= 1 h)

relief is observed. In addition to the surface areas characterised by the presence of regular open pores (d_p ~ 10–20 nm), there are also unevenly located microcones of different sizes. Effective base diameters of d_o range from 150 to 600 nm. The height of the microcones varies from 50 to 300 nm. It follows that after 2 hours of anodising at j_a = 0.05 mA/cm^2, a porous oxide film is formed on the powder microparticles with individual microcone formations on its surface.

As Fig. 6c shows, the morphology of the AOF formed at j_a = 0.1 mA/cm^2 for t_a = 1 h is similar to that revealed by SEM (Fig. 3a). Closely located microcone formations of different sizes are observed on the surface of the AOF. The assessment of sizes of the bases of the microcones provides values ranging from 0.3 to 1.3 µm and heights of 0.3–0.6 µm, which correlates well with the data obtained when processing the corresponding SEM images (Fig. 3, 4).

AFM images of surface areas of the AOFs formed for 1 hour at high values of current density 0.15 mA/cm^2 and 0.2 mA/cm^2 are presented in Fig. 7a, b. Ensembles of round microcone formations with the height of 0.6 µm are observed on the surface of the AOF. It should be highlighted that while the result of anodizing at j_a = 0.05 mA/cm^2 (t_a = 2 h) on top of the regular porous layer of the AOF is only the presence of individual microcones, at j_a = 0.10–0.20 mA/cm^2 (t_a = 1 h) they completely cover the surface of the film.

The analysis of the distribution of the microcones by effective base diameters of d_b for surface areas with S = 25 µm^2 (Fig. 7c) shows that for the AOFs formed at j_a = 0.15 mA/cm^2 (Fig. 7a), ~ 80 % of the microcones have values of d_o in the range from 0.2 to 0.4 µm, while the weighted mean value of the effective base diameter equals $\langle d_o \rangle \approx 0.34$ µm. For the AOFs obtained at j_a = 0.2 mA/cm^2, the value of d_o for ~ 50 % of the microcones

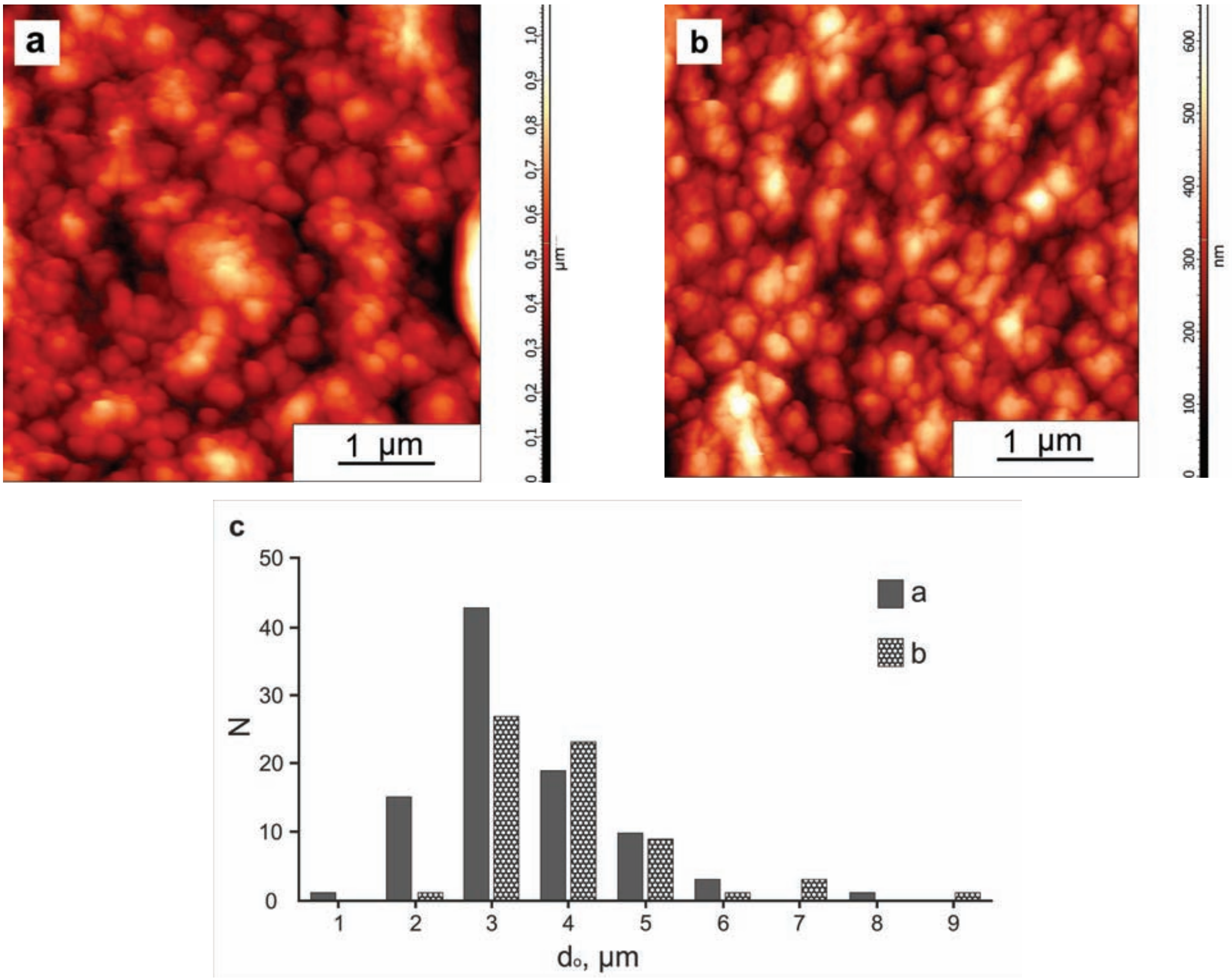

Fig. 7. AFM images of the surface of sintered Nb powders after anodizing in 1 M H_2SO_4 +1% HF (t_a = 1 h) with different values of current density: a) 0.2 mA/cm^2; b) 0.15 mA/cm^2; c) corresponding distributions of oxide microcones by size

is in the range from 0.2 to 0.3 μm, while ~ 20 % of them have 0.3 μm < d_o < 0.4 μm. In this case, the weighted mean value is $\langle d_o \rangle \approx$ 0.29 μm. As for the AOFs formed for 1 hour at j_a = 0.15 and 0.20 мА/см^2, the microcone layer is characterised by a more homogeneous distribution of microcones by sizes as compared to the same distribution for the AOF formed at j_a = 0.1 mA/cm^2 (Fig. 4).

Such microstructures were previously found in the surface layer of the AOF during the anodizing of niobium foil in different electrolytes [7, 15, 18–20, 26, 29, 30], including aqueous solutions of H_2SO_4 with the addition of HF [18, 20, 26]. Generally, in order to obtain a continuous microcone layer, the anodizing of these electrolytes was conducted in voltstatic mode with the voltage from 20 to 60 V and at room temperature, but with a higher concentration of HF (1.5–2 wt%) or an increased duration of the process t_a = 5–12 h. For example, in [26], when anodizing niobium foil in the electrolyte 1 M H_2SO_4+ 1 wt% HF with the voltage U_a = 60 V, a microcone layer with d_o ~ 3–5 μm was formed during t_a = 5 h. Also, the size of the microcones formed on the foil in the electrolytes of similar composition is much bigger as compared to the microcone layers on sintered Nb powders.

Therefore, the anodizing of sintered Nb powders at j_a = 0.1–0.2 mA/cm^2 in a fluorine-containing aqueous electrolyte (1 M H_2SO_4 + 1 % HF) at room temperature for 1 hour forms a continuous crystalline microcone layer on the surface of the AOF. In order to obtain AOF with similar morphology on the surface of niobium foil, it usually requires either considerable time of anodizing or increasing the temperature of the electrolyte [20, 21, 26]. Existing ideas [21, 29] about the initiation and development of microcones in the process of anodizing of niobium foil consider field crystallisation on the metal/AOF barrier layer interface as the main reason for their development. In the process of anodising of sintered Nb powders, the number of nuclei of the crystalline oxide phase of Nb_2O_5, formed under a strong electric field at the metal/oxide interface alongside with the growth of the barrier layer of AOF, will be much higher than in the process of anodizing foil. Apparently, this is caused by the developed relief of powder grains (high specific area of the sintered powder) as well as by substantial presence of oxide in their surface layer [40, 41], which is confirmed by EDXA results.

Therefore, in the process of anodizing sintered Nb powders in a fluorine-containing aqueous electrolyte in galvanostatic mode, with a current density in the range of j_a = 0.1–0.2 mA cm^2, a multilayer oxide film is formed on the surface of powder microparticles in the form of a complex of barrier and regular nanoporous layers adjacent to the substrate and upper crystalline microcone layer. Therefore, it can be said that using the developed technique of galvanostatic anodizing of sintered Nb powders, a new type of oxide crystalline microstructures can be obtained.

4. Conclusions

The anodizing of sintered niobium powder in the fluorine-containing aqueous electrolyte 1 M H_2SO_4 + 1 % HF in galvanostatic mode was studied for the first time. Through the study of the kinetics of growth of an AOF, it was established that the anodizing process (j_a = 0.05–0.20 mA/cm^2, t_a = 1–2 h, T = 21–25 °C) is characterised by transients of $U_a(t)$ typical for the formation of porous and tubular anodic oxide films. Using SEM and AFM methods, it was established that anodizing of sintered niobium samples under such conditions leads to the formation of a heterogeneous AOF with a total thickness of about 2 µm on top of a regular porous oxide layer of which there is a layer consisting of crystalline nanostructured microcones. The super-hydrophilicity, corrosion resistance in biomedia, as well as high level of protein adsorption confirm the potential of the suggested anodic modification technique for the creation of biocompatible powder implants.

Acknowledgements

The authors are grateful to Semenova L. A. and Yakovlev A. N. for their valuable consultations and participation in discussions.

Conflict of interests

The authors declare that they have no known competing financial interests or personal relationships that could have influenced the work reported in this paper.

References

1. Odynets L. L., Orlov V. M. *Anodnye oksidnye plenki* [Anodic oxide films]. Leningrad: Nauka; 1990. 200 p. (in Russ.)

2. Yakovleva N. M., Kokatev A. N., Chupakhina E. A., Stepanova K. V., Yakovlev A. N., Vasil’ev S. G., Shul’ga A. M. Surface nanostructuring of metals and alloys. Part 1. Nanostructured anodic oxide films on Al and Al alloys. *Kondensirovannye sredy i mezhfaznye granitsy* = *Condensed Matter and Interphases*. 2015;17(2): 137–152. Available at: https://journals.vsu.ru/kcmf/article/view/56 (In Russ., abstract in Eng.)

3. Yakovleva N. M., Kokatev A. N., Stepanova K. V., Yakovlev A. N., Chupakhina E. A., Shul’ga A. M., Vasil’ev S. G. Surface nanostructuring of metals and alloys. Part 2. Nanostructured anodic oxide films on Ti and Ti alloys. *Kondensirovannye sredy i mezhfaznye granitsy* = *Condensed Matter and Interphases*. 2016;18(1): 6–27. Available at: https://journals.vsu.ru/kcmf/article/view/104 (In Russ., abstract in Eng.)

4. Sieber I., Hildebrand H., Friedrich A., Schmuki P. Formation of self-organized niobium porous oxide on niobium. *Electrochemistry Communications*. 2005;7: 97–100. DOI: https://doi.org/10.1016/j.elecom.2004.11.012

5. Choi J., Lim J. H., Lee S. C., Chang J. H., Kim K. J., Cho M. A. Porous niobium oxide films prepared by anodization in HF/H_3PO_4. *Electrochimica Acta*. 2006;51: 5502–5507. DOI: https://doi.org/10.1016/j.electacta.2006.02.024

6. Tzvetkov B., Bojinov M., Girginov A., Pébère N. An electrochemical and surface analytical study of the formation of nanoporous oxides on niobium. *Electrochimica Acta*. 2007;52: 7724–7731. DOI: https://doi.org/10.1016/j.electacta.2006.12.034

7. Tzvetkov B., Bojinov M., Girginov A. Nanoporous oxide formation by anodic oxidation of Nb in sulphate–fluoride electrolytes. *J Solid State Electrochem*. 2009;13: 1215–1226. DOI: https://doi.org/10.1007/s10008-008-0651-y

8. Yoo J. E., Choi J. Surfactant-assisted growth of anodic nanoporous niobium oxide with a grained surface. *Electrochimica Acta*. 2010;55: 5142–5147. DOI: https://doi.org/10.1016/j.electacta.2010.04.021

9. Wei W., Lee K., Shaw S., Schmuki P. Anodic formation of high aspect ratio, self-ordered Nb_2O_5 nanotubes. *ChemComm*. 2012;48: 4244–4246. DOI: https://doi.org/10.1039/C2CC31007D

10. Kim H.-K., Yoo J. E., Park J., Seo E. W., Choi J. Formation of Niobium Oxide Film with Duplex Layers by Galvanostatic Anodization. *Bull. Korean Chem. Soc.* 2012;33(8): 2675–2678. http://dx.doi.org/10.5012/bkcs.2012.33.8.2675

11. Yoo J. E., Park J., Cha G., Choi J. Micro-length anodic porous niobium oxide for lithium-ion thin film battery applications. *Thin Solid Films*. 2013;531: 583–587.

12. Shul'ga A. M., Yakovleva N. M., Kokatev A. N., Stepanova K. V., Khanina E. Ya. Anodic surface nanostructuring of tantalum and niobium. *Trudy Kol'skogo nauchnogo tsentra RAN. Khimiya i materialovedenie* [Transactions of the Kola Science Centre of the Russian Academy of Science. Chemistry and material science]. 2015;5(31): 498 – 500. (In Russ.)

13. Minagar S., Berndt C. C., Wen C. Fabrication and characterization of nanoporous niobia, and nanotubular tantala, titania and zirconia via anodization. *J. Funct. Biomater.,* 2015;6: 153–170. DOI: https://doi.org/10.3390/jfb6020153

14. Ryshchenko I. M., Lyashok I. V., Gomozov V. P., Vodolazhchenko S. A., Deribo S. G. Formation of nanostructures on the basis of porous anodic niobium oxide. *Functional materials*. 2019;26(4): 729–733. DOI: https://doi.org/10.15407/fm26.04.729

15. Alias N., Rosli S. A., Hussain Z., Kian T. W., Matsuda A., Lockman Z. Anodised porous Nb_2O_5 for photoreduction of Cr(VI). *Materials Today: Proceedings*. 2019;17: 1033–1039. DOI: https://doi.org/10.1016/j.matpr.2019.06.505

16. Yao D. D., Rani R. A., O'Mullane A. P., Kalantar-Zadeh K., Ou J. Z. High performance electrochromic devices based on anodized nanoporous Nb2O5. *J. Phys. Chem. C*. 2014;118(1): 476-481. DOI: https://doi.org/10.1021/jp410097y

17. Rani R. A., Zoolfakar A. S., O'Mullane A. P., Austina M. W., Kalantar-Zadeh K. Thin films and nanostructures of niobium pentoxide: fundamental properties, synthesis methods and applications. *J. Mater. Chem. A*. 2014;2: 15683–15703. DOI:10.1039/c4ta02561j

18. Karlinsey R. L. Preparation of self-organized niobium oxide microstructures via potentiostatic anodization. *Electrochemistry Communications*. 2005;7: 1190–1194. DOI: https://doi.org/10.1016/j.elecom.2005.08.027

19. Karlinsey R. L. Self-assembled Nb2O5 microcones with tailored crystallinity. *J. Mater. Sci.* 2006;41: 5017–5020. DOI: https://doi.org/10.1007/s10853-006-0135-3

20. Zhao J., Wang X., Xu R., Mi Y., Li Y. Preparation and growth mechanism of niobium oxide microcones by the anodization method. *Electrochem. Solid-State Lett*. 2007;10(4): 31–33. DOI: DOI: https://doi.org/10.1149/1.2458528

21. Oikawa Y., Minami T., Mayama H., Tsujii K., Fushimi K., Aoki Y., Skeldon P., Thompson G. E., Habazaki H. Preparation of self-organized porous anodic niobium oxide microcones and their surface wettability. *Acta Materialia*. 2009;57: 3941–3946. DOI: https://doi.org/10.1016/j.actamat.2009.04.050

22. Yang, S., Aoki Y., Habazaki H. Effect of electrolyte temperature on the formation of self-organized anodic niobium oxide microcones in hot phosphate–glycerol electrolyte. *Applied Surface Science*. 2011;57: 8190–8195. DOI https://doi.org/10.1016/j.apsusc.2011.01.041

23. Yang S., Habazaki H., Fujii T., Aoki Y., Skeldon P., Thompson G. E. Control of morphology and surface wettability of anodic niobium oxide microcones formed in hot phosphate–glycerol electrolytes. *Electrochimica Acta*. 2011;56: 7446–7453. DOI: https://doi.org/10.1016/j.electacta.2011.07.005

24. Jung E., Chang J. H., Jeong B.-Y. Fabrication of niobium oxide nanorods by the anodization method. *Journal of the Korean Electrochemical Society*. 2011;14(4): 196–200. DOI: https://doi.org/10.5229/JKES.2011.14.4.196

25. Jeong B.-Y., Jung E. H. Micro-mountain and nano-forest pancake structure of Nb_2O_5 with surface nanowires for dye-sensitized solar cells. *Met. Mater. Int*. 2013;19(3): 617–622. DOI: https://doi.org/10.1007/s12540-013-3035-5

26. Skatkov, L., Lyashok L., Gomozov V., Tokareva I., Bayrachniy B. Anodic formation of nanoporous crystalline niobium oxide. *J. Electrochem. Sci. Eng*. 2014;4(2): 75–83. DOI: https://doi.org/10.5599/jese.2014.0050

27. Jeong B.-Y., Junga E.-H., Kim J.-H. Fabrication of superhydrophobic niobium pentoxide thin films by anodization. *Applied Surface Science*. 2014;307: 28–32. DOI: https://doi.org/10.1016/j.apsusc.2014.03.111

28. Shaheen B. S., Davenport T. C., Salem H. G., Haile S. M., Allam N. K. Rapid and controlled electrochemical synthesis of crystalline niobium oxide microcones. *MRS Communications*. 2015;5(03): 495–501. DOI https://doi.org/10.1557/mrc.2015.43

29. Bianchin A. C. V., Maldaner G. R., Fuhr L. T., Beltrami L. V. R., Malfatti C. F., Rieder E. S., Kunst S. R., Oliveira C. T. A model for the formation of niobium structures by anodization. *Materials Research*. 2017;20(4): 1010–1023. DOI: http://dx.doi.org/10.1590/1980-5373-MR-2016-0392

30. Wally Z. J., van Grunsven W., Claeyssens F., Goodall R., Reilly G. C. Porous titanium for dental implant applications. *Metals*. 2015;5: 1902–1920; DOI: https://doi.org/10.3390/met504190

31. Kulkarni M., Mazare A., Gongadze E., Perutkova Š., Kralj-Iglic V., Miloљev I., Schmuki P., Iglic A.,

Mozetic M. Titanium nanostructures for biomedical applications. *Nanotechnology*. 2015;26: 1–18. DOI https://doi.org/10.1088/0957-4484/26/6/062002

32. Kokatev A. N., Stepanova K. V., Yakovleva N. M., Tolstik V. E., Shelukhina A. I., Shulga A. M. Self-organisation of a bioactive nanostructured oxide layer on the surface of sintered titanium sponge powder subjected to electrochemical anodisation. *Technical Physics*. 2018;88(9): 1377–1383. DOI: https://doi.org/10.21883/JTF.2018.09.46424.25-18

33. Stepanova K. V., Yakovleva N. M., Kokatev A. N., Pettersson H. Nanoporistye anodno-oksidnye plenki na poroshkovom splave Ti-Al [Nanoporous anodic oxide films on Ti-Al powder alloy]. *Uch.zap. PetrGU.* Seriya Estestvennye i tekhnicheskie nauki. 2015;147(2): 81–86. Available at: http://uchzap.petrsu.ru/files/n147.pdf (In Russ., abstract in Eng.)

34. Stepanova K. V., Yakovleva N. M., Kokatev A. N., Pettersson H. Influence of annealing on the structure of nanoporous oxide films on the surface of titanium–aluminum powder alloy. *Journal of Surface Investigation. X-ray, Synchrotron and Neutron Techniques.* 2016;10(5): 933–941. DOI: https://doi.org/10.7868/s0207352816090134 (In Russ.)

35. Stepanova K. V., Yakovleva N. M., Kokatev A. N., Pettersson H. The structure and properties of nanoporous anodic oxide films on titanium aluminide. *Kondensirovannye sredy i mezhfaznye granitsy = Condensed Matter and Interphases.* 2019;21(1): 135–145. DOI: https://doi.org/10.17308/kcmf.2019.21/724

36. GOST 26252-84. *Poroshok niobievyy. Tekhnicheskie usloviya.* Moscow: Izdatel'stvo standartov; 1990. 47 p. (In Russ.)

37. Shul'ga A. M., Yakovleva N. M., Kokatev A. N., Pettersson H. Nanostrukturirovannye anodno-oksidnye plenki na spechennykh poroshkakh niobiya [Nanostructured anodic oxide films on sintered niobium powders]. In: *Sbornik nauchnykh statey "Nanostruktury v kondensirovannykh sredakh".* Minsk: Institut teplo- i massoobmena imeni A. V. Lykova NAN Belarusi; 2016. pp. 366–370. (In Russ.)

38. Yakovleva N. M., Stepanova K. V., Kokatev A. N., Shul'ga A. M. Chupakhina E. A., Vasil'ev S. G. Electrochemical anodising of sintered powders of metals and alloys. *Trudy Kol'skogo nauchnogo tsentra RAN. Khimiya i materialovedenie* [Transactions of the Kola science centre of the Russian Academy of Science] Iss. 2. P. 1. *The third all-Russian conference with international participation dedicated to the 60th anniversary of the Tananaev Institute of Chemistry and Technology of Rare Elements and Mineral Raw Materials of the Russian Academy of Sciences Kola Science Centre "Research and development in chemistry and technology of functional materials".* Apatity: FPFIS FRC "KSC of RAS" Publ.; 2018;1(9): 479 – 484. (in Russ.)

39. *Modul' obrabotki izobrazheniy Image Analysis P9: spravochnoe rukovodstvo.* Moscow: NT-MDT; 2014. 482 p. (In Russ.)

40. Habazaki H., OgasawaraT., Konno H., Shimizu K., Nagata S., Skeldon P., Thompson G. E. Field crystallization of anodic niobia. *Corrosion Science.* 2007;49(2): 580–593. DOI: https://doi.org/10.1016/j.corsci.2006.06.005

41. Habazaki H., Yamasaki M., Ogasawara T., Fushimi K., Konno H., Shimizu K., Izumi T., Matsuoka R., Skeldon P., Thompson G. E. Thermal degradation of anodic niobia on niobium and oxygen-containing niobium. *Thin Solid Films*. 2008;516(6): 991–998. DOI: https://doi.org/10.1016/j.tsf.2007.06.127

Information about the authors

Natalia M. Yakovleva, DSc in in Physics and Mathematics, Full Professor, Petrozavodsk State University, Petrozavodsk, Republic of Karelia, Russian Federation; e-mail: nmyakov@petrsu.ru, nmyakov@gmail.com. ORCID iD https://orcid.org/0000-0003-4294-0183

Alisa M. Shul'ga, Engineer, Petrozavodsk State University, Petrozavodsk, Republic of Karelia, Russian Federation; e-mail: shulga.alisa@gmail.com. ORCID iD https://orcid.org/0000-0002-3844-7110

Kristina V. Stepanova, PhD in Technology, Engineer, Petrozavodsk State University, Petrozavodsk, Republic of Karelia, Russian Federation; e-mail: lady.cristin4ik@yandex.ru. ORCID iD https://orcid.org/0000-0002-4737-497X lady.cristin4ik@yandex.ru. ORCID iD https://orcid.org/0000-0002-4737-497X

Alexander N. Kokatev, PhD in Technology, Engineer, Petrozavodsk State University, Petrozavodsk, Republic of Karelia, Russian Federation; e-mail: nelan-oksid@bk.ru. ORCID iD https://orcid.org/0000-0002-9449-1482

Vladimir S. Rudnev, DSc in Chemistry, Institute of Chemistry, Far-Eastern Branch of the Russian Academy of Sciences, Vladivostok, Russian Federation; e-mail: rudnevvs@ich.dvo.ru. ORCID iD https://orcid.org/0000-0002-1953-5617

Irina V. Lukiyanchuk, PhD in Chemistry, Senior Researcher, Institute of Chemistry, Far-Eastern Branch of the Russian Academy of Sciences, Vladivostok, Russian Federation; e-mail: lukiyanchuk@ich.dvo.ru. ORCID iD https://orcid.org/0000-0003-1680-4882

Valeriy G. Kuryavyi, PhD in Chemistry, Senior Researcher, Institute of Chemistry, Far-Eastern Branch of the Russian Academy of Sciences, Vladivostok, Russian Federation; e-mail: kvg@dvo.ru. ORCID iD: https://orcid.org/0000-0002-7129-8129

All authors have read and approved the final manuscript.

Translated by Marina Strepetova.
Edited and proofread by Simon Cox.

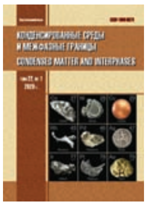

Condensed Matter and Interphases
(Kondensirovannye sredy i mezhfaznye granitsy)

Short communications

To the 90th anniversary of Zhores Alferov, Nobel Prize laureate and a Full Member of the Academy of Sciences

E. P. Domashevskaya

Voronezh State University, 1 Universitetskaya pl., Voronezh 394018, Russian Federation

Zhores Ivanovich Alferov was born on 15 March 1930 in Vitebsk, Belorussian SSR, Soviet Union. He graduated from secondary school No. 42 in Minsk and was awarded with a gold medal for academic excellence. Later he was admitted without entrance exams to the Faculty of Electronic Technology at Ulyanov (Lenin) Leningrad Electrotechnical Institute, which he graduated from in 1952.

From 1953, he worked as a junior researcher at Ioffe Physico-Technical Institute of the USSR Academy of Sciences in the laboratory of Vladimir Tuchkevich and contributed to the development of first Soviet transistors and germanium power devices. In 1961, he earned a PhD degree in Physics and Mathematics. In 1970, Zhores Alferov received a Doctor of Science degree in Physics and Mathematics. In his thesis, he generalised the results of research of semiconductor heterojunctions. In 1972, Zhores Alferov received the title of professor, and a year later he became the head of the Department Branch of Optoelectronics at Leningrad Electrotechnical Institute.

In 1979, Zhores Alferov was elected a full member of the USSR Academy of Sciences (currently Russian Academy of Sciences).

Between 1987 and 2003, he served as the director of Ioffe Physico-Technical Institute of the USSR Academy of Sciences, and was its research director till 2006. Around this time, in 1988, Zhores Alferov became the dean of the newly founded Faculty of Physics and Technology of St. Petersburg Polytechnic University.

From the early 1990s, Zhores Alferov was actively involved in the study of properties of low-dimensional nanostructures, including quantum wires and quantum dots. In 1990–1991, he was elected vice-president of the USSR Academy of Sciences and president of the Leningrad Scientific Centre. From 2003, he was the chair of the academic organisation “St. Petersburg Physics and Technology Research and Education Centre” of the Russian Academy of Sciences. He was editor in chief of the journal “Technical Physics Letters” (Pisma v Zhurnal tekhnicheskoi phisiki). His other titles include honorary full member of the Russian Academy of Education, vice-president of the Russian Academy of Sciences, and the president of Saint Petersburg Scientific Centre.

He was also editor in chief of the journal “Semiconductors” (Phisika i tekhnika poluprovodnikov), member of the editorial board of the journal “Surface: physics, chemistry, mechanics” (Poverkhnost: Phisika, khimia, mekhanika), and member of the editorial board of the journal “Science and Life” (Nauka i Zhizn). He was also on the boards of the RSFSR society “Knowledge” (Znanie).

Zhores Alferov was the author of over five hundred papers, three monographs, and fifty inventions. His Hirsh index was 52. His research has had a great impact on the development of physics and informatics.

As a deputy of the State Duma of the Russian Federation, he initiated the establishment of the Global Energy Prize in 2002 and was the Head of the international award committee till 2006. He was the rector and organiser of the new Academic University in St. Petersburg. On 5 April 2010, Zhores Alferov was appointed the head of the innovation centre Skolkovo and from 2010 he was a co-chairman of the Skolkovo foundation advisory committee.

Zhores Alferov was a Soviet and Russian physicist, Russian Nobel Prize laureate in Physics who received the prize in 2000 for the development of semiconductor heterostructures and the creation of fast opto-electronic and microelectronic components. He was a full member of the Russian Academy of Sciences, an honorary member of the Academy of Sciences of Moldova (from 2000), an honorary member of the Azerbaijan National Academy of Sciences (from 2004), an international member of the National Academy of Sciences of Belarus, an honorary member of the Armenian National Academy of Sciences (from 2011), and an honorary doctor of Voronezh State University (from 2013).

Scientific cooperation between Voronezh physicists and Zhores Alferov goes back to the early 1970s and international conferences dedicated to chemical bonds in semiconductors and solids which were regularly held in Minsk by Nikolai Sirota, the Director of the Institute of Solid-State Physics and Semiconductors and full member of the Academy of Sciences of the Belorussian SSR. Among the participants of these conferences were many prominent American and European scientists. In 1970, at one such conference in Minsk, Evelina Domashevskaya, a young physicist from VSU, heard a plenary presentation dedicated to semiconductor heterostructures based on A^3B^5 semiconductor compounds by Zhores Alferov, a young and well-known scientist from Leningrad who had just completed an internship in the USA. Later, VSU physicists developed scientific connections with the Zhores Alferov's laboratory at Ioffe Physico-Technical Institute (Leningrad) and even sent their students to the laboratory for a few months to complete pre-graduation practical trainings and internships. Evelina Domashevskaya supervised such trainings and internships. Ivan Arsentiev, a graduate of the Department of Solid-State Physics, was among the Voronezh students who had a chance to take part in such programmes. After graduating from VSU, he returned to work at Alferov's laboratory at Ioffe Physico-Technical Institute and became a laureate of the Lenin Komsomol Prize as one of the leading engineers who contributed to the development of heterostructure technologies. He received a Doctor of Science degree and is now working as a leading researcher at Ioffe Physico-Technical Institute of the Russian Academy of Sciences (St. Petersburg). At present, he is the head of the joint laboratory of Ioffe Physico-Technical Institute of the Russian Academy of Sciences and VSU on the side of the Russian Academy of Sciences. On VSU's side, the head of the joint laboratory is Pavel Seredin, a young Doctor of Sciences, who in 2012 defended his doctoral thesis "Substructure and optical properties of epitaxial A^3B^5 heterostructures" supervised by Evelina Domashevskaya. His research was based on objects developed at the "Semiconductor Luminescence and Injection Emitters" laboratory at Ioffe Physico-Technical Institute.

Zhores Alferov holding his diploma of honourable doctorate from Voronezh State University (10 September 2013)

As a result of the many-year cooperation with Ioffe Physico-Technical Institute we have held in Voronezh a number of seminars dedicated to heterostructures. One of them was held just before Zhores Alferov was awarded a Nobel Prize in 2000. It took place at a recreation facility at a picturesque site along the River Usmanka in the Voronezh region. Among the participants of the seminar were scientists from leading research centres in St. Petersburg, Moscow, and Nizhny Novgorod as

The organising committee of the Heterostructures seminar in 2000. From left to right: E. P. Domashevskaya, head of the Department of Solid-State Physics of Voronezh State University, Zh. I. Alferov, director of Ioffe Physico-Technical Institute of the Russian Academy of Sciences, full member of the Russian Academy of Sciences (chair of the organising committee), I. N Arsentiev, leading researcher at Physico-Technical Institute of the Russian Academy of Sciences (graduate of VSU's Faculty of Physics), and N. N. Bezryadin, head of the Department of Physics of Voronezh State University of Engineering Technologies (graduate of VSU's Faculty of Physics).

Zhores Alferov and Evelina Domashevskaya at the meeting with laureates of the Nobel Prize dedicated to the 300th anniversary of St. Petersburg, 18 June 2003

well as developers of semiconductor equipment and heterostructures. The participants of the conference and Zhores Alferov had a trip to the then lively operational site of NPO "Elektronika". Zhores Alferov even expressed his admiration for its site and equipment.

In 2003, already a laureate of the Nobel Prize, Zhores Alferov organised a major International Conference of Laureates of the Nobel Prize in Natural Sciences dedicated to the 300th anniversary of St. Petersburg. The event was held in the office of the Praesidium of St Petersburg Centre of the Russian Academy of Sciences and the Concert hall of the Winter Palace. Evelina Domashevskaya received an invitation to the event.

Later, the laureate of the Nobel Prize, Zhores Alferov, came to Voronezh in 2007 and gave lectures in lecture halls of Voronezh State University and Voronezh State Technical University which were flooded with visitors.

The following year, in 2008, a scheduled International Heterostructures and Nanostructures Symposium took place in St. Petersburg at the academic organisation "St. Petersburg Physics and Technology Research and Education Centre" of the Russian Academy of Sciences. At the event, Evelina Domashevskaya presented the results of joint study of atomic and electronic structure of epitaxial A^3B^5 heterostructures which were obtained at Ioffe Physico-Technical Institute of the Russian Academy of Sciences and became the basis of the doctoral

Zhores Alferov, a Nobel Prize laureate, gives a lecture dedicated to heterostructures in Levitskaya Physics lecture hall. In the background, there is a mural depicting Maria Levitskaya surrounded by her students (VSU, 21 November 2007)

The team of the Department of Solid-State Physics and Nanostructures and Zhores Alferov after his lecture in laboratory 25 (VSU, 21 November 2007)

The personification of friendship and scientific cooperation between Voronezh and St. Petersburg science. Zhores Alferov and Evelina Domashevskaya just after the lecture by Zhores Alferov in Levitskaya Physics lecture hall.

dissertation of Pavel Seredin, the youngest Doctor of Sciences at the Faculty of Physics, who is now a professor (in the photo from 2007 he is standing behind Zhores Alferov).

On 9 September 2013, the Academic Council of Voronezh State University awarded Zhores Alferov with the gown and diploma of honourable doctorate of Voronezh State University during his lecture “Breakthrough technologies in the second half of the 20th century and their present role”.

“I am very grateful to be awarded the title of the Honorary Doctor of Voronezh State University. This is

Professor E.P. Domashevskaya presenting the results of joint research of Voronezh State University and Physico-Technical Institute of the Russian Academy of Sciences at the International Heterostructures and Nanostructures Symposium in St. Petersburg, 2008, headed by Zhores Alferov

Zhores Alferov, Evelina Domashevskaya, and Ivan Arsentiev in the room of the chairman of the organising committee before the beginning of the International Heterostructures and Nanostructures Symposium (St. Petersburg, 2008)

Nobel Prize laureate Zhores Alferov and VSU Rector Dmitry Endovitsky during the lecture, just after Zhores Alferov was awarded with the gown and diploma of honourable doctorate of Voronezh State University

The audience at the lecture of Zhores Alferov, Honorary Doctor of VSU, in the VSU auditorium on 6 September 2013. In the first row, fifth from left is his wife, Tamara Alferova, a well-known Voronezh beauty, a daughter of Georgy Darsky, a famous Voronezh solo singer from the musical theatre. Tamara Alferova accompanied her husband on his last trip to Voronezh.

Zhores Alferov after receiving the diploma of honourable doctorate of Voronezh State University surrounded by university staff and students. To his left is Rector Dmitry Endovitsky and to his right is Professor Evelina Domashevskaya, Honoured Scientist of the Russian Federation

a great honour for me," responded Zhores Alferov in response to the award given by Dmitry Endovitsky.

As usual, the lecture of Zhores Alferov during the extended meeting of the University Academic Council was held in the VSU auditorium, which was tightly packed with visitors.

During his last visit, at the invitation of the VSU rector, Zhores Alferov and his wife Tamara spent about a week in Voronezh and visited VSU and many of its sights in the near vicinity of the city.

At the VSU museum (from left to right) Arkady Minakov, director of the VSU library, Zhores Alferov, full member of Russian Academy of Sciences, Dmitry Endovitsky, VSU rector, and Evelina Domashevskaya

At the VSU museum and its rare books section, Arkady Minakov, director of the VSU library, showed the honorary guests unique and ancient tomes, many of which were inherited from the library of Yuriev university. Zhores Alferov eagerly listened to the remarkable history of our university and he keenly studied the exhibits, photos, and most of all the ancient tomes.

The following day, after the meeting with the Governor of the Voronezh region, Alexei Gordeyev, the guests visited VSU's nature reserve "Galichya Gora" which had been founded by scientists from the Faculty of Biology in 1925 in the area which now belongs to the Lipetsk region but used to be a part of the Voronezh region and prior to this to the vast Voronezh governorate. At the nature reserve the guests enjoyed the Indian summer, the welcoming Russian nature and its unique dwellers who are looked after by remarkable people, the staff of the nature reserve. These people are dedicated enthusiasts who live far from civilization.

Zhores Alferov, Tamara Alferova at the nature reserve “Galichya Gora”

The same day, they visited the D.M.Venevitinov museum which is located in the poet’s ancestral mansion in Novozhivotinnoye.

This eventful week of the last visit to Voronezh finished with a trip by Zhores Alferov and VSU rector Dmitry Endovitsky to our famous “Venevitinovo” recreation facility where the scientist gave a talk

Against the background of the monument to Venevitinov: Zhores Alferov, Tamara Alferova, and the director of the museum (first to the left)

Zhores Alferov and VSU Rector Dmitry Endovitsky (in the centre) surrounded by VSU lecturers and school teachers at the “Venevitinovo” recreation facility and met VSU deans and lectures and teachers from schools supervised by the university.

On 14 September 2018, when VSU celebrated its centenary, The Park of Scientists was opened next to the university's main building. The park has a Walk of Nobel Prize Laureates whose names are associated with Voronezh, including two writers, Ivan Bunin and Mikhail Sholokhov, and three physicists: Pavel Cherenkov, VSU graduate, Nikolai Basov, graduate of Voronezh school No. 11 located near VSU, and Zhores Alferov, Honorary Doctor of VSU. The monuments embodying the discoveries and achievements of the Nobel Prize laureates were created by a young Voronezh sculptor, Maxim Dikunov, who belongs to a family of well-known sculptors from Voronezh, the Pak-Dikunovs.

On 1 March 2019, soon after the end of the festivities dedicated to the anniversary of VSU, we received news of the death of Zhores Alferov, our teacher and dear friend. On the following day, a mourning stand was installed in the university and VSU Rector Dmitry Endovitsky gave a mourning speech in front of the teachers and students. He said that he was grateful of destiny and providence that had brought the genius scientist and great patriot of Russia to our glorious university.

The opening ceremony for the Park of Scientists and the Walk of Nobel Prize Laureates on 14 September 2018

The name of Zhores Ivanovich Alferov, the Grand Citizen and Genius Scientist, has sank deep into the mind of Voronezh State University and the glorious city of Voronezh and will remain there forever.

Note: The biographical data about Zhores Alferov presented in the beginning of the article was taken from the website of Ioffe Physico-Technical Institute.

Information about the author

Evelina P. Domashevskaya, DSc in Physics and Mathematics, Professor, Head of the Department of Solid State Physics and Nanostructures, Voronezh State University, Voronezh, Russian Federation; e-mail: ftt@phys.vsu.ru. ORCID iD: https://orcid.org/0000-0002-6354-4799.

Translated by Irina Charychanskaya.

Condensed Matter and Interphases
(Kondensirovannye sredy i mezhfaznye granitsy)

Short communications

Anniversary of Professor Pavel Fedorov

On 16 April 2020, we celebrate the 70th anniversary of Professor Pavel Pavlovich Fedorov, DSc in Chemistry, chemical process engineer specialising in crystallography and crystal physics, the Head of the Department of Nanotechnologies at Prokhorov General Physics Institute of the Russian Academy of Sciences.

Pavel Fedorov’s research is based on his deep knowledge of physicochemical analysis, he combines methodologies in inorganic chemistry, crystallography, and photonics. His scientific interests are focused on material science and involve the chemistry of inorganic fluorides, crystal growth, thermodynamics of heterogeneous equilibria, crystal chemistry, nanotechnologies, etc. He has developed new functional materials in the form of single crystals, glass, glass ceramics, ceramics (including laser ceramics), powders, nanomaterials, composites to be used as lasers, scintillants, luminophores, construction, optical, and acoustooptical materials, solid electrolytes, and materials for biomedical application. Pavel Fedorov keeps in mind scientific objectives and their possible applications and is also inclined to set and solve more general problems. Among his recent works are projects dedicated to the principles of the synthesis and evolution of nanoparticles assemblages, including proofs of non-classical mechanisms of crystal growth as a result of the coherent intergrowth of nanoparticles.

Pavel Fedorov is regularly involved in teaching, scientific, and organisational activities. He has supervised over 40 graduation papers, 9 PhD theses, and has consulted on 3 doctoral theses. He is well-known for his ability to create research teams, including informal teams. He is excellent at engaging young people in scientific work.

Pavel Fedorov is a laureate of the Prize of the USSR Academy of Sciences and the Academy of Sciences of the Czech Republic 1989. He has been awarded with a medal “850 Years of Moscow”, a Guo Moruo medal of the Academy of Sciences of the People’s Republic of China, and certificates of the Federal service for intellectual property “Top 100 of the best inventions in Russia” for 2012 and 2013. Pavel Fedorov is a member of the Council of the International Organisation for Crystal Growth, research councils of the Russian Academy of Sciences in physical chemistry, condensed matter physics, and inorganic chemistry.

Pavel Fedorov is very committed to his research and studies in science. He has published over 900 papers (according to Web of Science, his Hirsh index is 38) and has made over 35 inventions.

Among his papers are the following monographs:

1. Popov P. A., Fedorov P. P. *Teploprovodnost ftoridnykh opticheskikh materialov* [Thermal conductivity of fluoride optical materials]. Bryansk: “Desyatochka” group; 2012. 210 p. ISBN 978-5-91877-093-1.

2. Bekker T. B., Fedorov P. P. *Fazoobrazovanie i rost kristallov v chetvertoi vzaimnoi sisteme Na, Ba, B // O, F* [Phase formation and crystal growth

in a tetradic reciprocal system of Na, Ba, B // O, F]. Novosibirsk: Siberian Branch of the Russian Academy of Sciences Publ.; 2016. 217 p. ISBN 978-5-7692-1477-6.

3. Fedorov P. P. *Arkhaicheskoie myshlenie: vchera, segodnya, zavtra* [Archaic thinking: yesterday, today, tomorrow]. 3rd edition: modified and updated. Moscow: LENAND; 2017. 344 p.

4. Fedorov P. P. *Gde prokhodit granitsa mezhdu naukoi i lzhenaukoi? Kolichestvenny kriterii i priznaki lzhenauki.* [Where is the boundary between science and pseudo science? Qualitative criteria and indications of pseudo science]. Moscow: LENAND; 2019. 146 p. ISBN 978-5-9710-6505-0.

5. Fedorov P. P. Etudy po fiziko-khimicheskomu analizu [Exercises in physicochemical analysis] / Collected papers. Moscow: Nauka; 2019. 191 p. ISBN 978-5-02-040205-8.

The team of the Faculty of Chemistry have known Pavel Fedorov for a long time: he is the Head of the panel “Physicochemical analysis” at the All-Russian Conference with International Participation “PHYSICAL AND CHEMICAL PROCESSES IN CONDENSED MATTER AND INTERPHASE BOUNDARIES” which is organised and held in Voronezh State University every three years. His plenary presentations have always been of a very high standard. They have opened the way to many interesting discussions and have attracted a lot of young scientists.

Pavel Fedorov is a member of the editorial board and a reviewer of the journal “Kondensirovannye sredy i mezhfaznye granitsy” (Condensed matter and interphases). He provides consultation and support aimed at promoting the journal in international citation databases. We would like to thank him for his thoughtfulness and his assistance in preparing each issue of the journal.

We would like to congratulate Professor Fedorov with his anniversary and wish him good health, every success in his scientific, organisational, and teaching activities for the honour of Russian science.

The team of the Faculty of Chemistry and the editorial board
of the journal “Condensed matters and interphase boundaries”

Condensed Matter and Interphases
(Kondensirovannye sredy i mezhfaznye granitsy)

Guide for Authors – 2020

https://journals.vsu.ru/kcmf/authorguidelines

Manuscripts should be submitted as single **Microsoft Word 2003** files.

Preferred font 12 pt Times New Roman (please, do not use any other fonts, except for Symbol), 1.5 spaced lines, 1.25 cm first-line indent. Decimal values (e.g. 0.1; 0.9; 2.3) should be written using a decimal point.

DOI: https://doi.org/10.17308/kcmf.2020.22/0000 eISSN 2687-0711
Received 10 January 2020
Accepted 15 February 2020
Published online 25 March 2020

Modelling of Interdiffusion and Phase Formation in Thin-Film Two-Layer Systems of Polycrystalline Oxides of Titanium and Cobalt

(all proper nouns should be capitalized; titles and subtitles should be left-aligned)

©2020 N. N. Afonin*[a], V.A. Logacheva[b]

[a]*Voronezh State Pedagogical University,*
86 ul. Lenina, Voronezh 394043, Russian Federation
(official name and address of the organisation)

[b]*Voronezh State University,*
1 Universitetskaya pl., Voronezh 394018, Russian Federation

Abstract

The abstract should be 200-250 words and include the following sections.
Purpose: States the problem considered in the article, its importance, and the purpose of the research.
Experimental: Provides information about the objects being studied and the methods used.
Conclusions: Provides a brief description of the principal results, major conclusions, and their scientific and practical relevance.

Keywords: Please, provide 5-10 keywords for the principle concepts, results, and terms used in the article.

Funding: *Please, list the organisations that provided the funding for the research.*

The study was financially supported by the Russian Foundation for Basic Research (Grant No. …….)

For citation: Afonin N. N., Logacheva V. A. Modelling of interdiffusion and phase formation in the thin-film two-layer system of polycrystalline oxides of titanium and cobalt. *Kondensirovannye sredy i mezhfaznye granitsy = Condensed Matter and Interphases.* 2020; 22(1): 000-000. DOI: https://doi.org/10.17308/kcmf.2020.22/0000

---

*Nikolay N. Afonin, e-mail: nafonin@vspu.ac.ru (*the corresponding author*)

Article structure. The main text of the manuscript should have the following structure.

1. Introduction

THE INTRODUCTION (1–2 pages) states the problem under consideration, its relevance, and the most important tasks that need to resolved. Describe the scientific problems which have not yet been solved and which you seek to solve in your research. The introduction should contain a short critical review of previously published works in this field and their comparative analysis. It is recommended that the analysis is based on 20-30 studies. **The purpose** of the article is implied by the problem statement.

The Vancouver reference style is used in the journal: bibliographic references in the text of the article are indicated by numbers in square brackets; in the references section, the references are numbered in the order they are mentioned in the text.

Example of references:

Equilibria involving indium and gallium halides are very important for the creation of new framework channels with metal clusters [1] in order to develop new optical sources [2,3] and perform the ultrapurification of the corresponding simple substances (metals).

References should primarily be made to original articles published in scientific journals indexed by global citation databases. It is advisable to use 20-30 sources with at least 20 being published over the past 3 years. References should indicate the names of all authors, the title of the article, the name of the journal, year of publication, volume (issue), number, pages, and DOI (Digital Object Identifier https://search.crossref.org/). If a DOI is lacking, a link to the online source of the article must be indicated. References to dissertation abstracts are acceptable, if the texts are available online. It is vital that our readers can find any of the articles or other sources listed in the reference section as fast as possible. Links to unpublished literature sources or sources not available online are unacceptable.

2. Experimental

The EXPERIMENTAL section (2–3 pages) provides the details of the experiment, the methods and the equipment used. The object of the study and the stages of the experiment are described in detail and the choice of research methods is explained.

3. Results and discussion

RESULTS AND DISCUSSION (6–8 pages) should be brief, but detailed enough for the readers to assess the conclusions made. It should also explain the choice of the data being analysed. Measurement units on graphs and diagrams are separated with a coma. **Formulae should be typed using Microsoft Office Equation 3 or Math Type** and aligned on the left side. Latin letters should be in italics. Do not use italics for Greek letters, numbers, chemical symbols, and similarity criteria.

All subheadings should be in italics.

Example

2.1. X-ray diffraction analysis

Example of figure captions in the text of the article: Fig. 1, curve *1*, Fig. 2b.

A complete list of figures should be provided at the end of the paper after the information about the authors.

Figures and tables should not be included in the text of the article. They should be placed on a separate page. Figures should also be **submitted as separate** *tif, *jpg, *cdr, or *ai. files. **All figures should have a minimum resolution of 300 dpi.** Name each figure file with the name of the first author and the number of the figure.

Example:

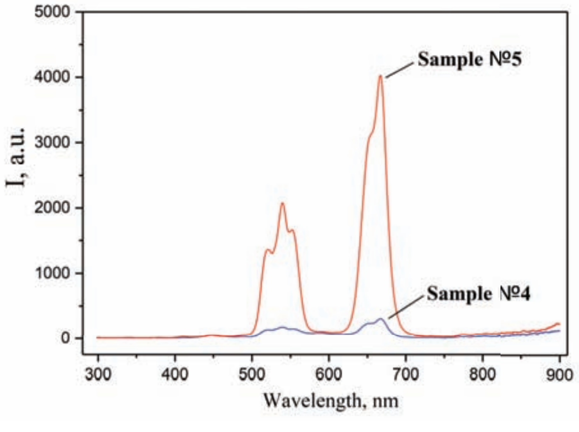

Fig. 5. Luminescence spectra of samples No. 4 and 5. The wavelength of the pumping laser is 974 nm

Example:

Table 1. Synthesis conditions and actual yield

Sample No.	Reference number	Annealing temperature, °C	Annealing time, hours	Concentrations of the starting materials, mol. (M, Ln)(NO3)x:NaF:$NaNO_3$	Actual yield, wt%
1	F1804	300	1	1:3:2	87.0
2	F1814	300	1	1:3:2	86.2
3	F1826	300	3	1:3:2	91.2
4	F1699	400	1	1:3:10	77.2
5	F1836	400	3	1:3:2	76.0

4. Conclusions

CONCLUSIONS (1 paragraph) should briefly state the main conclusions of the research. Do not repeat the text of the article. The obtained results are to be considered with respect to the purpose of the research. This section includes the conclusions, a summary of the results, and recommendations. It states the practical value of the research and outlines further research problems in the corresponding field.

Acknowledgements

List here those individuals who provided help during the research.

Conflict of interests

The authors declare that they have no known competing financial interests or personal relationships that could have influenced the work reported in this paper.

References

The references are to be formatted according to the ***VANCOUVER STYLE****. The reference list should only include articles published in peer-reviewed journals.*

Examples:

Reference to a journal publication

1. Afonin N. N., Logacheva V. A. Interdiffusion and phase formation in the Fe–TiO_2. *Semiconductors*. 2017;51(10): 1351–1356. DOI: https://doi.org/10.21883/FTP.2017.10.45012.8531

2. Domashevskaya E. P., Ryabtsev S. V., Min C., Ivkov S. A., Avilov S. V. Effect of the gas transport synthesis temperature on the ZnO crystal morphology. *Kondensirovannye sredy i mezhfaznye granitsy = Condensed Matter and Interphases*. 2016;18(4): 513–520. Available at: https://journals.vsu.ru/kcmf/article/view/160/84

Reference to a book

3. Kofstad P. *Nonstoichiometry, diffusion, and electrical conductivity in binary metal oxides*. Wiley-Interscience; 1972. 382 p.

4. McCafferty E. *Introduction to corrosion science*. New York: Springer; 2010. 583 p.

5. Vvedenskii A. V., Kozaderov O. A. Linear voltammetry of anodic selective dissolution of homogeneous metallic alloys. In: Saito Y., Kikuchi T. (eds.) *Voltammetry: theory, types and applications.* New York: Nova Science Publishers, Inc.; 2014. 363 p.

Reference to conference proceedings

6. Afonin N. N., Logacheva V. A., Khoviv A. M. Synthesis and properties of functional nanocrystalline thin-film systems based on complex iron and titanium oxides. *In: Amorphous and microcrystalline semiconductors: Proc. 9th Int. Conf., 7–10 July 2014.* St. Petersburg: Polytechnic University Publ.; 2014. p. 356–357.

Reference to online sources

7. NIST Standard Reference Database 71. *NIST Electron Inelastic-Mean-Free-Path Database: Version 1.2.* Available at: www.nist.gov/srd/nist-standard-reference-database-71

Information about the authors

This section should include the full last and first name(s) of the author(s), their academic degree, academic title, affiliation, position, city, country, e-mail, and ORCID (register for an ORCID here https://journals.vsu.ru/kcmf/user/register).

Example

Nikolay N. Afonin, DSc in Chemistry, Research Fellow, Professor at the Department of *Science and Technology Studies, Voronezh State Pedagogical University, Voronezh,* Russian Federation; e-mail**:** nafonin@vspu.ac.ru. ORCID iD: https://orcid.org/0000-0002-9163-744X.

Vera A. Logachova, PhD in Chemistry, Research Fellow at the Department of General and Inorganic Chemistry, Voronezh State University, Voronezh, Russian Federation; e-mail: kcmf@main.vsu.ru. ORCID iD: https://orcid.org/0000-0002-2296-8069.

Valery V. Voronov, PhD in Physics and Mathematics, Head of the Laboratory, Prokhorov General Physics Institute of the Russian Academy of Science, Moscow, Russian Federation; e-mail: voronov@lst.gpi.ru. ORCID iD: https://orcid.org/0000-0001-5029-8560.

All authors have read and approved the final manuscript.

Accompanying documents: *The following documents should be submitted as PDF files:* covering letter (with authorisation for open access publication)

license agreement *(signed by all authors)* https://journals.vsu.ru/kcmf/navigationMenu/view/authorguidelines

EDITING AND PROOFREADING

When the layout is ready it is sent back to the authors for proofreading. The article should be sent back to the publisher within a maximum of three days. The authors may only correct printing mistakes and introduce minor changes to the text or tables.